

BMO TR-81-61

SAI DOCUMENT NO. SAI-063-81R-051



LEVEL III 1710 88

ADA108848

**PERFORMANCE TECHNOLOGY PROGRAM  
(PTP-S II)**

**VOLUME IX**

**EVALUATION OF REENTRY VEHICLE NOSETIP TRANSITION  
AND HEAT TRANSFER IN THE AEDC HYPERBALLISTICS TRACK G**

SCIENCE APPLICATIONS, INC.  
APPLIED MECHANICS OPERATION  
EL SEGUNDO, CALIFORNIA 90245

JANUARY, 1981

FINAL REPORT FOR PERIOD DECEMBER 1977 - SEPTEMBER 1979

CONTRACT NO. F04071-77-C-0126

APPROVED FOR PUBLIC RELEASE; DISTRIBUTION UNLIMITED.

AIR FORCE BALLISTIC MISSILE OFFICE  
NORTON AIR FORCE BASE, CALIFORNIA 92409

DTIC  
ELECTE  
S DEC 28 1981

412 705 81 12 28 D  
122

DTIC FILE COPY

This final report was submitted by Science Applications, Inc., 1200 Prospect Street, La Jolla, California 92038, under Contract Number F04701-77-C-0126 with the Ballistic Missile Office, AFSC, Norton AFB, California. Major Kevin E. Yelmgren, BMO/SYDT, was the Project Officer in charge. This technical report has been reviewed and is approved for publication.

*Kevin E. Yelmgren*

---

KEVIN E. YELMGREN, Major, USAF  
Chief, Vehicle Technology Branch  
Reentry Technology Division  
Advanced Ballistic Reentry Systems

FOR THE COMMANDER

*Nicholas C. Belmonte*

---

NICHOLAS C. BELMONTE, Lt Col, USAF  
Director, Reentry Technology Division  
Advanced BALLISTIC Reentry Systems

UNCLASSIFIED

SECURITY CLASSIFICATION OF THIS PAGE (When Data Entered)

REPORT DOCUMENTATION PAGE		READ INSTRUCTIONS BEFORE COMPLETING FORM
1. REPORT NUMBER BMO TR-81-61	2. GOVT ACCESSION NO. AD-A208	3. RECIPIENT'S CATALOG NUMBER 848
4. TITLE (and Subtitle) Performance Technology Program (PTP-S II), Vol. IX, "Evaluation of Reentry Vehicle Nose- tip Transition and Heat Transfer in the AEDC Hyperballistics Track G		5. TYPE OF REPORT & PERIOD COVERED Final Report: 12/77-9/79
7. AUTHOR(s) A. T. Wassel W. C. L. Shih R. J. Curtis		6. PERFORMING ORG. REPORT NUMBER SAI-063-81R-051
9. PERFORMING ORGANIZATION NAME AND ADDRESS Science Applications, Inc. 101 Continental Blvd., Suite 310 El Segundo, California 90245		8. CONTRACT OR GRANT NUMBER(s) F04701-77-C-0126
11. CONTROLLING OFFICE NAME AND ADDRESS Ballistic Missile Office (BMO) Norton AFB, California 92409		10. PROGRAM ELEMENT, PROJECT, TASK AREA & WORK UNIT NUMBERS
14. MONITORING AGENCY NAME & ADDRESS (if different from Controlling Office)		12. REPORT DATE January 1981
		13. NUMBER OF PAGES 203
		15. SECURITY CLASS. (of this report) Unclassified
		15a. DECLASSIFICATION/DOWNGRADING SCHEDULE
16. DISTRIBUTION STATEMENT (of this Report)  Approved for public release: Distribution unlimited Distribution Statement "A": of AFR 80-45 applies.		
17. DISTRIBUTION STATEMENT (of the abstract entered in Block 20, if different from Report)		
18. SUPPLEMENTARY NOTES		
19. KEY WORDS (Continue on reverse side if necessary and identify by block number)  Reentry vehicle, nosetip, boundary layer transition		
20. ABSTRACT (Continue on reverse side if necessary and identify by block number)  Boundary layer transition and surface heating distributions on graphite fine weave carbon-carbon, and metallic nosetip materials were derived from surface temperature responses measured in nitrogen environments during both free-flight and track-guided testing in the AEDC Hyperballistics Range/Track G.  Innovative test procedures were developed, and heat transfer results were vali- dated against established theory through experiments using a super-smooth tung-		

DD FORM 1473 EDITION OF 1 NOV 65 IS OBSOLETE

UNCLASSIFIED

SECURITY CLASSIFICATION OF THIS PAGE (When Data Entered)

sten model. Quantitative definitions of mean transition front locations were established by deriving heat flux distributions from measured temperatures, and comparisons made with existing nosetip transition correlations. Qualitative transition locations were inferred directly from temperature distributions to investigate preferred orientations on fine weave nosetips. Levels of roughness augmented heat transfer were generally shown to be below values predicted by state of the art methods.

Accession For	
NTIS GRA&I	<input checked="" type="checkbox"/>
DTIC TAB	<input type="checkbox"/>
Unannounced	<input type="checkbox"/>
Justification	
By _____	
Distribution/ _____	
Availability Codes	
Dist	Avail and/or Special
A	

## TABLE OF CONTENTS

	<u>Page</u>
LIST OF FIGURES . . . . .	-v-
LIST OF TABLES . . . . .	-xii-
1.0 INTRODUCTION . . . . .	1
2.0 FACILITY AND MODEL DESCRIPTION . . . . .	4
2.1 Facility Description . . . . .	4
2.1.1 Range Description . . . . .	4
2.1.2 Range Instrumentation . . . . .	6
2.2 Track G Models . . . . .	6
3.0 MODEL SURFACE PREPARATION AND CHARACTERISTICS . . . . .	10
3.1 Model Surface Preparation . . . . .	10
3.1.1 Tungsten Models . . . . .	10
3.1.2 Graphitic Models . . . . .	10
3.2 Model Surface Characterization . . . . .	15
3.2.1 Pre-Flight Surface Characterization . . . . .	22
3.2.2 Post-Flight Surface Characterization . . . . .	27
4.0 TEST DESCRIPTION . . . . .	49
4.1 Test Matrix . . . . .	49
4.2 Surface Temperature Data Reduction . . . . .	49
4.3 Data Uncertainty . . . . .	55
4.4 Track G Related Problems . . . . .	55
4.4.1 Luminosity Effects from Extraneous Sources . . . . .	55
4.4.2 Other Considerations . . . . .	66
5.0 ANALYSIS . . . . .	67
5.1 Data Format . . . . .	67
5.2 Modeling and Data Reduction . . . . .	70

	<u>Page<sup>1</sup></u>
5.3 Codes Utilized in the Analysis . . . . .	76
5.3.1 The ABRES Shape Change Code (ASCC) . . . . .	76
5.3.2 The SAI CAPER-2D Code . . . . .	79
5.3.3 Matrix of the Analyzed Shots . . . . .	80
6.0 TRANSITION RESULTS . . . . .	86
6.1 Nosetip Transition Correlations . . . . .	86
6.1.1 Anderson - PANT Correlation . . . . .	86
6.1.2 Bishop's Transition Correlation . . . . .	86
6.1.3 Dirling's Transition Correlation . . . . .	87
6.2 Data Inferred Transition Location . . . . .	88
6.3 Comparisons with Transition Correlations . . . . .	92
6.3.1 Comparisons with the PANT Correlation . . . . .	92
6.3.2 Comparisons with Dirling's and Bishop's Transition Correlations . . . . .	93
6.3.3 Comparisons with Reda-Raper Transition Data . . . . .	93
7.0 HEAT TRANSFER RESULTS . . . . .	123
7.1 Stagnation Point Heat Transfer Augmentation . . . . .	123
7.1.1 Augmentation Factors . . . . .	123
7.1.2 Comparisons with the PANT and Phinney's Laminar Augmentation Correlations . . . . .	125
7.2 Transitional/Turbulent Heat Transfer Augmentation. . . . .	127
7.2.1 Data Derived Rough Wall Heat Transfer Augmentation Factors . . . . .	139
7.2.2 Comparisons with the ASCC Turbulent Heating Augmentation Methodology . . . . .	163
8.0 SUMMARY AND CONCLUSIONS . . . . .	179
9.0 RECOMMENDATIONS . . . . .	186
10.0 REFERENCES . . . . .	188

## LIST OF FIGURES

		<u>Page</u>
Figure 2.1	Track Photopyrometer Arrangement . . . . .	5
Figure 2.2	In-Flight Laser Photos at 152M from Range Entrance . . . . .	7
Figure 2.3.A	Model Design Detail . . . . .	9
Figure 2.3.B	Track Constrained Model. . . . .	9
Figure 3.1	Aerotherm Operating Envelope for Stagnation Point Model Testing in Air. . .	11
Figure 3.2	CAPER-1D Pretest Predictions . . . . .	13
Figure 3.3	Definition of Surface Characterization Parameters . . . . .	21
Figure 3.4	Typical GE 223 CC Nosetip . . . . .	23
Figure 3.5	Recovered Tungsten Nosetip (W/SSR 30). . .	24
Figure 3.6	Preconditioned GE 223 Nosetip. . . . .	25
Figure 3.6.C	Full Section Photomicrograph of GE 223 Nosetip . . . . .	26
Figure 3.6.D	Cross Sectional Photomicrograph of GE 223 Preconditioned Nosetip . . . . .	28
Figure 3.7	Cross Sectional Photomicrograph of Pre-Roughened Tungsten Replica Nosetip . .	29
Figure 3.8	Full Section Photomicrograph of 994-2 Preconditioned Model . . . . .	30
Figure 3.9	Cross Sectional Photomicrograph ATJ-S Nosetip . . . . .	31
Figure 3.10	Cross Sectional Photomicrograph of 994-2 Nosetip . . . . .	32
Figure 3.11	Microroughness Height Distribution for Preconditioned GE CC-223 . . . . .	33
Figure 3.12	Microroughness Height Distribution for Grit Blasted Tungsten . . . . .	34

		<u>Page</u>
Figure 3.13	Microroughness Height Distribution for Preconditioned 994-2 . . . . .	35
Figure 3.14	Microroughness Height Distribution for Preconditioned ATJ-S . . . . .	36
Figure 3.15	Full Section Photomicrograph of CC-223 Nosetip - Shot 4871 . . . . .	38
Figure 3.16	Full Section Photomicrograph of CC-223 Nosetip - Shot 4880 . . . . .	39
Figure 3.17	Full Section Photomicrograph of 994-2 Nosetip - Shot 4886 . . . . .	40
Figure 3.18	Cross Sectional Photomicrograph of CC-223 Nosetip - Shot 4871 . . . . .	41
Figure 3.19.A	Microroughness Height Distribution for GE223 - Shot 4871 (Post Flight) . . . . .	43
Figure 3.19.B	Microroughness Height Distribution for GE223 - Shot 4871 (Post Flight) . . . . .	44
Figure 3.20	Cross Sectional Photomicrograph of 944-2 Nosetip - Shot 4886 . . . . .	45
Figure 3.21	Microroughness Height Distribution for 994-2 - Shot 4886 . . . . .	46
Figure 3.22	Pre and Postflight Photographs of 994-2 Graphite . . . . .	47
Figure 4.1	Arrangement of Points of Projection for Temperature Recording (Viewing Up Range) .	56
Figure 4.2	Brightness Temperature Distribution on 0.4 <sup>n</sup> Radius Tungsten Hemisphere. . . . .	58
Figure 4.3	Measurement of Low Temperature Surface, Adjacent to High Temperature Zone . . . . .	59
Figure 4.4	Minimum Measurable Temperature vs Distance from High Temperature Background	60
Figure 4.5	ICC Photographs of Graphite and Carbon- Carbon Nosetips . . . . .	62
Figure 4.6	ICC Photographs of Tungsten Nosetips . . .	63
Figure 4.7	Brightness Temperature Distribution on 1/4 <sup>n</sup> Radius Tungsten Hemisphere . . . . .	64

		<u>Page</u>
Figure 4.8	Mean Brightness Temperature Distribution Around Hemispherical Nosetip . . . . .	65
Figure 5.1	Nosetip Mean Temperature Profiles . . . . .	68
Figure 5.2	Mean, Maximum, Minimum and Standard Deviation Profiles . . . . .	69
Figure 5.3	Wall Temperature Interpolation . . . . .	74
Figure 5.4	Heat Transfer Rate Calculations . . . . .	75
Figure 5.5	Computed Heat Transfer Distributions Used in Evaluations of Data Reduction Procedures	77
Figure 5.6	Computed Surface Temperature Distributions Used in Evaluations of Data Reduction Procedures . . . . .	78
Figure 6.1	Transition Statistics for Tungsten (Shot 4882) . . . . .	95
Figure 6.2	Transition Statistics for ATJ-S (Shot 4974)	96
Figure 6.3	Transition Statistics for 994-2 (Shot 4951)	97
Figure 6.4	Transition Statistics for 994-2 (Shot 5018)	98
Figure 6.5	Transition Statistics for CC-223 (Shot 4880) . . . . .	99
Figure 6.6	Transition Statistics for CC-223 (Shot 5068) . . . . .	100
Figure 6.7	Transition Statistics for CC-223 (Shot 5069) . . . . .	101
Figure 6.8	Circumferential Distributions of Transition Locations for Tungsten (Shot 4882) . . . . .	102
Figure 6.9	Circumferential Distributions of Transition Locations for ATJ-S (Shot 4974) . . . . .	103
Figure 6.10	Circumferential Distributions of Transition Locations for 994-2 (Shot 7951) . . . . .	104
Figure 6.11	Circumferential Distributions of Transition Locations for 994-2 (Shot 5018) . . . . .	105

	<u>Page</u>
Figure 6.12	Circumferential Distributions of Transition Locations for CC-223 (Shot 4880) . . . . . 106
Figure 6.13	Circumferential Distributions of Transition Locations for CC-223 (Shot 5068) . . . . . 107
Figure 6.14	Circumferential Distributions of Transition Locations for CC-223 (Shot 5069) . . . . . 108
Figure 6.15	Comparison Between Data and PANT Correlation for $K_{RMS}$ (Free-Flight) . . . . . 111
Figure 6.16	Comparison Between Data and PANT for W, ATJ-S and 994-2 and $K_{mean}$ . . . . . 112
Figure 6.17	Comparison Between Data and PANT for CC-223 and $K_{mean}$ . . . . . 113
Figure 6.18	Comparisons Between Mean Transition Front Data and Dirling's Correlation for $K = K_{mean}$ . . . . . 116
Figure 6.19	Comparison Between Mean Transition Front Data and Dirling's Correlation for $K = K_{mean} / (1 + 350K_{mean} / R_N)$ . . . . . 117
Figure 6.20	Comparison Between Mean Transition Front Data and Bishop's Correlation . . . . . 118
Figure 6.21	Mean Transition Front Data vs. Freestream Pressure . . . . . 119
Figure 6.22	Mean Heat Flux-Inferred Transition Front Data vs. Freestream Pressure . . . . . 120
Figure 6.23	Mean Transition Front Data vs. $(K/\theta)$ . . . . . 121
Figure 6.24	Mean Transition Front Data vs. Freestream Reynolds Number . . . . . 122
Figure 7.1	Comparison Between Data and PANT Predictions for the Stagnation Point Heat Transfer Augmentation Factors . . . . . 126
Figure 7.2	Comparison Between Data and Phinney's Correlation for the Stagnation Point Augmentation Heat Transfer Factors . . . . . 128
Figure 7.3	Stagnation Point Augmentation Factors for CC-223 vs. Freestream Reynolds Number . . . . . 129

		<u>Page</u>
Figure 7.4	Stagnation Point Augmentation Factors for 994-2, ATJ-S, W vs. Freestream Reynolds Number . . . . .	130
Figure 7.5	Stagnation Point Augmentation Factors for CC-223 vs Normal Shock Reynolds Number . . . . .	131
Figure 7.6	Stagnation Point Augmentation Factors for 994-2, ATJ-S, W vs. Normal Shock Reynolds Number . . . . .	132
Figure 7.7	Stagnation Point Augmentation Factors for CC-223 vs. $K/\theta$ . . . . .	133
Figure 7.8	Stagnation Point Augmentation Factors for 994-2, ATJ-S, W vs. $K/\theta$ . . . . .	134
Figure 7.9	Stagnation Point Augmentation Factors for CC-223 vs. $K/\delta^*$ . . . . .	135
Figure 7.10	Stagnation Point Augmentation Factors for 994-2, ATJ-S, W vs. $K/\delta^*$ . . . . .	136
Figure 7.11	Data-Inferred and Predicted Smooth Wall Heat Transfer Distribution Around Nose- tip - Shot 4882 . . . . .	140
Figure 7.12	Ratio of Data-Inferred to Predicted Smooth Wall Heat Transfer Coefficients Around Nosetip - Shot 4882 . . . . .	141
Figure 7.13	Data-Inferred and Predicted Smooth Wall Heat Transfer Distribution Around Nosetip - Shot 4963 . . . . .	142
Figure 7.14	Ratio of Data-Inferred to Predicted Smooth Wall Heat Transfer Coefficients Around Nosetip - Shot 4963 . . . . .	143
Figure 7.15	Data-Inferred and Predicted Smooth Wall Heat Transfer Distribution Around Nosetip - Shot 4953 . . . . .	144
Figure 7.16	Ratio of Data-Inferred to Predicted Smooth Wall Heat Transfer Coefficients Around Nosetip - Shot 4953 . . . . .	145
Figure 7.17	Data-Inferred and Predicted Smooth Wall Heat Transfer Distribution Around Nosetip - Shot 4974 . . . . .	146

		<u>Page</u>
Figure 7.18	Ratio of Data-Inferred to Predicted Smooth Wall Heat Transfer Coefficients Around Nosetip - Shot 4974 . . . . .	147
Figure 7.19	Data-Inferred and Predicted Smooth Wall Heat Transfer Distribution Around Nosetip - Shot 4951 . . . . .	148
Figure 7.20	Ratio of Data-Inferred to Predicted Smooth Wall Heat Transfer Coefficients Around Nosetip - Shot 4951 . . . . .	149
Figure 7.21	Data-Inferred and Predicted Smooth Wall Heat Transfer Distribution Around Nose-tip - Shot 5018 . . . . .	150
Figure 7.22	Ratio of Data-Inferred to Predicted Smooth Wall Heat Transfer Coefficients Around Nosetip - Shot 5018 . . . . .	151
Figure 7.23	Data-Inferred and Predicted Smooth Wall Heat Transfer Distribution Around Nose-tip - Shot 4871 . . . . .	152
Figure 7.24	Ratio of Data-Inferred to Predicted Smooth Wall Heat Transfer Coefficients Around Nosetip - Shot 4871 . . . . .	153
Figure 7.25	Data-Inferred and Predicted Smooth Wall Heat Transfer Distribution Around Nosetip - Shot 4880 . . . . .	154
Figure 7.26	Ratio of Data-Inferred to Predicted Smooth Wall Heat Transfer Coefficients Around Nosetip - Shot 4880 . . . . .	155
Figure 7.27	Data-Inferred and Predicted Smooth Wall Heat Transfer Distribution Around Nose-tip - Shot 4954 . . . . .	156
Figure 7.28	Ratio of Data-Inferred to Predicted Smooth Wall Heat Transfer Coefficients Around Nosetip - Shot 4954 . . . . .	157
Figure 7.29	Data-Inferred and Predicted Smooth Wall Heat Transfer Distribution Around Nose-tip - Shot 5068 . . . . .	158
Figure 7.30	Ratio of Data-Inferred to Predicted Smooth Wall Heat Transfer Coefficients Around Nosetip - Shot 5068 . . . . .	159
Figure 7.31	Data-Inferred and Predicted Smooth Wall Heat Transfer Distribution Around Nose-tip - Shot 5069 . . . . .	160

	<u>Page</u>
Figure 7.32	Ratio of Data-Inferred to Predicted Smooth Wall Heat Transfer Coefficients Around Nose- tip - Shot 5069 . . . . . 161
Figure 7.33	Ratio of Data-Inferred to ASCC Predicted Rough Wall Heat Transfer Coefficients Around Noretip - Shot 4882 . . . . . 167
Figure 7.34	Ratio of Data-Inferred to ASCC Predicted Rough Wall Heat Transfer Coefficients Around Noretip - Shot 4953 . . . . . 168
Figure 7.35	Ratio of Data-Inferred to ASCC Predicted Rough Wall Heat Transfer Coefficients Around Noretip - Shot 4974 . . . . . 169
Figure 7.36	Ratio of Data-Inferred to ASCC Predicted Rough Wall Heat Transfer Coefficients Around Noretip - Shot 4951 . . . . . 170
Figure 7.37	Ratio of Data-Inferred to ASCC Predicted Rough Wall Heat Transfer Coefficients Around Noretip - Shot 5018 . . . . . 171
Figure 7.38	Ratio of Data-Inferred to ASCC Predicted Rough Wall Heat Transfer Coefficients Around Noretip - Shot 4871 . . . . . 172
Figure 7.39	Ratio of Data-Inferred to ASCC Predicted Rough Wall Heat Transfer Coefficients Around Noretip - Shot 4880 . . . . . 173
Figure 7.40	Ratio of Data-Inferred to ASCC Predicted Rough Wall Heat Transfer Coefficients Around Noretip - Shot 4954 . . . . . 174
Figure 7.41	Ratio of Data-Inferred to ASCC Predicted Rough Wall Heat Transfer Coefficients Around Noretip - Shot 5068 . . . . . 175
Figure 7.42	Ratio of Data-Inferred to ASCC Predicted Rough Wall Heat Transfer Coefficients Around Noretip - Shot 5069 . . . . . 176
Figure 7.43	Ratios of Data Derived to ASCC-Predicted Rough Wall Heat Transfer Coefficients . . . 177

## LIST OF TABLES

		<u>Page</u>
Table 3.1	APG Operating Conditions . . . . .	16
Table 3.2	Model Number Designations for Ablation Preconditioning Tests . . . . .	17
Table 3.3	Ablation Preconditioning Results . . . . .	18
Table 3.4	Summary of Preflight Surface Microroughness Characteristics . . . . .	48
Table 4.1	Test Matrix . . . . .	50
Table 4.2	Test Conditions . . . . .	53
Table 5.1	Matrix of Analyzed Shots . . . . .	81
Table 5.2	Launch Conditions of Analyzed Shots. . . . .	82
Table 5.3	Trajectory Information of Analyzed Shots . . . . .	83
Table 6.1	Nosetip Transition Front Location . . . . .	89
Table 6.2	Transition Location Statistics . . . . .	109
Table 6.3	Calculated Flow Properties at Measured Transition Location . . . . .	110
Table 6.4	Inferred Roughness Results using PANT Correlation . . . . .	114
Table 6.5	Comparison of Range Data with Transition Models . . . . .	115
Table 7.1	Stagnation Point Heat Transfer Augmentation. . . . .	124
Table 7.2	Heat Transfer Augmentation Factors . . . . .	162
Table 7.3	Maximum Roughness Reynolds Number on Nosetip . . . . .	164
Table 7.4	Ratio of Data Derived to Computer Heat Transfer Rates . . . . .	166

### ACKNOWLEDGEMENTS

This research was sponsored by the Space and Missile Systems Organization (SAMSO) of the Air Force Systems Command. Capt. R. Chambers was the project officer. The project monitor was Mr. W. Portinier of the Aerospace Corporation. The authors wish to express their thanks to Mr. Richard Raper and the staff of the AEDC VKF Range G facility for their competent support and many valuable contributions to this research effort.

## 1.0 INTRODUCTION

Analysis of the flight data base, coupled with key ground test programs, has shown that nosetip related effects markedly influence reentry vehicle performance. In clear air environments the two major phenomena affecting performance are nosetip transition and heating augmentation. The understanding of these effects is essential for both advanced ballistic vehicles and for evolving maneuvering vehicle designs.

Nosetip transition is triggered by some roughness height characteristic of the particular material. Since real materials possess a definite statistical distribution of roughness height it is not certain which roughness height causes transition. Also, real material may not have a uniform surface roughness distribution, which in turn results in asymmetry in the transition process. For woven carbon-carbons, for example, there may exist a transition-front shape which is related to the weave pattern of the material. Once the onset of transition occurs on the nosetip, transitional and turbulent flows exist and cause higher surface heat transfer rates (which can be further augmented by the surface roughness) which will accelerate the ablation process. These effects will bring about geometry variations in the nosetip that will greatly affect the vehicle accuracy and survivability.

To properly understand whether or not nosetip shaping presents a problem to any vehicle design, and to intelligently pursue materials and designs for advanced system nosetips, it is necessary to have at least an adequate understanding of those physical processes which control the tendency of the nosetip to change shape.

The desire to predict the fine structure of nosetip transition, and the rough wall heat transfer that follows it, has been part of reentry vehicle work for a decade. Early well regarded work under the ABRES PANT program generated volumes of

wind tunnel data on rough surface heat transfer and transition. Similar wind tunnel experiments were carried out under ABRES STREET programs, and complementary data has been collected under a number of other DOD and university programs. Until recently, however, this data base has been almost exclusively wind tunnel derived, using metallic models with artificial roughness in low Mach number/marginal Reynolds number flows.

The need for a validation of this existing data base via experiments using real materials in flight-replicating environments has been recognized for some time. Holden, (Ref. 1) at CALSPAN, has been conducting high Mach/Reynolds number experiments on room temperature metallic models in his shock tunnel facility, and has produced results in serious conflict with the existing data base. Reda, (Ref. 2) at NSWC, has utilized the ballistics range to study transition and heat transfer on graphitic models, and has generated results contrary to the earlier wind tunnel findings. SAI (Ref. 3) collected transition data on tungsten and graphite models at the AEDC ballistic range and showed results that are also contradicting to the wind tunnel data.

Several key questions remain unanswered, and these are:

- 1) What is the form of the transition process in flight environments.
- 2) What is the characteristic material roughness height that triggers transition.
- 3) What are the magnitudes of heating augmentation brought about by the surface roughness.

The object of the present program is to address the above questions. Tungsten and graphitic materials were tested in simulated flight environments. These environments are characterized by high enthalpy, stagnation pressure and freestream Reynolds numbers similar to those of flight environments. The object of the testing was to:

- 1) Investigate roughness effects on nosetip transition.
- 2) Investigate roughness effects on heating augmentation.

- 3) Verify state-of-the-art predictive models as to their applicability to flight environments.

This document presents the analysis of the data collected in the AEDC Track G facility as well as some free flight data. The various problems encountered in the development and calibration of the track are briefly discussed. Transition and heat transfer results are presented and compared with state-of-the-art predictive methodologies. Recommendations are made for future facility utilizations and directions to be taken for additional work.

## 2.0 FACILITY AND MODEL DESCRIPTION

### 2.1 Facility Description

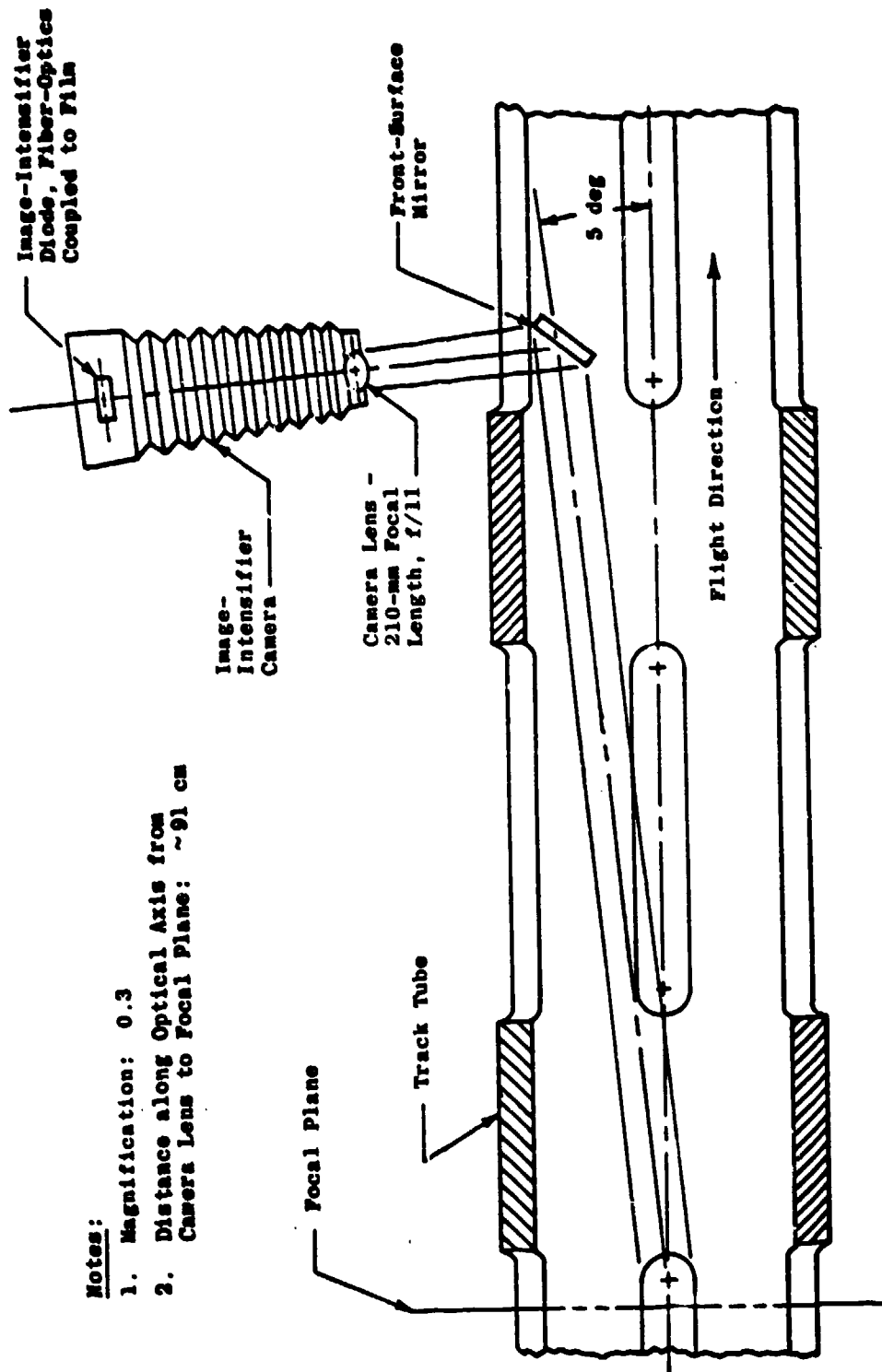
#### 2.1.1 Range Description

The AEDC Hypervelocity Track G is an advanced ground test facility in which a gun-launched test article is confined to a straight-line trajectory by four surrounding guide rails (Figure 2.1a). The facility is designed so that models can be launched at velocities up to 20,000 ft/sec, guided through 1000 feet of controlled test environment, and recovered without damage in a 500 foot long decelerator tube. This unique facility, which became operational in early 1977, overcomes hyperballistic range limitations associated with dispersion of the free-flight model and the absence of a model recovery capability.

The major subsystems comprising the Track G test facility are:

- 1) A model launcher device;
- 2) a model guidance system including the track and its ancillary hardware;
- 3) a model recovery system that is used to dissipate the kinetic energy of the test article without significant damage;
- 4) a test model that is either a full- or reduced-scale flight vehicle;
- 5) an environmental system, the basic component of which is the 10-foot-diameter range tank, to provide a wide range of environmental simulation such as high altitude flight in clear air, erosive particle encounter, or special chemically inert environments;
- 6) an instrumentation system capable of in-flight data acquisition.

Detailed description of the facilities have been provided in References 4 and 5. The basic capabilities of the range are similar to the Range G free flight test configuration used for the studies in Reference 3.



Notes:

1. Magnification: 0.3
2. Distance along Optical Axis from Camera Lens to Focal Plane: ~91 cm

FIGURE 2.1. TRACK PHOTOPYROMETER ARRANGEMENT

### 2.1.2 Range Instrumentation

The same basic instrumentation was used for the Track G tests as was used for the free flight tests discussed in Reference 3. In-flight surface brightness temperatures of the model nosetip were measured by five photopyrometer systems (References 3, 4, 5) Figure 2.1b, that could be located at the following down-range locations:

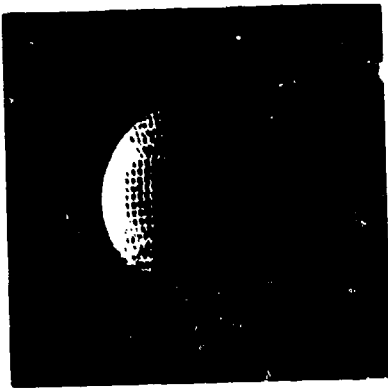
Photopyrometer (ICC) Station	Distance from Range Entrance, m (ft)
1	10.59 ( 34.73)
4	30.38 ( 99.63)
11	72.55 (237.48)
19	121.38 (398.11)
29	181.85 (596.48)
41	255.02 (836.48)

For the current series of launches, the ICC Station 1 was not available. The optical system was arranged such that the luminous nosetip was viewed from 5 degrees off the flight axis, thus minimizing motion blur and shadowing effects. As in the free flight configuration, extraneous shock layer radiation and surface chemiluminescence which may influence the surface temperature measurements were suppressed by purging the region where the image was to be recorded by helium.

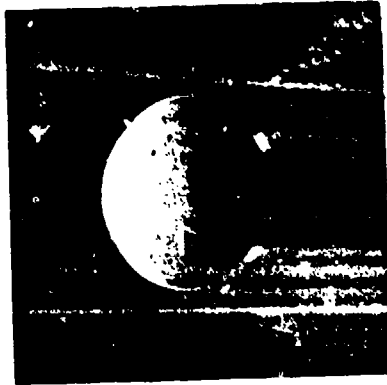
Various other high speed photographic, electro/optical and electronic systems used in aeroballistics ranges are also used in Track G (Reference 4). Given the accurate location of the in-flight model, stereo-photographic techniques permit monitoring the noseitp surface conditions photographically (Figure 2.2).

### 2.2 Track G Models

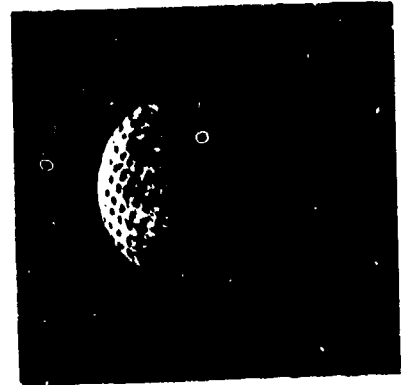
A Track G model is required to withstand acceleration loads of up to 200,000 g's during launch as well as extreme



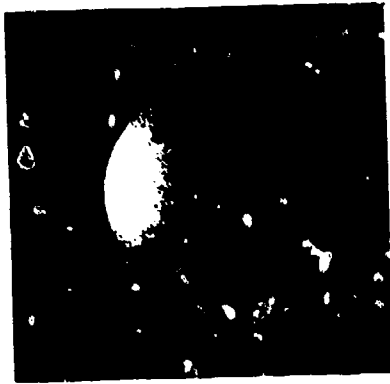
4880  
223CC



4886  
994-2



4955  
FWPFCC



4882  
W/PR



4883  
W/SSR 30



4884  
W/SS



4887  
W/SSR 15



4963  
W/SS

FIGURE 2.2. IN-FLIGHT LASER PHOTOS AT 152 M FROM RANGE ENTRANCE

heating rates, encounters with erosive fields, thermal degradation over the 1000-foot test environment, and finally deceleration loads of up to 120,000 g's during recovery. In addition, the carrier for the test specimen (nosetip) must continually reconform to the launch tube bore to compensate for carrier wear during the launch process and to form an adequate bearing surface while in contact with the rail guidance system and recovery tube. The external model components (Figure 2.3a) are (a) carrier, (b) carrier heatshield, (c) specimen holder, and (d) test specimen. Attachment of the specimen carrier to the specimen support shaft is by means of a shock-absorbing thread pattern, whereas the test specimen is attached using a swaging process. The test specimens comprising the nosetip of the model were  $\frac{1}{4}$ " and 0.4" radii hemispheres fabricated from a variety of materials depending on the specific test objectives. Phenomenology tests used the better characterized tungsten and graphitic materials, ATJ-S and 994-2. Real-material assessments were made on carbon-carbon composites such as GE 223 and fine weave pierce fabric (FWPF) woven materials. A photograph of one of the current models in flight guided by the rails is shown in Figure 2.3b.

Details of the model surface preparation and characterization are discussed in Section 3.0.

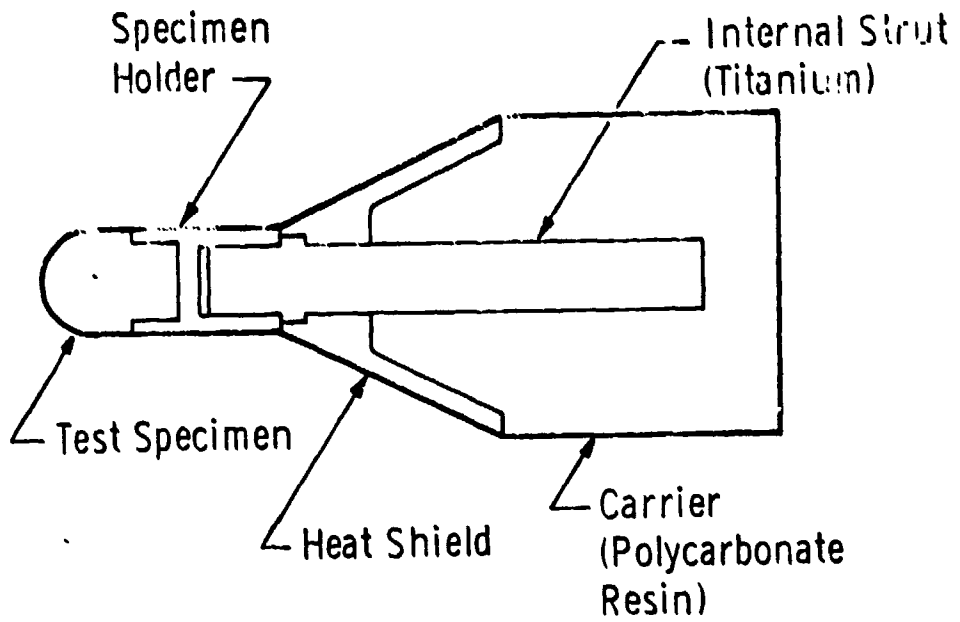


FIGURE 2.3A. MODEL DESIGN DETAIL

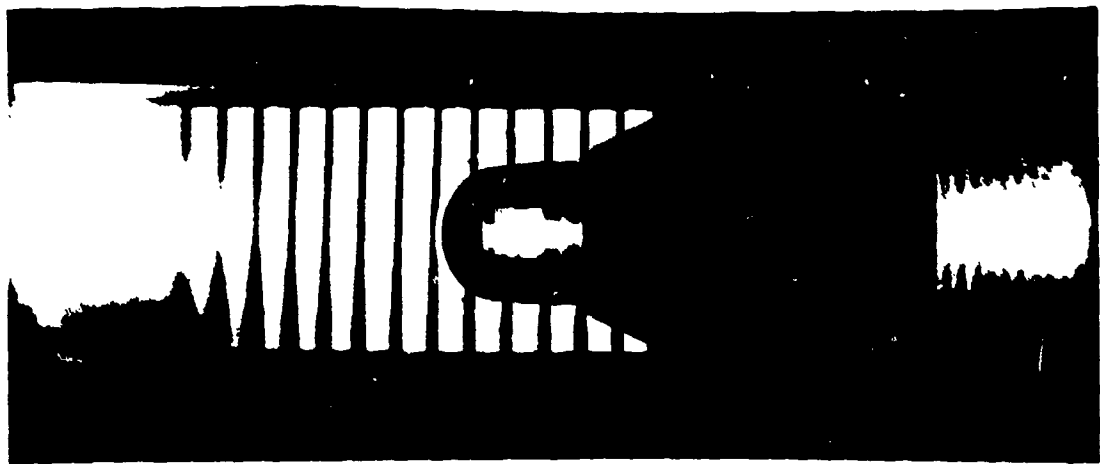


FIGURE 2.3B. TRACK CONSTRAINED MODEL

### 3.0 MODEL SURFACE PREPARATION AND CHARACTERIZATION

Model nosetips were fabricated by AEDC from tungsten, ATJ-S, 994-2 graphites and carbon-carbon composites, GE 223 and fine weave pierced fabric (FWPF). The tungsten models were  $\frac{1}{4}$ " and 0.4" radii hemispheres and the graphitic models were  $\frac{3}{8}$ " prior to preflight preparation in the Aerotherm Arc Jet and approximately 0.4" after preconditioning.

Samples of each type of model was sent to the SAI Materials Sciences Division in Santa Ana for careful characterization.

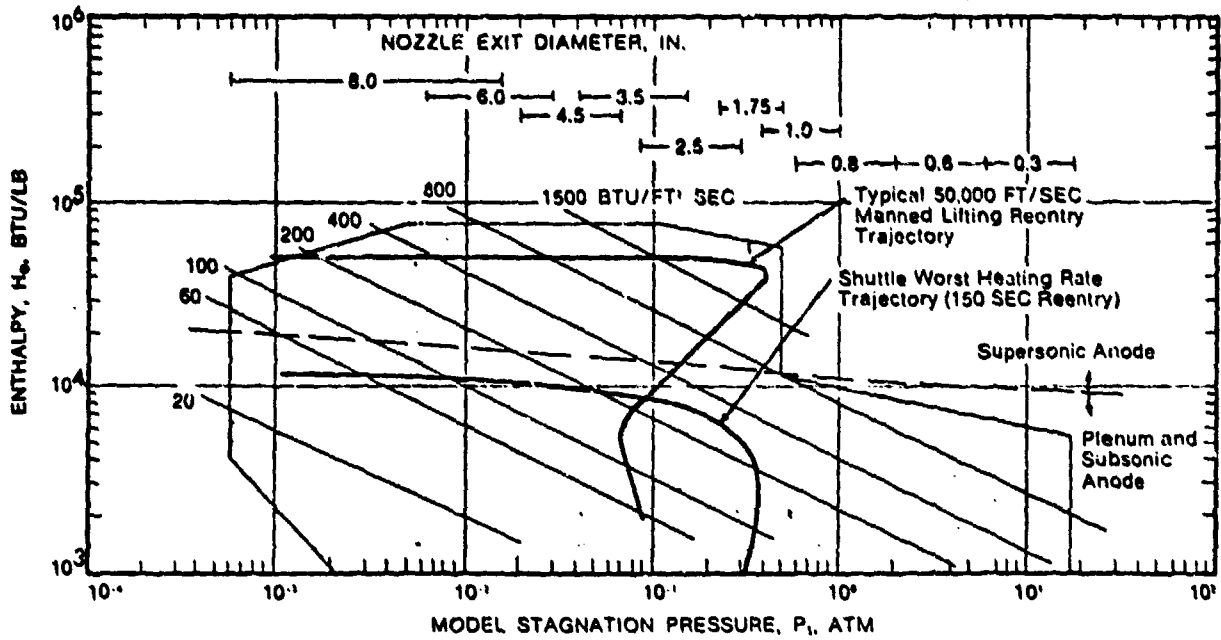
#### 3.1 Model Surface Preparation

##### 3.1.1 Tungsten Models

Tungsten models were preconditioned in the same manner as previously described in Reference 3. The resulting surfaces were termed 1) nominally smooth for surface roughnesses of rms values of about 25  $\mu$ in.; 2) super smooth for a surface roughness of rms values less than about 10  $\mu$ in., and 3) preroughened surface using grit blasting to achieve surface roughnesses in the range of 100-300  $\mu$ in. Only limited tungsten models were used in the current test series.

##### 3.1.2 Graphitic Models

To simulate pre-transition surface roughnesses occurring in actual flight, graphitic models were preconditioned in a plasma arc facility. Conditions were chosen such that laminar ablation occurred on the nosetip. The preconditioning tests were performed at the Aerotherm 1.5 MW Arc Plasma Generator (APG) Facility. Figure 3.1 describes the operating performance envelope of the facility. Test conditions were chosen such that the nosetip models would experience laminar sublimation and the stagnation point would recede approximately 30-40 mils.



(Convective Heat Flux to a 1/4 Inch Diameter Flat Face Model as a Parameter)

FIGURE 3.1. AEROTHERM OPERATING ENVELOPE FOR STAGNATION POINT MODEL TESTING IN AIR

### 3.1.2.1 Ablation Pretest Predictions in Arc-Jet Environment

CAPER-1D predictions were made using nominal arc-jet conditions ( $H_t = 45,000$  btu/lbm,  $P_{stag} = .07$  atm,  $\dot{q}_{cw} = 3330$  btu/ft<sup>2</sup> sec) to determine recession rates and thus, enabling test times to be chosen to obtain the desired recession. The Aerotherm (Ref. 6), G. E. (Ref. 7), and Kratch (Ref. 8) ablation models were utilized and the resulting stagnation point recessions are depicted in Figure 3.2. Since the Kratch model best represented stagnation point recession data in previous arc-jet tests (Reda, Ref. 2), test times were chosen using this model. Nevertheless, in the present tests, CAPER-1D with the Kratch ablation model overpredicted stagnation recession by 30%.

### 3.1.2.2 Models

Graphitic models and three model-sting adaptors were supplied by AEDC for the preconditioning tests.

Preconditioned models D23, 175-9994-4 and MT-4411A3 were then sent to the Materials Science Division of SAI for surface characterization and the remaining models were returned to AEDC for ballistics range testing.

### 3.1.2.3 Ablation Test and Flow Calibration

The tests were performed in Aerotherm's Arc Plasma Generator (APG) Facility and utilized the vacuum chamber test leg with a segmented constrictor arc heater. A supersonic anode configuration combined with a 3.5 inch exit diameter nozzle produced a test stream with a uniform core of at least 2.0 inch diameter. In all cases, the test gas was simulated air, 76.8 percent N<sub>2</sub> and 23.2 percent O<sub>2</sub>. The stagnation point of the test model was positioned  $\frac{1}{2}$  nozzle exit diameters (1.75 inch) from the nozzle exit plane, insuring immersion of the model in the jet uniform core.

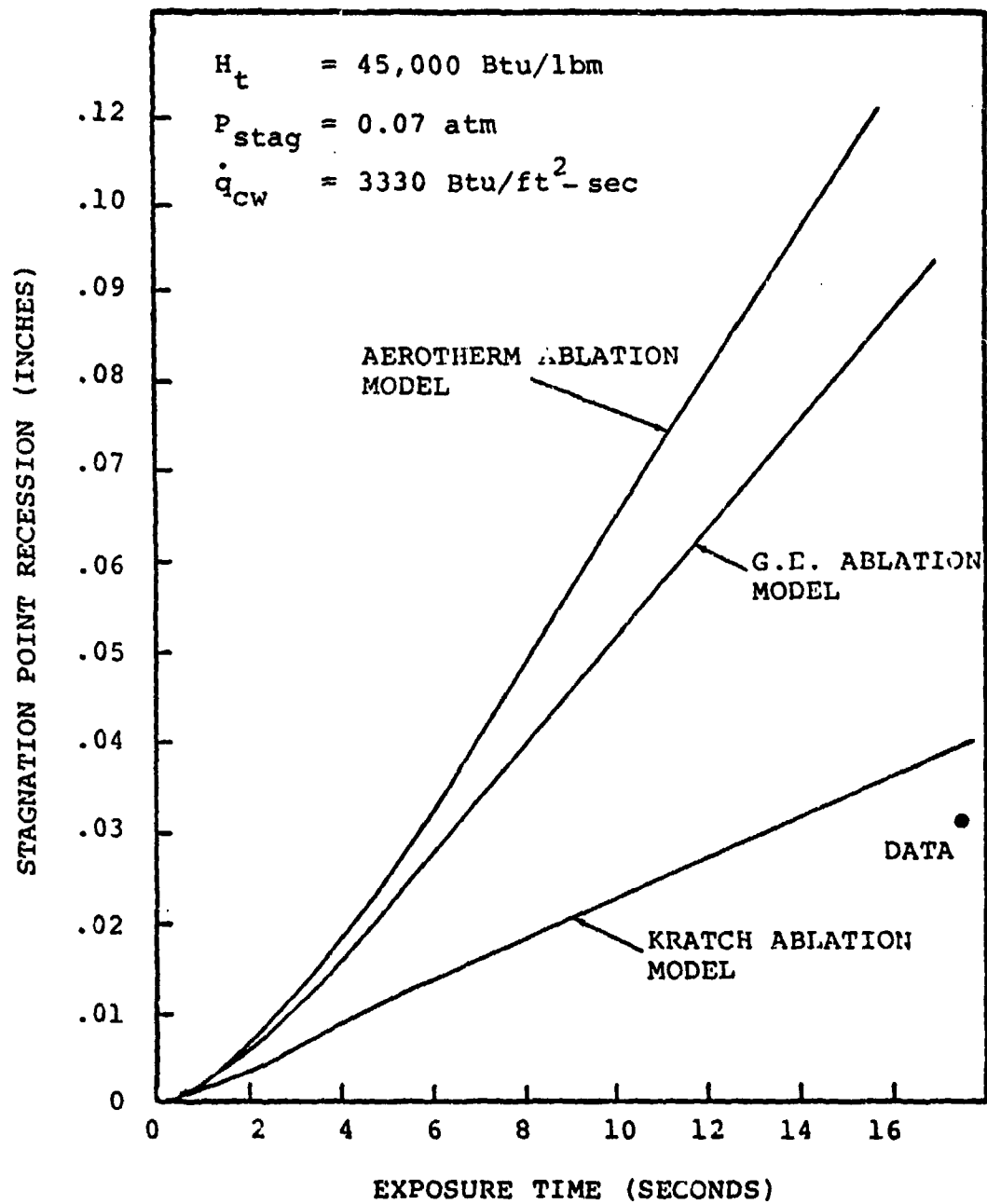


FIGURE 3.2. CAPER-1D PRETEST PREDICTIONS

The stagnation heating rate,  $\dot{q}$ , was measured on the jet stream centerline at the point corresponding to the model nosetip through the use of a 2 -  $\frac{1}{4}$  inch diameter, flat faced, transient calorimeter with a  $\frac{1}{8}$  inch corner radius ( $\sqrt{R_{eff}} = .421 \text{ ft}^{\frac{1}{2}}$ ). The stagnation pressure was measured with a  $\frac{1}{4}$  inch diameter pitot tube also positioned at a point corresponding to the model nosetip. Stagnation pressures were determined to the nearest .001 atmosphere.

The centerline enthalpy was inferred from the centerline measurement of heating rate and stagnation pressure through the equation

$$H_C = 23.8 \dot{q} \sqrt{\frac{R_{eff}}{P_{t_2}}}$$

where

$H_C$  = local enthalpy on centerline (Btu/lb<sub>m</sub>)

$\dot{q}$  = cold wall calorimeter heating rate (Btu/ft<sup>2</sup>-sec)

$P_{t_2}$  = stagnation pressure (atm)

$R_{eff}$  = effective calorimeter nose radius (ft)

The test model surface temperature was measured with an infrared pyrometer. For all tests, the pyrometer sensing area was centered on the 43° point (corresponding to an axial distance of .1 inch from nosetip). Because the model moved forward in its holder, approximately .05 inch when under test conditions, the pyrometer would be aligned at an axial distance of 0.05 inches from the nose. The spread in surface temperatures could be accounted for by variations in axial movement by the model from test to test. The pyrometer viewed the model through a quartz window and the pyrometer output was corrected for the transmittance of the quartz. The surface emittance was assumed to be 1.0 for all tests.

Each model was sized and weighed before and after each test firing to determine the stagnation point recession and the total mass loss. Model exposure times were nominally 18 seconds, with the exact times determined to the nearest .1 seconds from oscillograph data. Only the very first run had a test time appreciably lower than 18 seconds in order to check for uniform ablation around the nosetip.

The arc-jet operating conditions and the model test results are summarized in Tables 3.1 through 3.3 respectively.

### 3.2 Model Surface Characterization

Surface roughness characterizations were performed by taking photomicrographs of model surface cross-sections or their replica and measuring the surface macro and micro roughness. Surface macroroughness and microroughness are defined as the surface roughness measurements made under a magnification of 50X and 350X respectively. (The definition of macroroughness here is different from that used for weaved carbon-carbon materials, e.g., CC-223.) The measurements taken were roughness element height  $h$ , roughness element width  $w$ , and the spacing between the roughness element peaks,  $L_p$  (Figure 3.3). The equivalent sand roughness,  $k_s$ , has been calculated from the measurements using the method presented in Reference 9. The average element spacing,  $D$  is given by

$$D = \left[ \frac{3\pi}{8} \frac{\bar{L}_p \sqrt{\bar{w}^2}}{\bar{w}} \right]^{1/2} \quad (3.1)$$

and the sand grain roughness by the equations

$$\frac{k_s}{k} = 139.0 \lambda^{-1.90}, \quad \lambda > 4.93$$

$$\frac{k_s}{k} = 0.0164 \lambda^{3.78}, \quad \lambda > 4.93 \quad (3.2)$$

TABLE 3.1. APG OPERATING CONDITIONS

APG TEST NUMBER	ARC CURRENT (AMPS)	ARC VOLTAGE (VOLTS)	ARC EFFIC. (%)	GAS BULK ENTHALPY (BTU/LBm)	ARC CHAMBER PRESSURE (ATM)	VACUUM TANK PRESS. (mmHg)	GAS MASS FLOW (LBm/SEC)	COMMENTS
2934,01	1006	432	65	8993	0.515	0.35	0.0301	Ran Model Only 10 secs
2934,02	1004	430	66.7	8995	0.51	0.35	↓	Reran Model
2935,01	1005	432	66	9052	0.51	0.35		Switched to TD-9CH Pyrometer
2935,02	1004	432	66	9017	0.513	0.34		Water Leak in Exit Nozzle at End of Test
2936,01	1006	432	65.5	8990	0.513	0.35		Heat Exchanger Failure, Aborted Run
2936,02	1010	433	66	9059	0.513	0.35		
2937,01	1007	433	66	9064	0.513	0.32		
2937,02	1004	434	67	9185	0.513	0.32		
2938,01	1010	429	65.5	9023	0.516	0.34		
2938,02	1006	430	66	8967	0.514	0.34		
2938,03	1002	431	65.5	8954	0.515	0.34		
2939,01	997	427	65.5	8778	0.507	0.40		
2939,02	—	—	—	—	—	—		

TABLE 3.2. MODEL NUMBER DESIGNATIONS FOR  
ABLATION PRECONDITIONING TESTS

MATERIAL	MODEL NO.
223 Carbon-Carbon	MT4411 A1
"	MT4411 A2
"	MT4411 A3
"	MT4411 A3
ATJ-S	F23
"	F45
"	D67
"	D23
994	17S-9994-1
"	17S-9994-2
"	17S-9994-3
"	17S-9994-4

TABLE 3.3. ABLATION PRECONDITIONING RESULTS

APC TEST NUMBER	MODEL TYPE AND NUMBER	STAG PRESSURE (ATM)	STAG. P. HEAT FLUX $Btu/Ft^2 SEC$	TEMP. $\theta$ SONIC POINT (°F) <sub>0</sub>	CENTERLINE ENTHALPY (Btu/lbm)C.	TEST TIME (SEC)	CENTERLINE RECESSION (IN)	WEIGHT CHANGE (gms)	REMARKS
2934.01	MT 4411 A1	.0705	1260.2	5113	47,556	8.3	—	—	Model not measured after run
2934.02	MT 4411 A1	.071	1316.8	5116	49,516.5	17.4	.045	.404	rerun of Model A1
2935.01	ATJ-S 023	.072	1331	4909	48,955	17.7	.031	.287	
2935.02	175-9994-1	.072	1339.5	5535	50,019	17.9	.033	.286	Changed to 18-908 Pyrometer
2936.01	MT 4411 A2	.071	1321.1	5550	49,678	18.1	.030	.278	
2936.02	ATJ-F23	.072	1342.1	5600	56,116	18.1	.032	.294	
2937.01	MT 4411 A3	.072	1352.6	5360	50,508	18.3	.0295	.281	
2937.02	MT 4411 A4	.073	1341.3	5190	49,742	20.3	.033	.320	
2938.01	ATJ-F45	.070	1319.6	5430	49,975	18.6	.030	.294	
2939.02	175-9994-1	.070	1306.8	5492	49,490	18.2	.031	.282	
2939.03	175-9994-2	.070	1285.6	5103	48,607	19.3	.033	.297	Pyrometer read low, reason unknown
2939.04	ATJ-067	.066	1291.2	4808	49,613	18.2	.0305	.277	Pyrometer read low, reason unknown

a: 1/4" diameter flat faced transient calorimeter;  
 b: Emittance of surface = 1.0. Pyrometer set to sonic point of flow -410 location.

c: Calculated:  $W_L = 23.8 \frac{\sqrt{K_{eff}}}{\sqrt{P_{02}}}$

TABLE 3.3.(CONT.) ABLATION PRECONDITIONING RESULTS

$\dot{m} = 0.0301$  lbm/sec Air  $P_{\infty} = 0.24$  mm Hg

ARC TEST NO.	AEDC MODEL NO.	MATERIAL	$P_o$ (ATM)	$H_o$ (Btu/lb)	$\dot{q}$ (Btu/ft <sup>2</sup> -sec)	$H_c$ (Btu/lb)	$P_t$ (ATM)	$T_s$ max (°F)	Test Time (Sec)	$\Delta S$ (inches)	$A_m$ (grams)
2961.02	17	994-2	.51	9286	1261.1	48104	0.069	6080	19	.032	.270
	19	GE223	.51	9336	1261.1	48104	0.069	6057	19	.024	.274
2962.01	13	FMPF	.51	9333	1250.4	47696	0.069	6052	19.1	.023	.270
2962.02	14	FMPF	.51	9354	1227.9	46838	0.069	6070	20.1	.025	.290
2963.02	18	994-2	.50	9359	1226.7	46792	0.069	6048	19.85	.034	.287
2763.03	20	ATJ-S	.51	9353	1241.1	47341	0.069	5577*	18.3	.029	.264

\*Pyrometer may have been misaligned

$\dot{m} = 0.031$  lbm/sec Air  $P_{\infty} = 0.24$  mm Hg

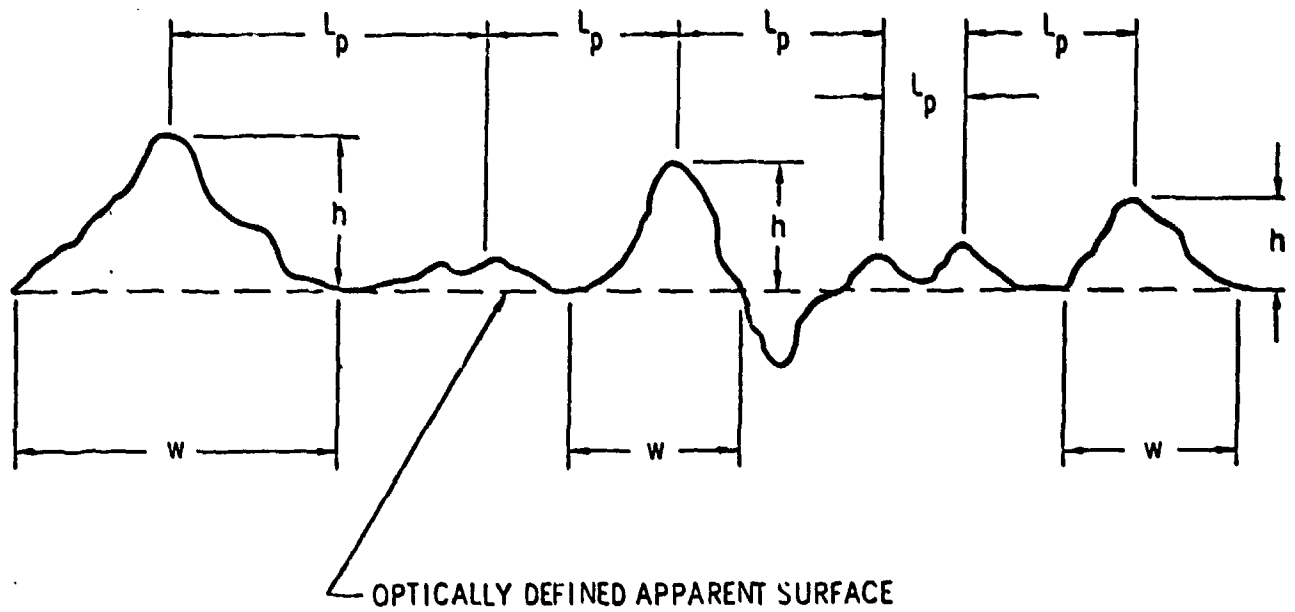
ARC TEST NUMBER	AEDC MODEL NUMBER	MATERIAL	$P_o$ (ATM)	$H_o$ (Btu/lbm)	$\dot{q}$ (Btu/ft <sup>2</sup> sec)	$H_c$ (Btu/lbm)	$P_{t2}$ (atm)	$T_{sMAX}$ (°R)	TEST-TIME (SEC)	$\Delta S$ INCHES	$A_m$ (GRAMS)
2990.01	21	GE223	.523	9218	1222.5	47,752	.0658	5989	19.9	.032	.324
2991.02	15	FMPF	.526	9373	1053.2	42,415	.0619	6002	19.4	.026	.311
2991.03	16	FMPF	.524	9325	1058.1	41,082	.0666	5998	19.5	.027	.315
2991.04	22	GE223	.523	9345	1105.3	44,878	.061	5997	19.4	.025	.318
2991.05	23	17S-9	.527	9442	1020.3	39,614	.067	5990	20.3	.036	.307
2991.06	24	ATJ-S #11 D7	.524	9412	1077	43,374	.062	5930	20.4	.037	.323

TABLE 3.3. (CONT.) ABLATION PRECONDITIONING RESULTS

AEROTHERM 1 MW VAC APG FACILITY       $\dot{M}_t = 0.0301 \text{ LB}_m/\text{SEC}$        $P_{\infty} = 0.27 \text{ mm Hg.}$

ARC TEST NO.	MATERIAL	AEDC NO.	$P_0$ (ATM)	$H_0$ (Btu/lbm)	$\dot{q}_w$ (Btu/ft <sup>2</sup> sec)	$H_4$ (Btu/lbm)	$P_{t2}$ (atm)	$T_s^*$ (OR) max.	$t$ (Sec)	$\Delta S$ (in)	$\Delta M$ (gms)	REMARKS
3025.01	994.2	28	.55	8799	--	--	.063	5801	21.0	.038	.343	No Cal Signal
3055.02	994.2	29	.53	8664	1076.97	42,004	.066	5743	19.8	.035	.313	Pitot assumed for all runs based on prior pitot values run same day
3055.02	994.2	30	.53	8928	1076.97	42,004	.066	5581	19.9	.033	.307	
3055.03	994.2	31	.53	8677	1070.17	41,739	.066	5760	19.9	.033	.313	
3055.04	GE 223	32	.53	8894	1088.31	42,446	.066	5722	19.5	.028	.289	
3055.04	GE 223	33	.535	8864	1088.31	42,446	.066	5830	19.7	.031	.305	
3055.05	GE 223	34	.54	8890	1069.42	41,709	.066	5821	19.7	.028	.301	
3055.05	FMPF	35	.535	8839	1069.42	41,709	.066	5687	19.5	.027	.282	
3055.06	FMPF	36	.53	8727	1076.8	42,000	.066	5831	20.6	.032	.312	
3055.06	FMPF	37	.53	8711	1076.8	42,000	.066	5658	20.5	.032	.294	

\* Except for test 3025.01, all Pyro. data from TD-9FH, calibrated March, 1978



- $\bar{h}$  Average of all roughness heights measured
- $\bar{r}$  Adjusted roughness height (by a factor of  $4/\pi$ )
- $k_s$  Equivalent sand roughness
- $\bar{w}$  Average width of roughness elements
- $L_p$  Average peak-to-peak spacing between roughness elements

FIGURE 3-3. DEFINITION OF SURFACE CHARACTERIZATION PARAMETERS

The scaling parameter,  $\lambda$ , is given by

$$\lambda = 2.9 \frac{D}{\bar{k}} \quad (3.3)$$

Where the average roughness height,  $\bar{k}$  is given by

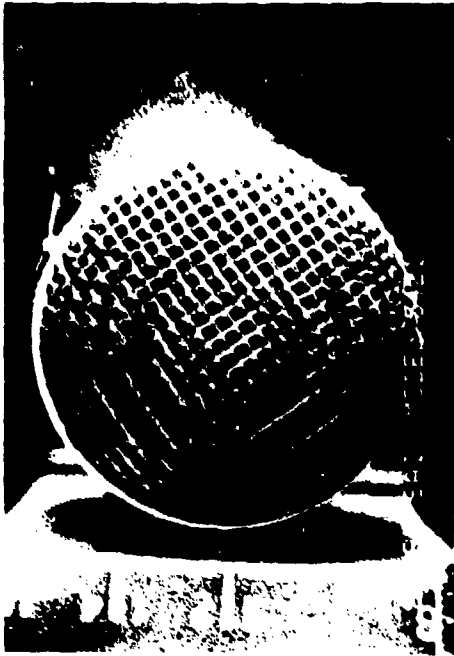
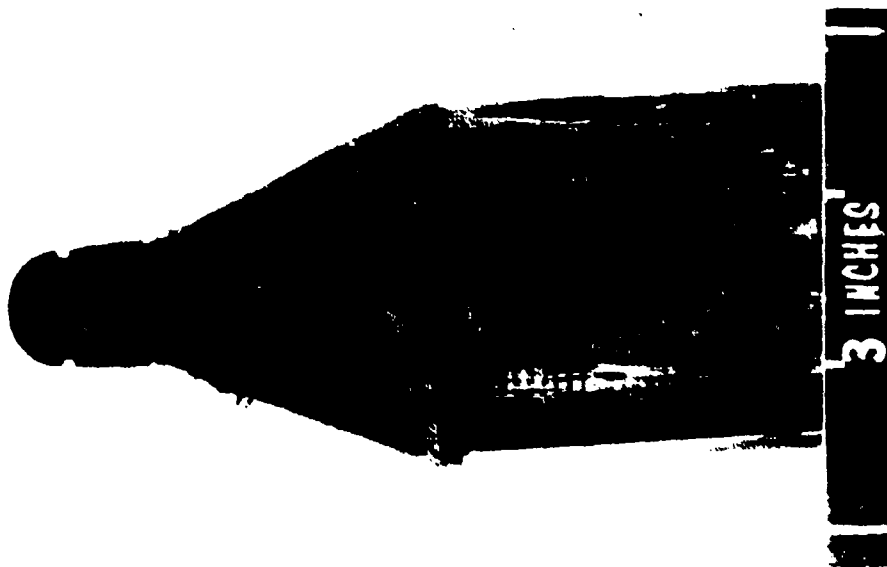
$$\bar{k} = \frac{4}{\pi} \bar{h} \quad (3.4)$$

The  $4/\pi$  factor accounts for the failure of a plane cross-section to pass through the peak of a hemispherical roughness element.

Since the roughness characterization of the tungsten models was to be performed on a sample which was not to be damaged, a replica was made which accurately duplicated the tungsten sample's surface. Photomicrographs were then taken and analyzed. Since the graphite and carbon-carbon samples were made in duplicate, an actual sample was cut, polished and characterized using standard techniques. Both preflight and postflight characterizations were performed on the arc jet pre-conditioned model nosetip. Typical preflight and recovered postflight nosetip photographs are shown in Figure 3.4 and 3.5.

### 3.2.1 Pre-flight Surface Characterization

Three graphite models, pre-conditioned in the Aerotherm Arc Jet and a tungsten model were characterized. Stereo, macro-photographs were taken of two graphite specimens (994-2 and ATJ-S) one carbon-carbon sample (from billet 4411-3) and a tungsten model which had been grit blasted. The carbon-carbon sample was unusual in that it had matrix material as the least ablated phase on the face of the sample (Figure 3.6a). Photographs taken at  $45^\circ$  (Figure 3.6b) indicate a stair-step pattern in this orientation. The extension of the matrix phase above the surface of the specimen is also indicated in low magnification photomicrographs (Figure 3.6c). Photomicrographs at approximately 340X of



A)



B)

A) PREFLIGHT NOSETIP  
B) POSTFLIGHT NOSETIP

RECOVERED MODEL

FIGURE 3.4, TYPICAL GE 223 CC NOSETIP

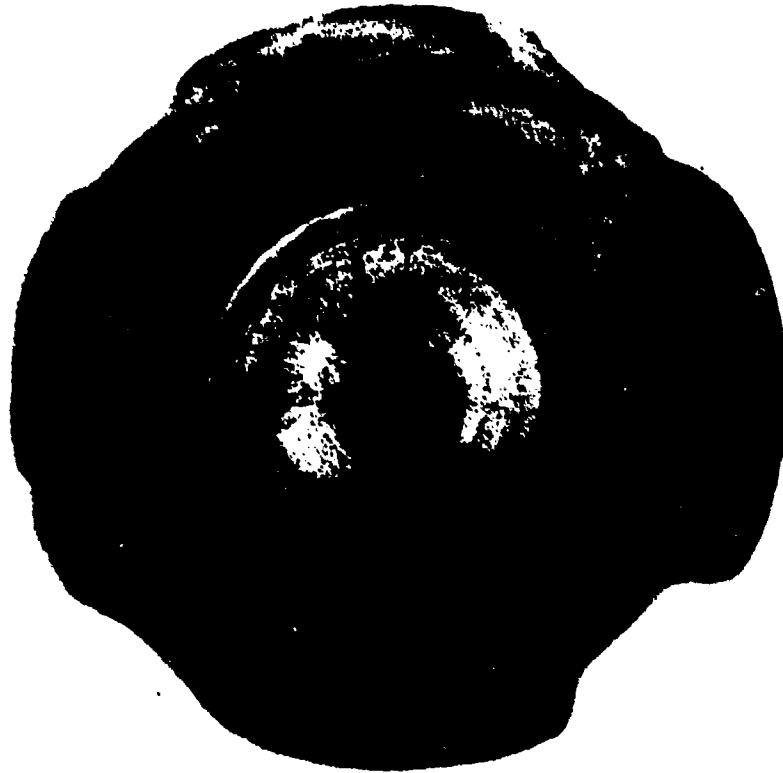
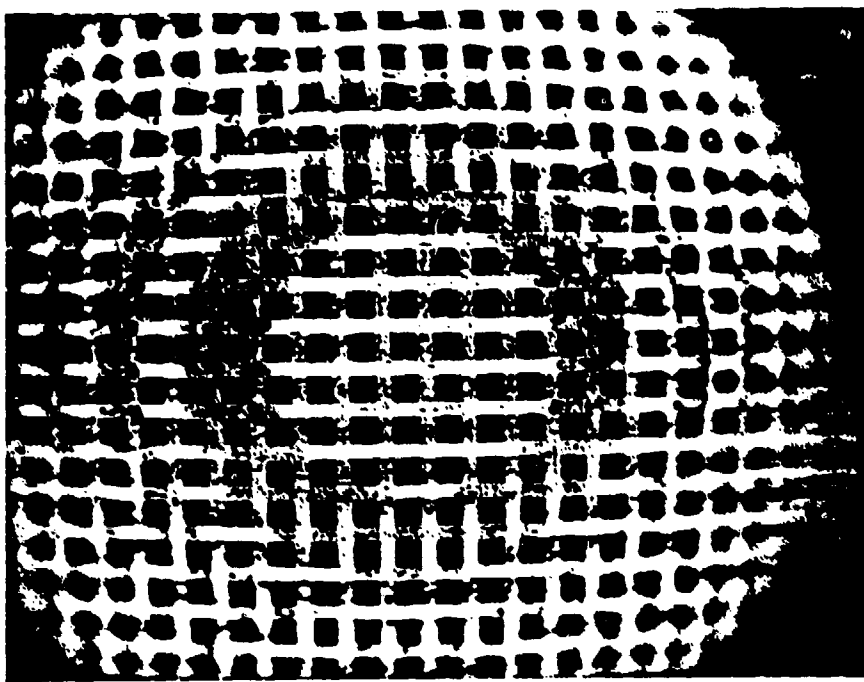


FIGURE 3.5. RECOVERED TUNGSTEN NOSETIP (W/SSR 30) - SHOT 4883

A)



B)

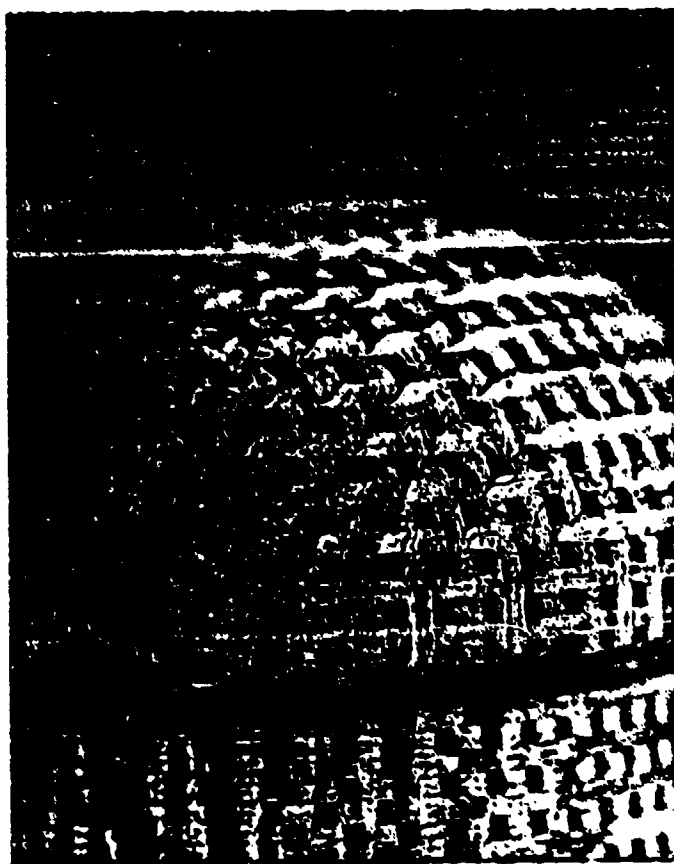


FIGURE 3.6. PRECONDITIONED GE 223 NOSETIP A) HEADON VIEW  
B) 45° VIEW

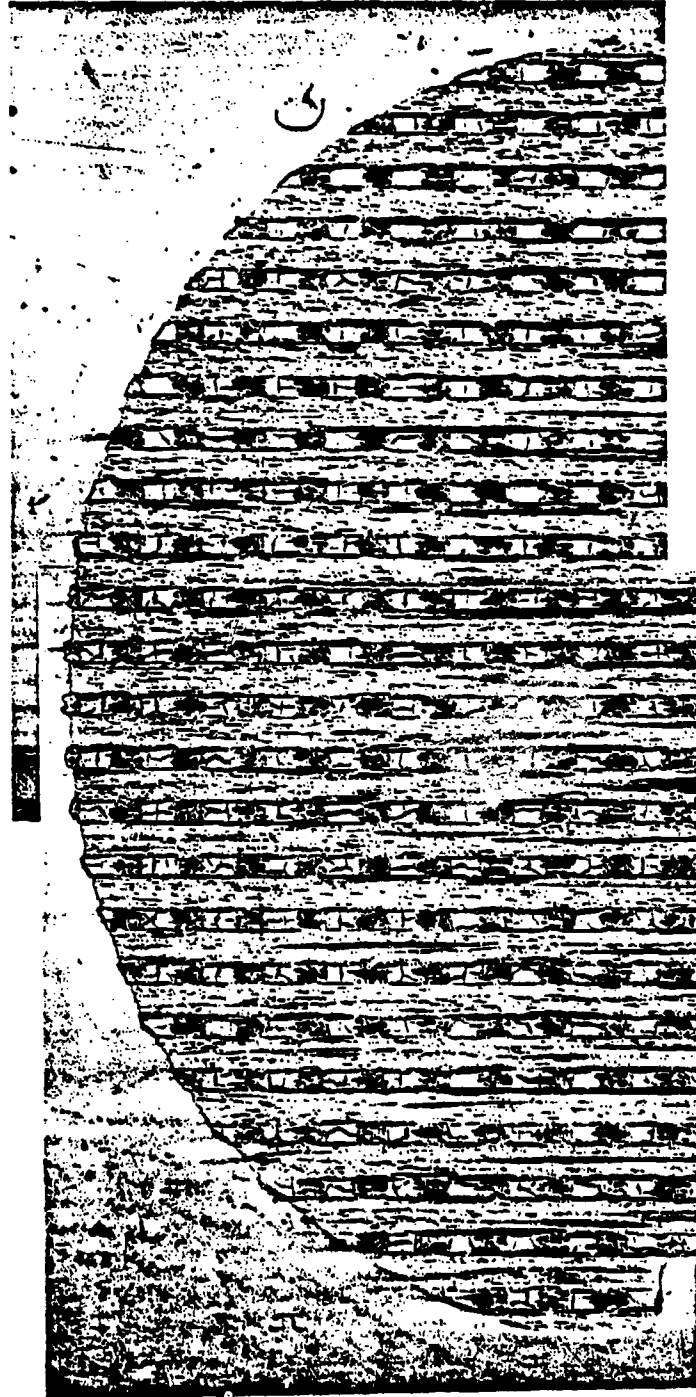


FIGURE 3.6c. FULL SECTION PHOTOMICROGRAPH OF GE 223 NOSETIP, 10X (PREFLIGHT)

the 223 specimen cross sections (Figure 3.6d) were taken with polarized light and clearly show the presence of transverse oriented graphite in the z yarn bundles. This is evidenced by the brightly appearing globules between the individual filaments in the z yarn bundles. Very few transverse yarn bundles were on the surface of the specimen which is an unusual condition for a laminar CC-223 model.

An epoxy replica was taken of the tungsten specimen which was then cross-sectioned, mounted, and polished. A 340 magnification photomicrograph is shown in Figure 3.7. The actual tungsten sample was then submitted for ballistic range tests. The remaining two graphite samples were also sectioned, mounted, and polished. A low magnification photomicrograph of the 994-2 model is shown in Figure 3.8. Photomicrographs of the sections were taken at approximately 340X are shown in Figures 3.9 & 3.10. Measurements were then made to determine the microroughness on the surface of the specimen.

These measurements are summarized as distribution plots showing cumulative roughness heights (Figures 3.11 - 3.14). As can be seen, the roughness height for the two graphite specimens are very similar. The average roughness heights for both the carbon-carbon material and the tungsten replica are nearly the same but the distributions are not.

### 3.2.2 Post Flight Surface Characterization

Models from the following shots were recovered from the track tests and were submitted for microstructural characterization.

<u>Shot Number</u>	<u>Material</u>
4871	CC-223
4880	GE CC-223
4886	Graphite 994-2

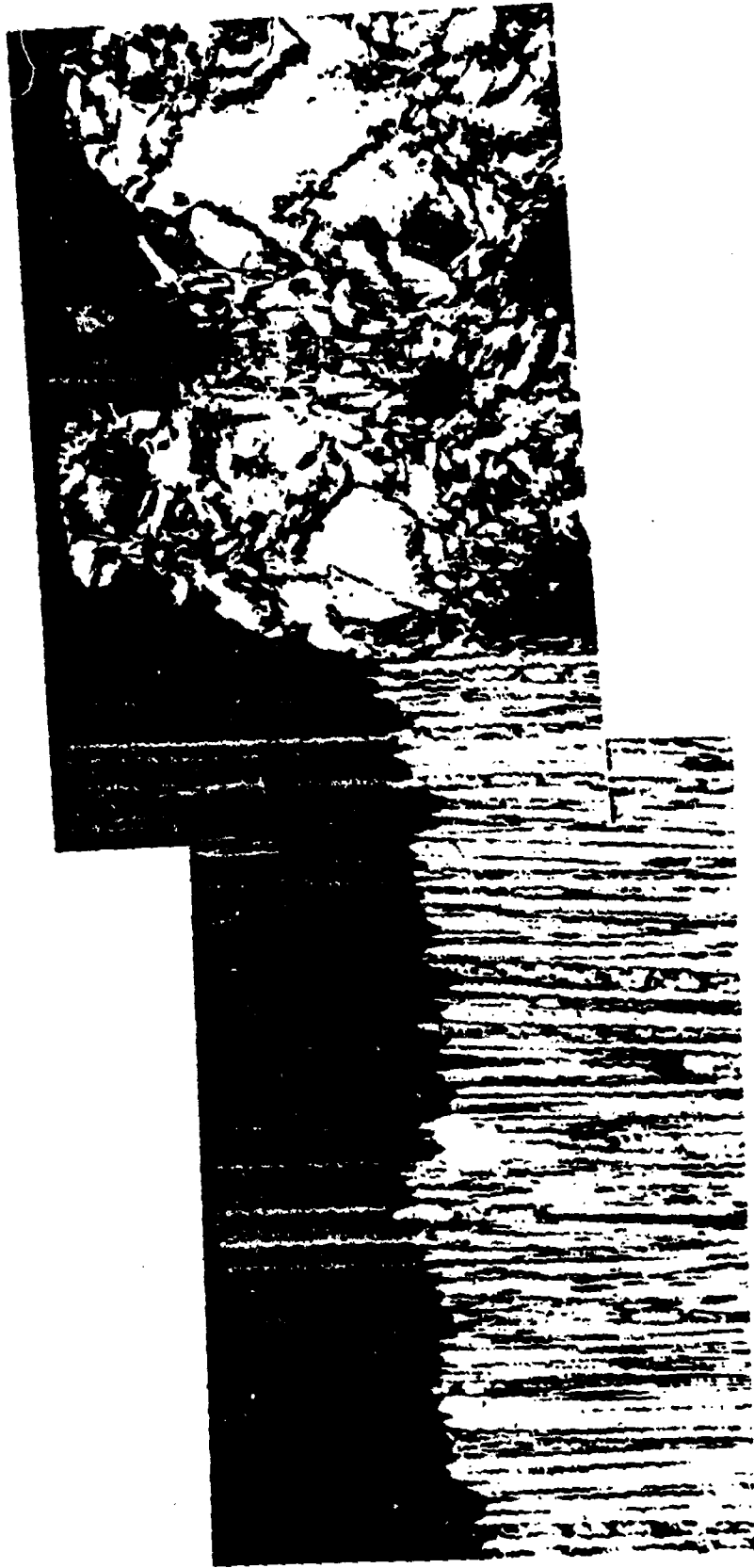


FIGURE 3.6D. CROSS SECTIONAL PHOTOMICROGRAPH OF GE 223 PRECONDITIONED NOSETIP, 338X  
(PREFLIGHT)

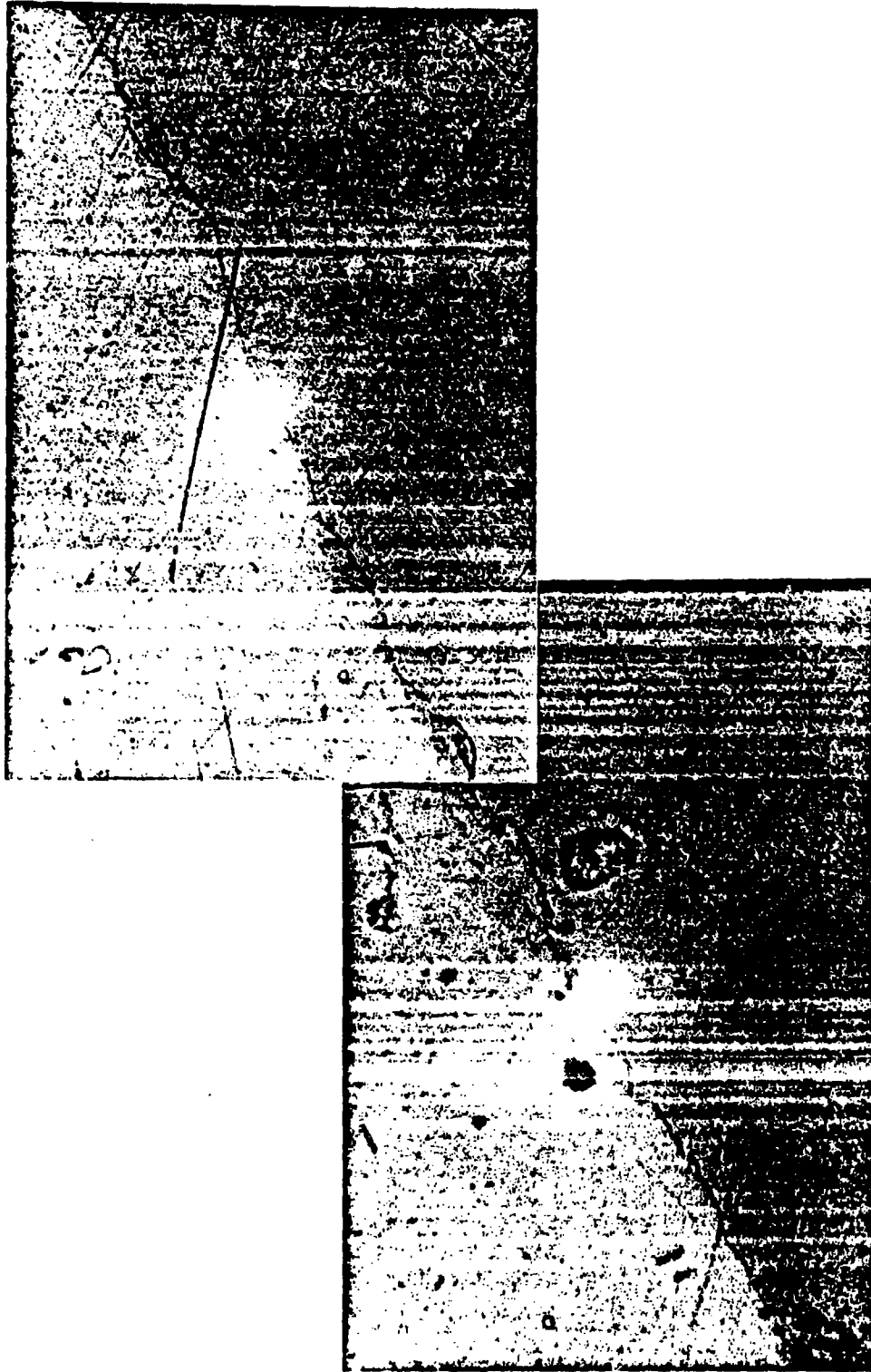


FIGURE 3.7. CROSS SECTIONAL PHOTOMICROGRAPH OF PRE ROUGHENED TUNGSTEN REPLICA  
NOSETIP, 338x (PREFLIGHT)

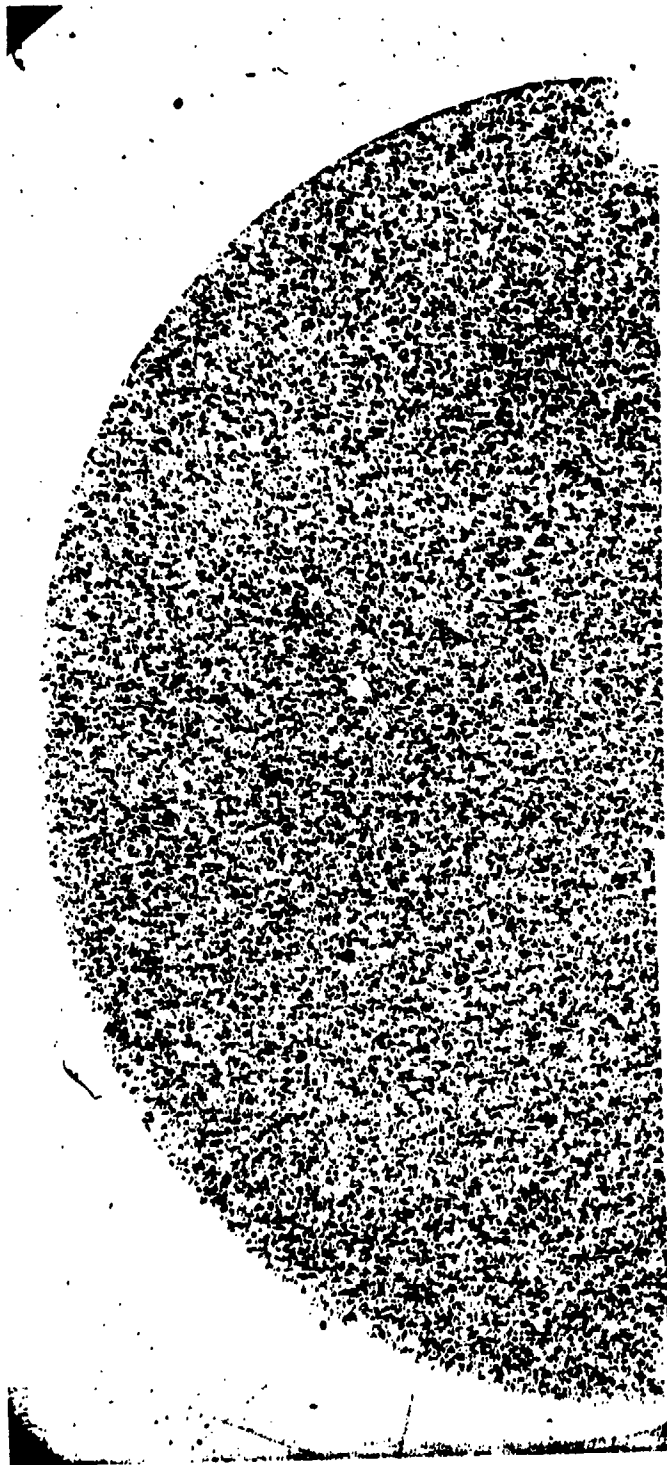


FIGURE 3.8. FULL SECTION PHOTOMICROGRAPH OF 994-2 PRECONDITIONED MODEL, 10x (PREFLIGHT)

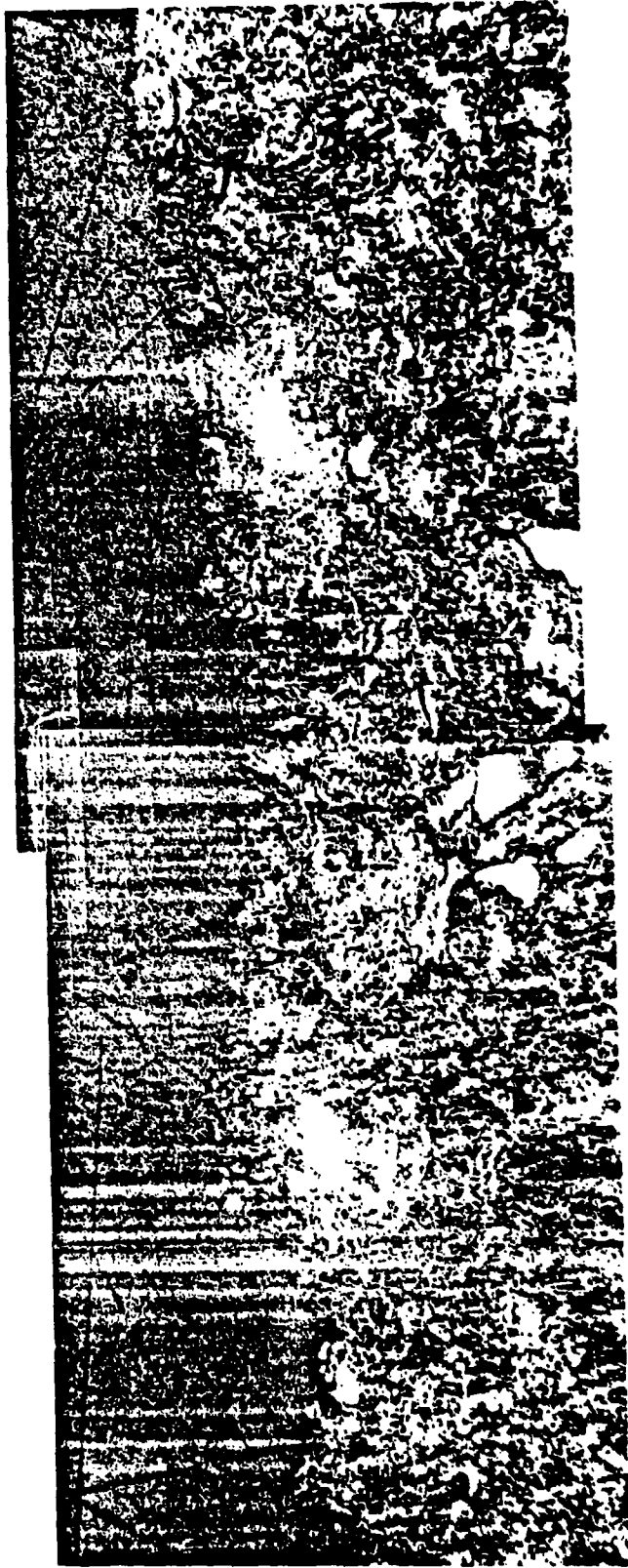


FIGURE 3.9. CROSS SECTIONAL PHOTOMICROGRAPH ATJ-S NOSETIP, 338X (PREFLIGHT)



FIGURE 3.10. CROSS SECTIONAL PHOTOMICROGRAPH OF 994-2 NOSETIP, 338X (PREFLIGHT)

Z Yarn Roughness

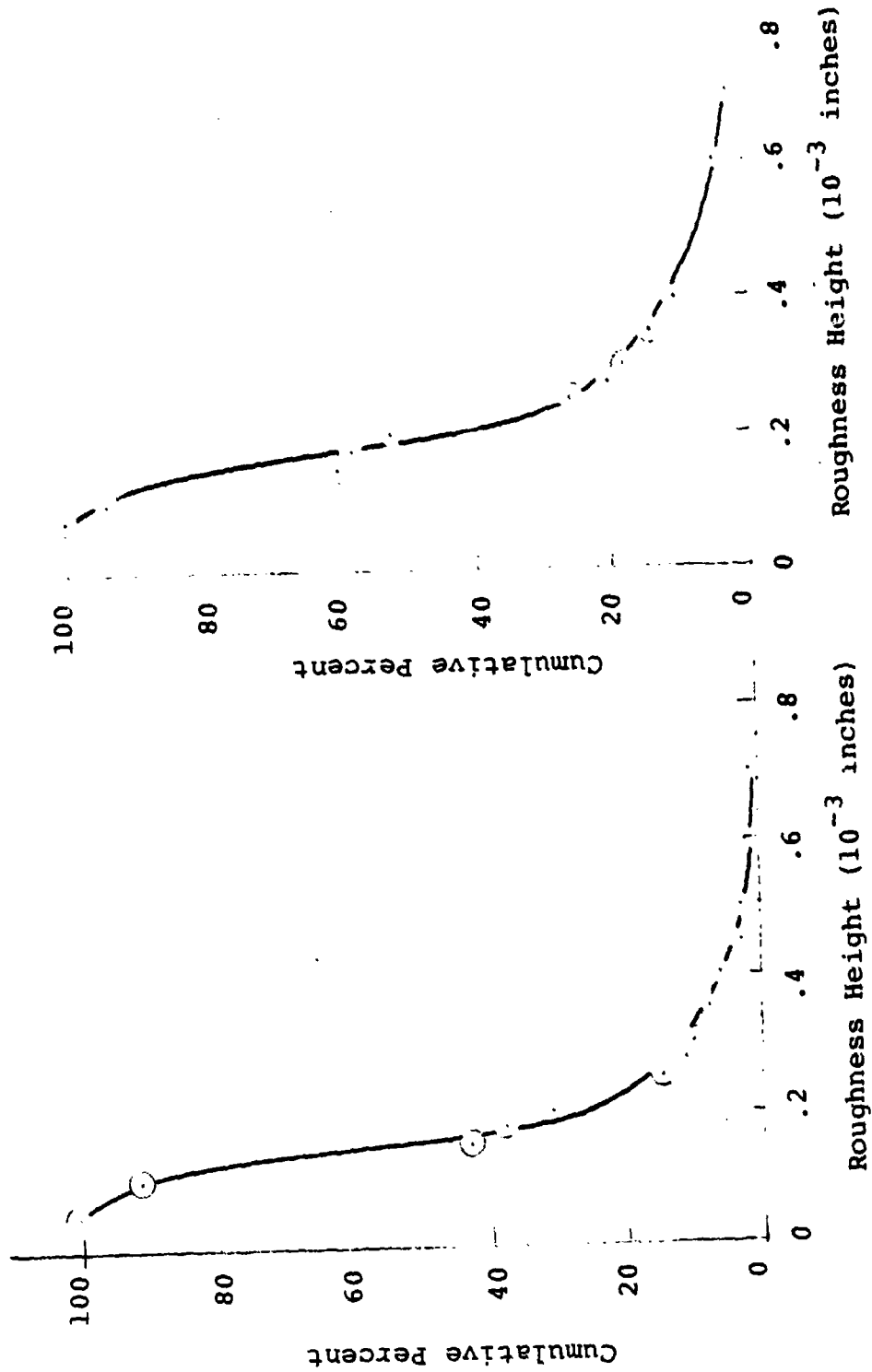


FIGURE 3.11. MICROROUGHNESS HEIGHT DISTRIBUTION FOR PRE CONDITIONED GE CC-223 (PREFLIGHT)

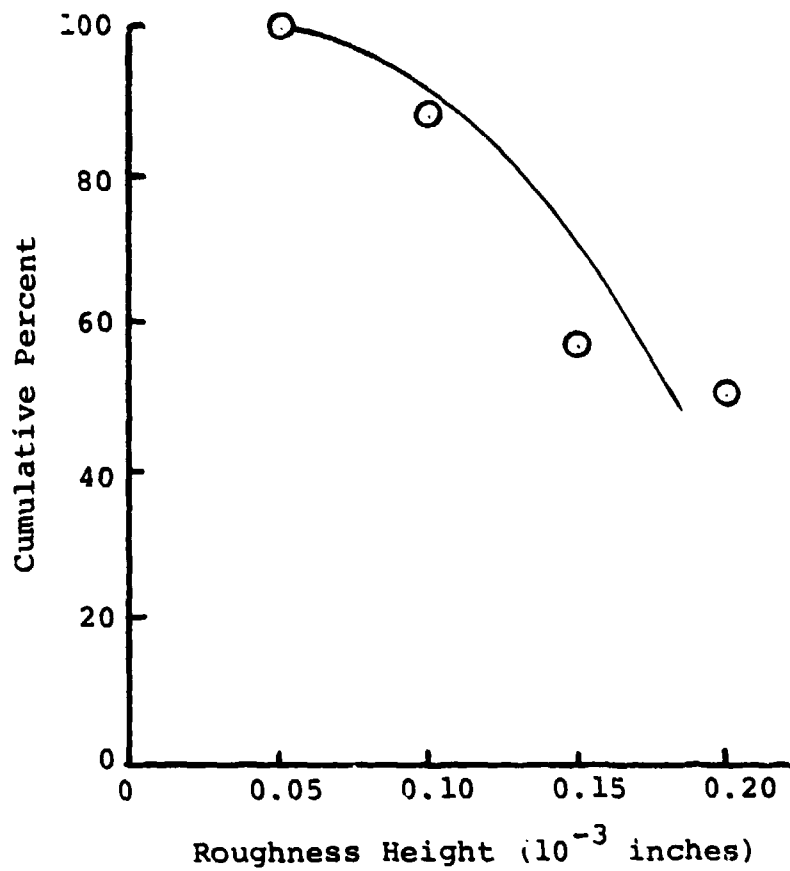


FIGURE 3.12. MICROROUGHNESS HEIGHT DISTRIBUTION FOR GRIT BLASTED TUNGSTEN (PREFLIGHT)

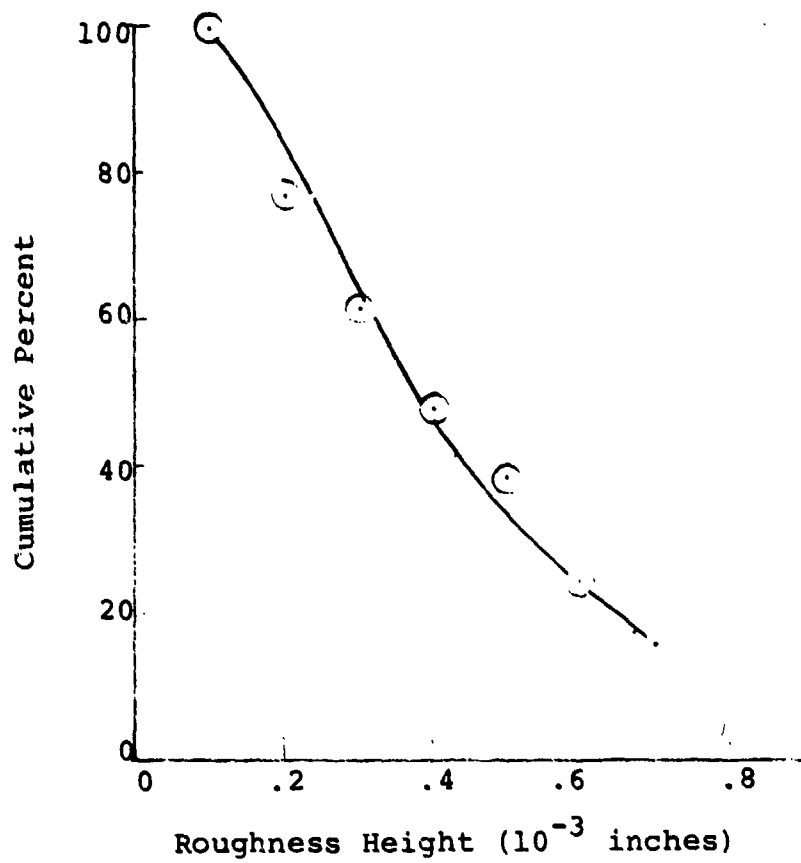


FIGURE 3.13. MICROROUGHNESS HEIGHT DISTRIBUTION FOR PRECONDITIONED 994-2 (PREFLIGHT)

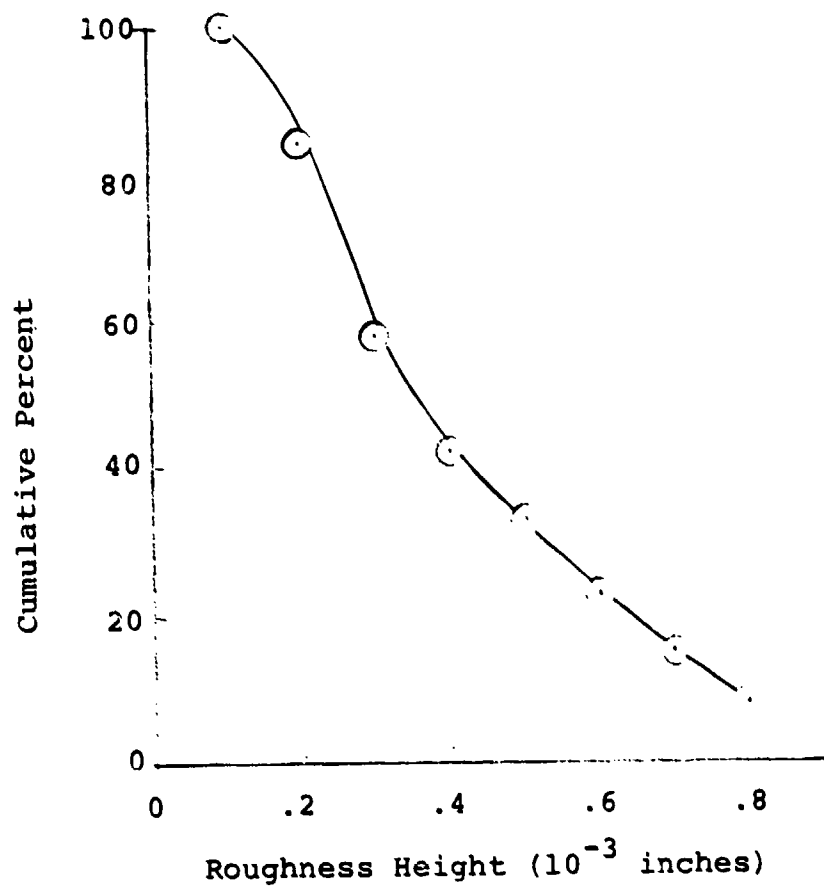


FIGURE 3.14. MICROROUGHNESS HEIGHT DISTRIBUTION FOR PRECONDITIONED ATJ-S (PREFLIGHT)

Each of the models were sectioned and low magnification photomicrographs (10X) were taken to determine the general appearance of both the surface and indepth microstructure. These photomicrographs are shown in Figures 3.15 - 3.17. The appearance is not significantly different from the preflight photomicrographs 3.6c and 3.7. Model 4880 exhibited gross damage in some of the Z yarns of the type generally attributed to processing. This type of damage has been observed and reported (Reference 10) in most 223 ablation models that have been evaluated over the past two years. Unless this type of damage intersects the surface, it does not appear to affect ablation recession or transition performance. The general yarn spacing and pore distribution were similar in all of the 223 models. Only the shot 4871 model was characterized in detail, since 4880 is quite similar.

Measurements of the surface roughness on model 4871 made from CC-223, were made on a microscale at higher magnifications (approximately 200X). Photomicrographs showing the typical appearance of the matrix Z yarns and transverse yarns at the surface of the ablation model are shown in Figure 3.18. What appears to be a localized tensile fracture is evident in one of the Z yarns. This may have been caused by some isolated debris in the ballistic range. In general, it appears that the Z yarns eroded uniformly and preferentially and the matrix material was most resistant to ablation recession. These photomicrographs were taken under polarized light in order to observe the amount of transverse oriented graphite (TOG) contained in each of the Z yarn models. The TOG appearance in Z yarn bundles of CC-223 is characterized by globules of very bright material when examined under polarized light. Only a small amount of these globules appear to be present in these models which is generally characteristic of material taken from central locations in carbon-carbon 223 billets. Cumulative plots of the

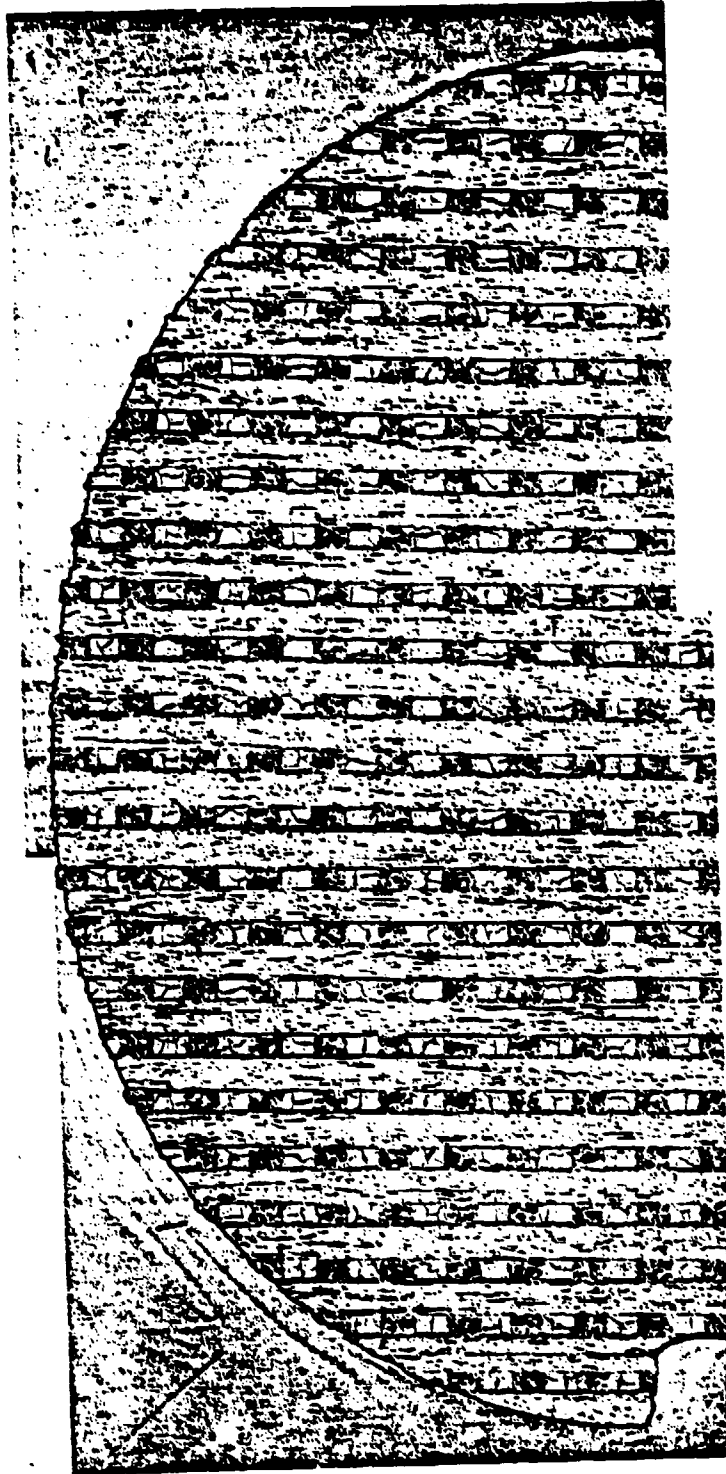


FIGURE 3.15. FULL SECTION PHOTOMICROGRAPH OF CC-223 NOSETIP,  
SHOT 4871, 10X, (POST FLIGHT)

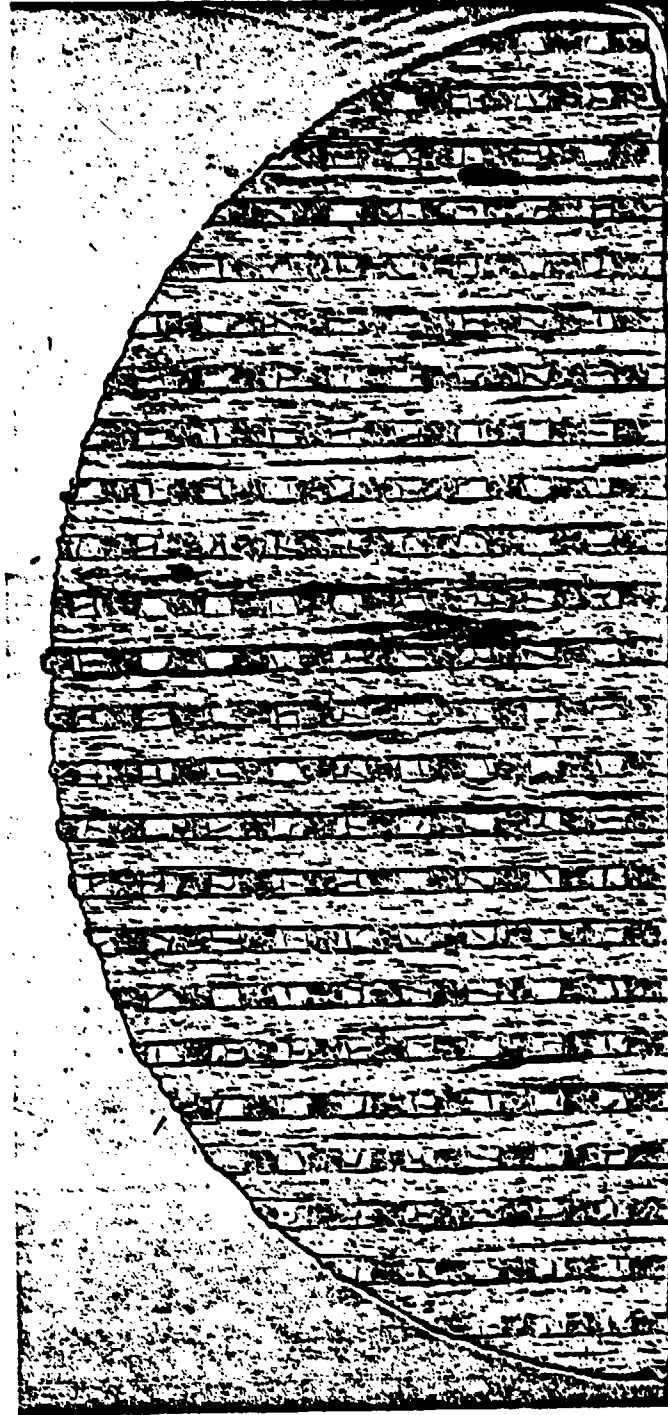


FIGURE 3.16. FULL SECTION PHOTOMICROGRAPH OF CC-223 NOSETIP,  
SHOT 4880, 10x, (POST FLIGHT)

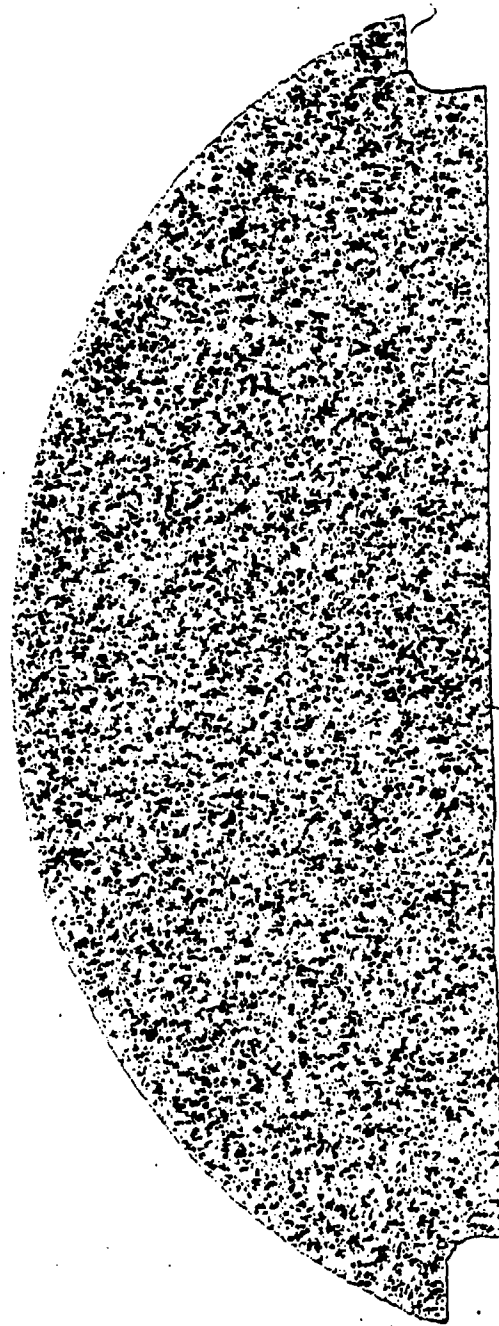


FIGURE 3.17. FULL SECTION PHOTOMICROGRAPH OF 994-2 NOSETIP,  
10X, SHOT 4886, (POST FLIGHT)



FIGURE 3.18. CROSS SECTIONAL PHOTOMICROGRAPH OF CC-223 NOSETIP,  
SHOT 4871, 200X

roughness heights measured for each phase in the composite and for a summation of the phases are shown in Figure 3.19. Although the roughness distributions (Figure 3.19) are narrower for the post flight models, the limited samples and test conditions do not permit a general conclusion concerning the effects of flight on roughness distribution.

High magnification (200X) photomicrographs were also taken of model 4886, made of 994-2 graphite, for roughness measurements. Typical photomicrographs taken using polarized light are shown in Figure 3.20. Both the small grain size and the highly uniform distribution of porosity is evident in these photomicrographs. The largest roughness elements appear to occur when pores intersect the surface, rather than from preferential etching of the individual grains in the graphite. Accumulative distribution of roughness heights measured is shown in Figure 3.21 and compares closely with the curve obtained from the preflight sample. However, relatively large isolated defects do develop in the 994 graphite surface during flight as seen in Figure 3.22 of preflight and postflight nose-tips. The pits in the postflight model may result from range debris or thermal stress in the graphite from the large temperature gradients, their influence on transition or heat transfer is not known. While the actual mean roughness height of each element is greater than the heights measured in the CC-223 model, the large width and spacing of each element gives the model a much smoother surface appearance. At this time, however, appropriate means for considering the effect of roughness spacing differences on a microscale level have not been developed.

A summary of the relevant roughness parameters are given in Table 3.4.

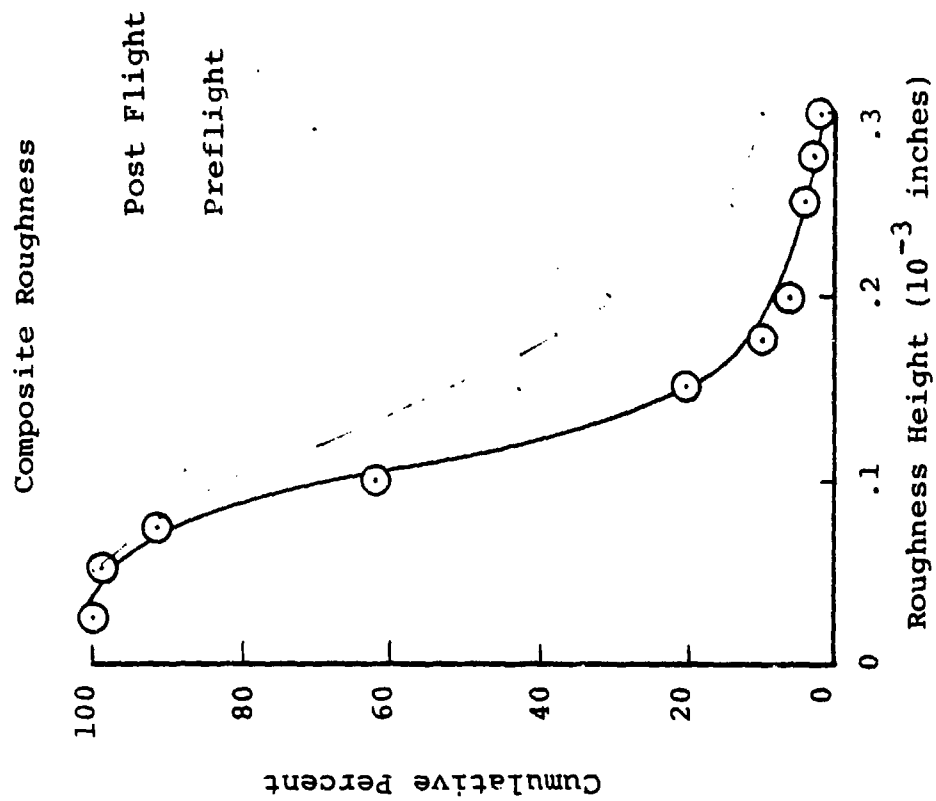
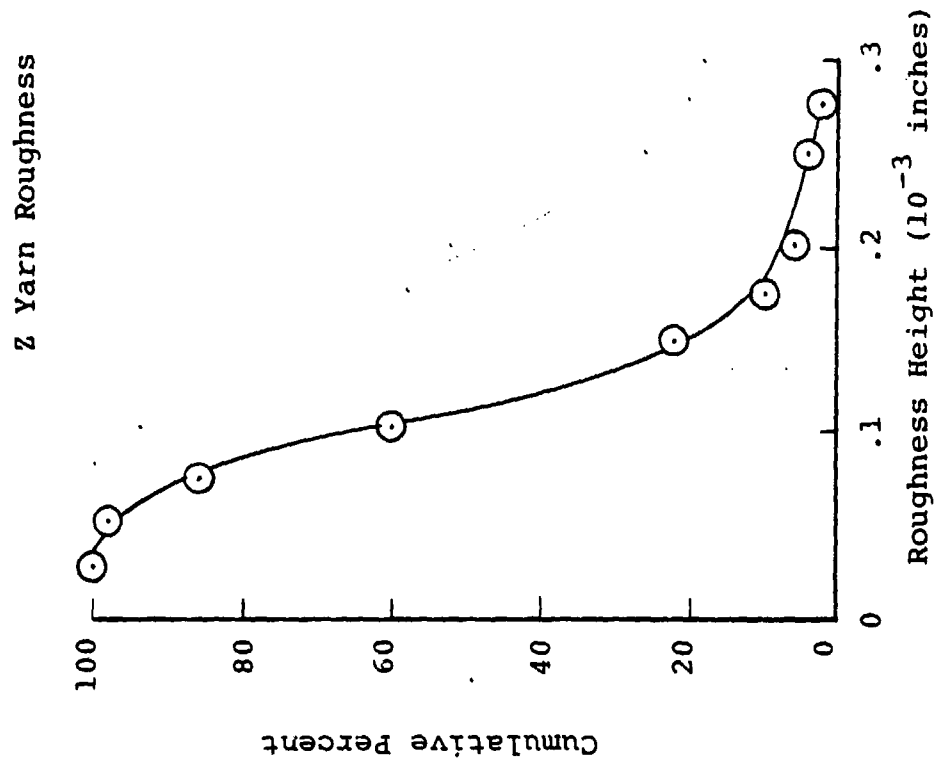


FIGURE 3.19A. MICROROUGHNESS HEIGHT DISTRIBUTION FOR GE 223,  
SHOT 4871 FULL SECTION (POST FLIGHT)

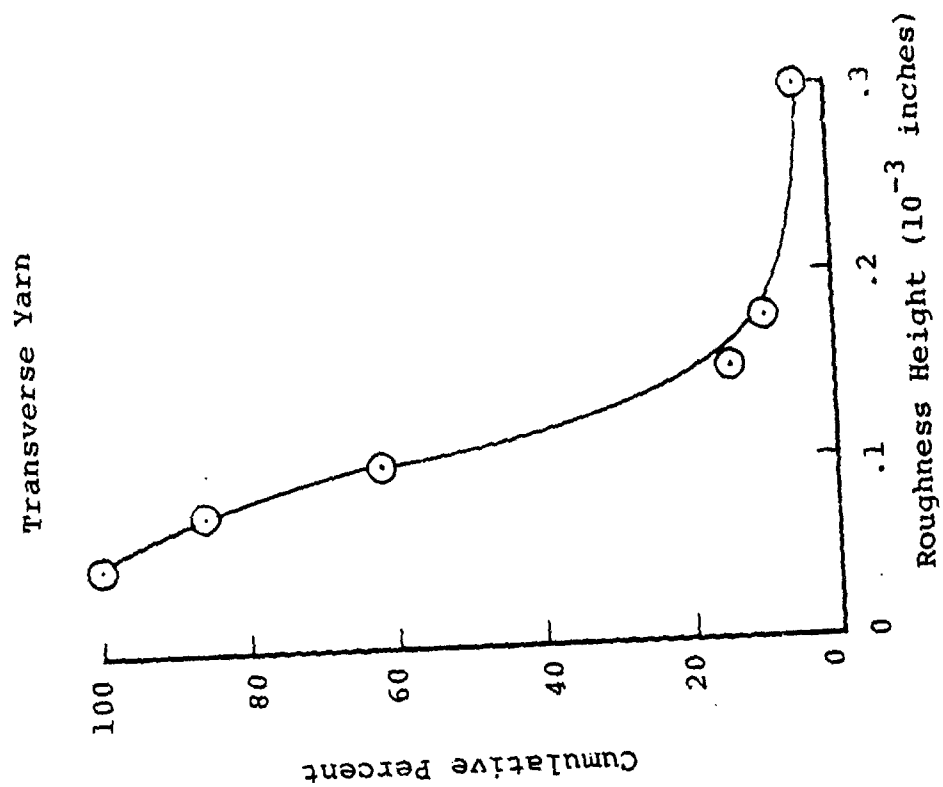
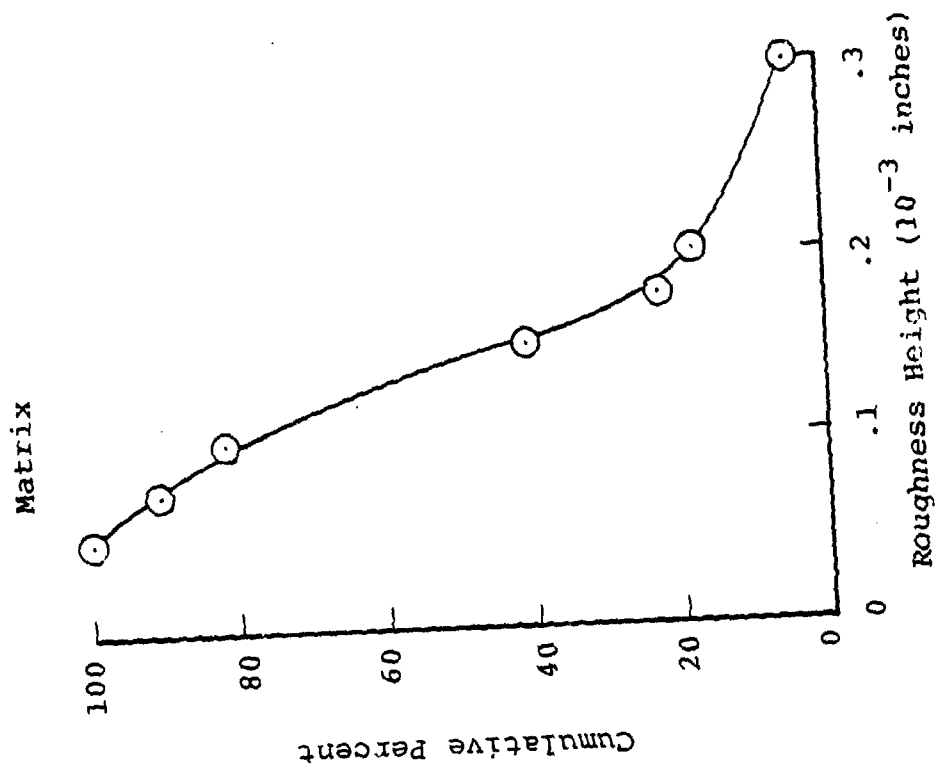


FIGURE 3.19B. MICROROUGHNESS HEIGHT DISTRIBUTION FOR GE 223,  
SHOT 4871, FULL SECTION (POST FLIGHT)



FIGURE 3.20. CROSS SECTIONAL PHOTOMICROGRAPH OF 944-2 NOSETIP,  
200X, SHOT 4886, (POST FLIGHT)

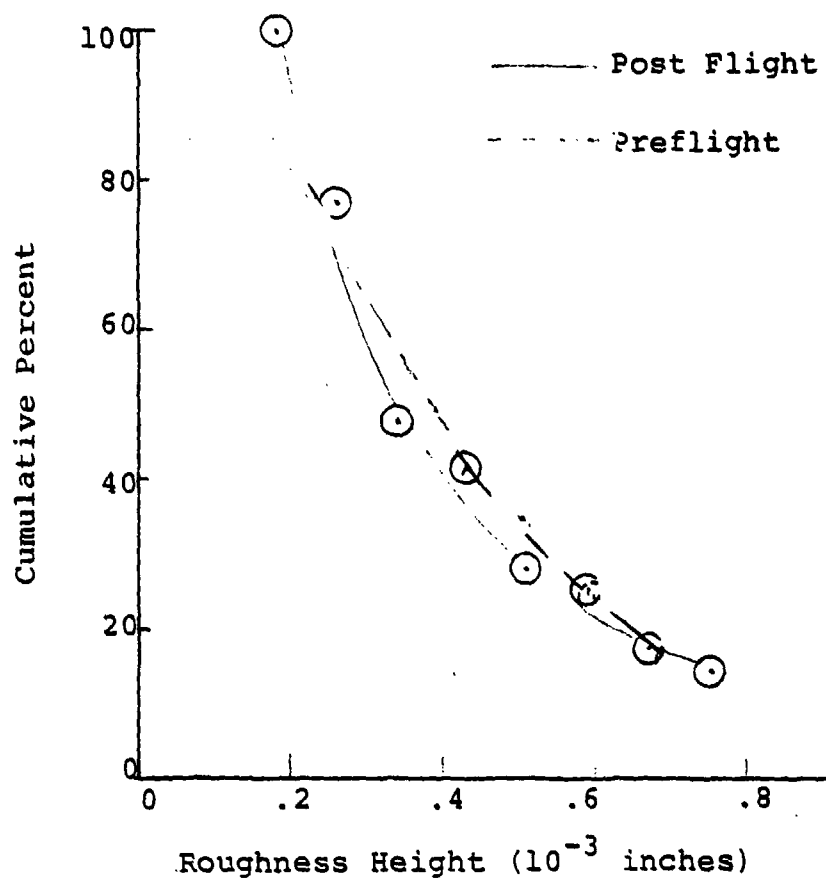
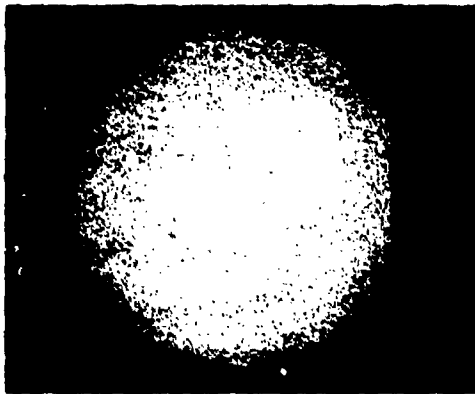


FIGURE 3.21. MICROROUGHNESS HEIGHT DISTRIBUTION FOR 994-2, SHOT 4886 FULL SECTION, (POST FLIGHT)



(A) PREFLIGHT



(B) POSTFLIGHT

FIGURE 3.22. PRE AND POSTFLIGHT PHOTOGRAPHS OF 994-2 GRAPHITE

TABLE 3.4. SUMMARY OF PREFLIGHT SURFACE MICROROUGHNESS CHARACTERISTICS

Model	$h_{ave}$ (mils)	$k_{ave}$ (mils)	$k_s$ (mils)	$W_{ave}$ (mils)	$L_{p_{ave}}$ (mils)
xx4 (994-2)	0.447	0.569	0.609		
[4886]	0.385	0.491	0.136	2.52	3.72
K-223 CC#2	0.196	0.25			
[4871]	0.214	0.272			
Replica (W)	0.229	0.292	0.141		
D-23 (ATJ-S)	0.431	0.548	0.763		

#### 4.0 TEST DESCRIPTION

##### 4.1 Test Matrix

The complete test matrix for the guided track G shots is listed in Table 4.1 in sequence as they were launched. Test conditions are listed in Table 4.2.

##### 4.2 Surface Temperature Data Reduction

Photographic pyrometry techniques used here have been adequately described in the literature (References 11,12,13). The basic data reduction procedure consists of:

1. Recording on film, nearly head-on, images of self luminous models with a high speed image converter camera (ICC).
2. Recording the image of a carbon arc calibration source on identical film and processing it simultaneously with the model photograph.
3. Microdensitometer scanning of the film and conversion of the film density of the model image to temperature distribution using the carbon arc calibration photographs.

Geometric projection of the nosetip into the film plane yields a one-to-one relation between points on the photographic image and the actual hemispherical nosetip. The brightness temperature data obtained from AEDC are arranged on the nosetip, provided a reference point (the stagnation point) on the photographic image and the projection can be related. For the last few shots small holes were drilled in the graphitic nosetip equally spaced approximately  $60^\circ$  from the stagnation point. This did not affect the overall performance of the nosetip, but did serve as reference points which were identifiable in the temperature contour plots. The use of raised pegs may be more effective.

TABLE 4.1. TEST MATRIX<sup>1</sup>

AEDC Shot No.	Temperature Data Available at ICC No.	Comments
4869-Z/PA <sup>2</sup>	19,29,41	Ran thru welding debris. Severely damaged.
4871-Z/PA	4,11,19,19,41	Recovered. Motion blur observed in ICC photographs.
4875-W/SS	4,11,19,29,41	Model tilted. Flare problem.
4877-W/NS	4,11,19,29,41	Model tip chipped. Flare problem.
4878-9/PA	-	Tip failed in launch.
4879-A/PA	-	Tip failed in launch.
4880-2/PA	4,11,19,29,41	Recovered. Strong preferential heating along fibers.
4882-W/PR	4,11,19,29	Laminar/turbulent distribution.
4883-W/SSR60	4,11,19,29	Recovered. Flare problem on smooth portion.
4884-W/SS	4,11,19,29,41	Flare problem.
4886-9/PA	4,11,19,29,41	Temperature too low.
4887-W/SSR30	4,11,19,29,41	Flare problem on smooth portion.
4909-W/SS	4,11,19,29,41	Verification of free flight results. $R_N = 0.25''$
4951-9/PA <sup>3</sup>	4,11,19,29,41	Resin rich heatshield. Optical stops. Parts of heatshield still hot. Laser photos indicate rough nosetip; 4, 11, 19 ICC's saturated.
4952-W/SS <sup>3</sup>	11,19,29,41	TFE heatshield stripped off after launch; exposed AL aft body very hot. Edge of W nosetip chipped badly. Much ablation from tip holder. No apparent model tilt.

TABLE 4.1. TEST MATRIX<sup>1</sup> CONTINUED

AEDC Shot No.	Temperature Data Available at ICC No.	Comments
4953-A/PA <sup>3</sup>	4, 11, 19, 29, 41	Resin rich heatshield, hot. Chunk missing on nosetip. Partially recovered nosetip indicates rough surface, 4, 11 ICC's saturated.
4954-2/PA <sup>3</sup>	4, 11, 29, 41	Resin rich heatshield. Nosetip image indicates preferential heating along x-y weave; local hot spots. Model recovered.
4955-F/PA <sup>3</sup>	4, 11, 29, 41	Resin rich HS with extra 30 mils epoxy. Chunk missing in nosetip - hot spot. Model recovered.
4963-W/SS	4, 11, 20, 29, 41	Excellent results at all ICC stations.
4964-F/PA	4, 11, 19, 29, 41	Heatshield hot at ICC 11. Model recovered.
4974-A/PA	4, 11, 19, 29, 41	Heatshield hot at ICC 11.
5003-W/SS	4, 11, 19	Tip broken all along edge.
5018-9/PA	4, 11, 19, 29, 41	100 toor He in blast tank model recovered.
5068-2/PA	4, 11, 19, 29, 41	Model recovered. Heat shield hot at ICC 11.
5069-2/PA	4, 11, 19, 29	Model recovered.

TABLE 4.1. TEST MATRIX<sup>1</sup> CONTINUED

1. All models are hemispherical with  $R_N = 0.4"$  except 4909, 4963 which are  $\frac{1}{4}"$ . All tests in N<sub>2</sub>.

2. Material Symbol

9 - 994-2  
 W - Tungsten  
 A - ATJ-s  
 Z - GE 223  
 F - FWPF

Surface Finish

NS - Nominally Smooth  
 SS - Super Smooth  
 PR - Pre-roughened ring with smooth  
 PRRXY - Pre-roughened stagnation region subtending XY degrees.

3. These shots were impacted by unknown quantity of range debris.

TABLE 4.2. TEST CONDITIONS

AEDC Shot No.	Launch Weight (kg)	Initial Velocity (kfps)	Recovery Tube Velocity (kfps)	$\rho_{\infty}$ (mm Hg)	Initial P <sub>stagnation</sub> (atm)	Initial H <sub>stagnation</sub> (btu/lb)	Drag Coefficient	$\beta$ (psf)
4869-2/PA <sup>1</sup>	0.482	16.324	15.028	151.16	56.633	5447	0.398	78.353
4871-2/PA	0.485	16.222	14.974	144.3	53.403	5380	0.400	78.414
4875-W/SS	0.523	15.253	10.548	735.6	273.25	5402	0.468	72.352
4877-W/NS	0.523	15.402	11.979	566.8	214.34	5500	0.438	77.308
4880-9/PA	0.493	15.856	14.97	100.4	35.509	5147	0.426	74.827
4882-W/PR	0.528	16.364	12.05	569.7	214.46	5475	0.428	79.802
4883-W/SSR	0.534	16.064	11.678	572.1	207.67	5280	0.449	76.906
4884-W/SS	0.532	16.201	11.928	567.5	209.47	5369	0.433	79.451
4886-9/PA	0.484	15.83	14.591	150.2	52.948	5131	0.396	79.004
4887-W/SS	0.530	16.157	12.012	564.8	207.38	5339	0.42	81.676
4909-W/SS	0.492	16.578	11.914	574.4	221.75	5616	0.427	74.532
4951-9/PA	0.601	15.45	15.01	200.1	76.099	5529	0.416	93.6
4952-W/SS	0.640	15.75	10.25	738.2	157.58	5079	0.584	70.87
9453-A/PA	0.623	16.17	15.12	148.8	54.72	5348	0.425	94.96
4954-2/PA	0.629	16.35	15.83	70.3	26.42	5464	0.433	94.03
4955-F/PA	0.635	15.51	15.30	100.6	38.53	5569	0.728	56.44
4963-W/SS	0.630	16.20	12.48	567.5	209.47	5367	0.437	93.29
4964-F/PA	0.491	15.75	15.21	100.8	35.08	5079	0.405	78.45
4974-A/PA	0.589	15.75	14.42	198.3	69.18	5081	0.595	96.37

TABLE 4.2. TEST CONDITIONS CONTINUED

AEDC Shot No.	Launch Weight (kg)	Initial Velocity (kfps)	Recovery Tube Velocity (kfps)	$\rho_{\infty}$ (mm Hg)	Initial P <sub>stag</sub> (atm)	Initial H <sub>stag</sub> (btu/lb)	Drag Coefficient	$\beta$ (psf)
5003-W/SS	0.525	15.23	11.94	567.9	210.37	5387	0.429	79.27
5018-9/PA	0.499	15.92	14.12	200.65	71.54	5186	0.450	71.68
5068-2/PA	0.493	16.03	14.18	148.9	53.83	5258	0.614	51.93
5069-2/PA	0.496	15.97	13.52	300.4	107.78	5220	0.414	77.46

1. Material Symbol

- 9 - 994-2
- W - Tungsten
- A - ATJ-S
- 2 - GE 223
- F - FWPF

Surface Finish

- NS - Nominally Smooth
- SS - Super Smooth
- PR - Pre-roughened
- PRRXY - Rre-roughened ring with smooth stagnation region subtending XY degrees

The brightness temperature data on the nosetip is arranged according to the schematic in Figure 4-1. Temperature is given in  $3^\circ$  increments in both  $\theta$  (streamwise around nosetip) and  $\phi$  (aximuthal) and is stored on magnetic tape to facilitate computer processing.

#### 4.3 Data Uncertainty

Several sources of error in the temperature measurements were considered in the free flight test report (Reference 3). Except for some problems unique to the track tests, as will be discussed below, the uncertainty in the temperature measurements is still approximately  $\pm 150 - \pm 200^\circ\text{K}$ . As in the free flight tests, the estimated uncertainty (95 percent confidence level) of the free-stream measurements and calculated stagnation conditions are as follows:

<u>Parameter</u>	<u>Estimated Bias Percent</u>	<u>Random Error Percent</u>
Free Stream Pressure	0.7	0.3
Free Stream Temperature	0.1	0.2
Free Stream Velocity	Negligible	0.5
Total Enthalpy	Negligible	1.0
Stagnation Pressure	0.8	1.2

#### 4.4 Track G Related Problems

A number of problems unique to the operation of the track were encountered at the beginning of the track test series, these were considered sufficiently serious that the brightness temperature results were in doubt. A brief discussion of each of these problems and their solution is given in this section.

##### 4.4.1 Luminosity Effects from Extraneous Sources

Early in the test as in the free flight series, smooth tungsten models were flown (Shots 4875, 4877) to validate the

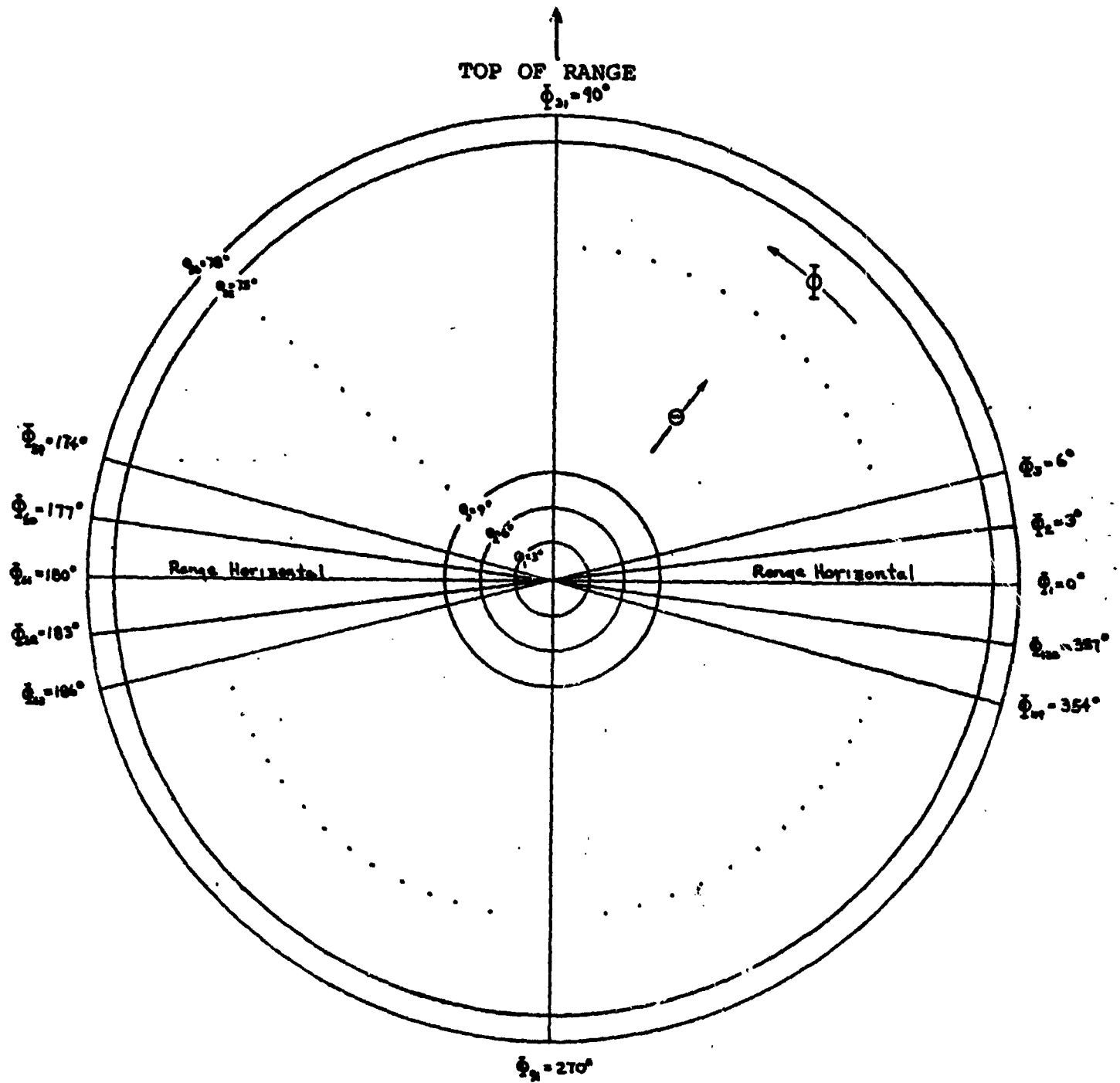


FIGURE 4.1. ARRANGEMENT OF POINTS OF PROJECTION FOR TEMPERATURE RECORDING (VIEWING UP RANGE)

test and data reduction procedures by reproducing a fully laminar flow over the nosetip. Results from the super smooth shot 4875, Figure 4.2, are significantly higher than predicted by laminar theory at the early ICC's and furthermore the distributions are not consistent with either laminar or turbulent predictions. Since similar free flight data were in excellent agreement with laminar theory, the present data were considered suspect. Extraneous illumination sources were thought to influence the apparent brightness temperature of the nosetip. The possible sources considered by AEDC were as follows:

- 1) Exposure flare: internal reflections within tube allow transfer of light from hot image areas to adjacent cool image areas.
- 2) Lens reflections: reflections between elements of optical system produce out-of-focus images which overlay the primary image.
- 3) Extraneous illumination of model: system cannot distinguish between self luminosity and light reflected from model surface.
- 4) Bleed thru: finite transmission of image converter tube when "off" allows exposure of model and wake to overlay model image.
- 5) Presence of self luminous, reflecting or absorbing particulate or gaseous cloud overlaying surface.

The first source appeared to be the most serious and the effect is shown schematically in Figure 4.3. The magnitude of the effect varies with the image intensifier tube, e.g., Figure 4.4 shows the exposure flare for the System 82, Gen II tube for various background brightness temperature levels.

The temperature for unity signal to noise ratio refers to the temperature for which the radiance of the signal is twice that of the background. Thus, even though the minimum detectable temperature is  $1200^{\circ}\text{K}$ , if the position of the measured temperature of  $1200^{\circ}\text{K}$ , is, say, 0.25" away from a temperature

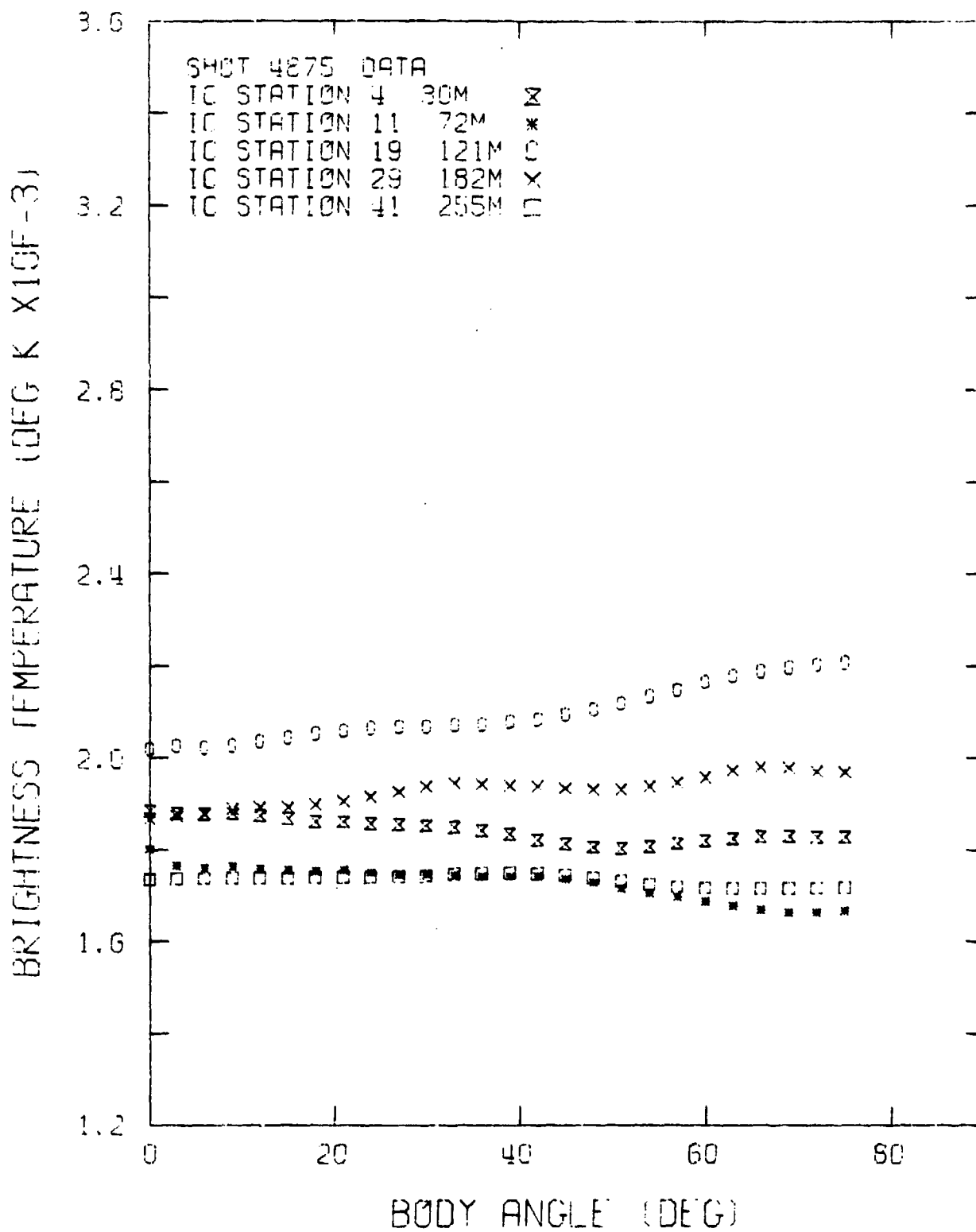


FIGURE 4.2. BRIGHTNESS TEMPERATURE DISTRIBUTION ON 0.4' RADIUS TUNGSTEN HEMISPHERE

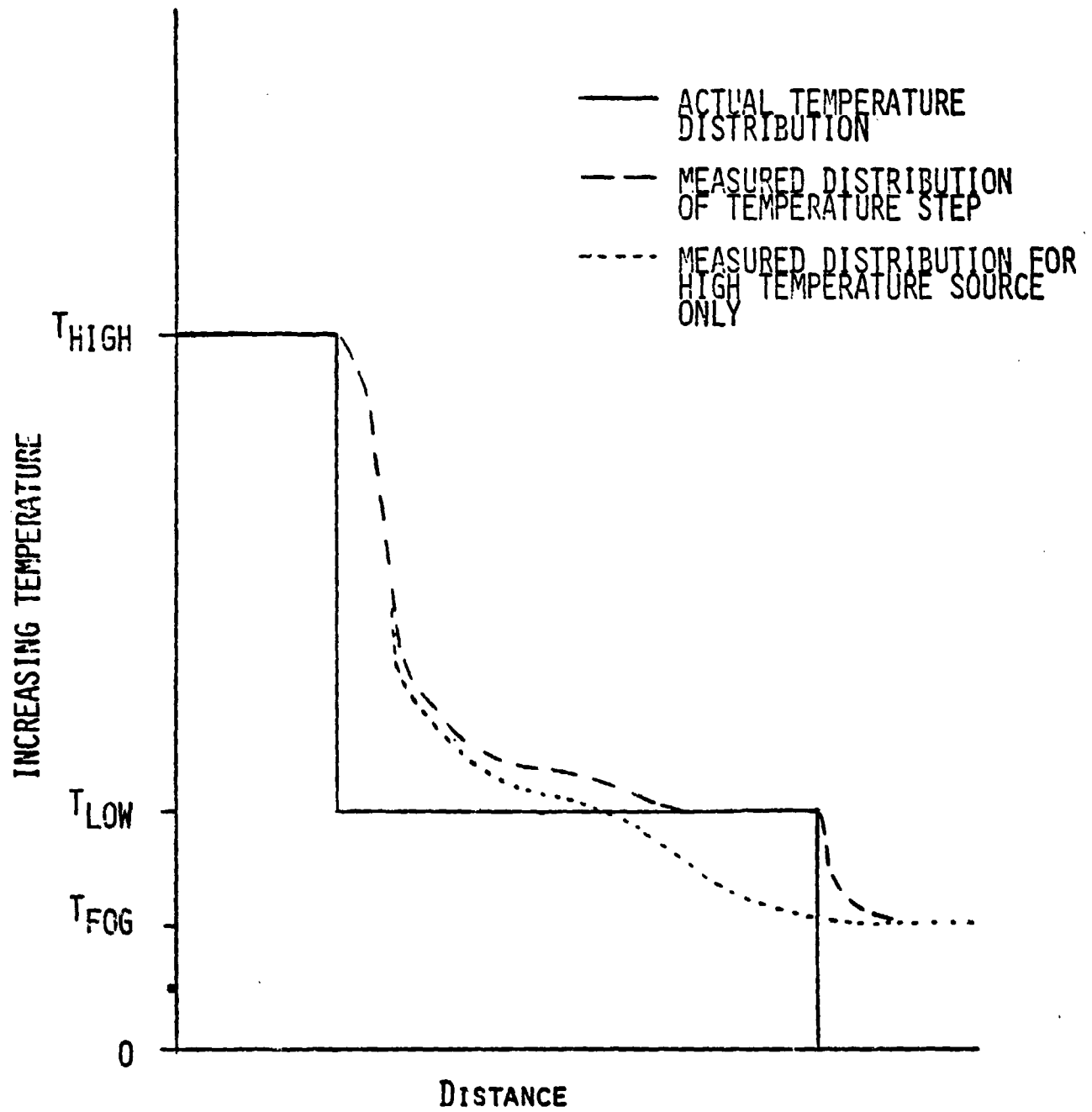


FIGURE 4.3. MEASUREMENT OF LOW TEMPERATURE SURFACE, ADJACENT TO HIGH TEMPERATURE ZONE

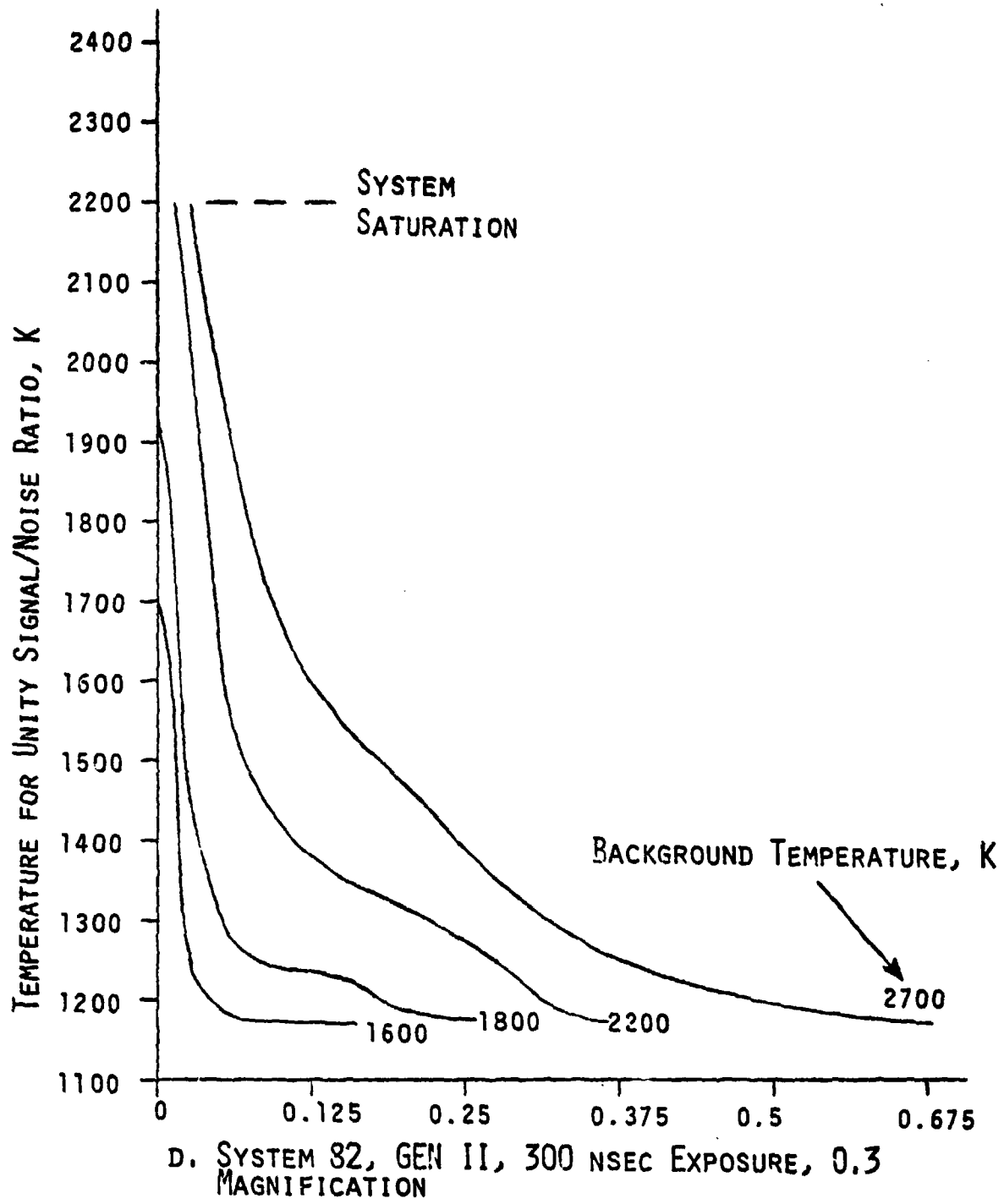


FIGURE 4.4. MINIMUM MEASURABLE TEMPERATURE VS DISTANCE FROM HIGH TEMPERATURE BACKGROUND

of  $2700^{\circ}\text{K}$ , the exposure flare effect results in a reading of  $\sim 1400^{\circ}\text{K}$ . The luminous source for such potential error was the hot heatshield as seen in some of the ICC photographs for various shots in Figures 4.5 and 4.6. The use of a resin-rich heatshield has alleviated this luminosity source as evidenced in Figure 4.6 shot 4963 ICC photographs on which the new heatshield was used. Other modifications to eliminate or reduce the effects of extraneous illumination included honeycomb light absorbers inside the rail sections in the vicinity of the focal plane, mechanical light blockers, rails painted flat black, and optical blockers in the ICC's. The 4th item (Bleed through) was determined not to be a problem and the 5th item, although may be a source of error in the presence of an erosion environment or TCNT models, should not influence the current test results. The effectiveness of these modifications is demonstrated in Figures 4.7 and 4.8 which are plots of the mean temperature distributions at the 5 ICC stations for shots 4909 and 4963. The corresponding ICC photographs in Figure 4.6, particularly at ICC's 4 and 11, show the effectiveness of the resin rich heatshield used in 4963, but not 4909 where a significant amount of luminescence is observed on the standard heatshield. Results in Figure 4.7 for ICC4 which show a flat temperature distribution is probably due to the exposure flare from the hot heatshield. The corresponding temperature distribution in Figure 4.8 is consistent with those obtained at the other ICC's and agree well with calculations. These results indicate that the exposure flare problem along with other extraneous illumination problems have been substantially reduced and probably does not degrade the data. The exposure flare may still affect the stagnation region temperature when a turbulent temperature distribution occurs which results in a higher temperature ring surrounding the stagnation point on the nosetip. However, estimates of the effect from studies such as that shown in Figure 4.4 indicate that the majority of the current results should not be influenced by this.

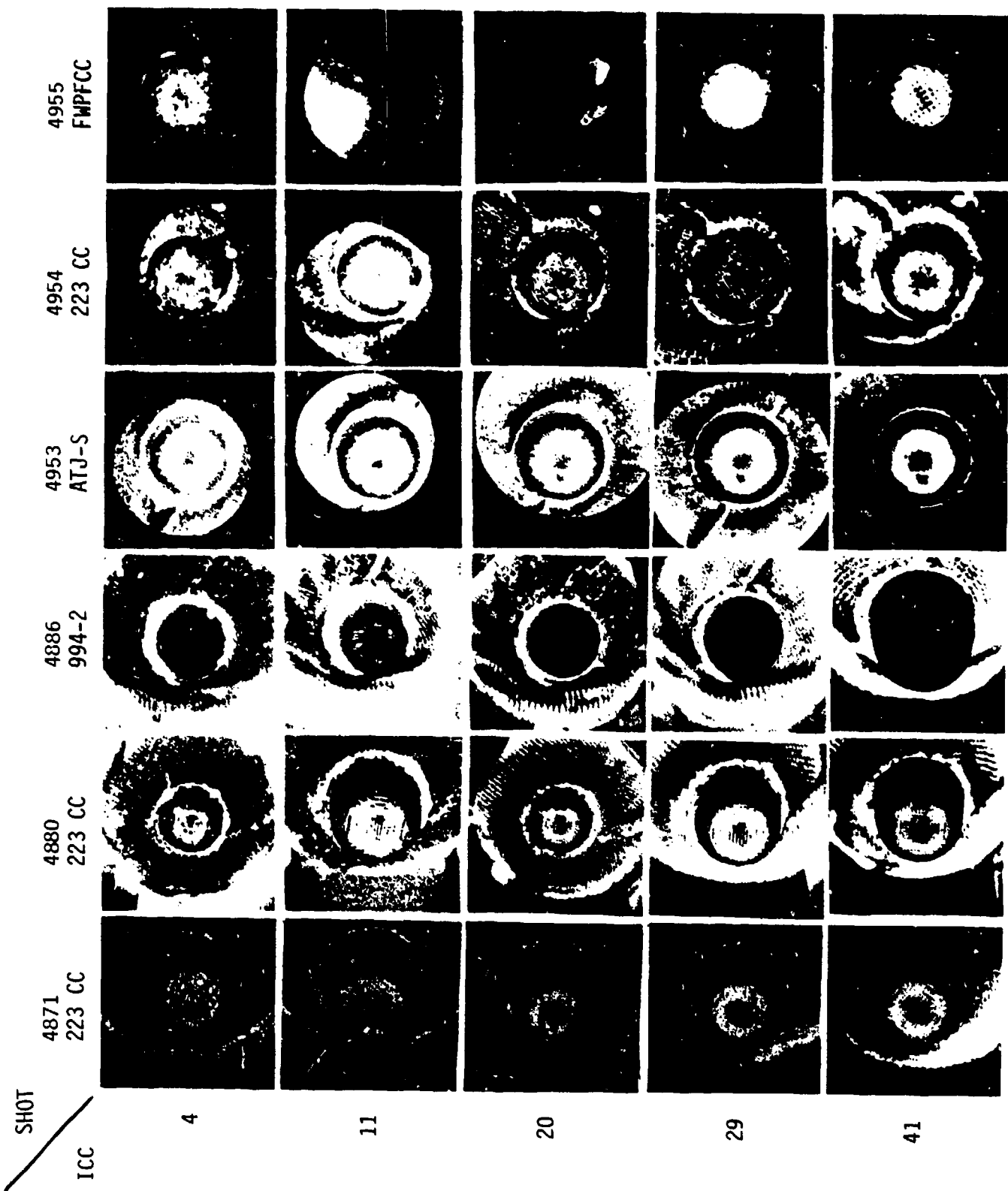


FIGURE 4.5. ICC PHOTOGRAPHS OF GRAPHITE AND CARBON-CARBON NOSETIPS

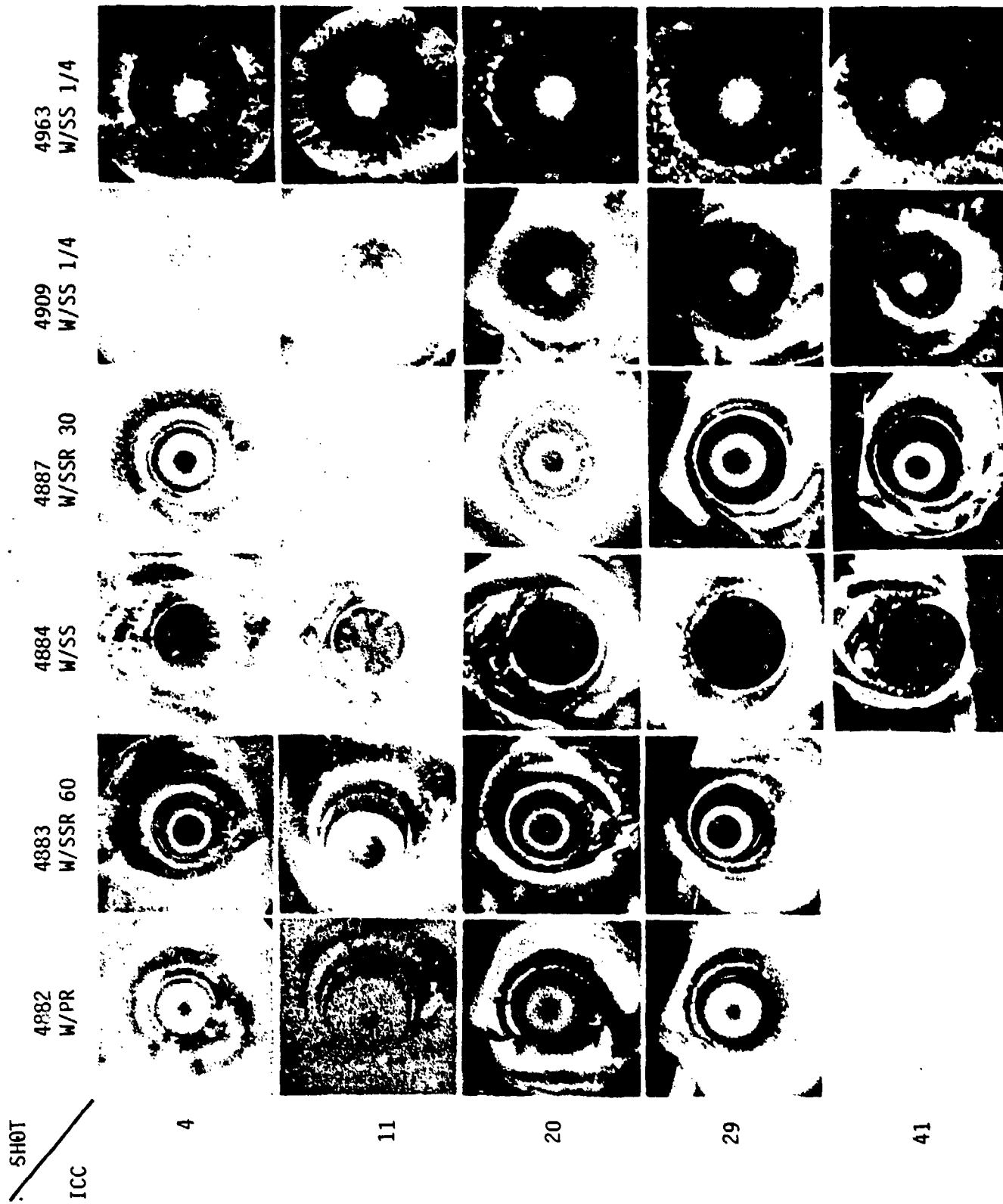


FIGURE 4.6. ICC PHOTOGRAPHS OF TUNGSTEN NOSETIPS

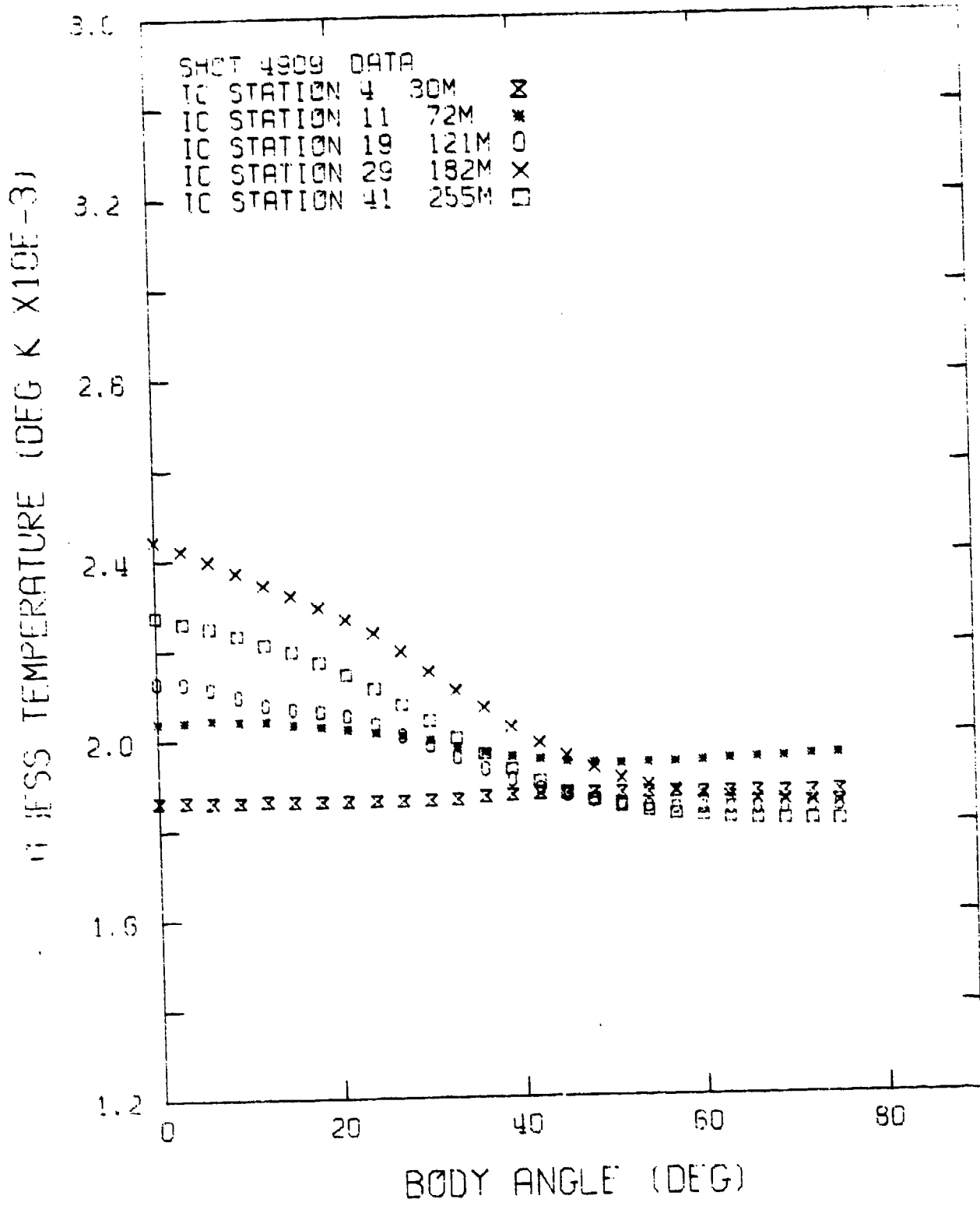


FIGURE 4.7. BRIGHTNESS TEMPERATURE DISTRIBUTION ON 1/4" RADIUS TUNGSTEN HEMISPHERE

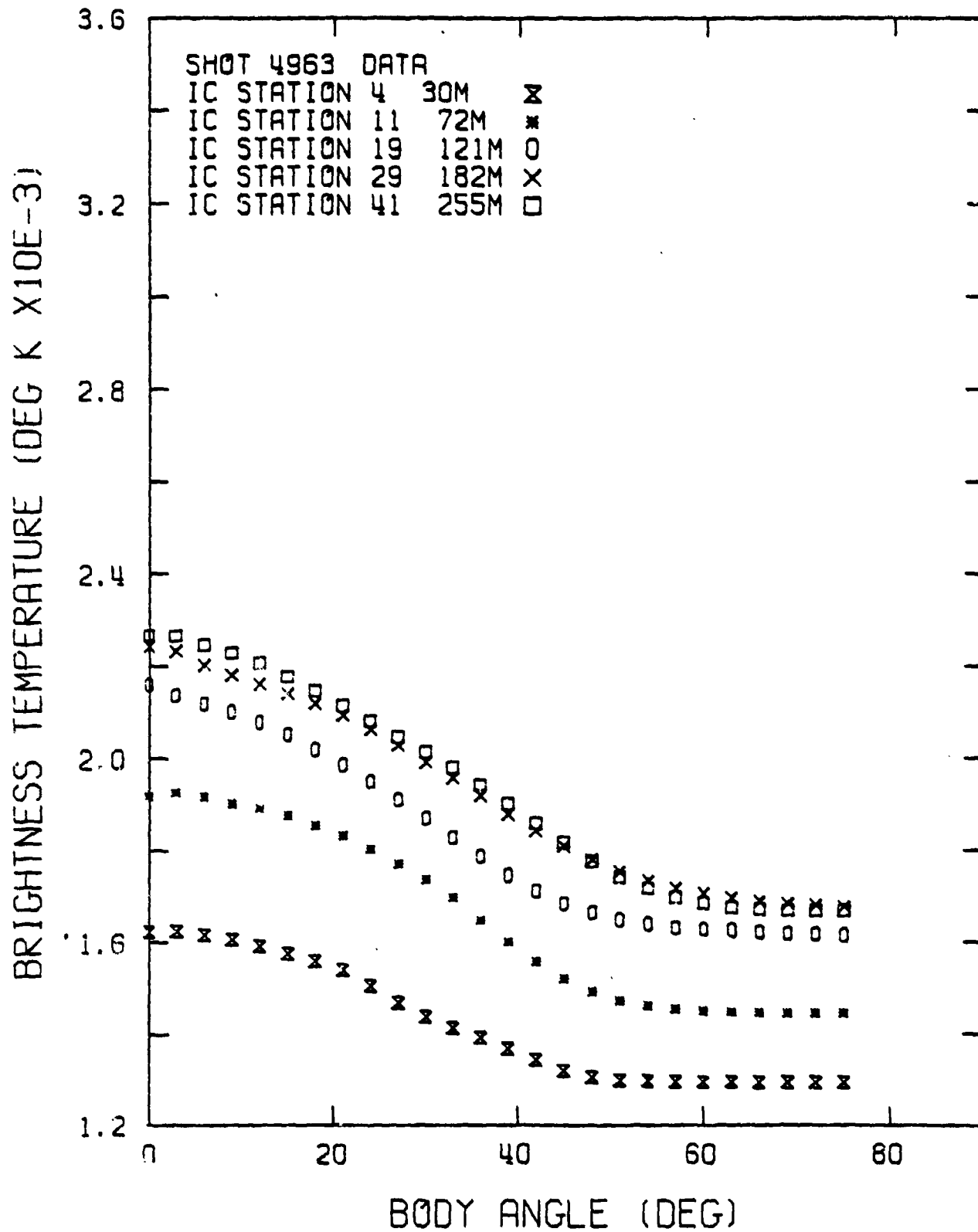


FIGURE 4.8. MEAN BRIGHTNESS TEMPERATURE DISTRIBUTION AROUND HEMISPHERICAL NOSETIP, W.

#### 4.4.2 Other Considerations

Other problem areas that have been considered were (1) model tilt which was rectified by using a longer wheelbase model, (2) potential pressure buildup in the blast tank prior to model passage through the quick opening valve which was determined to be minimal and can be accounted for, (3) rail vibrations due to the launch transients were determined to be preceded by the model and therefore should not affect the transition results and (4) range debris particularly near the blast tank exit where the jet blast may stir up loose particles of dust that would alter the model surface and possibly change the transition behavior. More effective prelaunch cleanup procedures and use of equal blast tank and range pressures to minimize the stirring effects will help to reduce the debris present.

## 5.0 ANALYSIS

### 5.1 Data Format

The brightness temperature data on the entire nosetip is available in 3-degree increments, both along the body (represented by the angle  $\theta$  or wetted distance  $s$ ) and around the nosetip (represented by the azimuthal angle  $\phi$ ). Therefore, there are 120 temperature profiles along the nosetip at each image converter camera location. If the freestream and surface conditions were such that complete axisymmetry exists, then these 120 profiles would be identical. However, due to the nonuniformity in the surface roughness elements, as well as the possibility that an angle of attack may exist, axisymmetric conditions are not generally obtained. The degree of deviation from the symmetric conditions in the data is indicative of how uniform the surface conditions are. A detailed look at the individual temperature profiles can shed some light on whether or not a preferred orientation of transition location exists. Also, the potential existence of gouges can be identified via hot spots. This task, however, requires detailed analysis of the large bank of data generated at each ICC for each shot (a maximum of 600 profiles for each shot).

The brightness temperature data were averaged in the  $\phi$  direction (i.e., over the 120 profiles) to give mean temperature profiles along the nosetip at each image converter camera location. Superposing the mean temperature profiles for all the ICC stations gives the nosetip mean temperature-time history down-range. Such information was plotted for each shot (Figure 5-1 depicts an example).

In addition to the mean temperature profiles, the maximum, minimum and standard deviations were obtained along the nosetip, as illustrated in Figure (5.2). The magnitude of the standard deviation represents the degree of departure from axial

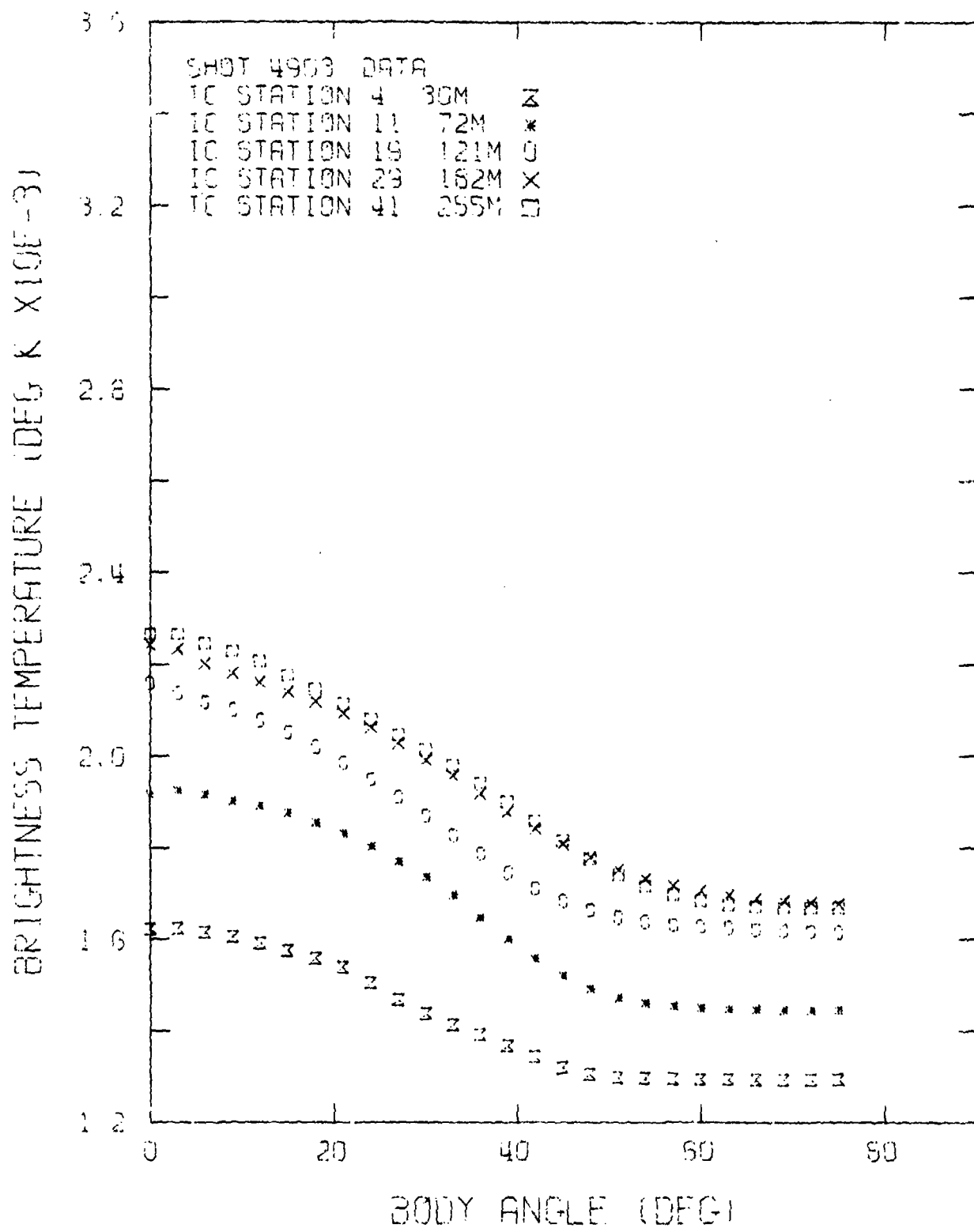


FIGURE 5.1. NOSETIP MEAN TEMPERATURE PROFILES  
FOR VARIOUS DOWNRANGE LOCATIONS, SHOT 4963

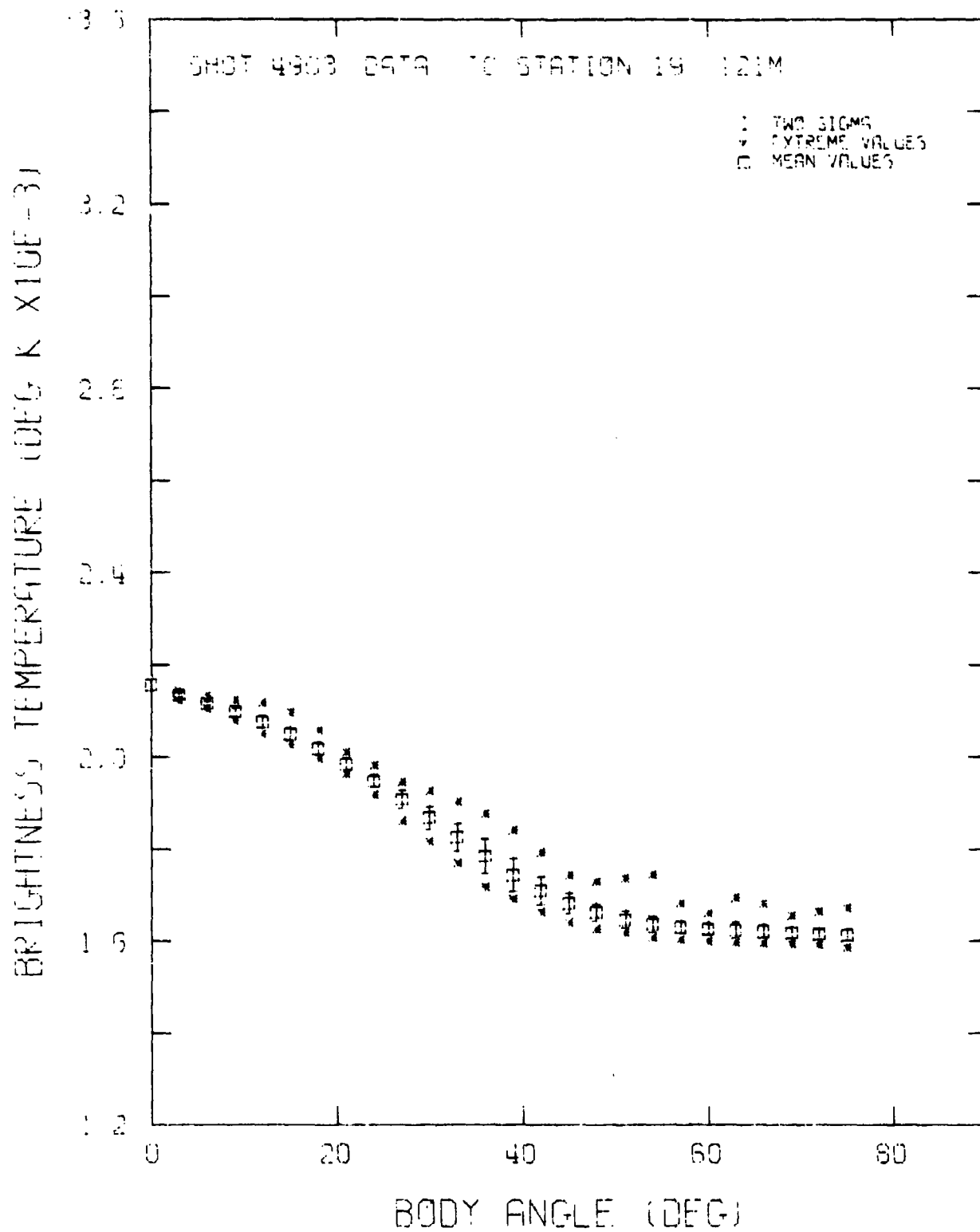


FIGURE 5.2. MEAN, MAXIMUM, MINIMUM AND STANDARD DEVIATION PROFILES, SHOT 4963

symmetry in the measured temperatures, and hence the nonuniformity in surface roughness spatial distribution.

## 5.2 Modeling and Data Reduction

The objective of the testing and data analysis was to investigate

- 1) transition-front location/offset,
- 2) stagnation region heating augmentation, and
- 3) transitional and turbulent heating augmentation,

under typical flight environments. Since state-of-the-art predictive models are mainly based on wind tunnel data generated under idealized conditions, a secondary objective of the analysis was to test the extrapolation of these predictive methodologies to flight environments. These environments are characterized by both high freestream Reynolds numbers, and stagnation pressures.

The problem of concern is a very difficult one; the phenomena involved are highly coupled. Transition from a laminar to turbulent flow is triggered by some roughness height characteristic of the particular surface. In the transitional and turbulent flow regimes, roughness further augments the heat transfer to the surface. Depending on the location of transition, the stagnation region temperature is markedly affected and may indicate a stagnation region - transition related heat transfer augmentation. Furthermore, the surface roughness of real materials is such that a statistical distribution exists, and most probably a single roughness height cannot adequately represent roughness effects on transition and heating augmentation. Finally, the roughness height that may correlate with transition data may not be the same for the heat transfer augmentation.

The steps undertaken in the data analysis are summarized as follows:

1. Derive the heat transfer distribution around the nosetip utilizing a two-dimensional transient heat conduction code. The code used was the SAI CAPER-2D heat conduction code. The approach was to utilize the mean temperature-time history around the nosetip to predict the corresponding heat flux. The nosetip is then acting like a thick wall calorimeter where both indepth and longitudinal conduction fluxes are accounted for.

#### Transition

2. Infer the location of the transition region front from the shape of the heat flux around the nosetip. The transition front was taken to be either the minimum heat flux point or the location of the intercept of the two tangents to the heat flux distribution curve.

3. Compare between the data inferred transition front location and that calculated using state-of-the-art transition models, e.g., Anderson (Ref. 14), Bishop (Ref. 15), and Dirling (Ref. 16) which are built in a boundary layer predictive code like the ABRES Shape Change Code (ASCC).

4. Infer the statistical distribution of the location of the transition front from the individual surface temperature profiles along the nosetip. The temperature-derived transition location was at first taken to be the minimum temperature point, i.e., the point where  $dT/d\theta = \text{Zero}$ . Due to possible ambiguities, the transition locations were determined manually to be at the intersection of tangents to the laminar and turbulent portions of the temperature profile. A comparison between the heat flux and the most probable surface temperature derived transition locations was then performed.

#### Laminar Region Heating Augmentation

5. Extract the laminar region heating augmentation by direct comparison between the data derived stagnation point heat transfer and that computed using a laminar theory, e.g., Fay-Riddell as given by ASCC.

6. Verify the extrapolation of state-of-the-art laminar rough wall heating augmentation methodologies to flight environments by direct comparison with the data derived augmentation levels. Phinneys' and the PANT rough wall laminar augmentation correlations were used in the analysis.

#### Transitional/Turbulent Region Heating Augmentation

7. Extract the transitional/turbulent region heating augmentation by direct comparison between the data derived heat transfer distribution around the nosetip and that computed by ASCC for the smooth wall conditions. Since the augmentation level is a strong function of the location of the transition front, the heat transfer coefficients were based on the same location of transition. That is, the location of the transition front was set equal to data derived values.

8. Verify extrapolating state-of-the-art transitional/turbulent heat transfer augmentation as given by ASCC methodology, to flight environments, by comparing the data derived and ASCC computed rough wall heat transfer distributions around the nosetip. Two situations were considered here for the ASCC calculations. In the first the transition locations were set equal to the data derived values, and in the second situation the transition was computed using the PANT transition correlation.

A different approach was also taken in the data analysis where the nosetip measured mean surface temperatures were compared with those predicted using the ABRES shape change code (ASCC). The degree of agreement between the two temperature profiles at all image converter camera locations determines the capability of the code and its built-in predictive models to simulate the transition location and heat transfer distribution.

Deviations between the measured and predicted temperature profiles can be due to inadequacies in the transition and/or heat transfer models, or due to incorrect representation of the surface roughness. This data reduction approach is difficult due to the strong coupling between transition, heat transfer and surface roughness characterization.

The advantage of the heat flux approach over the surface temperature one is that the derived heat flux is independent of any boundary layer theory one may use, and represents the net heat flux the model is subjected to. The approach, however, is sensitive to the nature of the temperature-time history and a maximum number of data points along the trajectory are needed for the approach to be reliable. Unfortunately only a maximum of five image converter cameras are available, and for a few of the shots the data at all locations were either not available or unreliable.

One-dimensional transient heat conduction calculations were first made to determine the sensitivity of the heat transfer to the time-interpolation of temperature data between the ICC stations. In Figure 5.3, the wall temperature history was calculated for an assumed cold wall heating input. Then discrete computed temperature data at times approximating ICC station locations were determined with  $T(t_0)$  assumed to be at room temperature. Interpolation schemes were tested to determine best fit to the calculated points in between the data points. From  $t_0$  to the first ICC (4), a quadratic interpolation fits the data very well as one might anticipate on theoretical grounds since  $\Delta T \sim t^{1/2}$  for short times. In between the other points, i.e., ICC locations, a 3 point Lagrangian interpolation appears quite good. A comparison of the derived heating rate, inputting the wall temperature in this discrete-interpolated manner, with the initially input heating rate is shown in Figure 5.4. The results are seen to be in some error for small  $t$ , but in good agreement elsewhere.

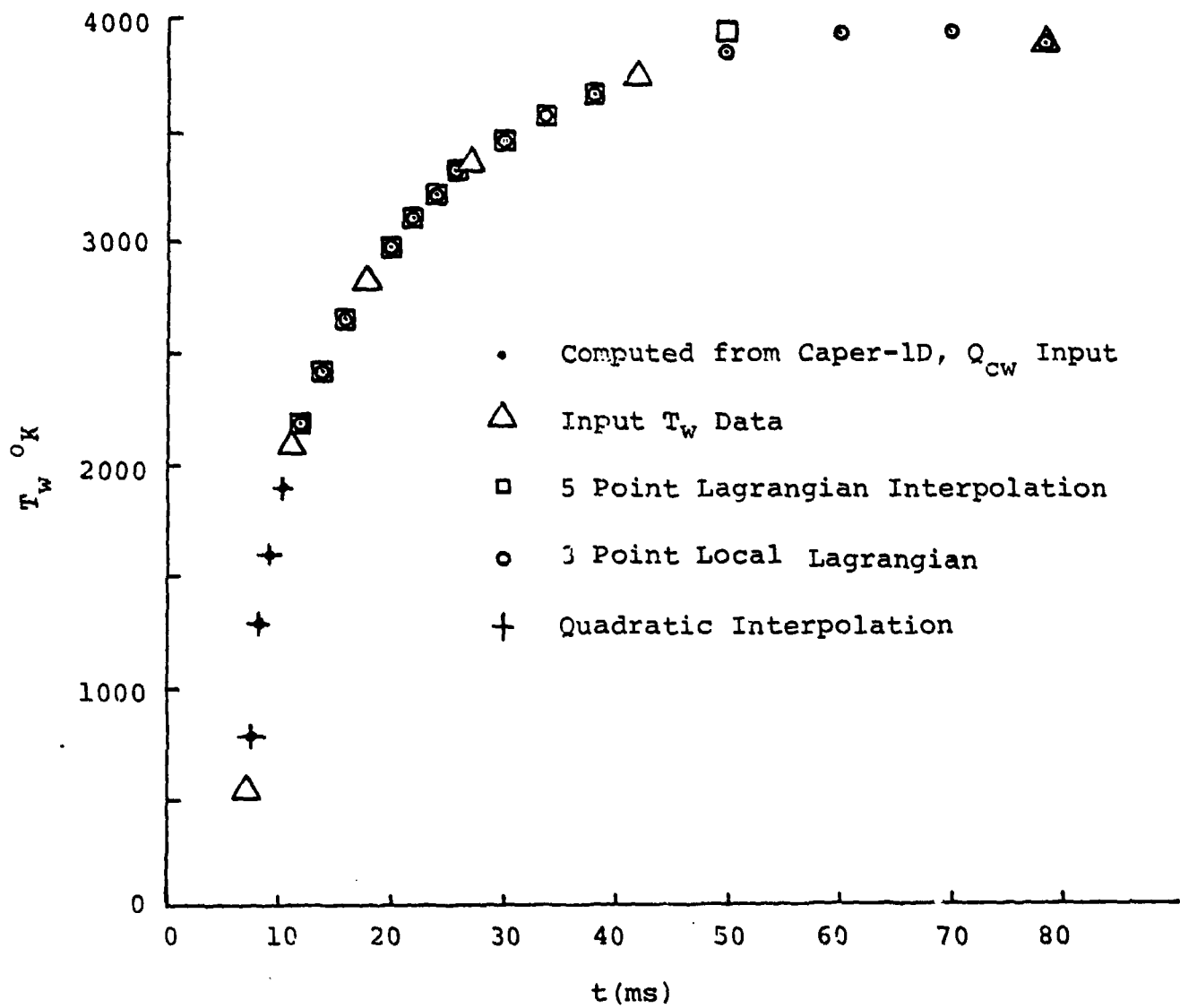


FIGURE 5.3. WALL TEMPERATURE INTERPOLATION

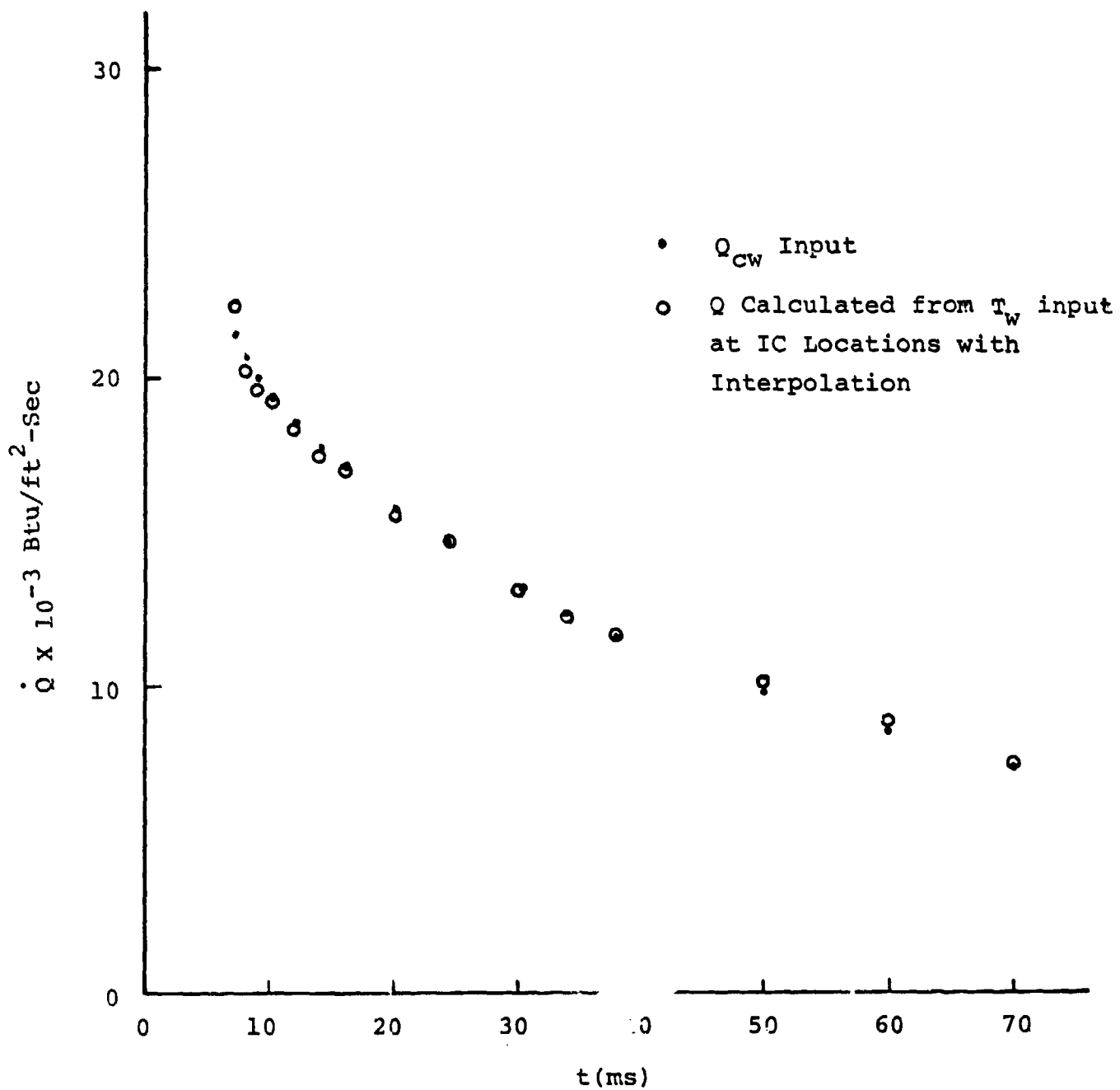


FIGURE 5.4. HEAT TRANSFER RATE CALCULATIONS

Similar to the one dimensional case, two-dimensional analyses were performed, utilizing the SAI CAPER-2D heat conduction code, in order to assess the effect of the temperature-time interpolation scheme between the ICC locations on the derived heat flux. The following was performed for a .25' tungsten model with a range pressure  $P_u/P_D = 570/570$  torrs, a launch velocity,  $U_I = 15,825$  ft/sec and a ballistic coefficient  $S = 110$  lb<sub>f</sub>/ft<sup>2</sup>.

1. For both laminar and turbulent situations the continuous temperature-time histories of the model surface temperature were generated. Figure 5.5 shows the laminar and turbulent heat fluxes input to the model surface at all ICC locations. Figure 5.6 depicts the corresponding thermal response of the model surface.

2. Generate the model surface heat fluxes which correspond to the discretized surface temperature at the ICC locations. Between launch and the first ICC a quadratic interpolation was used, i.e.,  $\Delta T \sim t^{3/2}$ . Downstream of the first ICC a 3-point lagrangian interpolation along the trajectory was used.

3. Compare between the input (step 1) and the generated (step 2) heat fluxes.

Similar to the 1D analysis, the comparison was found to be within 1% for both the laminar and turbulent cases, as expected. The heat flux is nearly one dimensional during the initial heat-up period of the model surface (the conduction depth is small, and heat is flowing mainly normal to the surface).

### 5.3 Codes Utilized in the Analysis

#### 5.3.1 The ABRES Shape Change Code (ASCC)

This code represents state-of-the-art in nosetip shape change calculations and utilizes boundary layer computations,

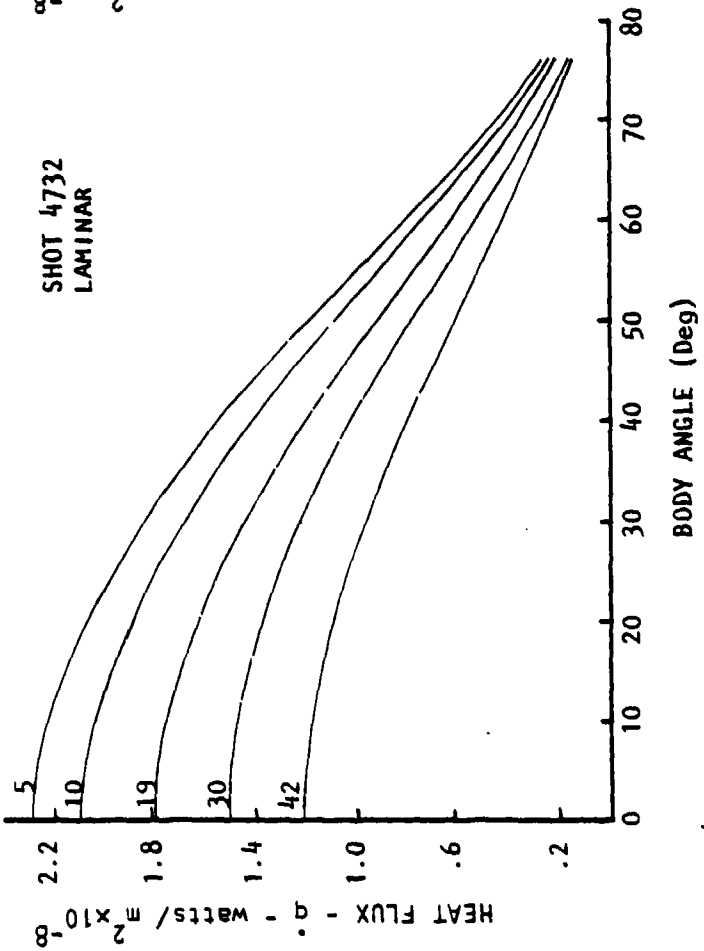
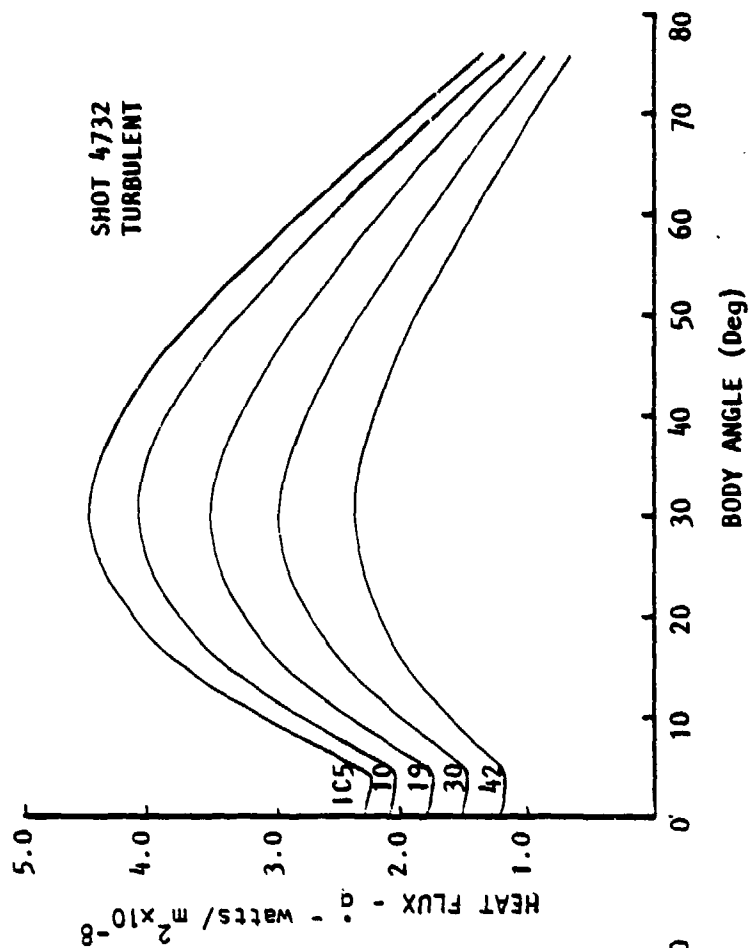


FIGURE 5.5 COMPUTED HEAT TRANSFER DISTRIBUTIONS USED IN EVALUATIONS OF DATA REDUCTION PROCEDURES.

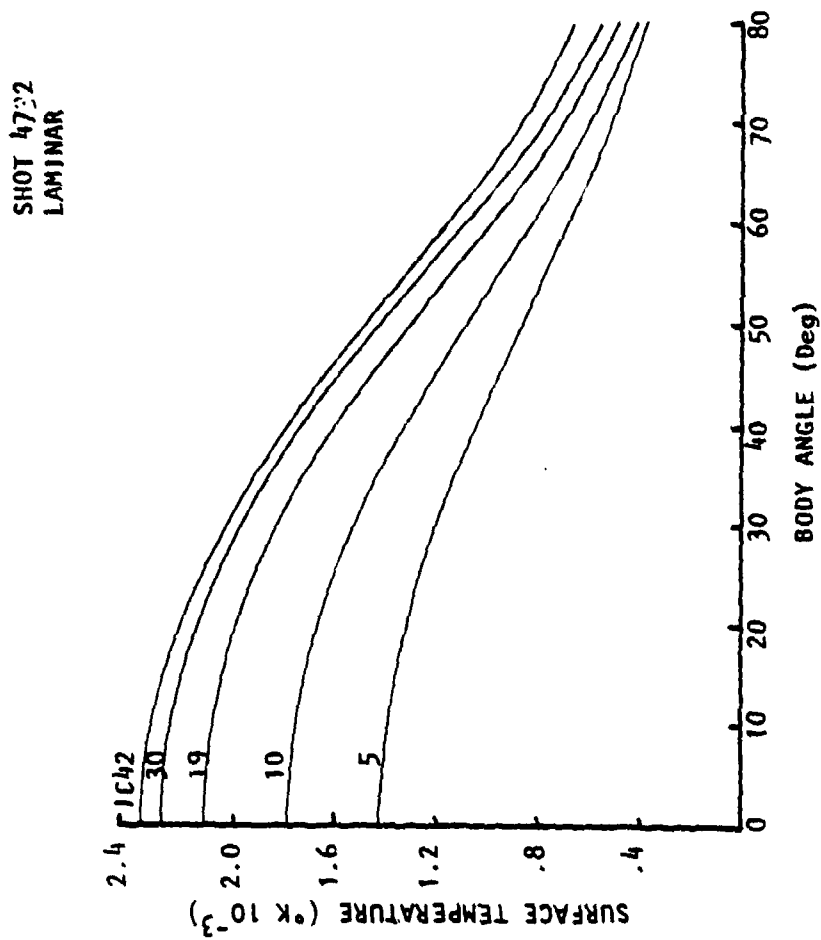
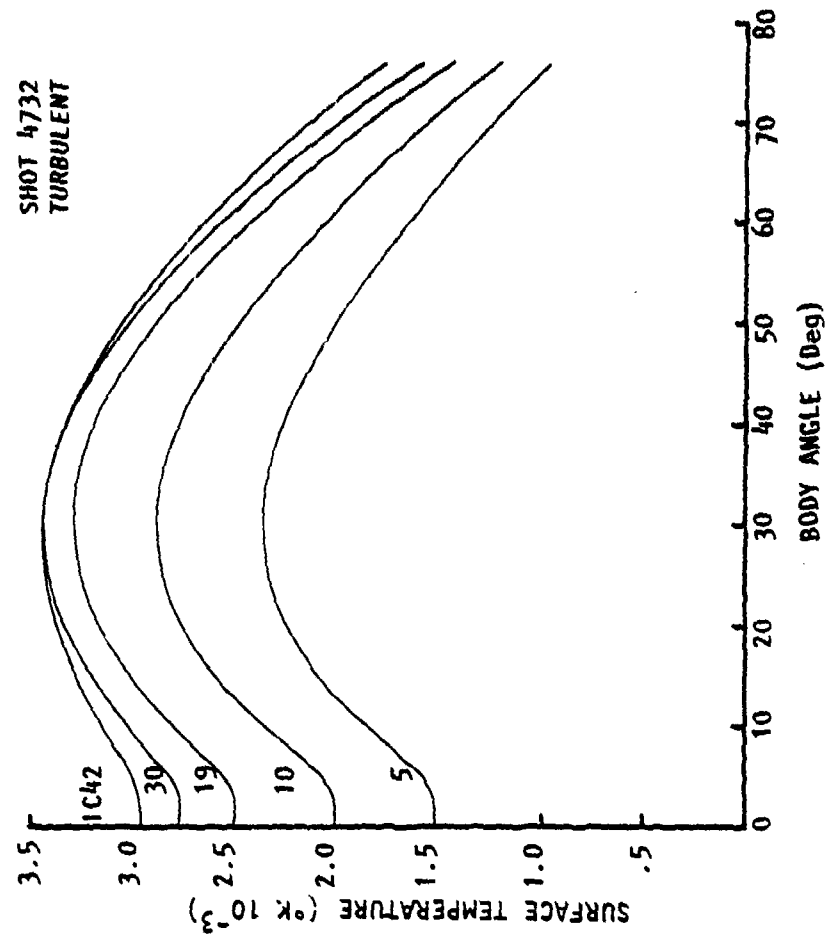


FIGURE 5.6. COMPUTED SURFACE TEMPERATURE DISTRIBUTIONS USED IN EVALUATION OF DATA REDUCTION PROCEDURES.

based on the integral technique. The aerothermal environment is obtained via predicting both the inviscid (pressure distribution and bow shock shape) and viscous (momentum and energy transport) flowfields. The inviscid flowfield solution establishes the boundary layer edge conditions necessary to perform the viscous calculations, accounting for entropy swallowing effects. The viscous solution provides wall fluxes (heat transfer and shear) as well as boundary layer characteristics (momentum thickness, shape factor, enthalpy thickness, etc.). The laminar, transitional and turbulent boundary layer regimes are also treated. The surface temperature, indepth temperature profiles and shape change are obtained from solutions to the coupled energy and mass balance equations at the surface, and the indepth two-dimensional transient conduction equations. The code can also be run in the aeroheating mode where the heat flux distribution is generated for an input surface temperature profile around the nosetip.

The boundary layer parameters and wall fluxes are obtained by solving the integral forms of the axial momentum and thermal energy equations. The basic heat transfer and wall shear laws are those of an incompressible flow over a flat plate. Influence factors are then applied to these laws to account for the effects of acceleration, blowing, variable properties, Mach number, and roughness. Details of the code can be found in Reference 17.

### 5.3.2 The SAI CAPER-2D Code

The CAPER-2D code is a two-dimensional transient code which solves the axisymmetric heat conduction equation accounting for variable properties and shape change. The numerical technique utilized is a fully implicit finite difference scheme, where the governing differential equation together with the surface relations are quasi-linearized and cast in their finite difference analogues. The resulting nonlinear algebraic equations

are solved using the alternating-direction-implicit (ADI) method. The solution procedure incorporates surface and internal regions in order to minimize the overall computational costs. There are two options for the code which are:

1. Heat Flux Boundary Condition: In this option the heat flux around the nosetip is input as function of time, for example utilizing an aeroheating boundary layer code, and the output is the temperature-time history of the model, i.e., the thermal response.

2. Surface Temperature Boundary Condition: Here the temperature-time history of the nosetip surface is input to the code and the output is the corresponding indepth heat conduction flux.

Details of the code are presented in Reference 18.

### 5.3.3 Matrix of the Analyzed Shots

Table 5.1 lists the shots analyzed. These shots were chosen based on availability and quality of temperature data. The model surface characterization, and the ICC locations at which the brightness temperature data was available are also given in the Table. The table indicates that some temperature smoothing was performed for a few shots to eliminate the effects of the hot heatshield. Also, the data at some ICC locations which were not consistent with the rest of the data due to ICC tube saturation were eliminated. The launch and trajectory information are given in Tables 5.2 and 5.3 respectively.

TABLE 5.1. MATRIX OF ANALYZED SHOTS

Shot #	Material	R <sub>N</sub> Inches	Surface Condition	Surface Microroughness			Temperature Data Available at ICC No.	Comments*
				K <sub>rms</sub>	K <sub>50%</sub>	K <sub>ave</sub>		
4882	W	.4	Pre-roughened		.21	.292	4,11,20,29	-Hot heatshield -Temperatures data at ICC 11 was not used in the analysis
4963	W	.25	Super Smooth	≤.01			4,11,20,29,41	-Good results at all ICC stations -.25" model radius -Temperature data at all ICC's was leveled for θ ≥ 60 to eliminate the effects of the hot heatshield
4953	ATJ-S	.4	Preablated		.35	.55	4,11,20,29,41	-Hot shield (resin rich heatshield) -Hot spot on nosetip due to chunk missing -Model broke up in recovery -Saturated ICC 11 -Debris present up range -Temperature data at ICC 41 was deleted and not used in analysis
4974	ATJ-S	.4	Preablated		.35	.55	4,11,19,29,41	-Hot heatshield at ICC 11 -Temperature data at all ICC's was leveled for θ ≥ 60 to eliminate the effect of the hot heatshield
4951	994-2	.4	Preablated		.37	.57	4,11,20,29,41	-Debris present up range/blast tank -Resin rich heatshield -Optical stops used -Parts of heatshield still hot
5018	994-2	.4	Preablated		.37	.57	4,11,20,29,41	-200 torr He in blast tank -Temperature data was leveled for θ ≥ 60
4871	CC-223	.4	Preablated		.175	.25	4,11,20,29,41	-Motion blur observed in IC photographs -Model recovered -ICC 19 data was not used in the analysis
4880	CC-223	.4	Preablated		.175	.25	4,11,20,29,41	-Strong preferential heating along fibers -Model recovered
4954	CC-223	.4	Preablated		.175	.25	4,11,20,29,41	-Model recovered
5068	CC-223	.4	Preablated		.175	.25	4,11,20,29,41	-Model recovered
5069	CC-223	.4	Preablated		.175	.25	4,11,19,29	-Model recovered

\*He may not be on at ICC 11 up through Shot 4974

TABLE 5.2. LAUNCH CONDITIONS OF ANALYZED SHOTS

AEDC Shot #	Material	R <sub>N</sub> (Inches)	Launch Conditions			
			T <sub>∞</sub> (°R)	PU/PD (torr)	UI (ft/sec)	β (lb/ft <sup>2</sup> )
4882	W	.4	543.37	570/570	16,364	79.8
4963	W	.25	538.4	570/570	16,200	93.29
4953	ATJ-S	.4	540.37	149/149	16,170	94.96
4974	ATJ-S	.4	541.07	198/198	15,750	96.37
4951	994-2	.4	535.87	200/200	16,450	93.6
5018	994-2	.4	533.2	201/201	15,920	71.68
4871	CC-223	.4	533.97	144/144	16,222	78.41
4880	CC-223	.4	540.0	100/100	15,856	74.83
4954	CC-223	.4	537.77	70/70	16,350	94.03
5068	CC-223	.4	538.84	149/149	16,030	51.928
5069	CC-223	.4	538.87	300/300	15,970	77.465

TABLE 5.3. TRAJECTORY INFORMATION OF ANALYZED SHOTS

Shot No.	ICC	Freestream Mach No.	Freestream Re No. ( $10^{-7}/ft$ )	Stagnation Enthalpy (BTU/lb <sub>m</sub> )	Stagnation Pressure (atm)
4882	4	13.85	6.98	4991	191.3
	19	12.48	6.3	4055	155.8
	29	11.65	5.88	3533	135.7
4963	4	13.78	6.95	4941	189.4
	11	13.23	6.67	4552	174.9
	19	12.60	6.35	4128	158.6
	29	11.89	6.0	3681	141.5
4953	4	14.06	1.85	5144	51.7
	11	13.91	1.83	5036	50.5
	19	13.69	1.8	4879	49.0
	29	13.55	1.78	4776	48.0
4974	4	13.66	2.4	4857	64.8
	11	13.46	2.35	4716	63.0
	19	13.25	2.32	4570	61.0
	29	13.00	2.27	4396	58.7
4951	4	14.26	2.53	5294	71.5
	11	14.06	2.49	5143	69.4
	19	13.83	2.45	4975	67.1
	29	13.54	2.40	4773	64.5

TABLE 5.3. TRAJECTORY INFORMATION OF ANALYZED SHOTS (CONT'D)

Shot No.	ICC	Freestream Mach No.	Freestream Re No. ( $10^{-7}/ft$ )	Stagnation Enthalpy (BTU/lb <sub>m</sub> )	Stagnation Pressure (atm)
5018	4	13.76	2.44	4926	66.4
	11	13.50	2.39	4744	64.1
	19	13.21	2.34	4541	61.4
	29	12.86	2.28	4303	58.1
4871	4	14.11	1.80	5177	50.4
	11	13.91	1.78	5034	49.0
	29	13.50	1.72	4743	46.2
	41	13.18	1.68	4522	44.1
4880	4	13.80	1.22	4956	33.5
	11	13.68	1.21	4869	33.0
	19	13.54	1.20	4767	32.3
	29	13.36	1.19	4644	31.5
4954	4	14.27	0.89	5300	25.2
	11	14.20	0.88	5248	24.9
	19	14.12	0.88	5187	24.6
	29	14.01	0.87	5110	24.3
5068	4	13.85	1.82	4991	50.0
	11	13.59	1.79	4802	48.3
	19	13.28	1.75	4592	46.1
	29	12.92	1.70	4345	43.7

TABLE 5.3. TRAJECTORY INFORMATION OF ANALYZED SHOTS (CONT'D)

Shot No.	ICC	Freestream Mach No.	Freestream Re No. ( $10^{-7}/ft$ )	Stagnation Enthalpy (BTU/lb <sub>m</sub> )	Stagnation Pressure (atm)
5069	4	13.73	3.65	4906	99.2
	11	13.38	3.55	4656	94.3
	19	12.98	3.45	4383	88.8
	29	12.50	3.32	4066	82.3

## 6.0 TRANSITION RESULTS

In this section the transition analysis results are presented. Transition-front locations were extracted from both the data derived heat flux and the temperature data distributions. Comparisons between the data inferred transition locations and those predicted by state-of-the-art nosetip transition models were also performed. A brief description of the transition correlations used in the analysis is given below.

### 6.1 Nosetip Transition Correlations

#### 6.1.1 Anderson - PANT Correlation (Ref. 14)

The PANT correlation represents state-of-the-art in predicting laminar to turbulent boundary layer transition. The model, which was based on wind tunnel testing, is given by the following relations

$$\begin{aligned} \text{Re}_\theta \left( \frac{k_i}{\psi \theta} \right)^{0.7} & \text{ (at sonic point) } = 255 \text{ for transition onset} \\ \text{Re}_{\theta, \text{tr}} \left( \frac{k_i}{\psi \theta} \right)^{0.7} & = 215 \text{ for transition location} \end{aligned} \tag{6.1}$$

where  $k_i$  is the intrinsic roughness, and  $\psi$  is a perturbation parameter given by

$$\psi = \frac{B'}{10} + \left( 1 + \frac{B'}{4} \right) \frac{\rho_e}{\rho_w} .$$

#### 6.1.2 Bishop's Transition Correlation (Ref. 15)

The Bishop transition criteria basically divides the nosetip into two regions: a forward region where the curvature of the concave streamlines (in the shock layer) influences transition, and a backward region where streamline curvature effects

on transition are small. This dividing point on the nosetip is approximately  $20^\circ$  off the stagnation point. In the flow regime close to the stagnation point transition location is given by

$$\frac{K}{D} = 152 \left[ \frac{(T_w/T_e)^{1.23}}{(S/R_N)} \frac{M_\infty}{Re_D^6} \right]^{1.96} \quad (6.2)$$

For  $\theta > 20^\circ$  the transition location is given by

$$5.6 \left( \frac{K}{D} \right)^{-1/3} = Re_\theta \left[ 1 + 4.5 \left( \frac{T_w}{T_e} \right) M_e^2 \right]^{-1/2} \quad (6.3)$$

Where  $K/D$  is the dimensionless roughness required to produce transition at a point on the nosetip where  $(K_i/D \geq K/D)$ .

### 6.1.3 Dirling's Transition Correlation (Ref. 16)

Dirling's approach is very similar to the PANT. The disturbance parameter, however, assumes a different form. The model is based on defining an effective roughness height,  $\tilde{K}$ , which accounts for the nosetip bluntness, at which the transition parameter is evaluated as follows

$$\frac{\tilde{K}}{K_i} = \left( 1 + 350 \frac{K_i}{R_N} \right), \text{ and} \quad (6.4)$$

$$\rho_\infty U_\infty \frac{\tilde{K}}{K} \frac{1}{\mu_w} = 160$$

The quantities  $\rho_\infty$  and  $U_\infty$  are obtained from the Pohlhansen fourth degree polynomial fit to the compressible laminar boundary profiles.

## 6.2 Data Inferred Transition Location

The nosetip transition-front location was determined in two ways:

1. From the mean temperature data-derived heat flux distributions the transition point was determined to be the point of either the minimum heat flux ( $dq/dS = \text{zero}$ ) or the intercept of the tangents to the laminar and transitional legs of the heat flux profile around the nosetip. The latter determination required some engineering judgement, but for the most part was unambiguous. Transition statistics may be obtained, in principle, from identical firings of many models of the same material.

2. Statistical transition information may be obtained from the data of a single flight if it is assumed that the brightness temperature distribution is directly related to the heat transfer distribution. The brightness temperature data on the entire nosetip is available in 3-degree increments, both along the body (represented by the angle  $\theta$  or  $S/R_N$ ) and around the nosetip (represented by the azimuthal angle). There are 120 temperature profiles along the nosetip at each image converter camera location.

Initially from the brightness temperature data the transition front location was determined to be the point of minimum temperature, i.e.,  $dT/dS = \text{zero}$ . At each ICC location the minima were obtained numerically for each of the 120 nosetip temperature distributions (each consists of 26 data points). The data points were first smoothed locally by applying a first-degree least squares approximation to three contiguous points (Ref. 19) sequentially until a new set of smoothed data points are obtained for the temperature distribution. The first derivative of the smoothed data was then calculated numerically and the zero slope point was determined. Histograms of the transition front location were then constructed. However, the results obtained numerically in this manner were greatly influenced by the numerical data smoothing and were judged to be inaccurate. Hence, the temperature deduced transition data were all hand processed at each ICC location as follows:

TABLE 6.1. NOSETIP TRANSITION FRONT LOCATION

Shot	Material	ICC*	Nose Tip Transition Location (Degrees off Stagnation Point)			Heat Flux Inferred	Temperature Inferred
			PANT <sup>†</sup> (K rms) ASCC T <sub>w</sub>	PANT <sup>†</sup> (K mean) ASCC T <sub>w</sub>	PANT <sup>x</sup> (K mean) DATA T <sub>w</sub>		
4882	W	11	9.7	8.0	6.0	7	4.4
		19	11.8	9.0	9.4	7	7.0
		29	13.4	10.0	11.3	7	6.7
4963	W	11	Laminar	Laminar	Laminar	Laminar	Laminar
		19	Laminar	Laminar	Laminar	Laminar	Laminar
		20	Laminar	Laminar	Laminar	Laminar	Laminar
4953	ATJ-S	11	18.4	13.0	13.3	5	---
		19	24.0	16.0	16.1	5	---
		29	23.7	16.0	19.0	5	---
4974	ATJ-S	11	-	11.0	10.0	17	14.6
		19	-	13.0	10.7	10	12.3
		29	-	14.0	12.0	5	11.8
4951	994-2	11	14.0	10.0	10.7	0-5	2.1
		19	18.0	14.0	13.0	2-5	5.2
		29	18.0	15.0	16.1	0-10	5.6
5018	994-2	11	15.3	10.0	8.2	0-10	11.0
		19	16.0	12.0	9.4	3-10	8.4
		29	24.0	14.0	11.7	0-10	6.5
4871	994-2	11	Laminar	27.0	Laminar	0-4	---
		29	Laminar	Laminar	Laminar	4	---
4880	994-2	11	Laminar	Laminar	Laminar	5-15	15.0
		19	Laminar	Laminar	Laminar	5-12	13.6
		29	Laminar	Laminar	Laminar	5-12	12.2
4954	223	11	Laminar	Laminar	Laminar	0-2	---
		19	Laminar	Laminar	Laminar	0-10	---
		29	Laminar	Laminar	Laminar	0-10	---
5068	223	11	Laminar	29.0	26.0	0-10	9.1
		19	Laminar	Laminar	31.8	0-10	8.0
		29	Laminar	Laminar	Laminar	2-10	7.7
5069	223	11	24.3	17.0	16.4	0-10	14.0
		19	Laminar	18.0	18.7	3-15	12.3
		29	Laminar	22.0	22.2	3-8	10.1

\*ICC 4 results for transition are not included since they yield very similar results as ICC 11.

† The surface temperature was given by the ASCC transient option.

x The surface temperature was given by the measured data.

(a) For each temperature profile, the transition front location was determined to be the point of intercept of the laminar and turbulent legs of the temperature profile.

(b) Histograms showing the percentage of occurrence of transition at a given location on the nosetip were constructed.

(c) Transition front density functions were then constructed from the histograms. The probability density curves determine the width and movement of the transition front for each nosetip material.

Table 6.1 shows a comparison between the transition locations inferred from the temperature-transition histograms and those inferred from the data derived heat flux distributions. Although, in principle, the heat flux-inferred transition location represents a more realistic location of transition, the derived heat flux distributions were based on mean temperature profiles at each ICC. As a result, any preferred orientation in the transition location was smoothed out in the averaging process. Furthermore, the results show an apparent heating augmentation at the stagnation point (see section 7) which gives a rather flat heat transfer distribution and causes difficulties in defining a transition point. Hence, the range of heat flux inferred transition locations are shown for some of the shots in Table 6.1. Also shown in Table 6.1 are PANT/ASCC predicted transition locations using different roughness and wall temperatures to show these effects on transition according to PANT. Inferring the transition location from the temperature data can be in error due to the lateral conduction smoothing effect of the surface temperature, and also due to the transient response of the model. That is, if transition offset took place the heat flux distribution becomes laminar while the surface temperature may still indicate a transitional/turbulent behavior. In this case, the temperature data may erroneously indicate a forward moving of the transition-

front. In any case, only temperature data are available to determine the transition statistics.

Detailed transition statistics have been generated for the Track G shots that had valid data. The specific shots analyzed were:

<u>Shot #</u>	<u>Material</u>	<u>Surface Conditions</u>
4882	W	Pre-roughened
4974	ATJ-S	Pre-ablated
4951	994-2	Pre-ablated
5018	994-2	Pre-ablated
4880	CC-223	Pre-ablated
5068	CC-223	Pre-ablated
5069	CC-223	Pre-ablated

For each shot, the following was determined

- (1) Circumferential histograms of the transition front location as shown in Figures 6.1-6.7.
- (2) Circumferential cumulative distribution of the transition front location (showing the transition front width) as shown in Figures 6.8-6.14.
- (3) Mean location of the transition front.
- (4) Standard deviations transition front.

The transition location statistics are summarized in Table 6.2 along with the previously discussed heat transfer derived transition location and PANT predicted values.

### 6.3 Comparisons with Transition Correlations

The data derived from the track G shots as well as data from earlier free flights in Range G, are compared with the correlations obtained in the PANT program, those derived by Bishop, and by Dirling. These correlations were summarized in Section 6.1. Table 6.3 is a summary of the calculated local flow properties required to compute the correlation parameters.

#### 6.3.1 Comparisons with the PANT Correlation

Two equivalent means of comparison were used. The first was to calculate the implied roughness according to PANT using the temperature data derived transition locations. The second method was to calculate transition locations using the characterized roughnesses in the PANT criteria and compare this with the ballistics range data.

Figures 6.15 to 6.17 show comparisons between the data inferred and PANT computed transition locations. In displaying the results the sand grain roughness type materials (W, ATJ-S, 994-2) were separated from the weave-type materials (CC-223). This was done to eliminate any material type effects on transition. For the sake of completeness some of the free flight results are displayed. Figure 6.15 shows that using the  $K_{rms}$  as the characteristic roughness height of the material in PANT does not correlate the data well. Some data points lie to the left of the laminar boundary as indicated in the figure for shot 4963, where the flow was completely laminar over the supersmooth nosetip. Also, the PANT correlation was based on peak to valley roughness heights (which was almost 4 times the  $K_{rms}$ ). Figures 6.16 and 6.17 show the comparisons based on  $K_{mean}$ . It can be seen there that most of the data lie below the PANT line, i.e., transition occurs upstream of predicted values and very close to the stagnation point. It was curious for the smooth tungsten free flight data that either the flow remained laminar on the supersmooth models, or, when transition occurred, it was always close to the stagnation point.

Table 6.5 lists the magnitudes of the inferred roughness heights that insures agreement between data and PANT predictions. For CC-223 the inferred roughnesses were found to be of the order of the macroroughness. For preablated 994-2 the inferred roughness heights were only 16% higher than the average values for the track shots, which indicated good agreement with the PANT correlation.

### 6.3.2 Comparisons with Dirling's and Bishop's Transition Correlations

Table 6.5 shows a comparison between the data inferred transition location and predictions by the PANT, Dirling's and Bishop's transition correlations. The comparisons cover a range of stagnation pressure from 40 to 197 atmospheres, freestream Reynolds number from 18 to  $70 \times 10^6$ /ft and mean roughness heights from 0.25 to 0.57 mils. The table lists the transition locations as predicted by the three predictive models and those inferred from the mean temperature distribution around each nosetip. In general, the Dirling correlation predicted the most forward location of transition based on K mean. Also, all the models predicted backward movement of the transition location as well as transition offset, i.e., relaminarization of the flow on the nosetip. The data however, indicated an almost fully turbulent flow for the flight conditions analyzed.

Shot 5068 was selected to investigate the effect of the characteristic roughness height, used in conjunction with the predictive correlations, on the transition-front location and its agreement with the data. The results showed excellent agreement between the data and the PANT prediction, if the macroroughness height ( $K = 2.5$  mils) was used instead of the microroughness ( $K = .25$  mils). However, the use of the macroroughness as the transition characteristics roughness height may not be justifiable. Comparisons of the data with the Dirling and Bishop correlations are shown in Figures 6.18-6.20.

### 6.3.3 Comparisons with Reda-Raper Transition Data

Recently (Reference 20) transition experiments were conducted on large preablated CMT graphite nosetips in the AEDC

Track G facility. The effects of nosetip radius and freestream static pressures on the transition-front movements were investigated. The data indicated that nosetip radius has no effect on the transition location. The mean transition front location was observed to progress forward with the freestream static pressure. The correlated relation between the mean transition-front location and range static pressure was given as

$$\frac{S}{R_{N_t}} = .0371 P_{\infty}^{-1.4127} \quad (6.5)$$

Figure 6.21 is a plot of this correlation with the current temperature-derived data, while Figure 6.22 shows the heat flux derived data. The current data do not show agreement with the Reda-Raper correlation.

Other correlations with  $k/\theta$ ,  $Re_{\theta}$  and  $Re_{\infty}$  are shown in Figures 6.23 and 6.24 and do not show much promise in correlating the current data.

It is felt that a larger sample of high quality data on a variety of well characterized materials as was intended in the current program, before its untimely demise, is necessary before any firm conclusions concerning the veracity of the existing transition correlations. The large CMT models flown by Reda and Raper were certainly in the right direction.

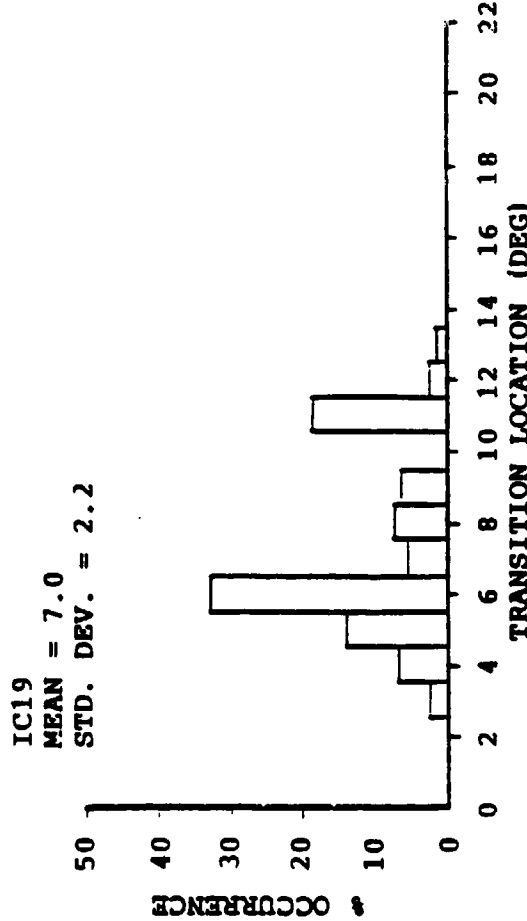
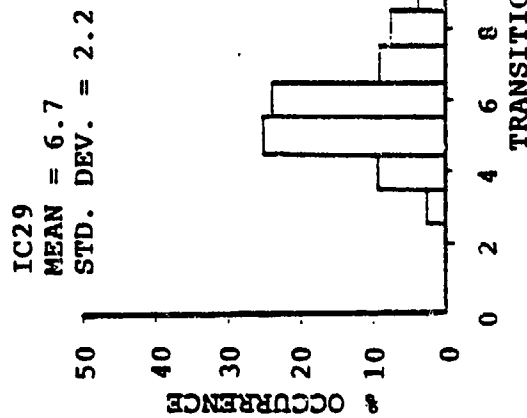
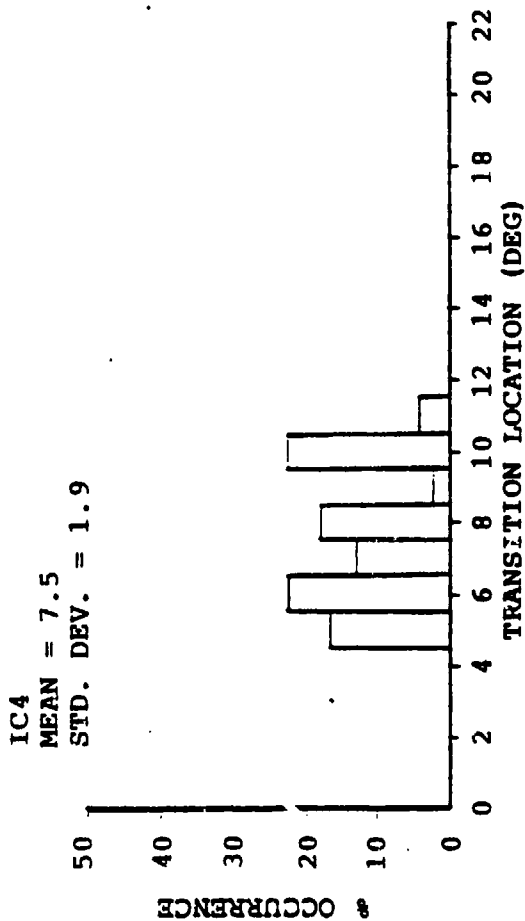
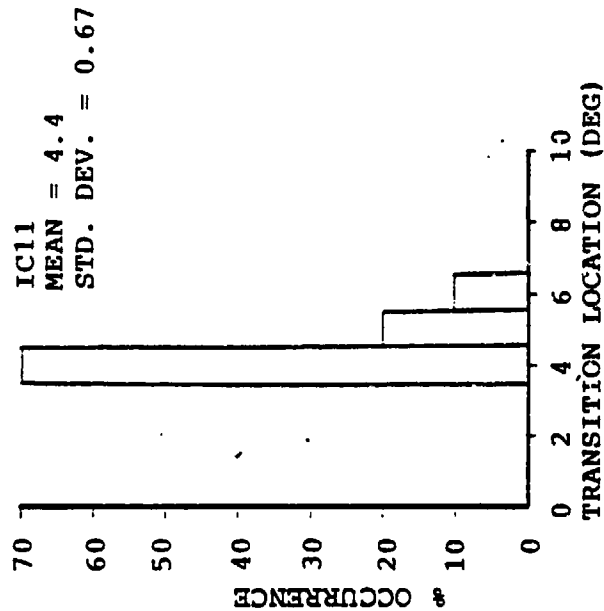
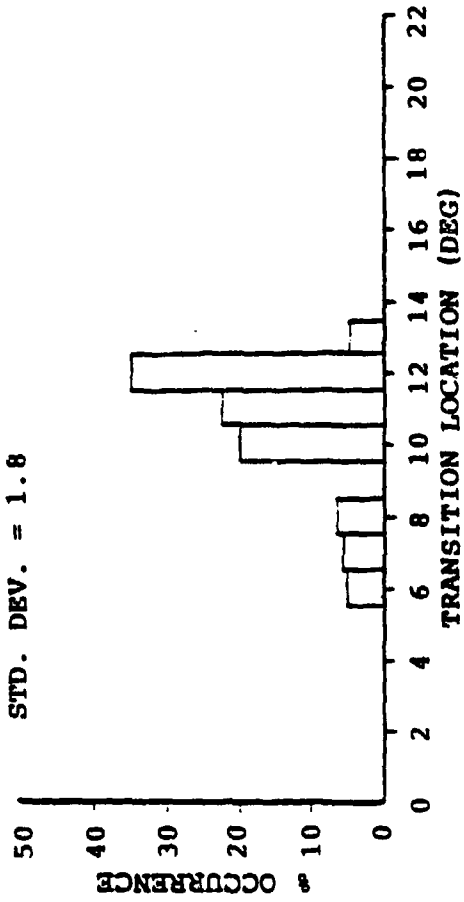
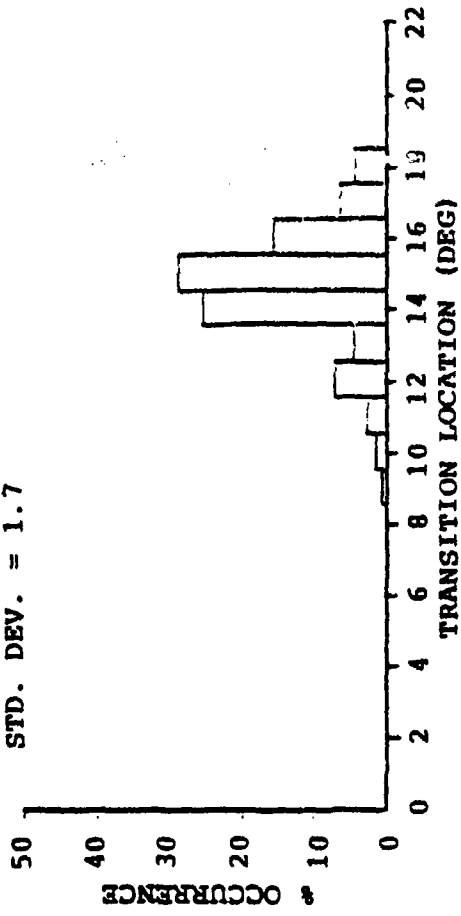


FIGURE 6.1 TRANSITION STATISTICS FOR TUNGSTEN (SHOT 4882)

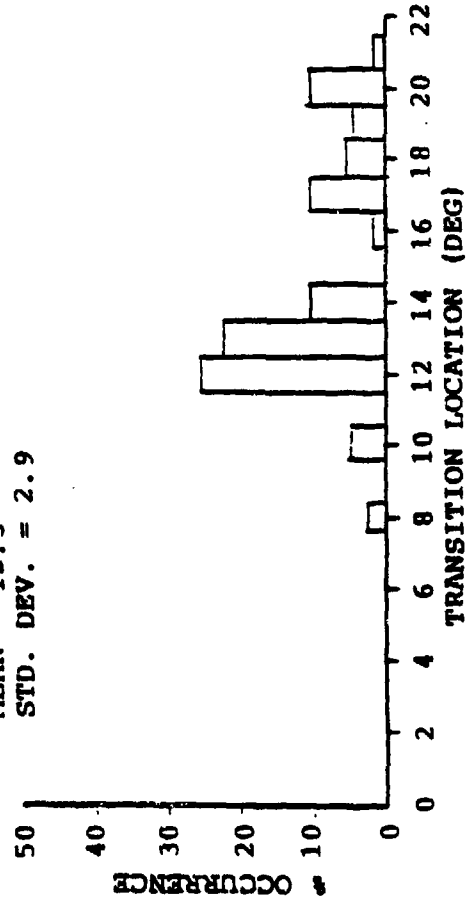
IC4  
 MEAN = 10.6  
 STD. DEV. = 1.8



IC11  
 MEAN = 14.6  
 STD. DEV. = 1.7



IC19  
 MEAN = 12.3  
 STD. DEV. = 2.9



IC29  
 MEAN = 11.8  
 STD. DEV. = 3.4

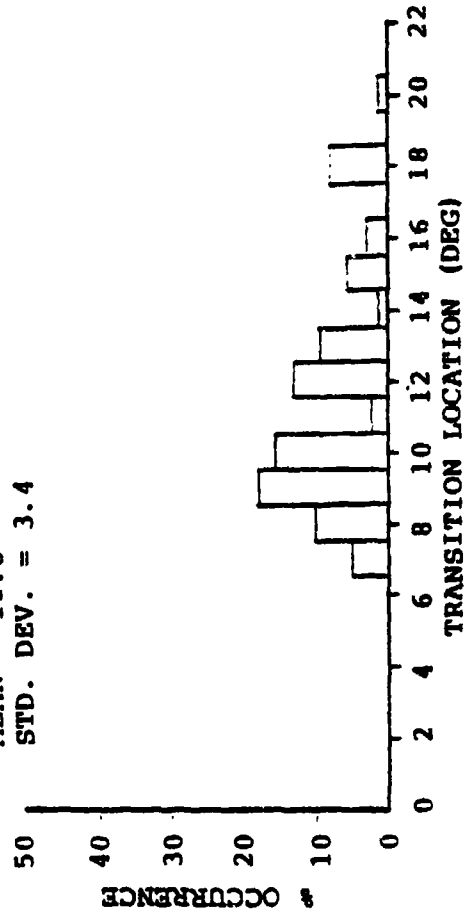


FIGURE 6.2 TRANSITION STATISTICS FOR ATJ-S (SHOT 4974)

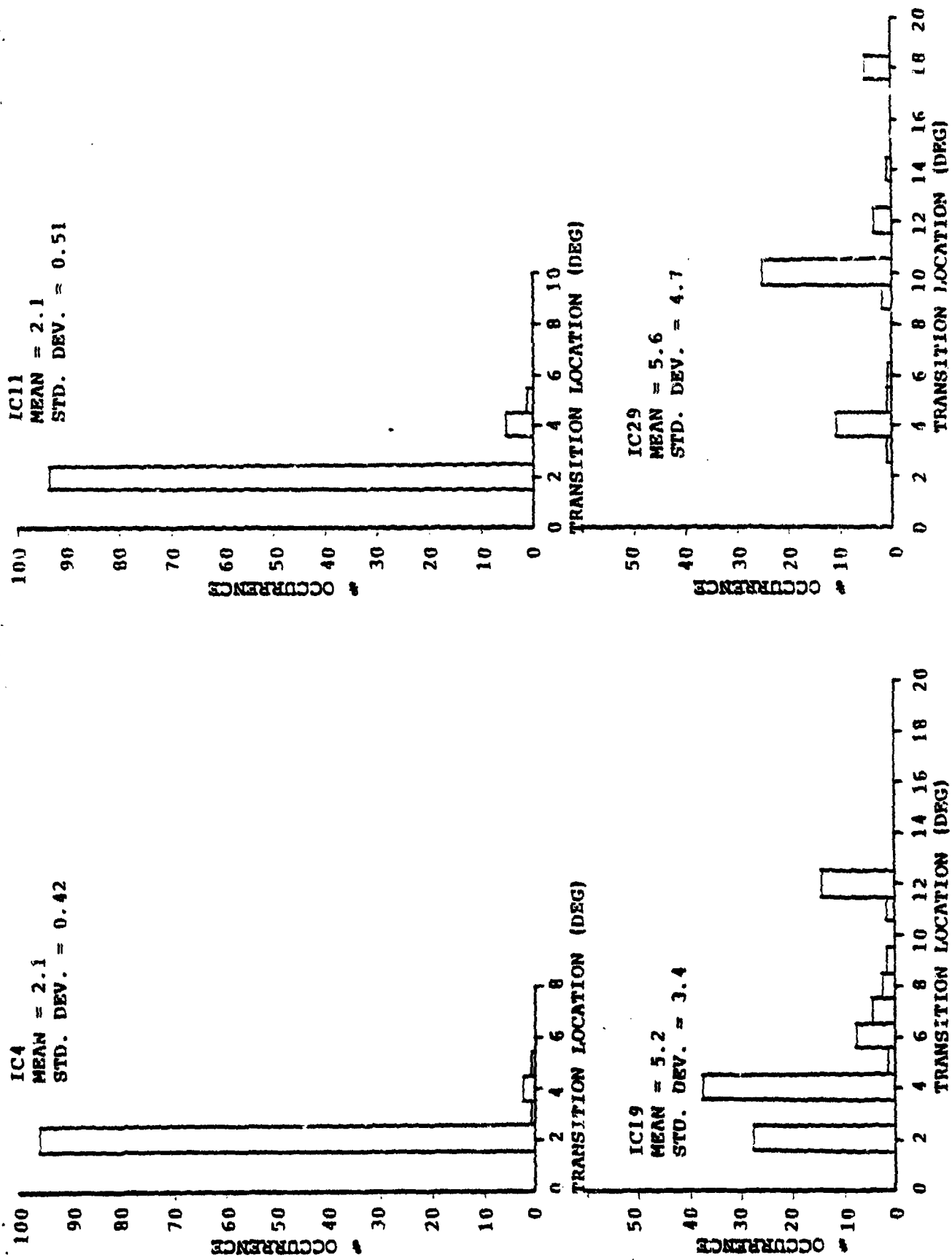


FIGURE 6.3 TRANSITION STATISTICS FOR 994-2 (SHOT 4951)

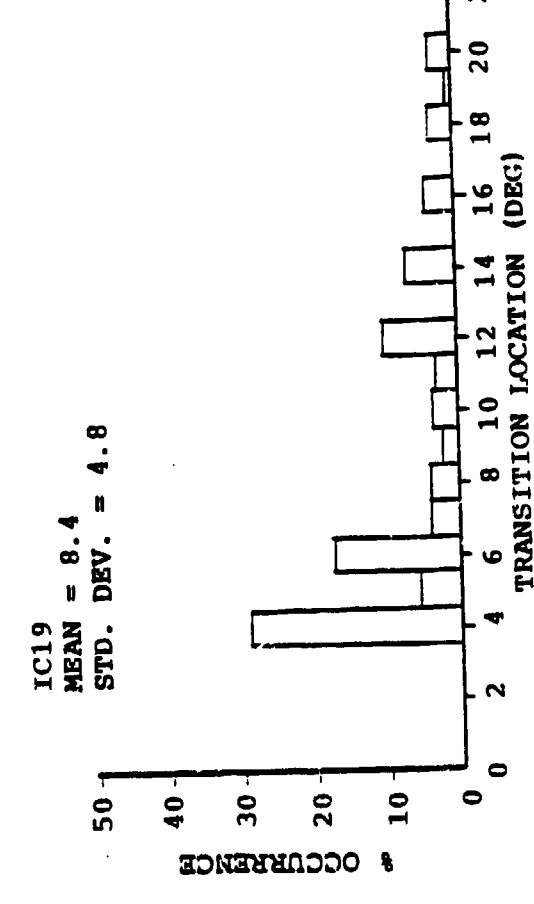
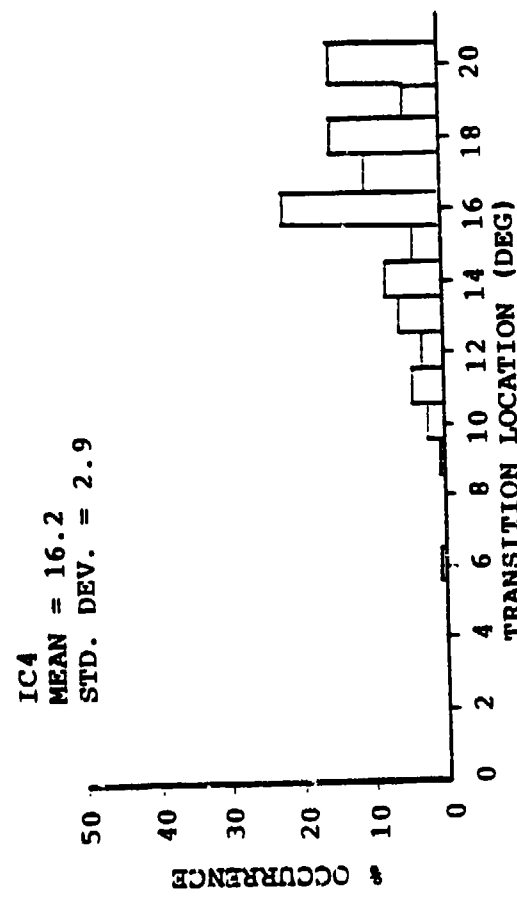
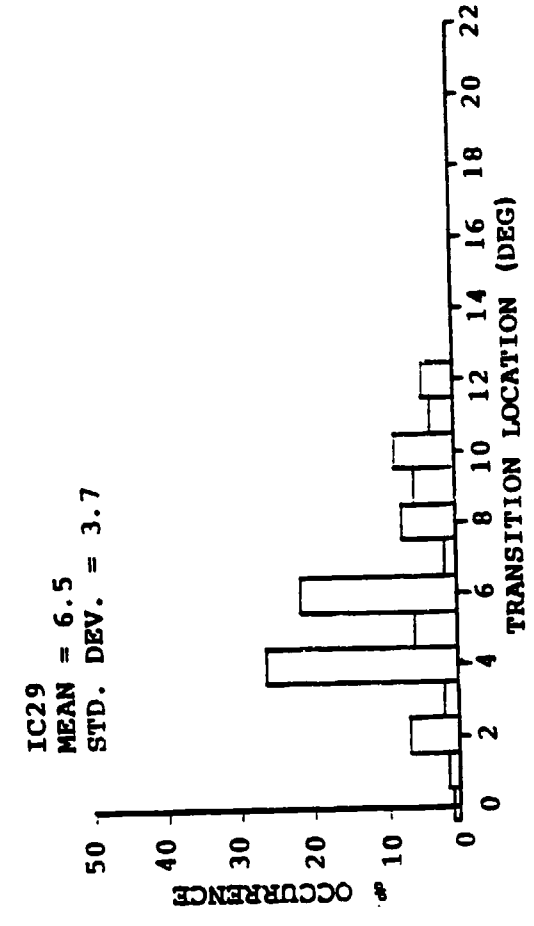
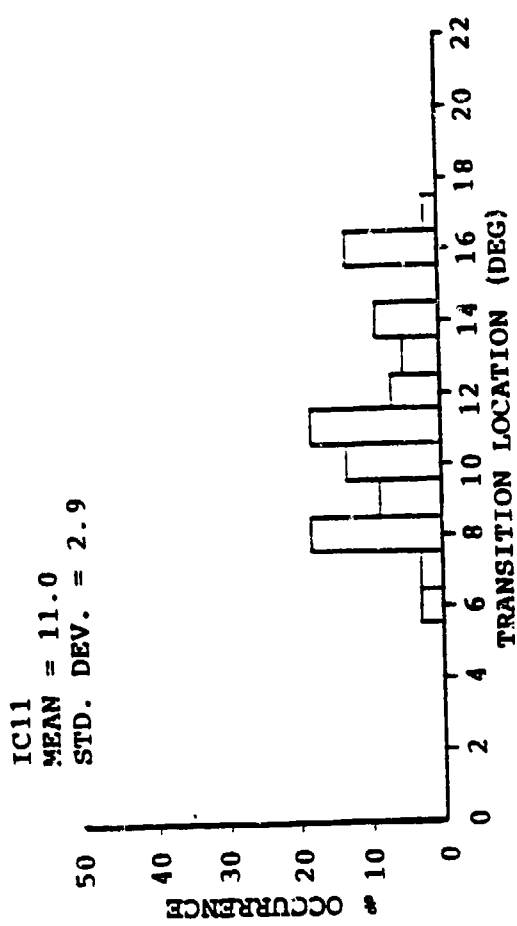


FIGURE 6.4 TRANSITION STATISTICS FOR 994-2 (SHOT 5018)

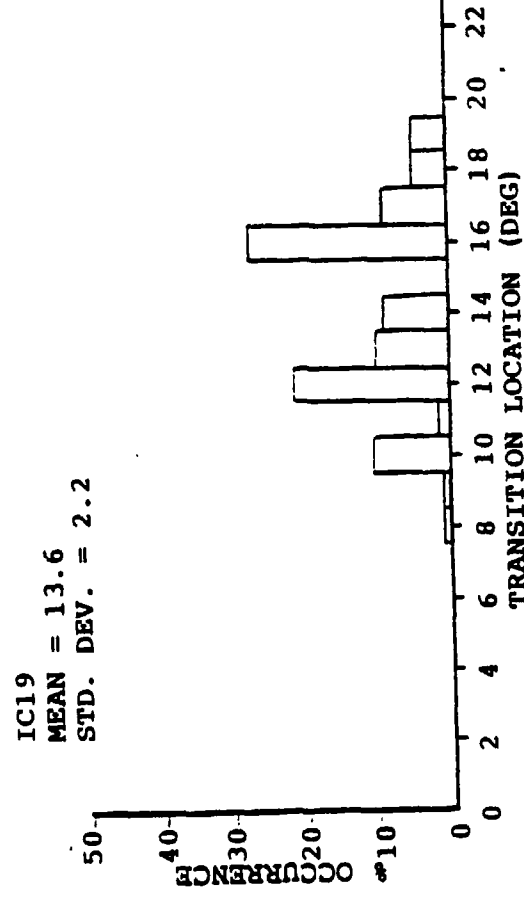
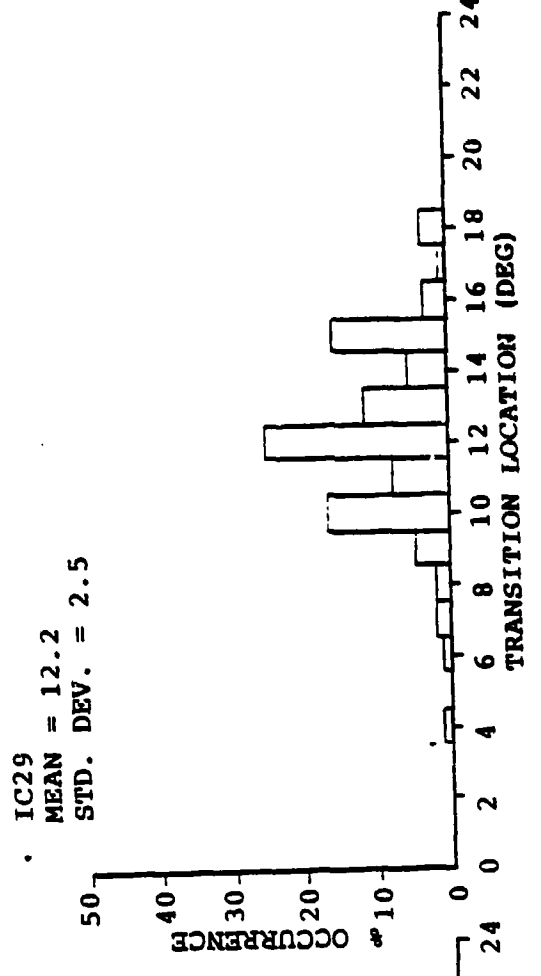
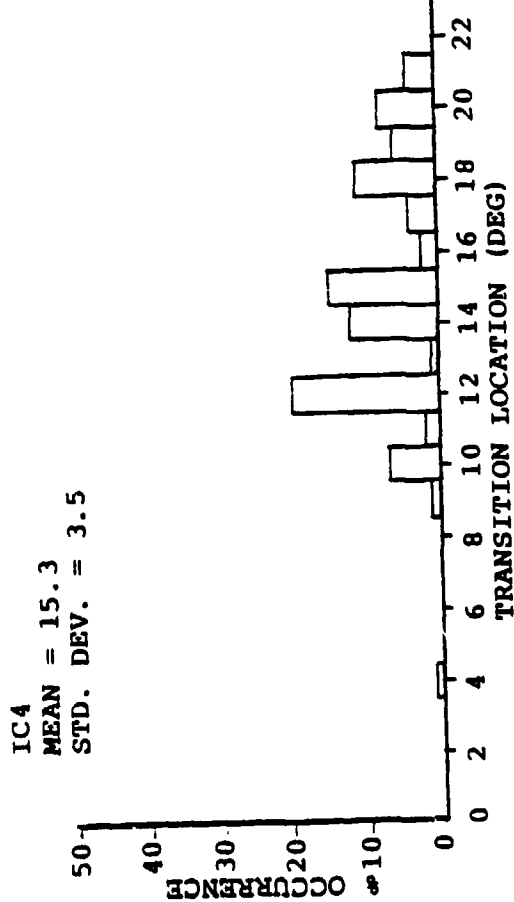
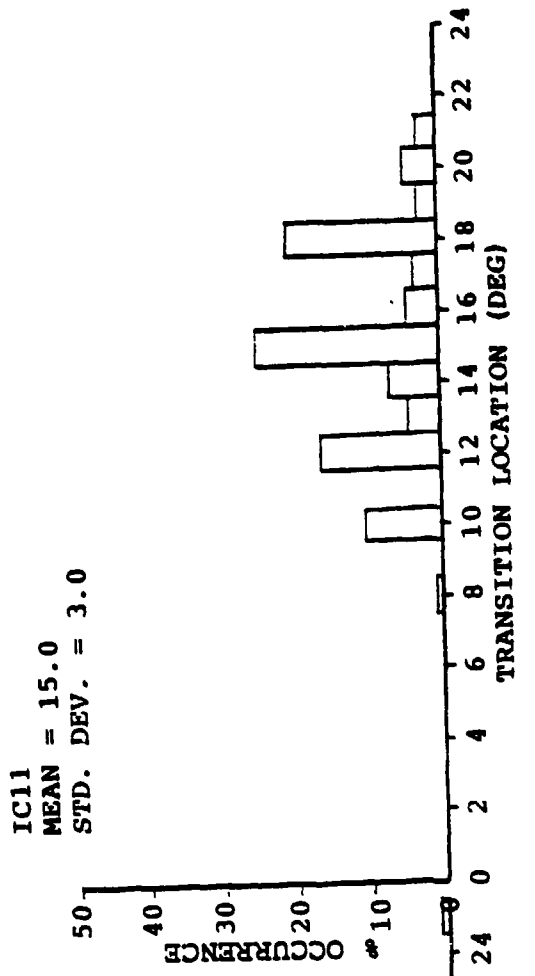
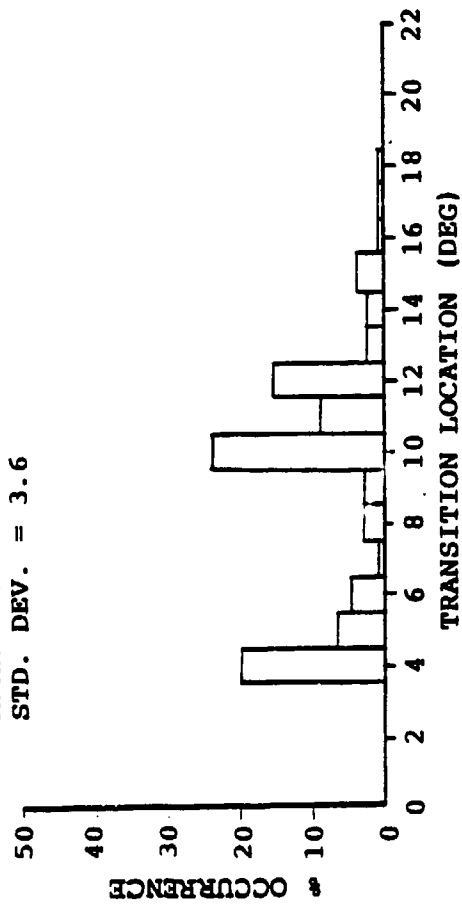
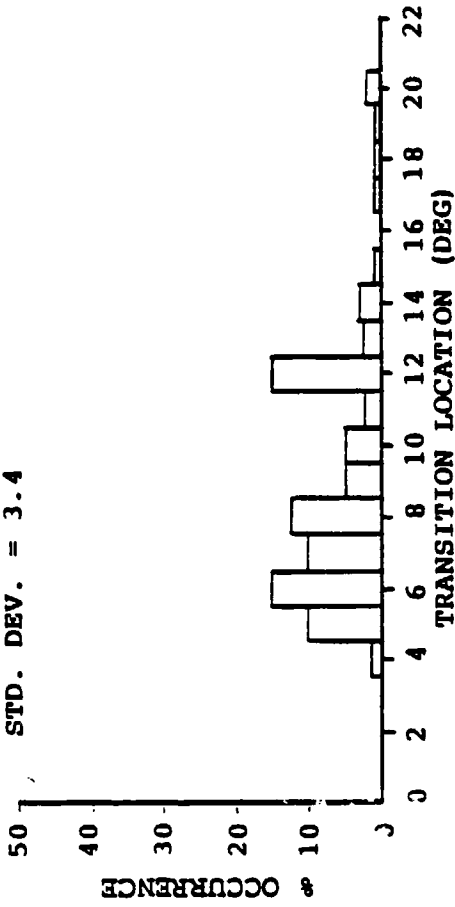


FIGURE 6.5 TRANSITION STATISTICS FOR CC-223 (SHOT 4880)

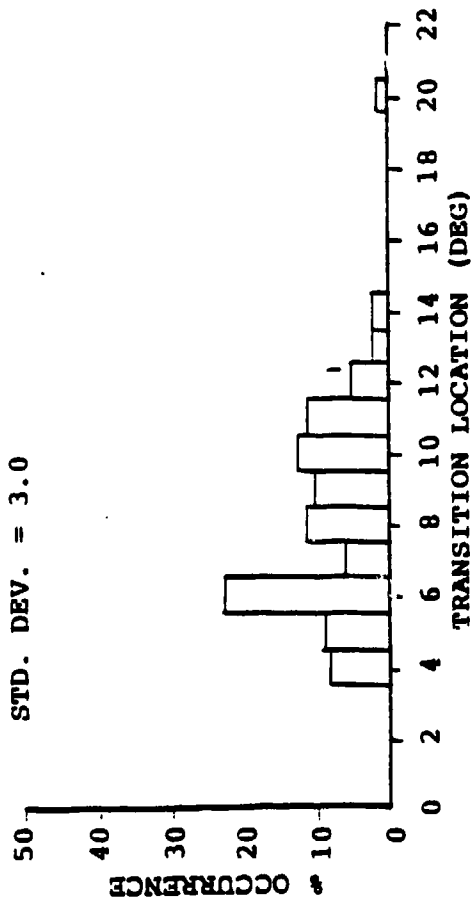
IC4  
 MEAN = 9.0  
 STD. DEV. = 3.6



IC11  
 MEAN = 9.1  
 STD. DEV. = 3.4



IC19  
 MEAN = 8.0  
 STD. DEV. = 3.0



IC29  
 MEAN = 7.7  
 STD. DEV. = 2.5

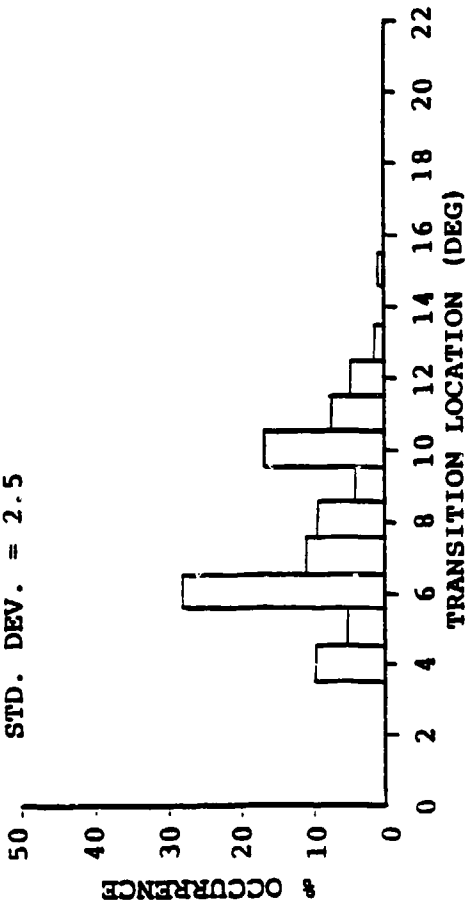


FIGURE 6.6 TRANSITION STATISTICS FOR CC-223 (SHOT 5068)

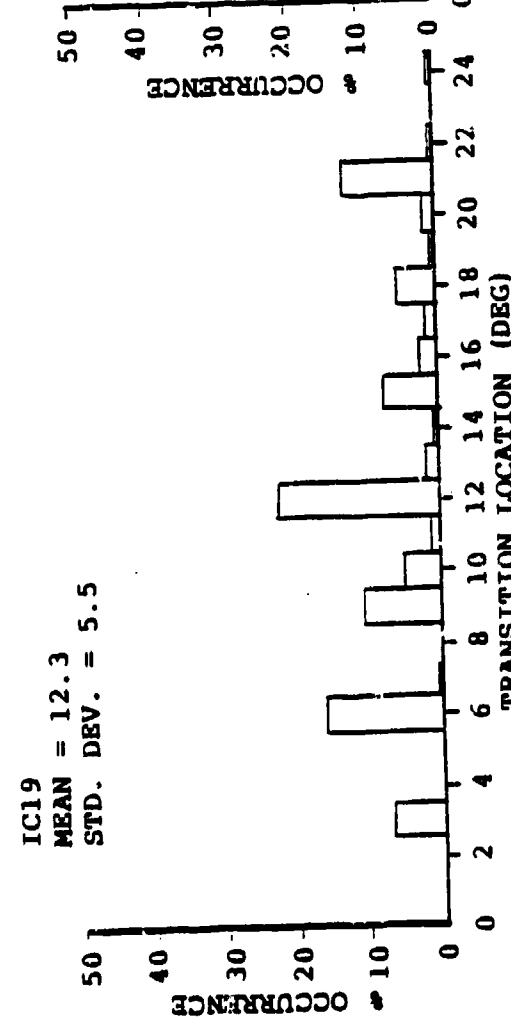
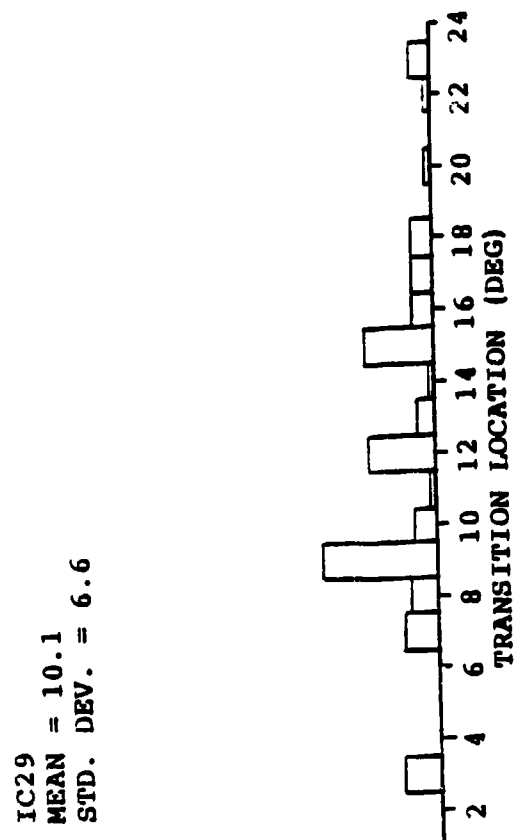
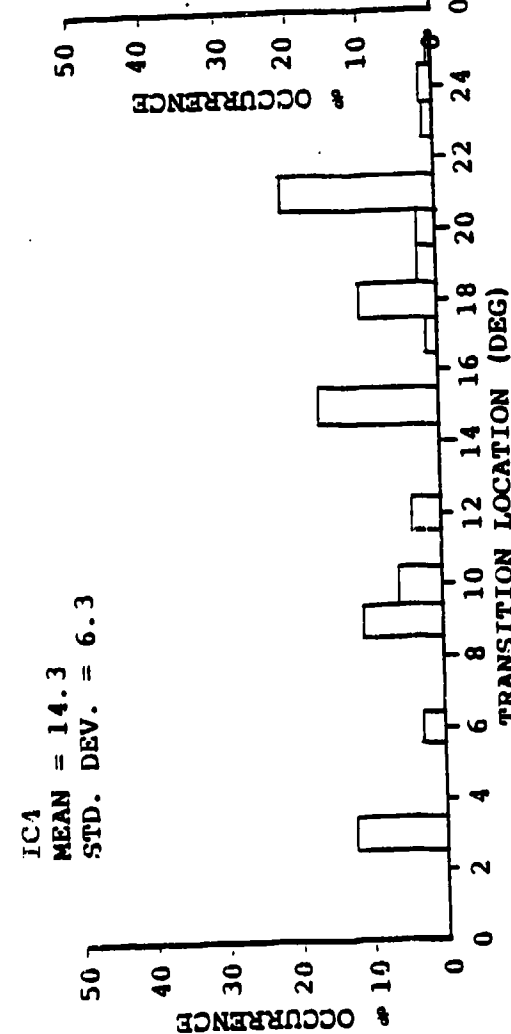
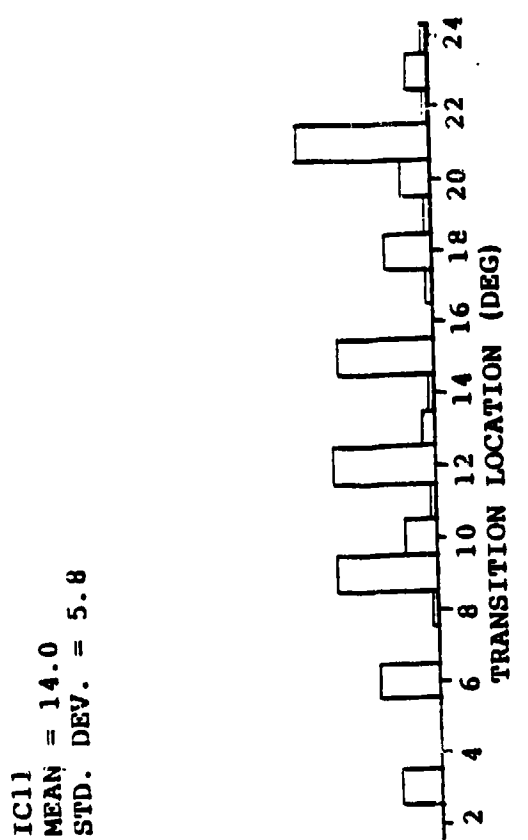


FIGURE G.7 TRANSITION STATISTICS FOR CC-223 (SHOT 5069)

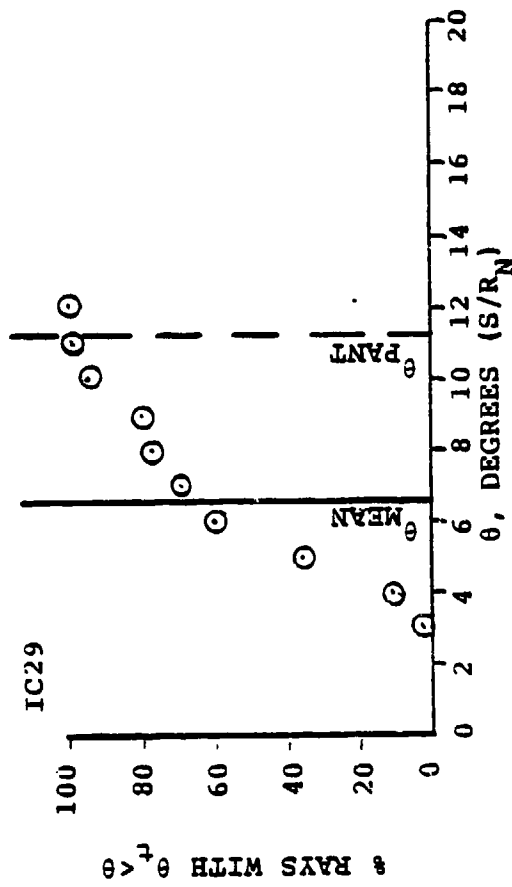
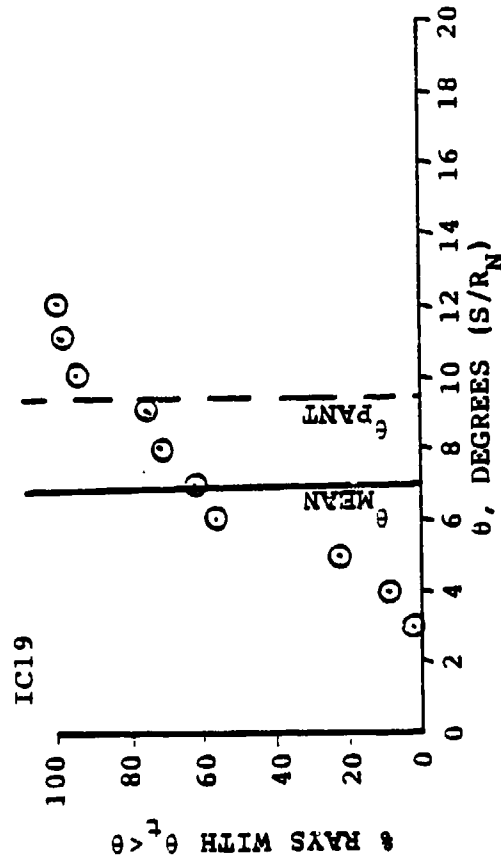
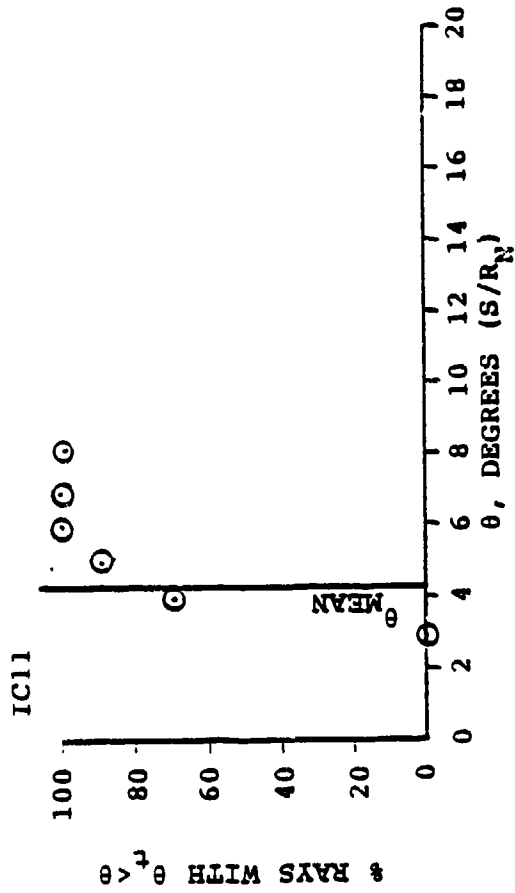
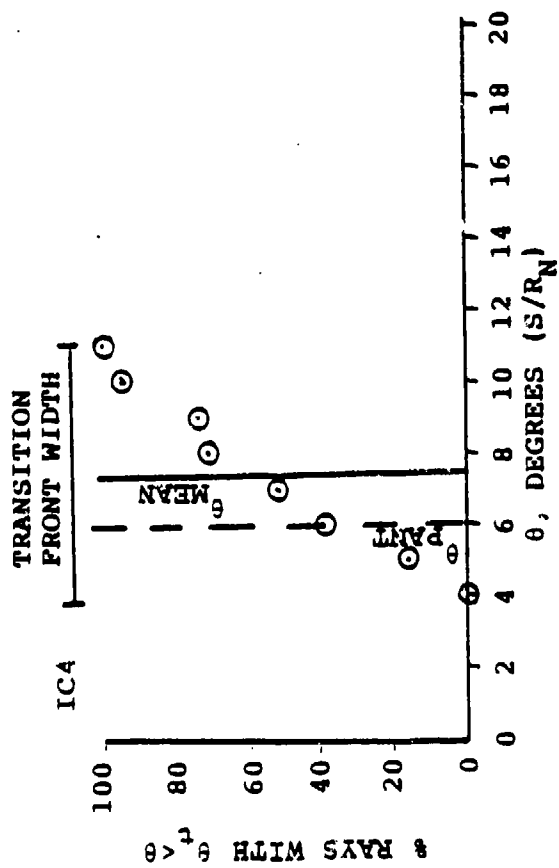


FIGURE 6.8 CIRCUMFERENTIAL DISTRIBUTION OF TRANSITION LOCATIONS FOR TUNGSTEN (SHOT 4882)

TRANSITION FRONT WIDTH

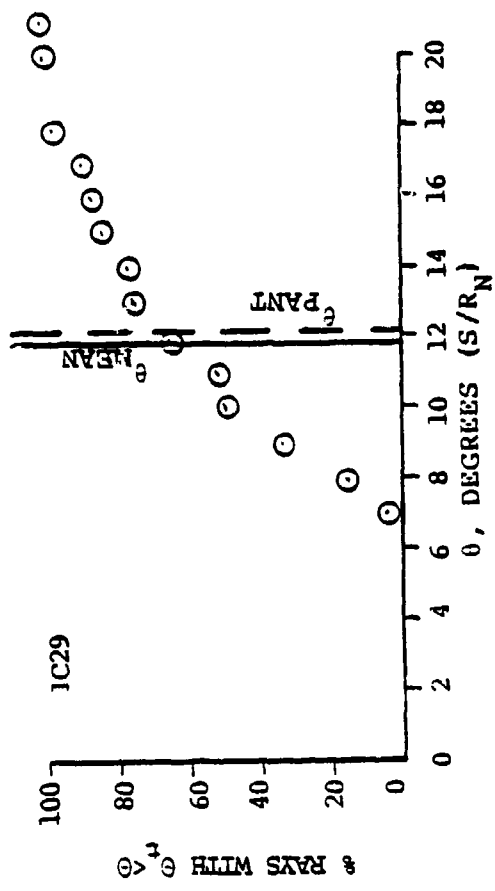
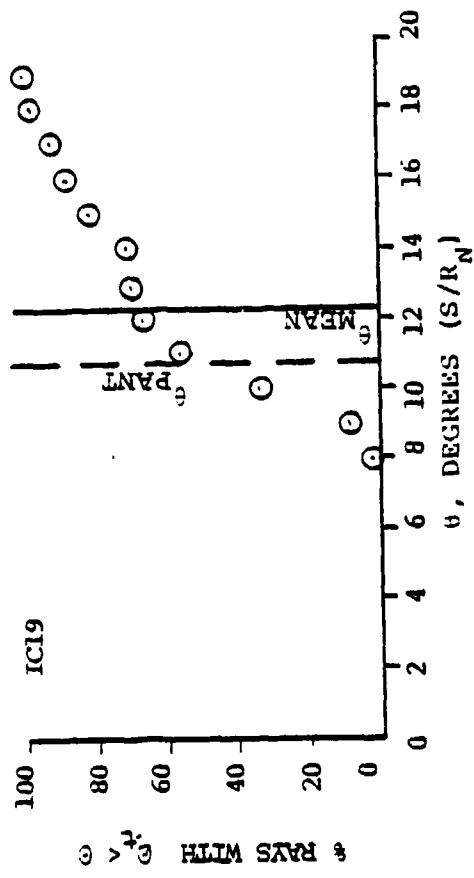
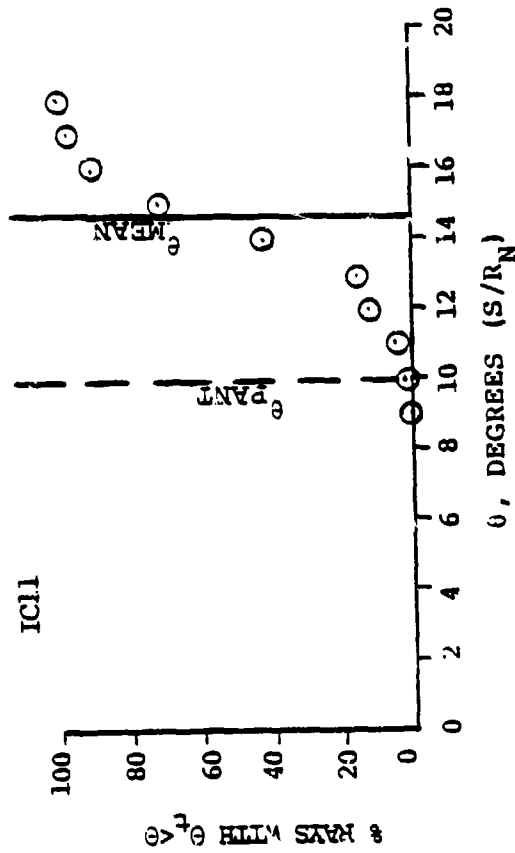
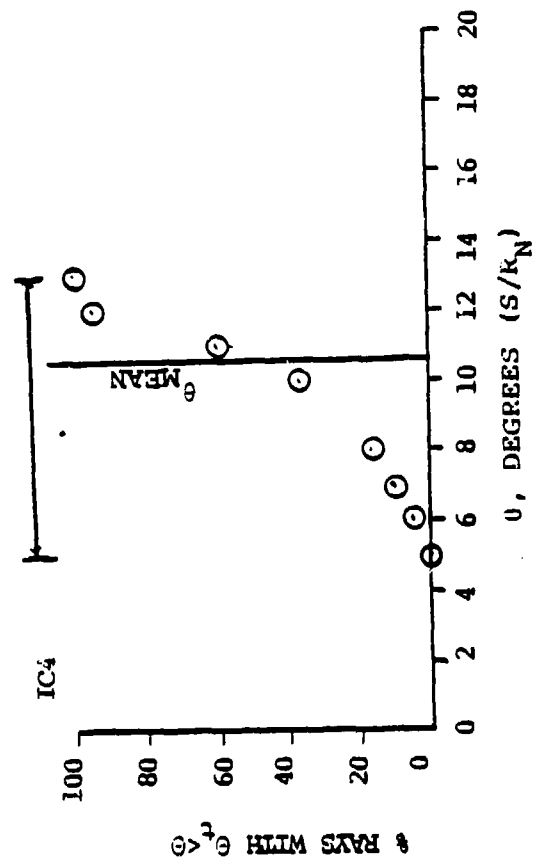


FIGURE 6.9 CIRCUMFERENTIAL DISTRIBUTION OF TRANSITION LOCATIONS FOR ATJ-S (SHOT 4974)

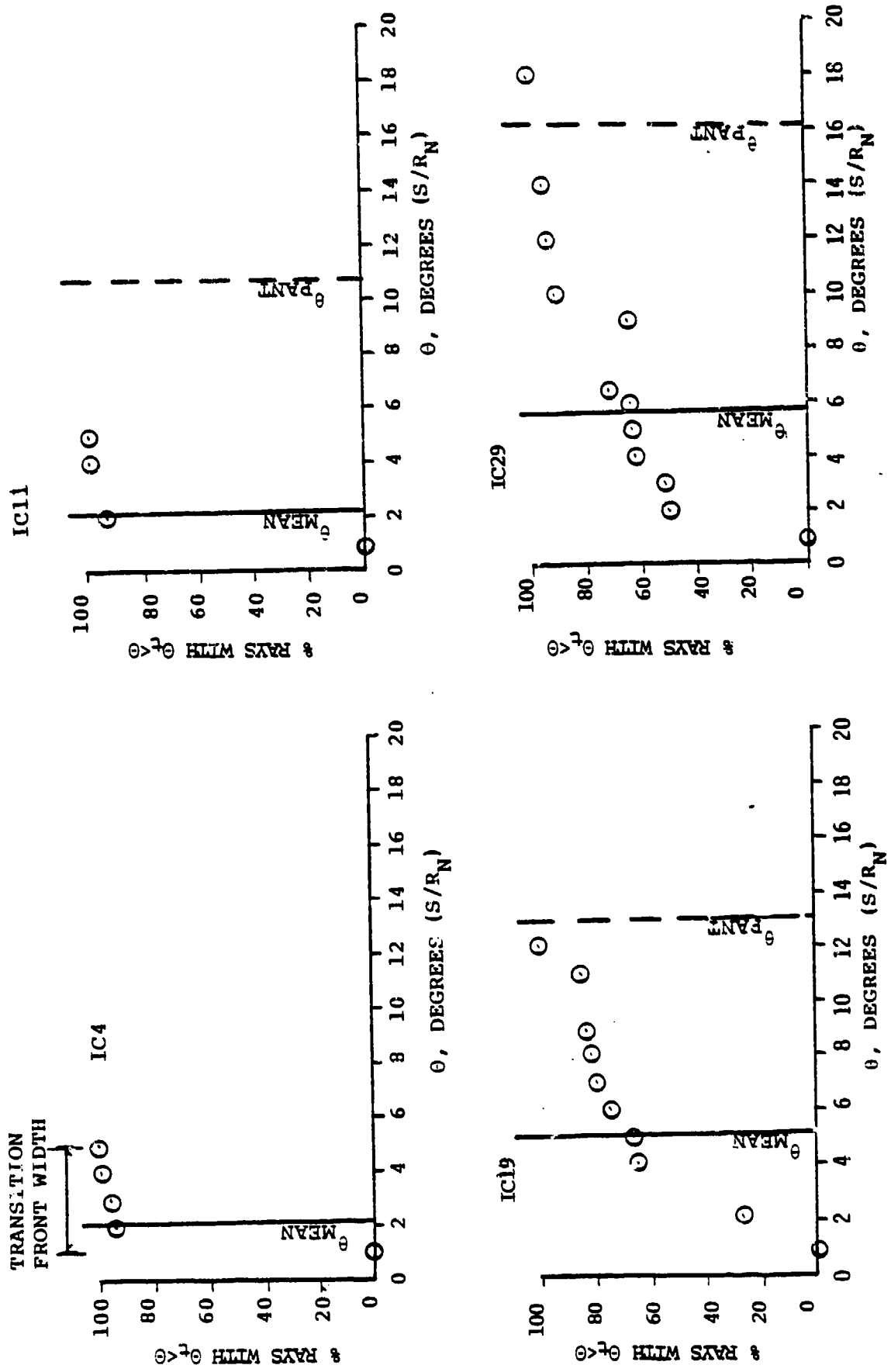


FIGURE 6.10 CIRCUMFERENTIAL DISTRIBUTION OF TRANSITION LOCATIONS FOR 994-2 (SHOT 4951i)

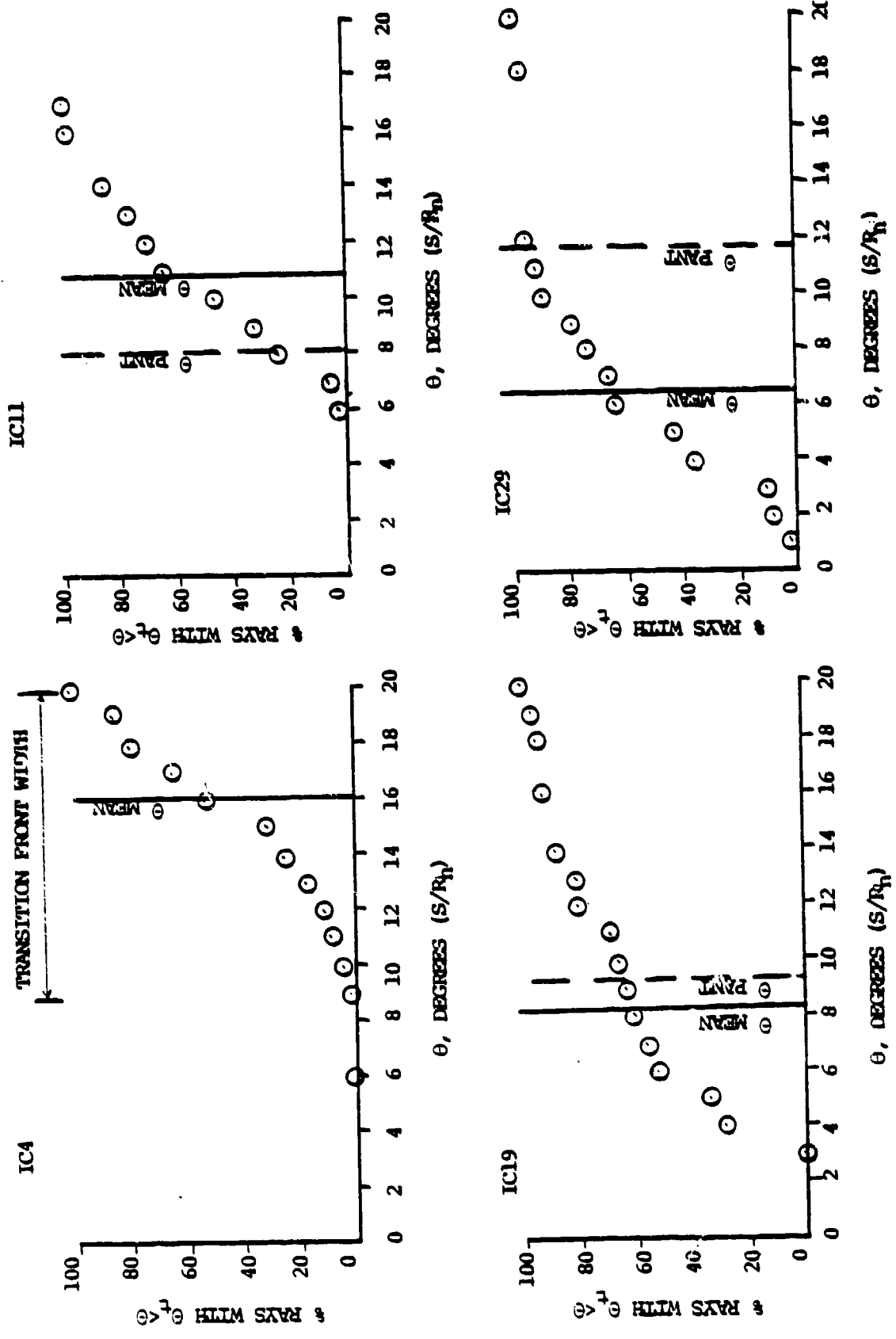


FIGURE 6.11 CIRCUMFERENTIAL DISTRIBUTION OF TRANSITION LOCATIONS FOR 994-2 (SHOT 5018)

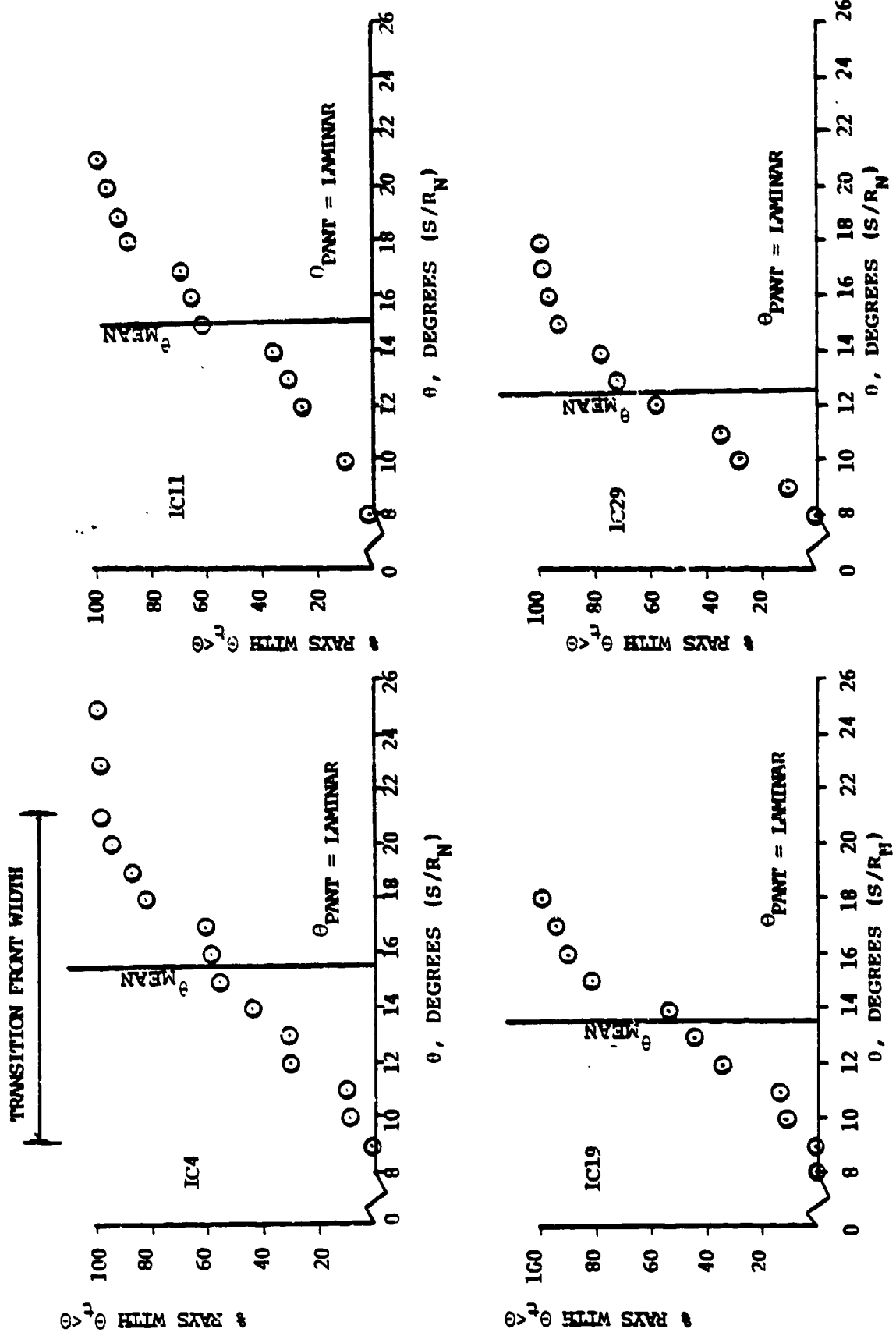


FIGURE 6.12 CIRCUMFERENTIAL DISTRIBUTION OF TRANSITION LOCATIONS FOR CC-223 (SHOT 4880)

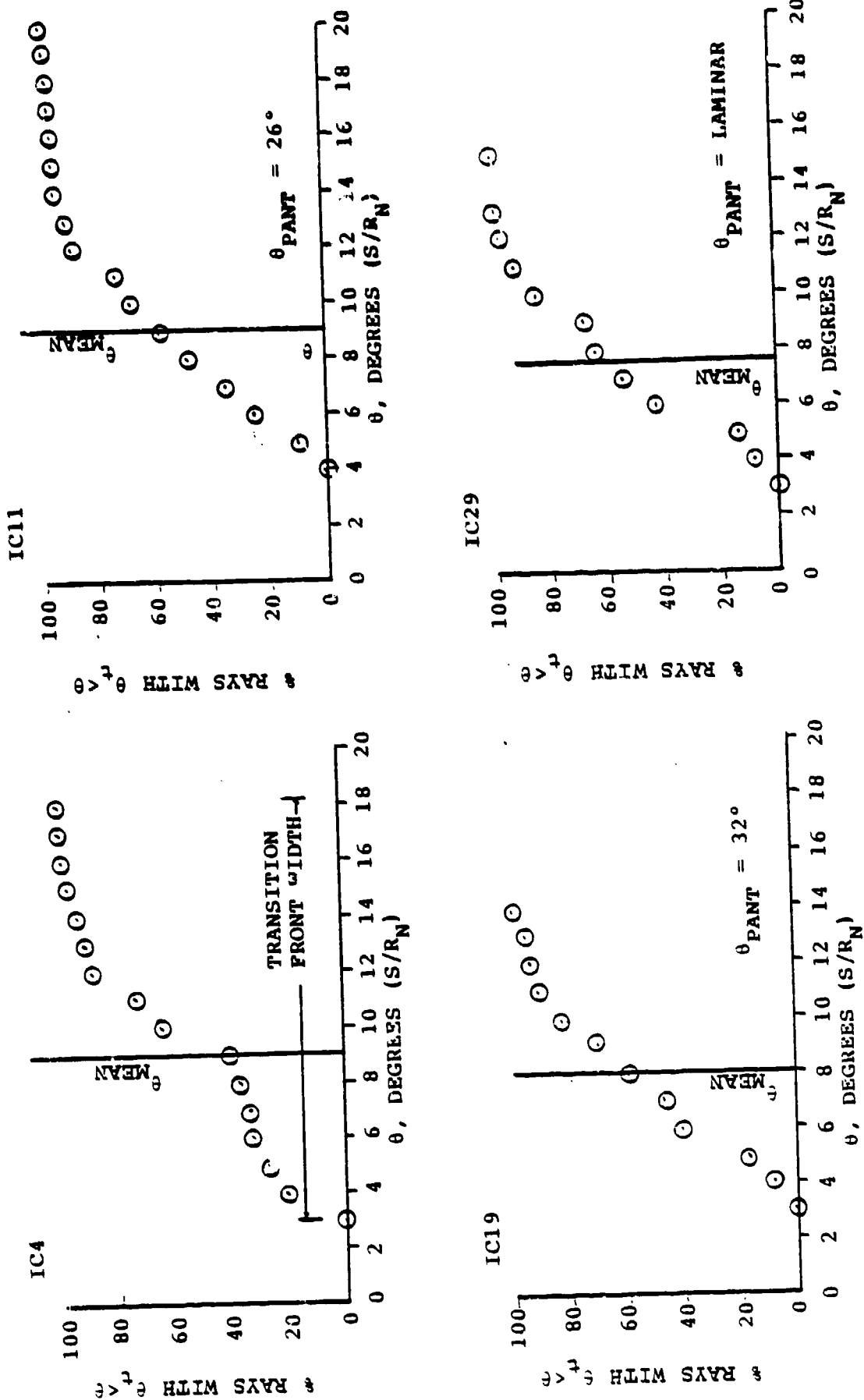


FIGURE 6.13 CIRCUMFERENTIAL DISTRIBUTION OF TRANSITION LOCATIONS FOR CC-223 (SHOT 5068)

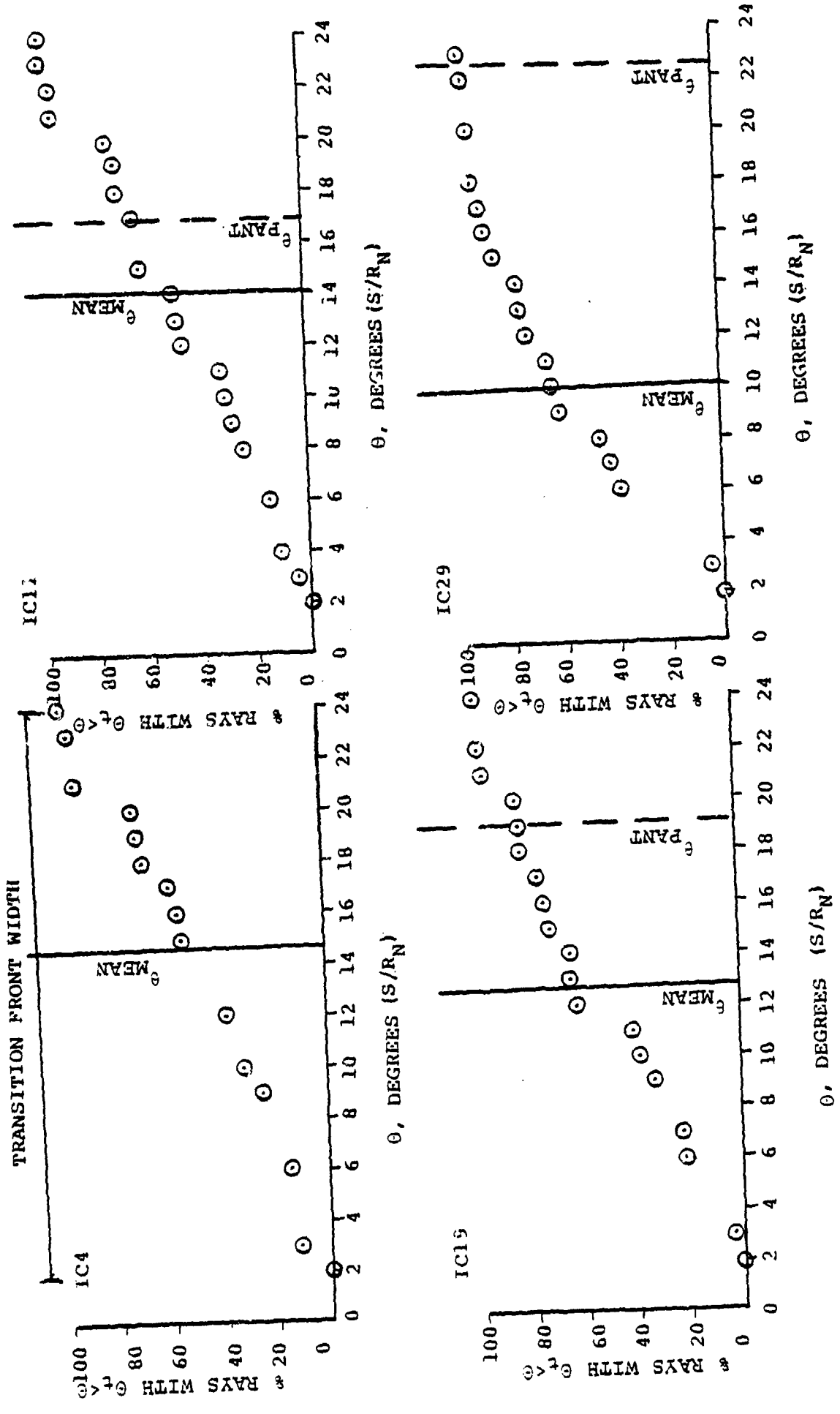


FIGURE 6.14 CIRCUMFERENTIAL DISTRIBUTION OF TRANSITION LOCATIONS FOR CC-223 (SHOT 5069).

TABLE 6.2 TRANSITION LOCATION STATISTICS

SHOT #	RANGE CAMERA NUMBER	$\theta_t$ MEAN	$\theta$ STANDARD DEVIATION	$\theta_t$ USING $T_w$ MEAN	$\theta_t$ FROM $q$ MEAN	$\theta_t$ PANT USING $T_w$ $K$ MEAN
4882 (W)	4	7.5	1.9	8.0	7	6.0
	11	4.4	0.67	4.0	-	--
	19	7.0	2.2	8.0	7	9.4
4974 (ATJ-S)	29	6.7	2.2	7.0	7	11.3
	4	10.6	1.8	11.0	-	--
	11	14.6	1.7	13.6	17	10.0
4951 (994-2)	19	12.3	2.9	11.5	10	10.7
	29	11.8	3.4	11.0	5	12.0
	4	2.1	0.42	2.0	-	--
5018 (994-2)	11	2.1	0.51	2.0	0-5	10.7
	19	5.2	3.4	5.0	2-5	13.0
	29	5.6	4.7	2.0	0-10	16.1
4880 (CC-223)	4	16.2	2.9	16.7	-	--
	11	11.0	2.9	11.6	0-10	8.2
	19	8.4	4.8	8.5	3-10	9.4
5068 (CC-223)	29	6.6	3.7	3.3	0-10	11.7
	4	15.3	3.5	10.5	-	Laminar
	11	15.0	3.0	18.4	5-15	Laminar
5069 (CC-223)	19	13.6	2.2	14.0	5-12	Laminar
	29	12.2	2.5	13.2	5-12	Laminar
	4	9.0	3.6	4.4	-	--
5068 (CC-223)	11	9.1	3.4	9.0	0-10	26.0
	19	8.0	3.0	7.3	0-10	31.8
	29	7.7	2.5	7.5	2-10	Laminar
5069 (CC-223)	4	14.3	6.3	9.6	-	--
	11	14.0	5.8	7.2	0-10	16.4
	19	12.3	5.5	8.8	3-15	18.7
29	10.1	6.6	4.8	3-8	22.2	

TABLE 6.3 CALCULATED FLOW PROPERTIES AT MEASURED TRANSITION LOCATION

SHOT	IC	$\theta_t$ (S/R <sub>N</sub> ) died.	Re $\theta$	$\theta$ (mils)	K (mils)	$\rho_w^3$ 16/ft <sup>3</sup>	$\rho_e^3$ 16/ft <sup>3</sup>	K/ $\theta$	$\rho_e/\rho_w$	Re $_{e,m}, R_N$	10 <sup>-6</sup>
4882 (W)	4	7.5	45.38	.114	.25	2.48	.5422	2.19	.22	2.33	
	11	4.4									
	19	7.0	41.59	.107	.25	1.41	.5307	2.34	.38	2.10	
	29	6.7	40.0	.104	.25	1.12	.5205	2.40	.46	1.96	
4974 (ATJ-S)	4	10.6	40.0	.195	.55	.92	.19	2.82	.21	.8	
	11	14.6	51.3	.192	.55	.6775	.1838	2.86	.27	.78	
	19	12.3	42.58	.187	.55	.6328	.186	2.94	.29	.77	
	29	11.8	41.56	.184	.55	.5544	.1856	2.99	.33	.76	
4951 (994-2)	4	2.1									
	11	2.1	8.73	.18	.57	.6861	.199	3.17	.29	.84	
	19	5.2	16.84	.173	.57	.5139	.1965	3.29	.38	.83	
	29	5.6	16.0	.169	.57	.4237	.1957	3.37	.46	.80	
5018 (994-2)	4	16.2									
	11	11.0	44.4	.195	.57	.8565	.1894	2.92	.22	.81	
	19	8.4	34.98	.188	.57	.7326	.1911	3.03	.26	.8	
	29	6.5	25.33	.179	.57	.5636	.1922	3.18	.34	.76	
4880 (CC-223)	4	15.3	38.8	.271	.25	.4614	.09515	.92	.21	.41	
	11	15.0	37.26	.267	.25	.3689	.09507	.94	.26	.4	
	19	13.6	36.92	.265	.25	.3468	.09485	.94	.27	.4	
	29	12.2	33.0	.261	.25	.322	.095	.96	.30	.4	
5068	4	9	31.52	.219	.25	.6796	.1445	1.14	.21	.61	
	11	9.1	30.48	.217	.25	.5692	.1439	1.15	.25	.6	
	19	8.0	28.0	.212	.25	.50	.140	1.18	.28	.58	
	29	7.7	28.0	.206	.25	.41	.143	1.21	.35	.57	
5069	4	14.3	61.8	.15	.25	.8053	.2772	1.67	.34	1.22	
	11	14.0	59.78	.148	.25	.7375	.2761	1.69	.37	1.18	
	19	12.3	52.0	.144	.25	.65	.276	1.74	.42	1.15	
	29	10.1	43.0	.140	.25	.58	.28	1.79	.48	1.11	

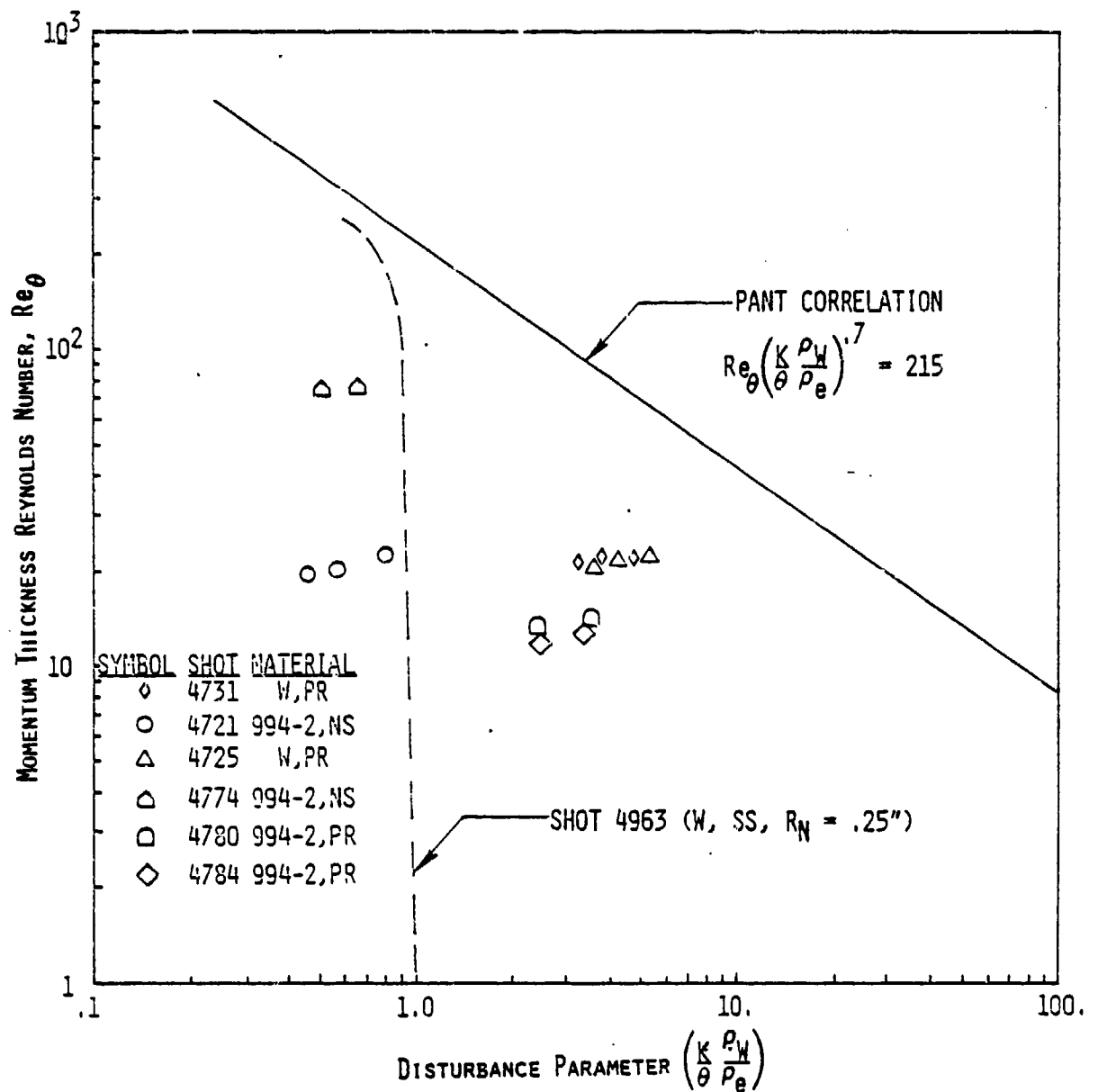


FIGURE 6.15 COMPARISON BETWEEN DATA AND PANT CORRELATION FOR  $K_{RMS}$  (FREE FLIGHT)

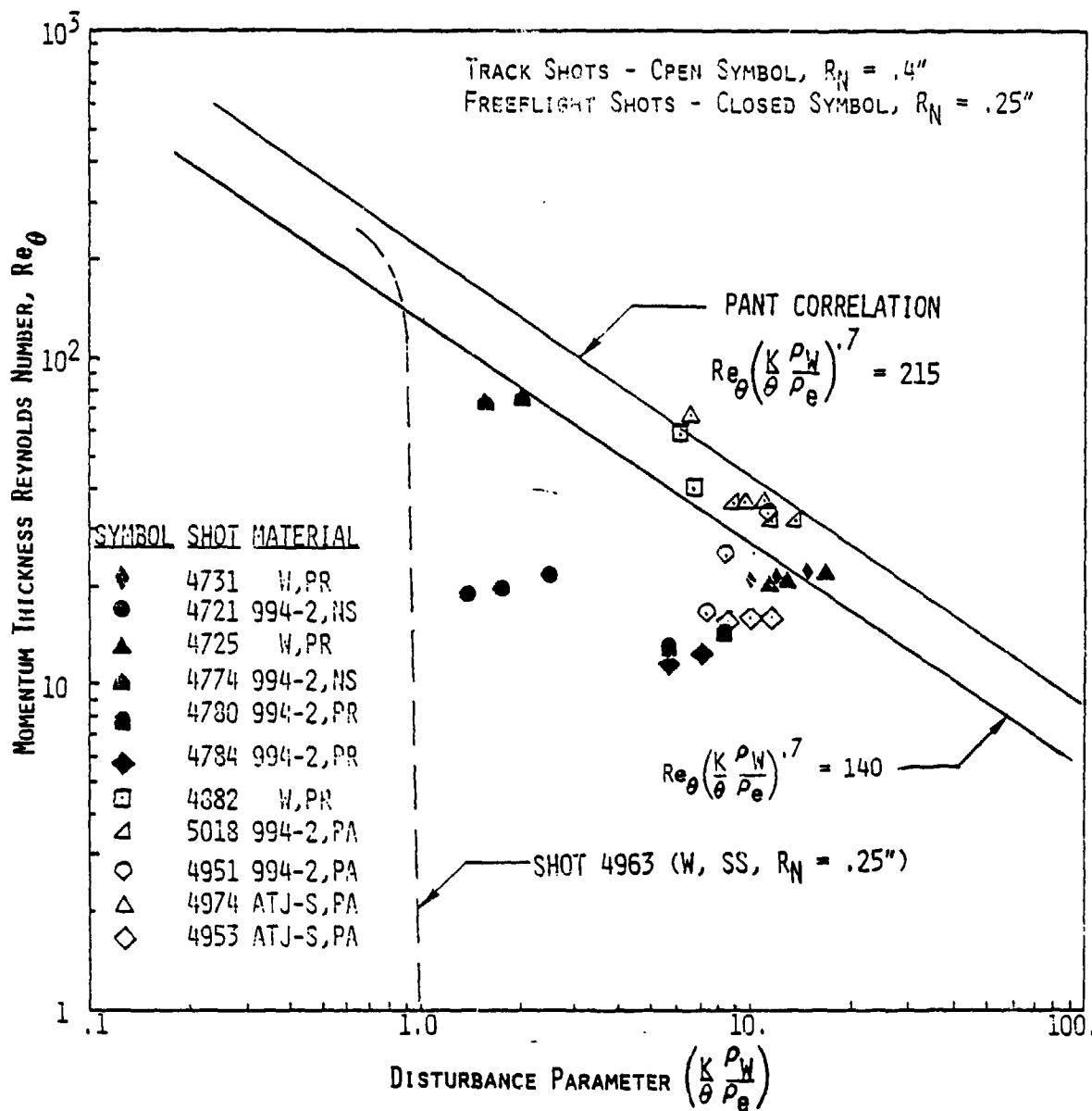


FIGURE 6.16 COMPARISON BETWEEN DATA AND PANT FOR W, ATJ-S AND 994-2 AND  $K_{MEAN}$

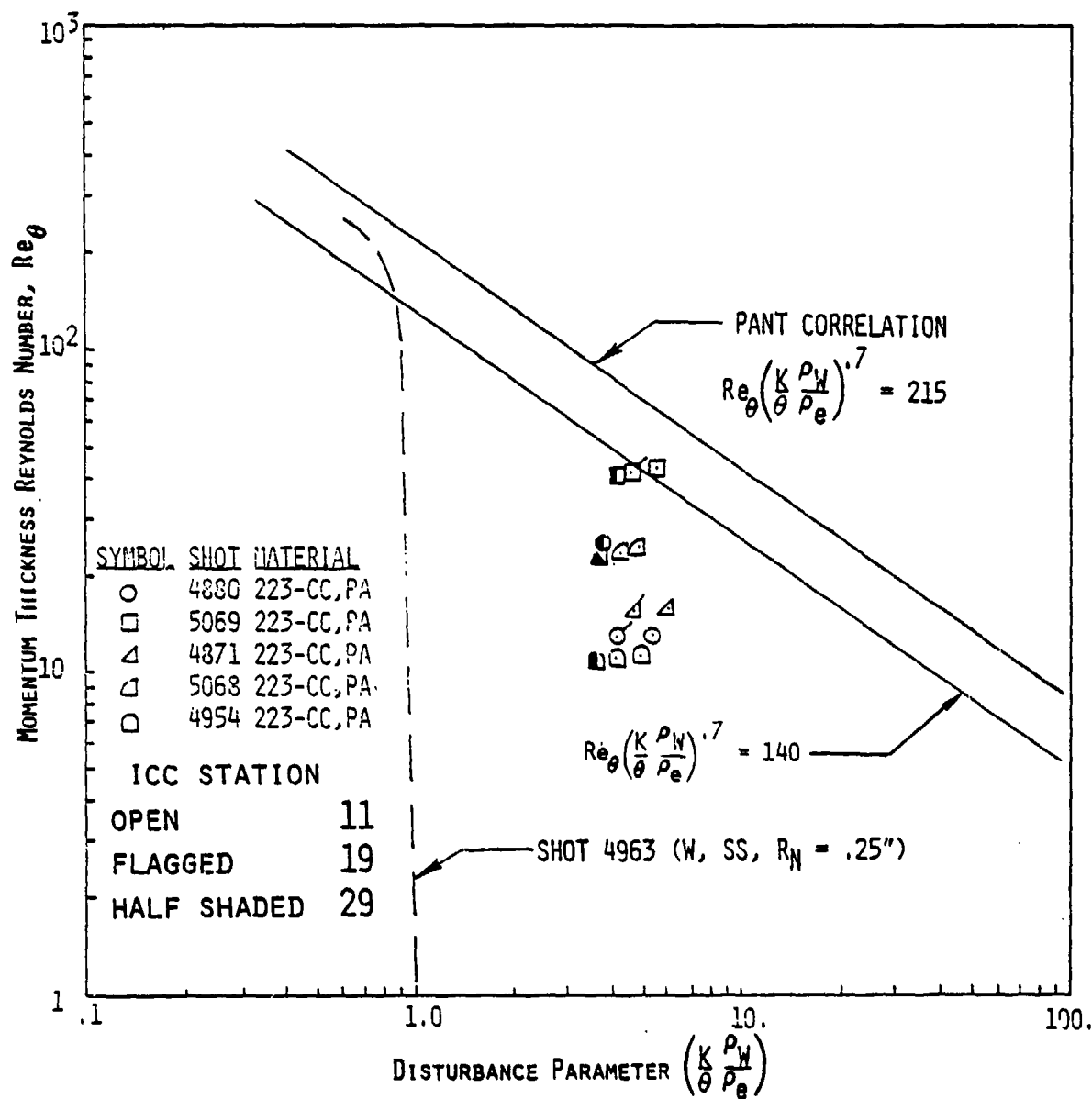


FIGURE 6.17 COMPARISON BETWEEN DATA AND PANT  
 FOR CC-223 AND  $K_{MEAN}$

TABLE 6.4 INFERRED ROUGHNESS RESULTS USING PANT CORRELATION  
(IC 11 - TRACK, IC 10 - FREEFLIGHT)\*\*

Material	Test Mode	Shot No.	P stag (atm)	Re <sub>∞</sub> /ft x 10 <sup>-7</sup>	Roughnesses (mils)		Ratio
					Average K	Inferred K	
223	Track	4954	24.9	0.883	.25, PA*	3.40	13.6
	Track	4880	33.0	1.21	.25, PA	2.40	9.6
	Track	5068	48.4	1.79	.25, PA	1.14	4.6
	Track	4871	49.0	1.78	.25, PA	1.66	6.6
	Track	5069	94.3	3.35	.25, PA	0.45	1.8
ATJ-S	Track	4953	50.5	1.83	.55, PA	1.90	3.5
	Track	4974	63.0	1.78	.55, PA	0.64	1.2
994-2	Track	5018	64.1	2.39	.57, PA	0.65	1.14
	Track	4951	69.4	2.49	.57, PA	0.66	1.16
W	Track	4882	174.2	6.65	.292, PR*	0.46	1.6
	Track	4963	174.9	6.67	≤ .03, SS*	Laminar	Laminar
994-2	Free Flight	4784	49.4	1.85	.30, PR	2.23	7.4
	Free Flight	4780	65.1	2.46	.30, PR	1.79	5.9
	Free Flight	4774	70.3	2.55	.075, NS*	0.17	2.2
	Free Flight	4721	169.0	6.60	.075, NS	0.80	10.7

\*PA = Preablated, PR = Pre-roughened, SS = Super Smooth, NS = Nominally Smooth  
\*\*Other ICC results are similar

TABLE 6.5 COMPARISON OF RANGE DATA WITH TRANSITION MODELS

SHOT	MATERIAL	P STAG	$Re_{\infty}$ ( $10^{-7}/ft$ )	ICC	$K_{MEAN}$	PANT	BISHOP	DIRLING		$\theta_{MEAN}$ DATA
								$K = K_{MEAN}$	$K = \frac{K_{MEAN}}{\left(1 + 350 \frac{K_{MEAN}}{R_N}\right)}$	
4880	994-2	33.5	1.22	4	.25	Laminar	Laminar	Laminar	Laminar	15.5
		33.0	1.21	11	"	"	"	"	"	15.0
		32.3	1.20	19	"	"	"	"	"	13.6
4882	W	31.5	1.18	29	"	"	"	"	"	12.2
		191.2	6.98	4	.292	6	9.0	3.0	5.0	4.4
		155.8	6.29	11	"	9.4	19.0	5.0	7.0	7.0
5018	994-2	135.7	5.87	29	"	11.3	20.0	7.0	10.0	6.7
		64.1	2.39	11	.57	8.2	10.0	5.0	9.0	11.0
		61.4	2.34	19	"	9.4	13.0	6.0	10.0	8.4
5068	CC-223	58.1	2.28	29	"	11.7	14.0	7.5	13.0	6.5
		50.0	1.82	4	.25	26.0	37.0	Laminar	Laminar	9.1
		48.2	1.78	11	"	31.8	Laminar	"	"	8.0
4951	994-2	46.1	1.75	19	"	Laminar	"	"	"	7.7
		43.6	1.70	29	"	"	"	"	"	"
		69.4	2.49	11	.57	10.7	20.6	7.0	13.0	2.1
4974	ATJ-S	67.0	2.45	19	"	13.0	23.0	9.5	18.0	5.2
		64.5	2.40	29	"	16.1	34.0	11.0	25.0	5.6
		64.8	2.39	4	.55	10.0	11.0	5.0	9.0	10.5
5069	CC-223	62.9	2.35	11	"	10.7	16.0	7.0	11.5	14.6
		61.0	2.32	19	"	10.7	20.6	8.0	13.0	12.3
		58.7	2.27	29	"	12.0	23.0	9.0	16.0	11.8
5069	CC-223	99.1	3.65	4	.25	18.7	23.0	16.0	29.0	14.5
		94.3	3.55	11	"	16.5	27.0	16.5	Laminar	14.0
		88.7	3.45	19	"	25.0	32.0	25.0	"	12.3
		82.3	3.32	29	"	22.2	Laminar	Laminar	10.1	

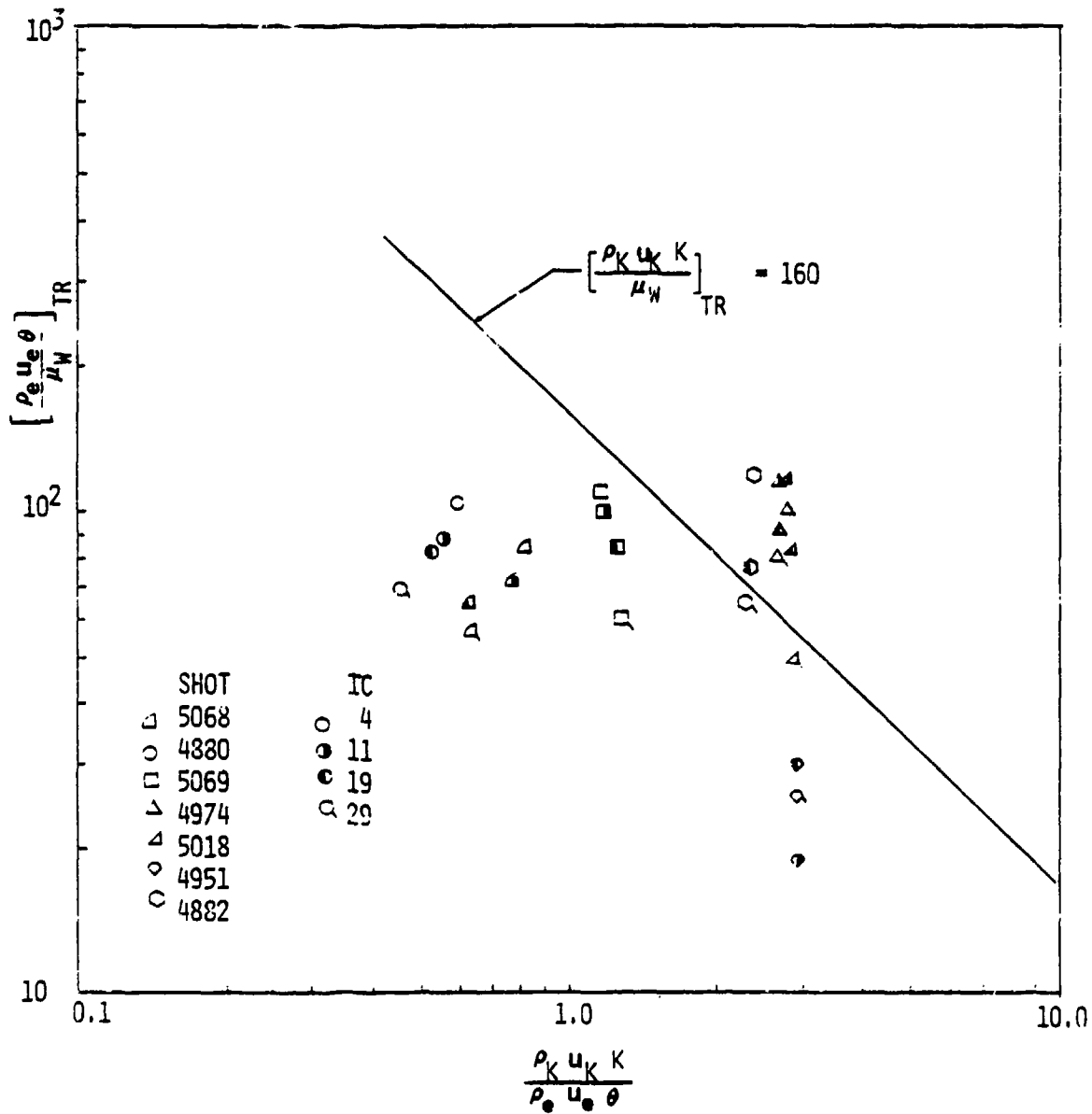


FIGURE 6.18. COMPARISONS BETWEEN MEAN TRANSITION FRONT DATA AND DIRLING'S CORRELATION FOR  $K=K_{MEAN}$

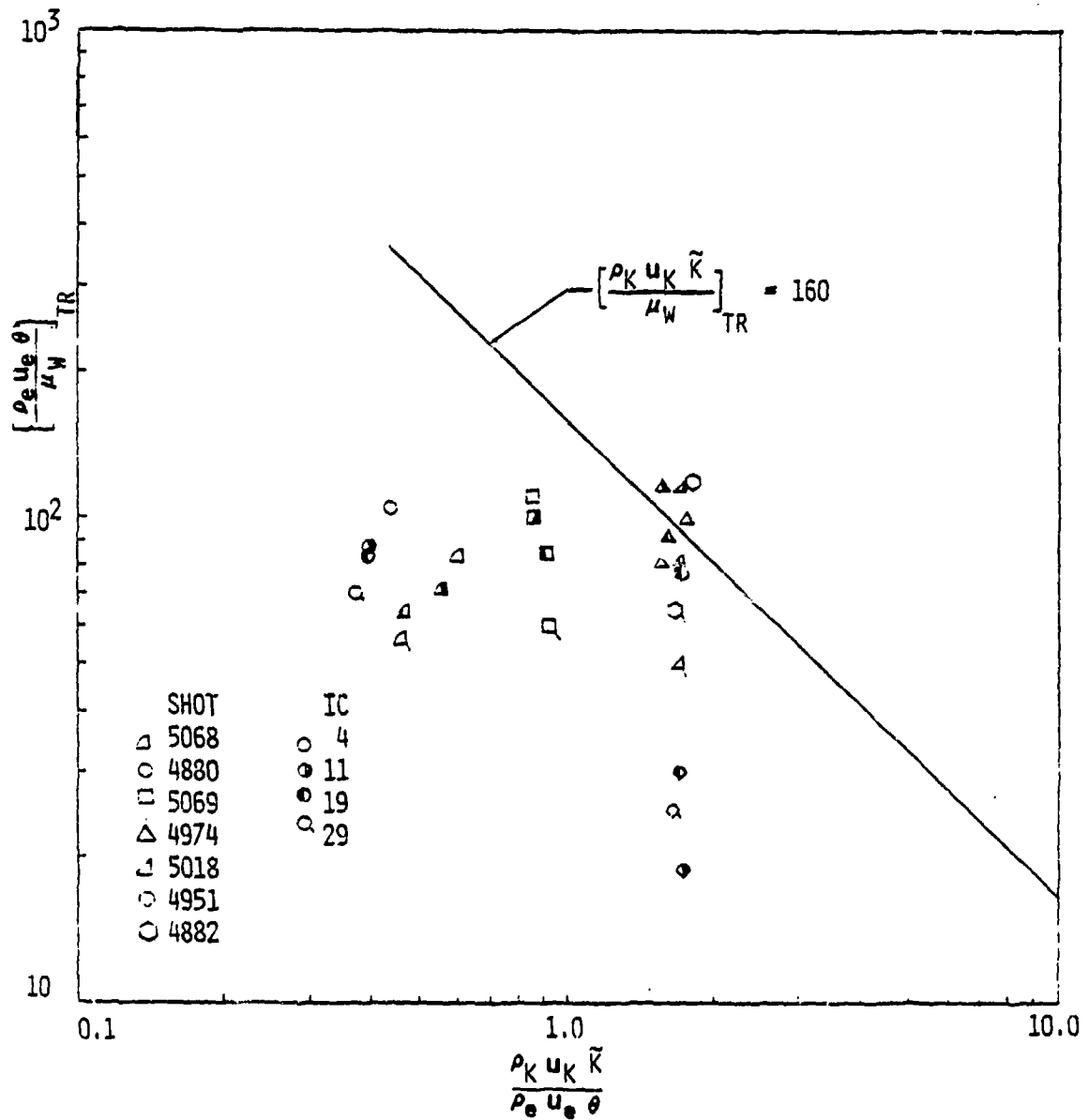


FIGURE 6.19 COMPARISON BETWEEN MEAN TRANSITION FRONT DATA AND DIRLING'S CORRELATION FOR  $\tilde{K} = K_{MEAN} / (1 + 350 K_{MEAN} / R_N)$

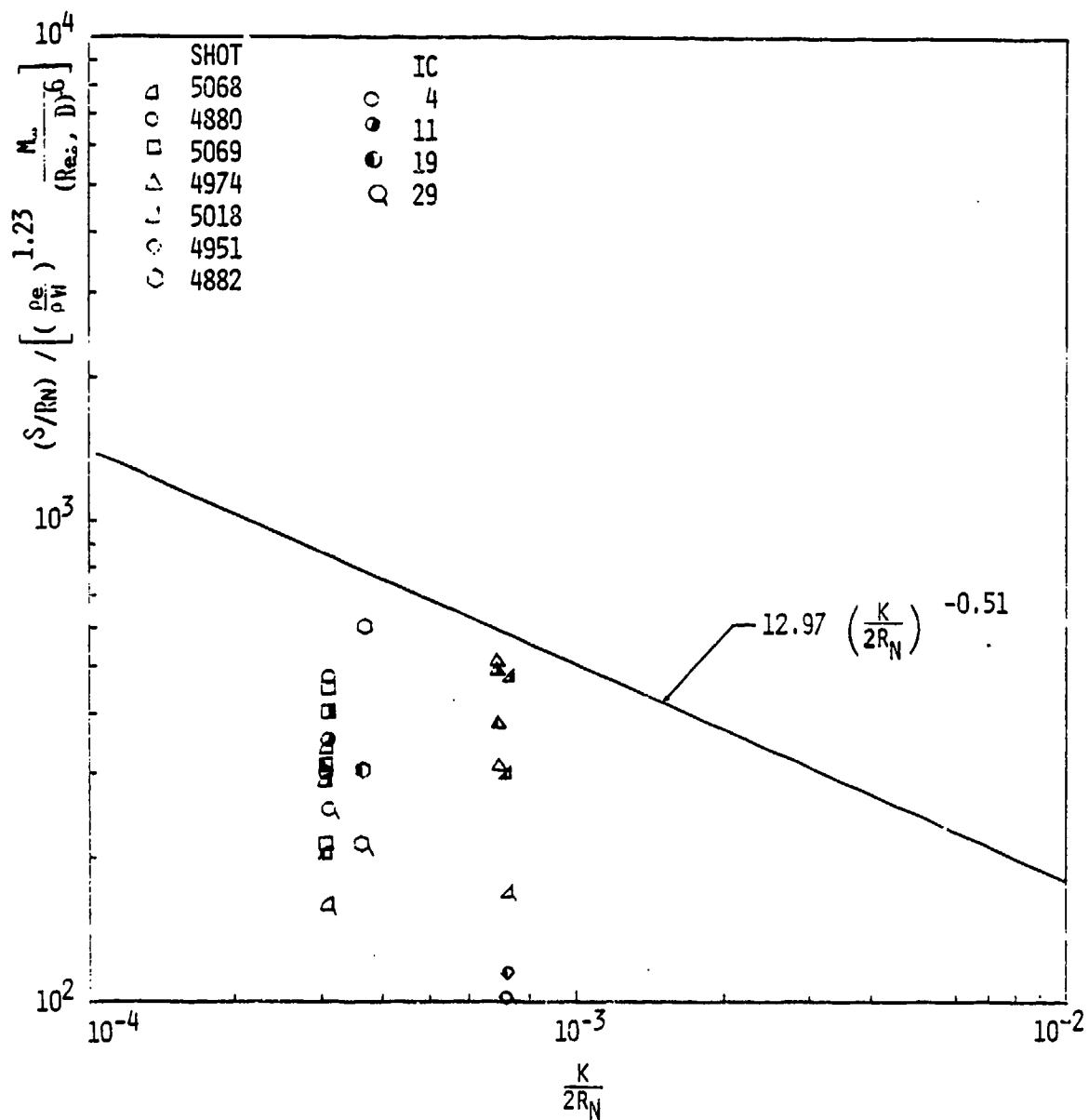


FIGURE 6.20 COMPARISON BETWEEN MEAN TRANSITION FRONT DATA AND BISHOP'S CORRELATION

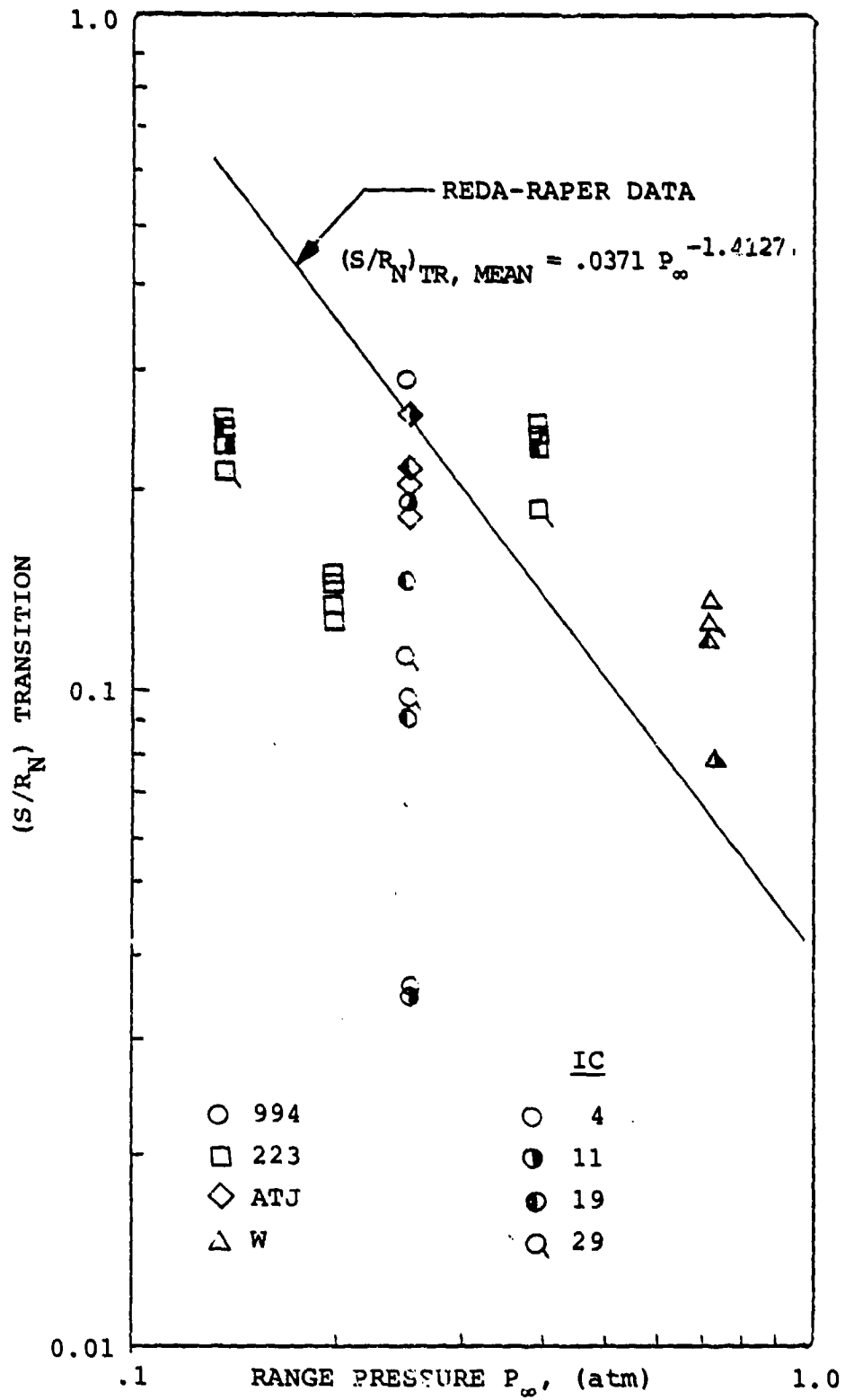


FIGURE 6.21 MEAN TRANSITION FRONT DATA VS FREESTREAM PRESSURE

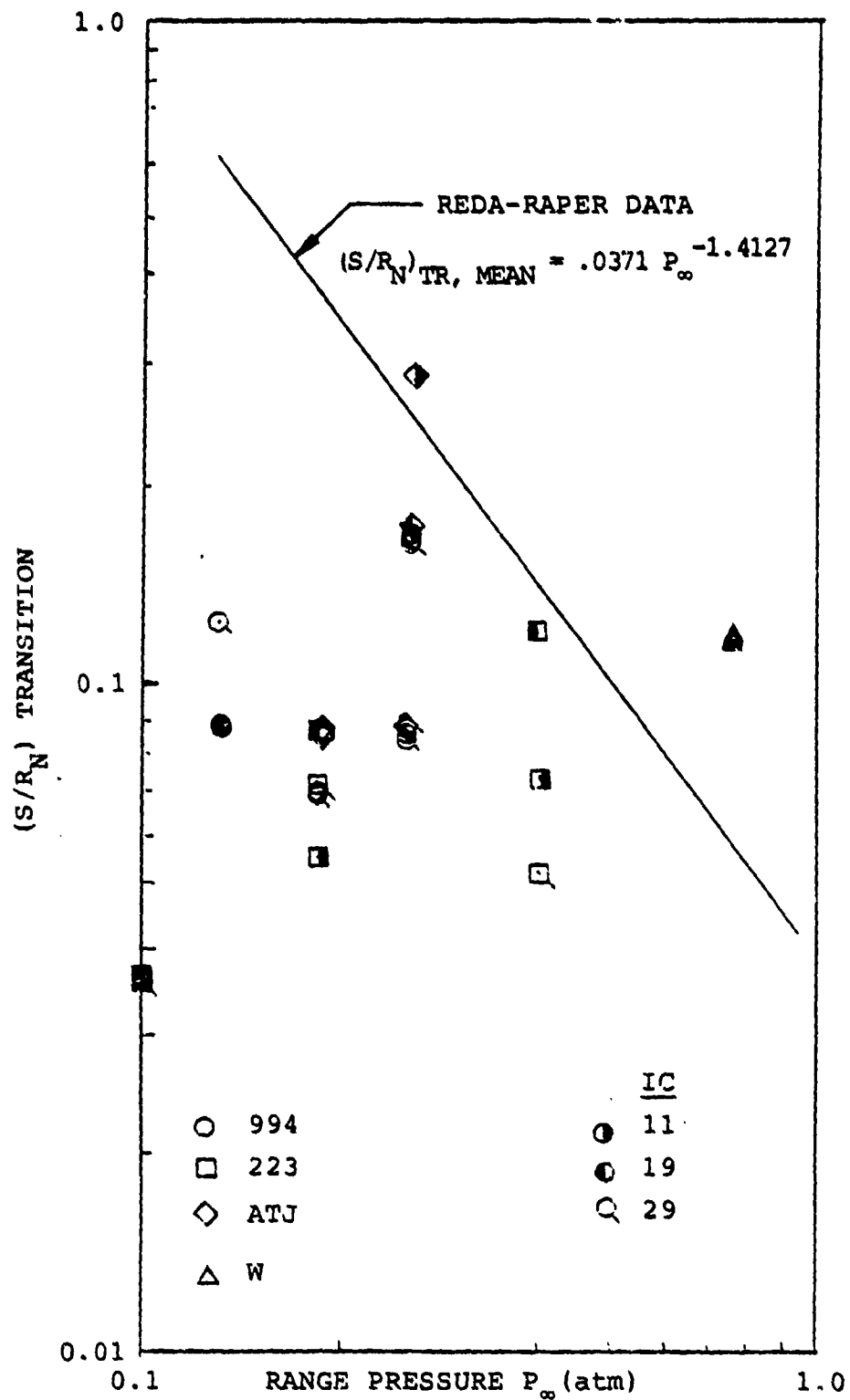
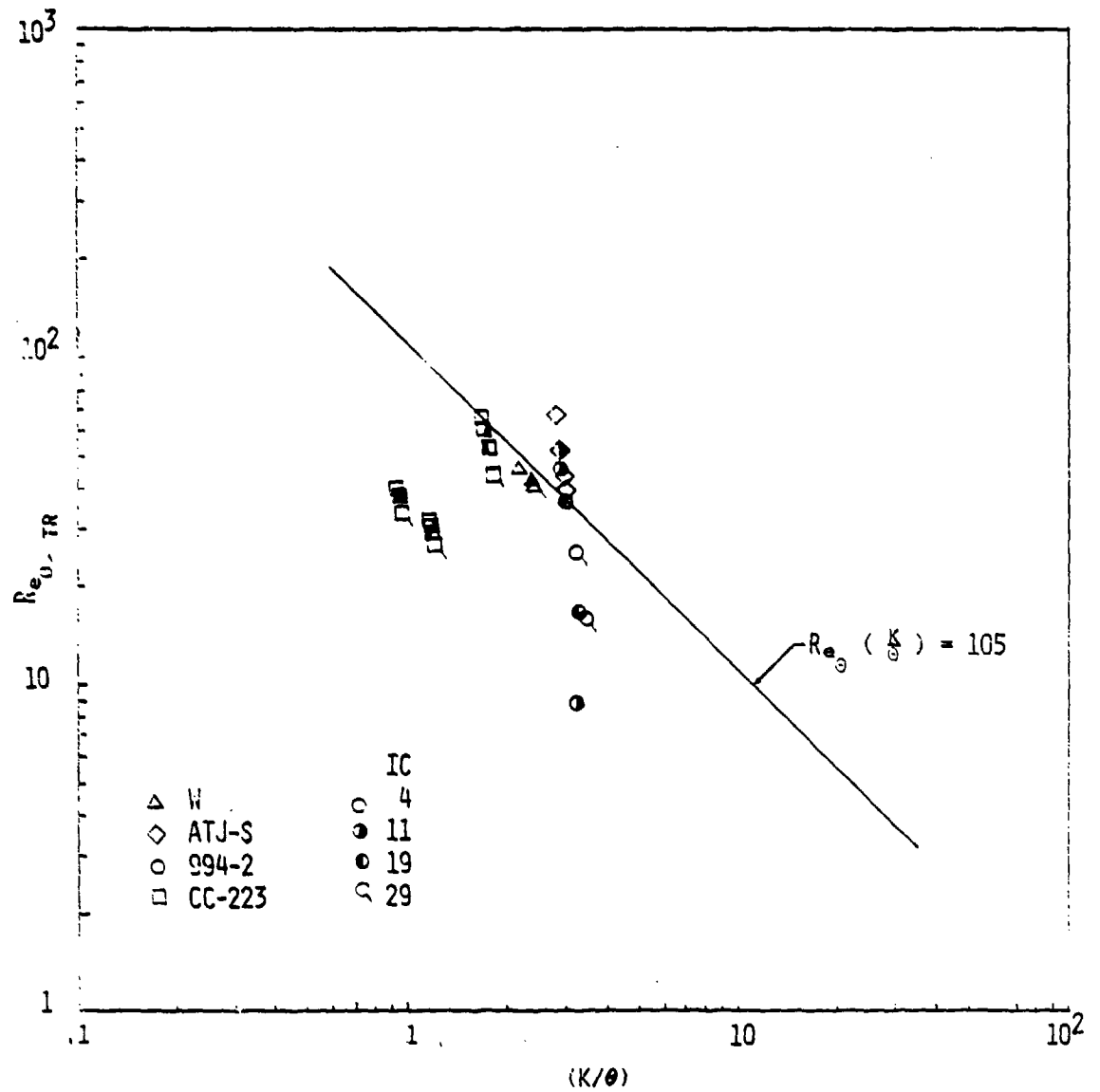


FIGURE 6.22 MEAN HEAT FLUX INFERRED TRANSITION FRONT DATA VS FREESTREAM PRESSURE



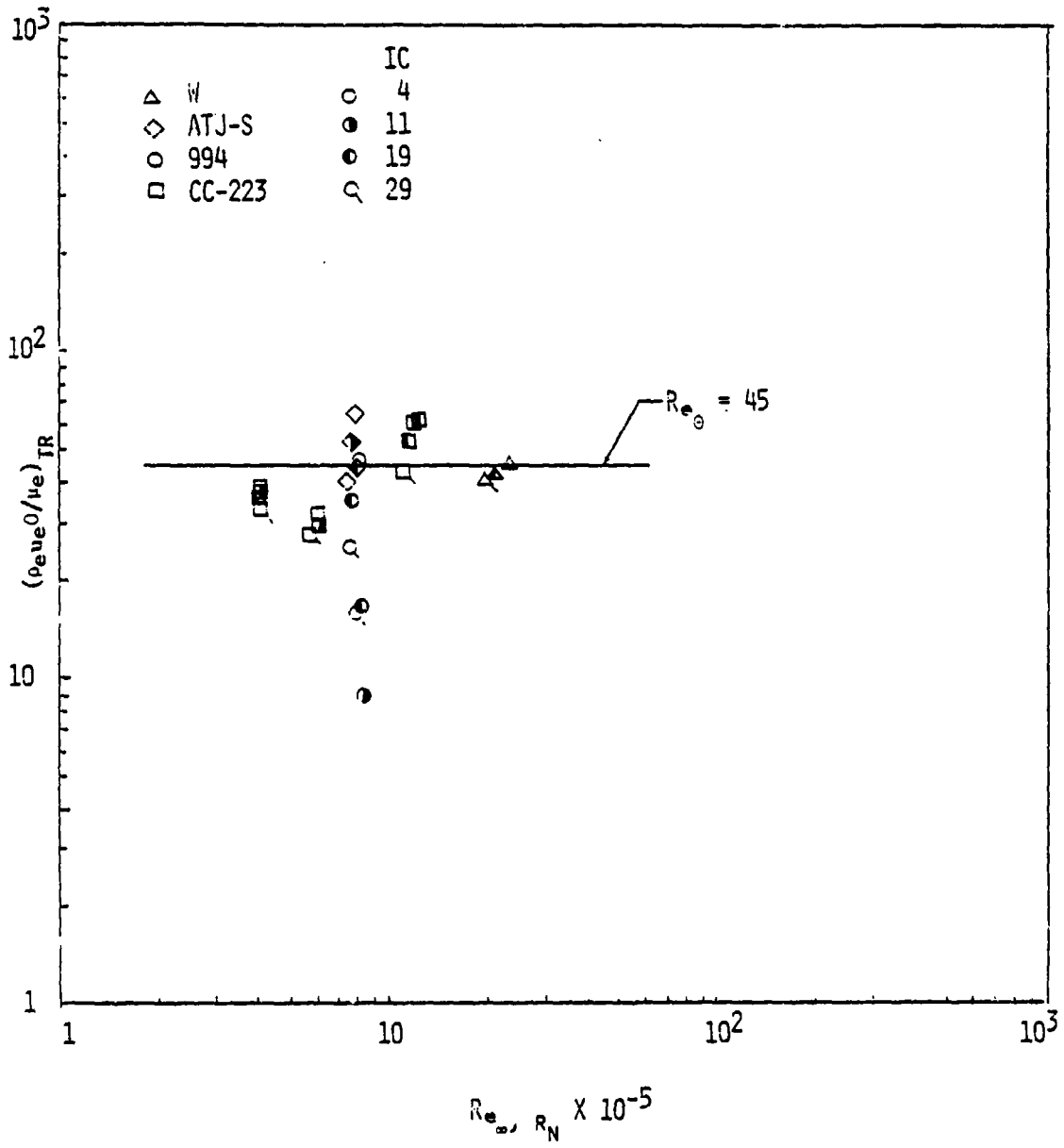


FIGURE 6.24 MEAN TRANSITION FRONT DATA VS FREESTREAM REYNOLDS NUMBER

## 7.0 HEAT TRANSFER RESULTS

The object of this section is to investigate the effects of surface roughness on the stagnation region and transitional/turbulent heat transfer augmentation. By direct comparisons between the data-inferred heat transfer to the model surface, and the smooth wall calculated values using the ASCC, augmentation levels can be extracted. Also, the various heat transfer augmentation predictive methodologies can be verified.

### 7.1 Stagnation Point Heat Transfer Augmentation

#### 7.1.1 Augmentation Factors

The heat transfer augmentation levels were extracted as follows:

1. Derive the model surface heat transfer using the CAPER-2D heat conduction code from the mean surface temperature-time histories down range.
2. Calculate the smooth wall stagnation point heat transfer using ASCC. The ASCC prediction should be in agreement with the Fay-Riddell theory.
3. Compute the heat transfer augmentation factors by taking the ratio of the data-inferred stagnation point flux to the smooth wall value.
4. Verify laminar augmentation methodologies by computing augmentation factors for the test conditions and compare with augmentation levels derived in step 3.

Table 7.1 lists the data derived augmentation factors at the stagnation point for all the shots analyzed. There is a good agreement between the theory and data for Shot 4963, where the model surface was super smooth. The data indicated augmentation factors around unity as expected. For the pre-roughened and pre-ablated models, augmentation due to roughness

TABLE 7.1. STAGNATION POINT HEAT TRANSFER AUGMENTATION

Shot #	Material	ICC	Stagnation Point Heat Transfer Augmentation Factors = $Q_{data}/Q_{calculated}$	
			ASCC Generated Wall Temperature	Wall Temperature Data
4882	W	19	-	1.22
		29	-	1.17
4963	W	11	.93	.96
		19	1.03	1.03
		29	1.03	.98
4953	ATJ-S	11	.99	1.02
		19	1.17	1.15
		29	1.2	1.17
4974	ATJ-S	11	1.04	1.06
		19	.88	.95
		29	.92	.97
4951	994-2	11	.92	.99
		19	1.34	1.27
		29	1.31	1.27
5018	994-2	11	.87	.93
		19	.91	.93
		29	1.22	1.12
4871	CC-223	11	1.05	1.06
		29	1.18	1.11
4880	CC-223	11	1.25	1.17
		19	.99	1.02
		29	.83	.92
4954	CC-223	11	1.02	1.02
		19	.77	.94
		29	.62	.79
5068	CC-223	11	-	1.10
		19	-	1.05
		29	-	1.17
5069	CC-223	11	-	1.17
		19	-	1.25
		29	-	1.28

was observed. For the flight conditions tested augmentation factors as high as 2.0 were observed (Figure 7.1). To eliminate the effects of wall temperature on the augmentation factors, the calculated stagnation flux was based on the measured wall temperature. Listed in the table also are augmentation factors where the ASCC computed fluxes were based on the ASCC generated surface temperatures using the transient option of the code.

#### 7.1.2 Comparisons with the PANT and Phinney's Laminar Augmentation Correlations

Comparisons were made between the measured stagnation point augmentation levels and those predicted using the PANT and Phinneys correlations, in order to verify extrapolation of the predictive methodologies to the ballistics range flight environments. The correlations have the following forms:

##### PANT Laminar Augmentation

$$K_{\ell} = 1 \text{ for } \ell < 50$$

$$K_{\ell} = 1.307 \ln \ell + 23.09 \ell^{-.606} - 6.269 \text{ for } \ell > 50$$

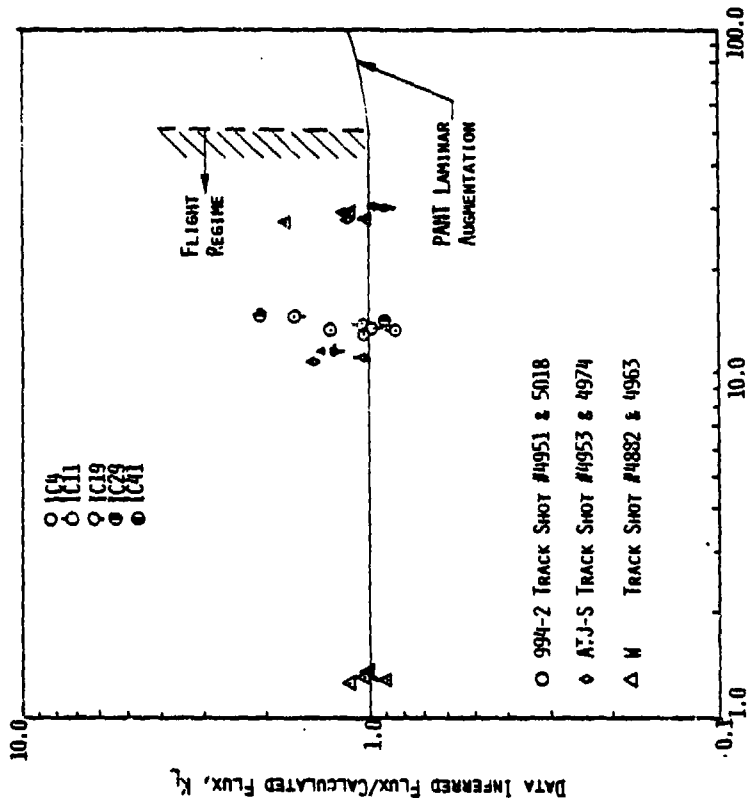
$$\text{where } \ell = \left( \frac{\rho_2 U_2 R_N}{\mu_2} \right)^{.2} \frac{k}{\theta}$$

##### Phinney's Heating Augmentation

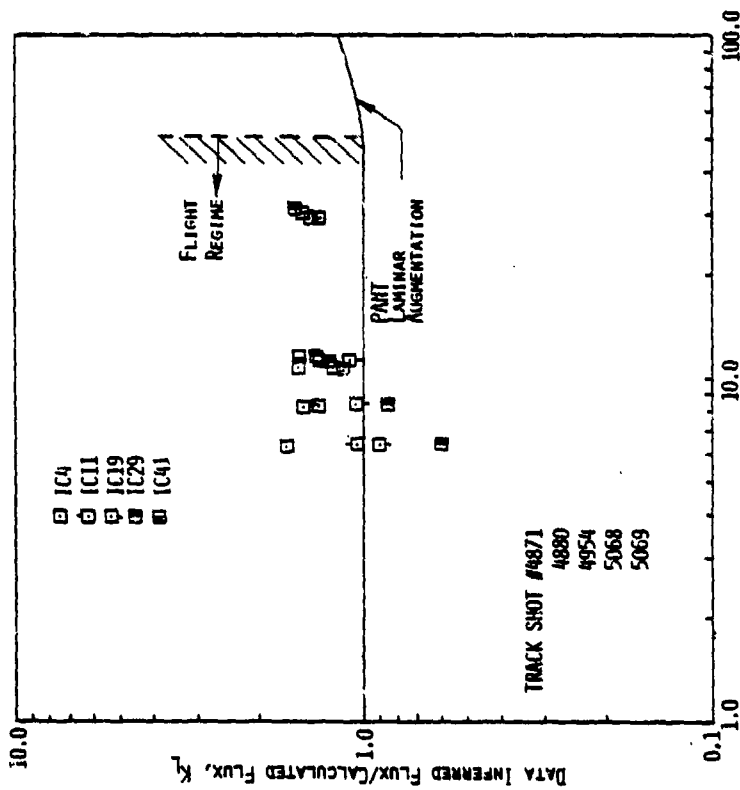
$$K_{\ell} = 1 + \left( \frac{\rho_2 U_2 R_N}{\mu_2} \right)^{.2} f \left( \frac{k}{\delta^*} \right)$$

$$f \left( \frac{k}{\delta^*} \right) = \begin{cases} .0017 \frac{k}{\delta^*}, & \text{for } \frac{k}{\delta^*} < 2.41 \\ .004 & , \text{ for } \frac{k}{\delta^*} > 2.41 \end{cases}$$

Figure 7.1 shows a comparison between the data and predictions of the PANT correlation for all the materials. The materials were divided into sand grain and weave type materials,



B) W, ATJ-S, 994-2



A) CC-223

FIGURE 7.1.1. COMPARISON BETWEEN DATA AND PANT PREDICTIONS FOR THE STAGNATION POINT HEAT TRANSFER AUGMENTATION FACTORS

in order to eliminate effects of the nature of the surface on the results. It can be seen that for the flight regime, augmentation factors up to 200% were observed, while the PANT correlation did not predict any augmentation. The comparison between the data and predictions using Phinney's correlation depicted in Figure 7.2, indicates that the correlation over-predicted the data for all the materials tested.

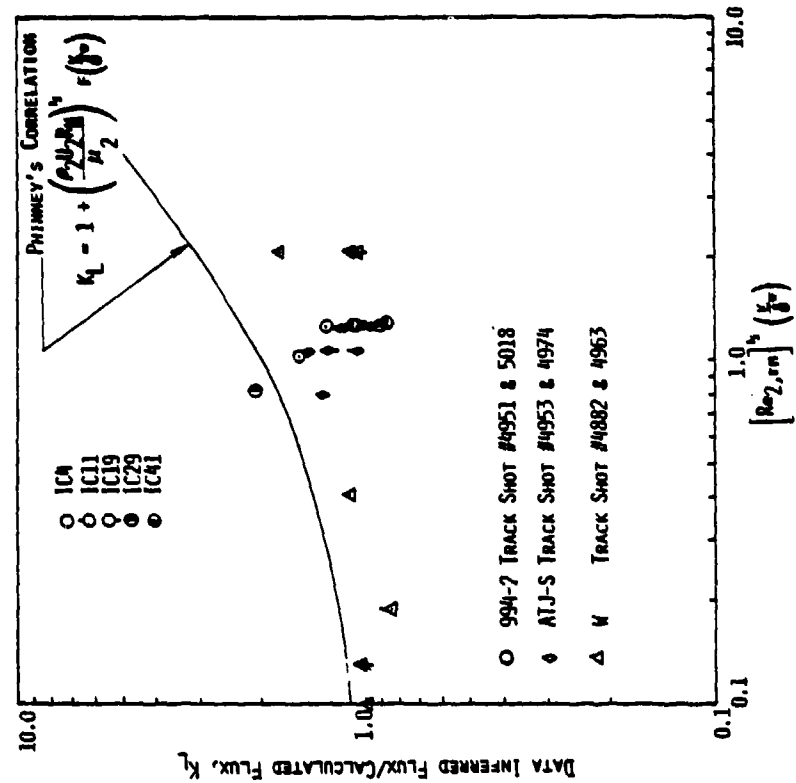
No attempt will be made here to correlate the observed augmentation factors. However, the data will be presented in terms of all the pertinent correlating parameters  $Re_{\infty}$ ,  $Re_2$ ,  $K/\theta$ ,  $K/\delta^*$  as presented in Figures 7.3 to 7.10.

## 7.2 Transitional/Turbulent Heat Transfer Augmentation

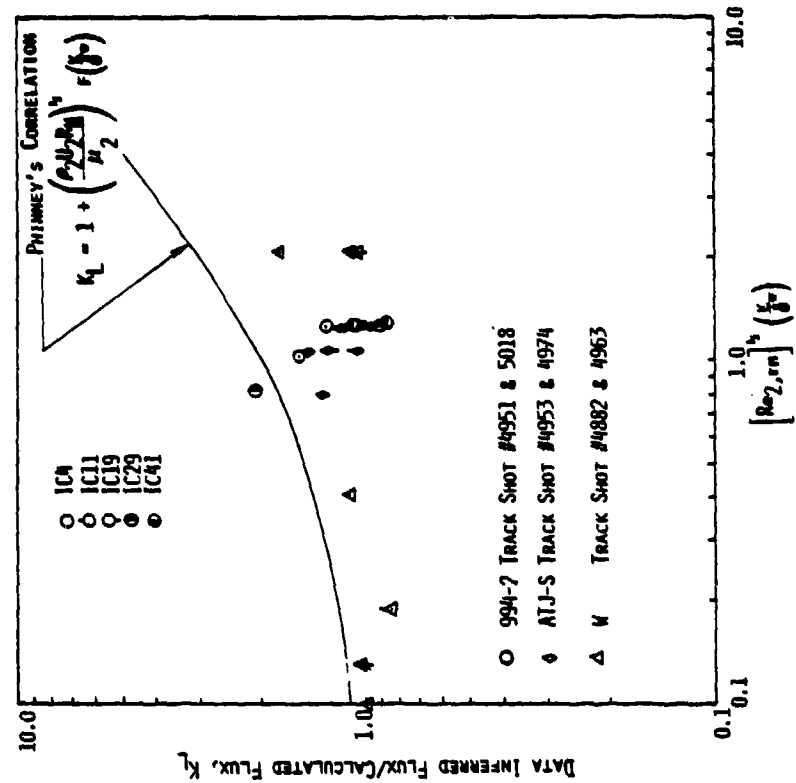
In this section the results of the heat transfer augmentation around the nosetip are presented for all the analyzed shots. First, the heat transfer augmentation factors in the ballistics range environments were derived by direct comparison of the derived heat transfer data to the calculated smooth wall values. Secondly, state-of-the-art turbulent heating augmentation methodology, as given by the ASC code, was compared with the data, in order to validate the extrapolation of the predictive model to flight environments.

The heat transfer around the nosetip is affected by the following parameters.

1. Transition-front location: transition from laminar to turbulent flow is triggered by some roughness height characteristic of the particular surface.
2. Roughness effects: heat transfer is augmented by some roughness height, which may be different from the height which correlates with transition data.
3. Real materials: surface roughness of real materials is such that a statistical distribution exists, and



A) CC-223



B) W, ATJ-S, 994-2

FIGURE 7.2. COMPARISON BETWEEN DATA AND PHINNEY'S CORRELATION FOR THE STAGNATION POINT AUGMENTATION HEAT TRANSFER FACTORS

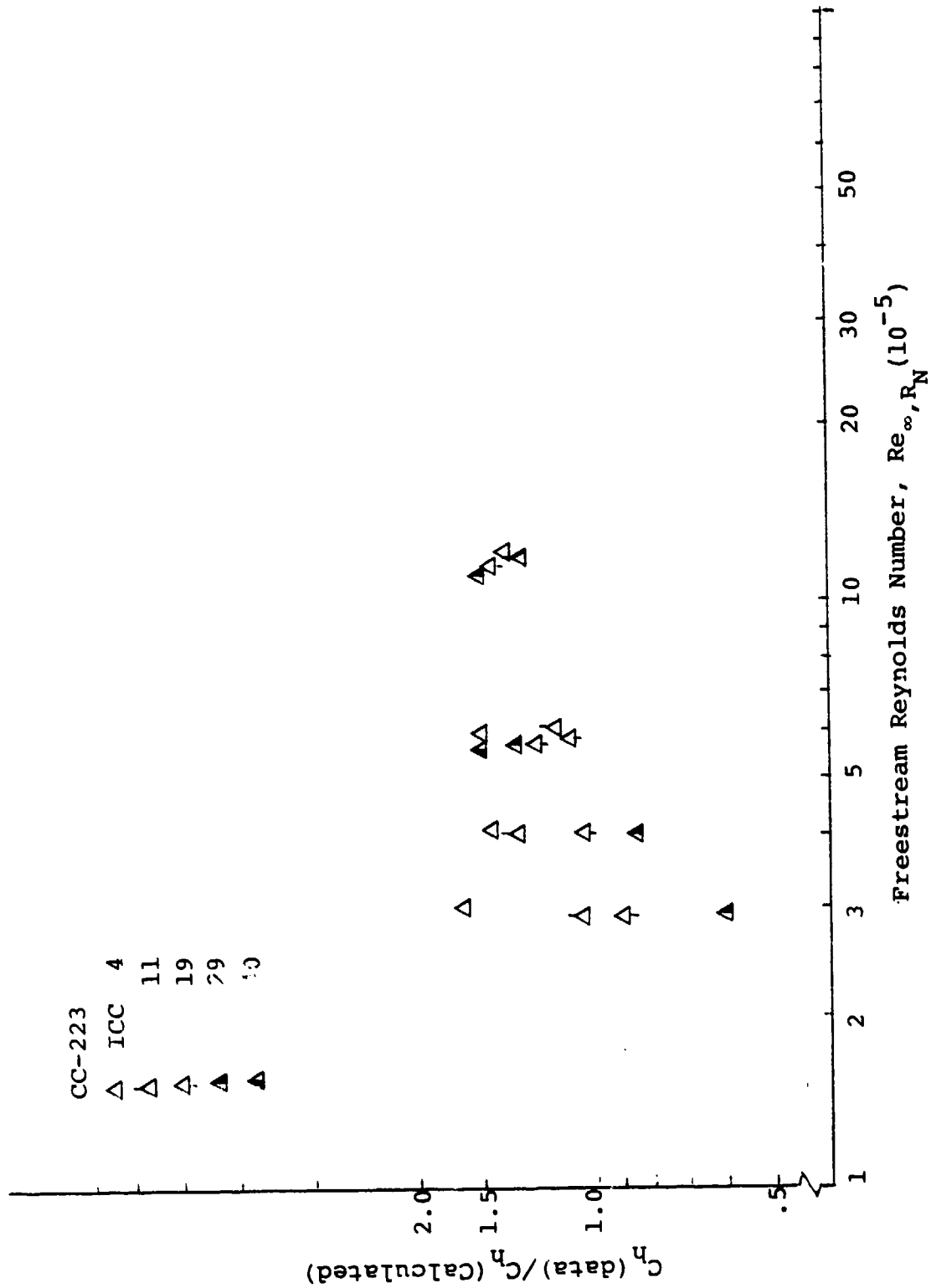


FIGURE 7.3. STAGNATION POINT AUGMENTATION FACTORS FOR  
 CC-223 VS. FREESTREAM REYNOLDS NUMBER

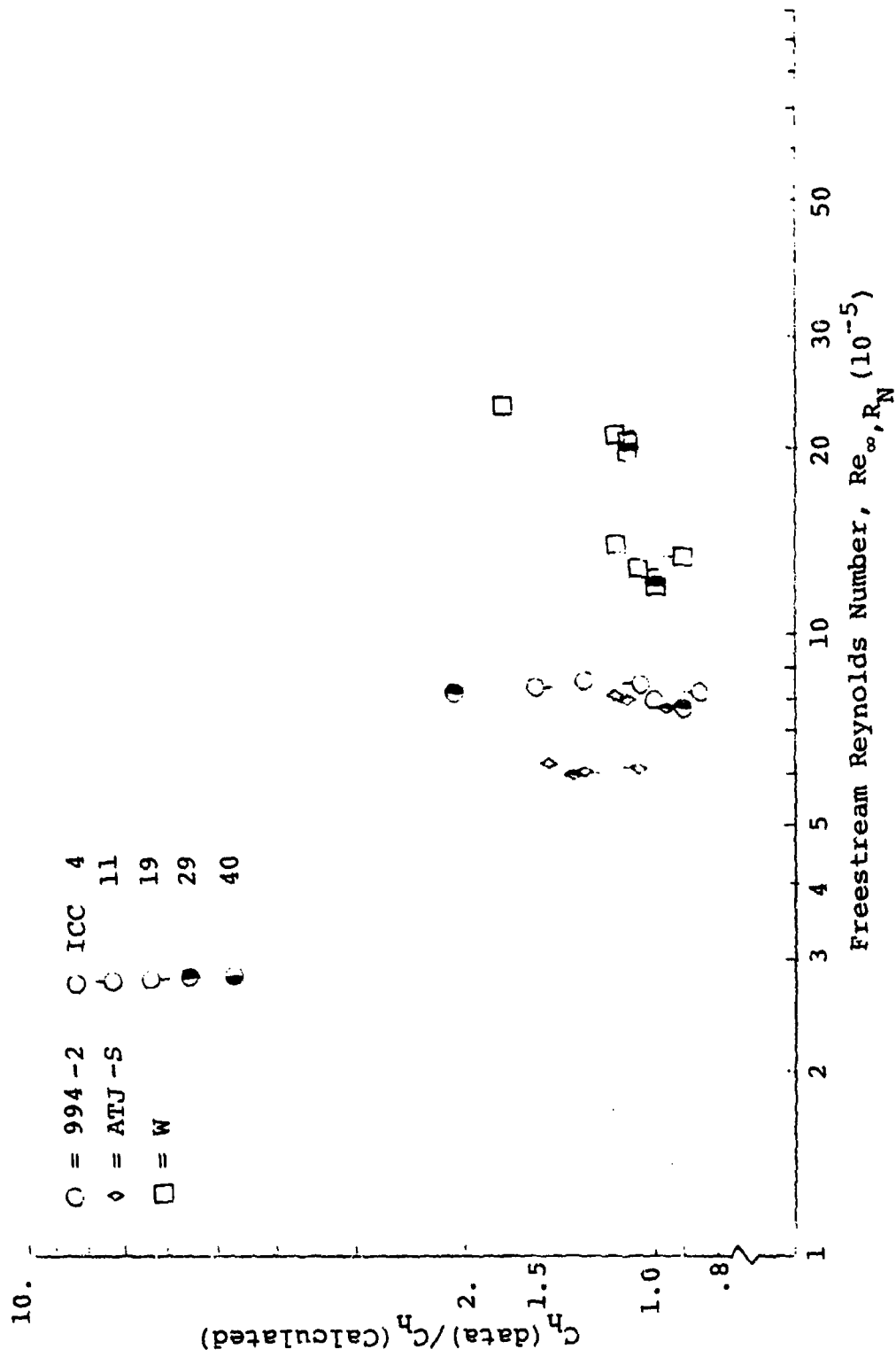


FIGURE 7.4. STAGNATION POINT AUGMENTATION FACTORS FOR 994-2, ATJ-S, W VS. FREESTREAM REYNOLDS NUMBER

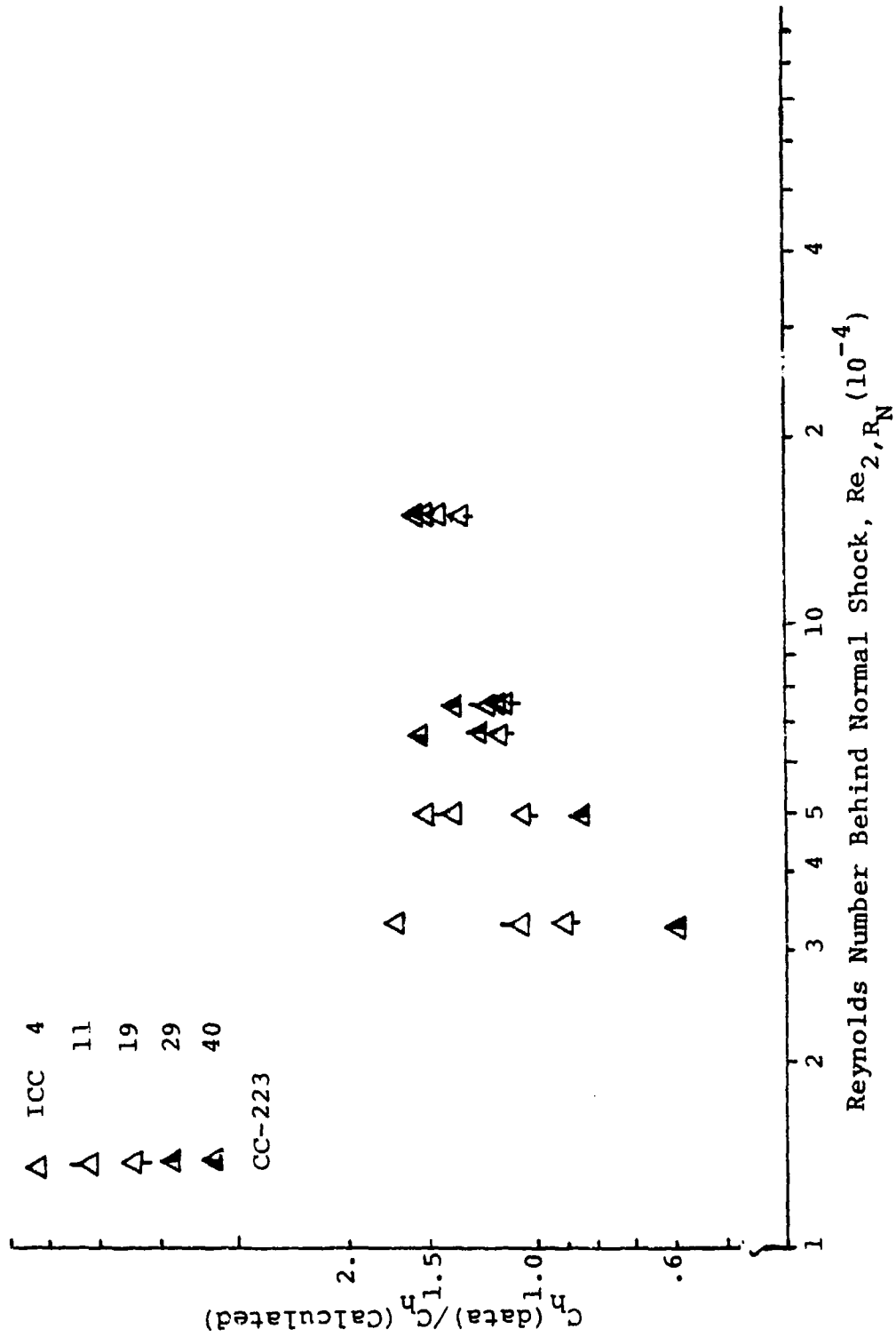


FIGURE 7.5. STAGNATION POINT AUGMENTATION FACTORS FOR CC-223 VS. NORMAL SHOCK REYNOLDS NUMBER

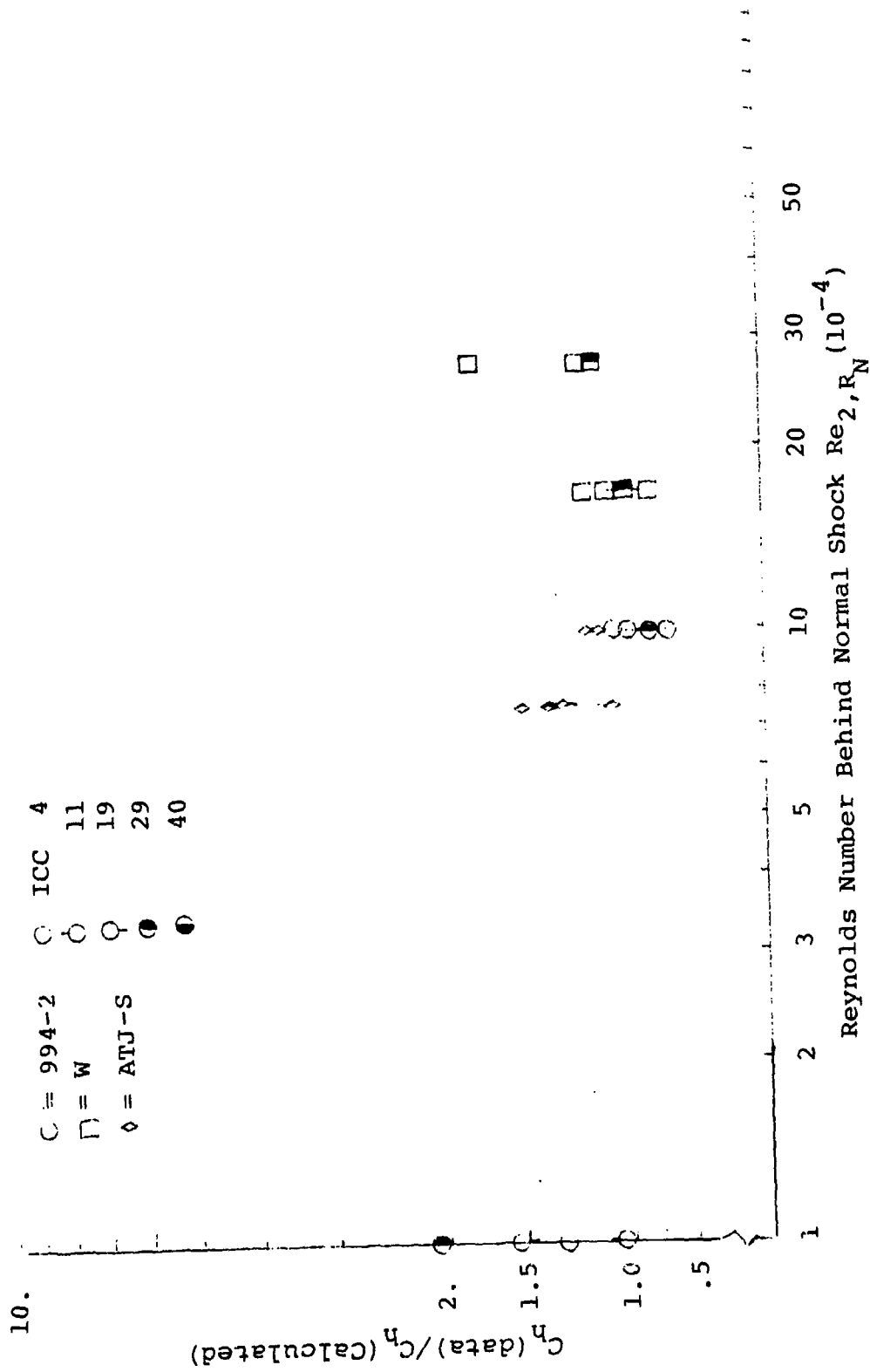


FIGURE 7.6. STAGNATION POINT AUGMENTATION FACTORS FOR  
 994-2, ATJ-S, W vs NORMAL SHOCK REYNOLDS NUMBER

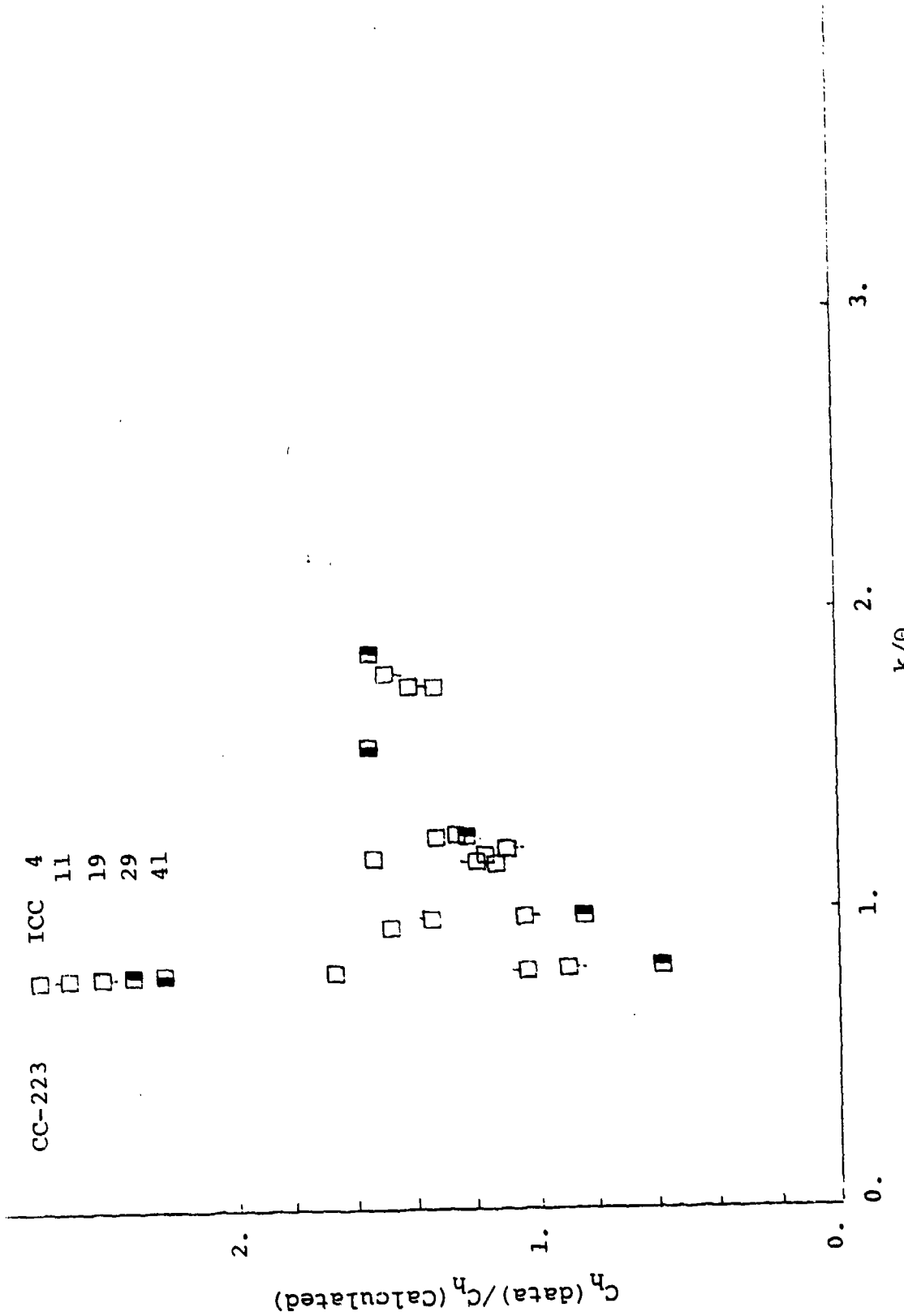


FIGURE 7.7. STAGNATION POINT AUGMENTATION FACTORS FOR  
CC-223 vs.  $k/\theta$

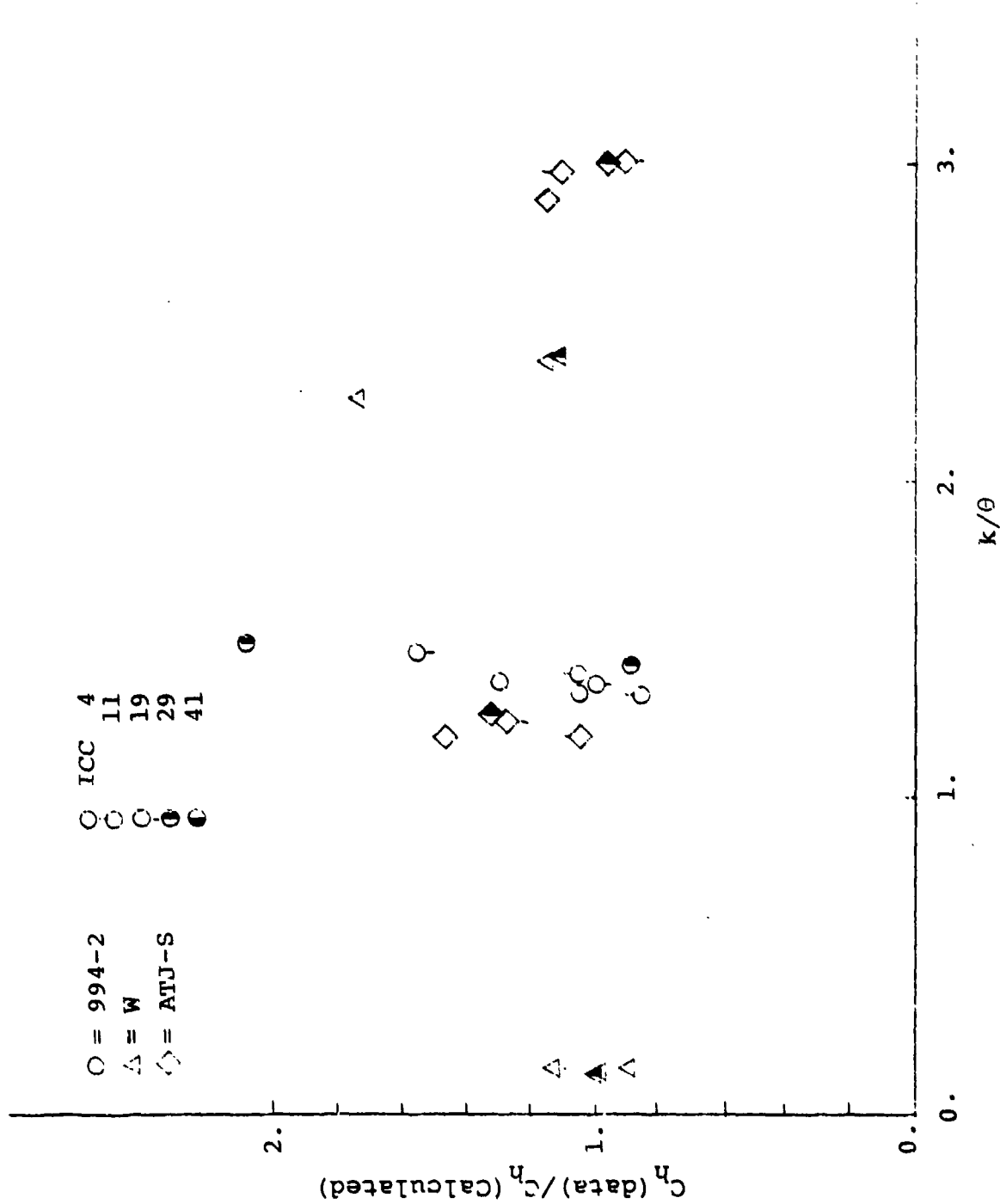


FIGURE 7.8. STAGNATION POINT AUGMENTATION FACTORS FOR 994-2, ATJ-S, W vs.  $k/\theta$

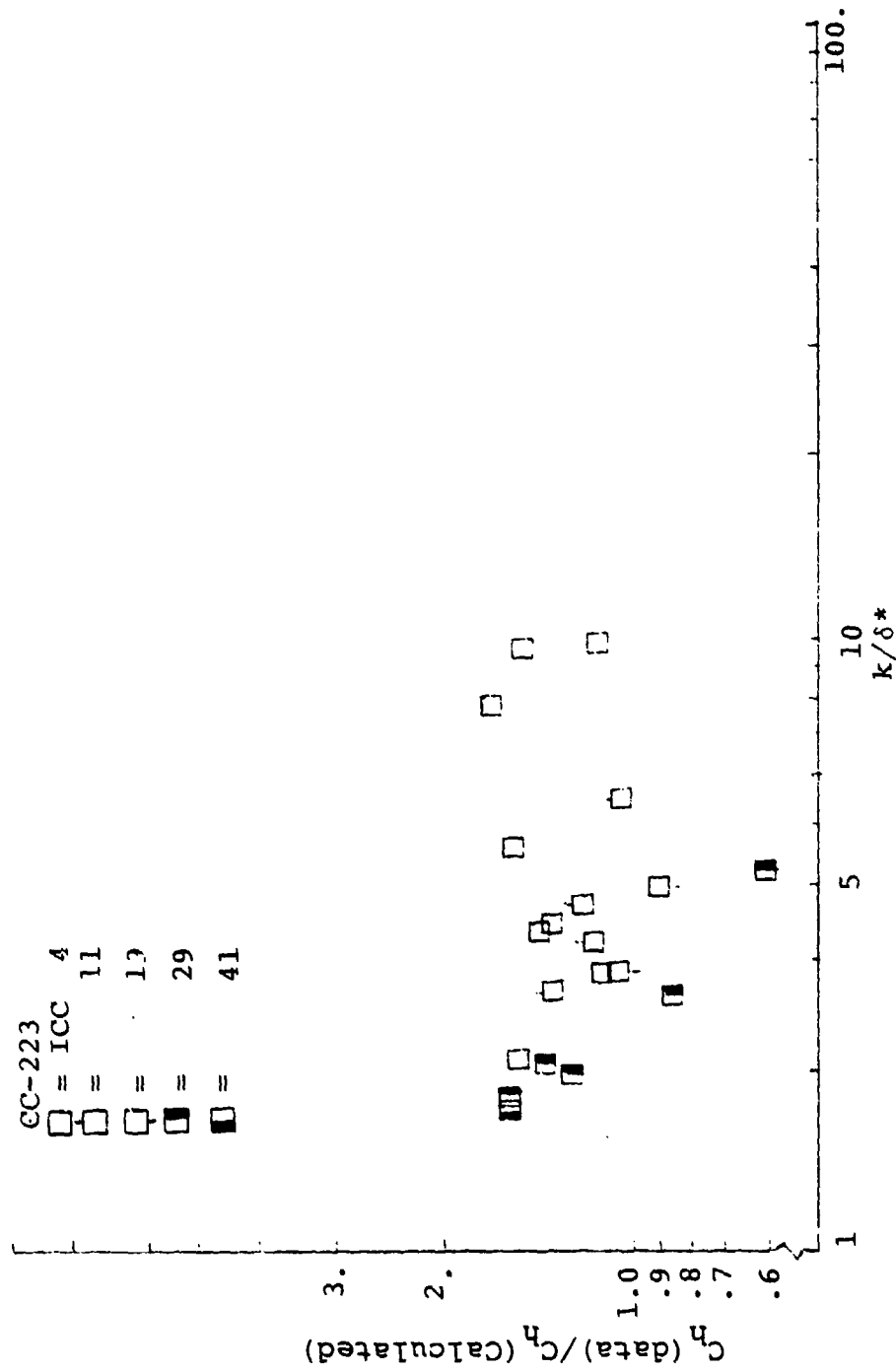


FIGURE 7.9. STAGNATION POINT AUGMENTATION FACTORS FOR  
CC-223 VS,  $k/\delta^*$

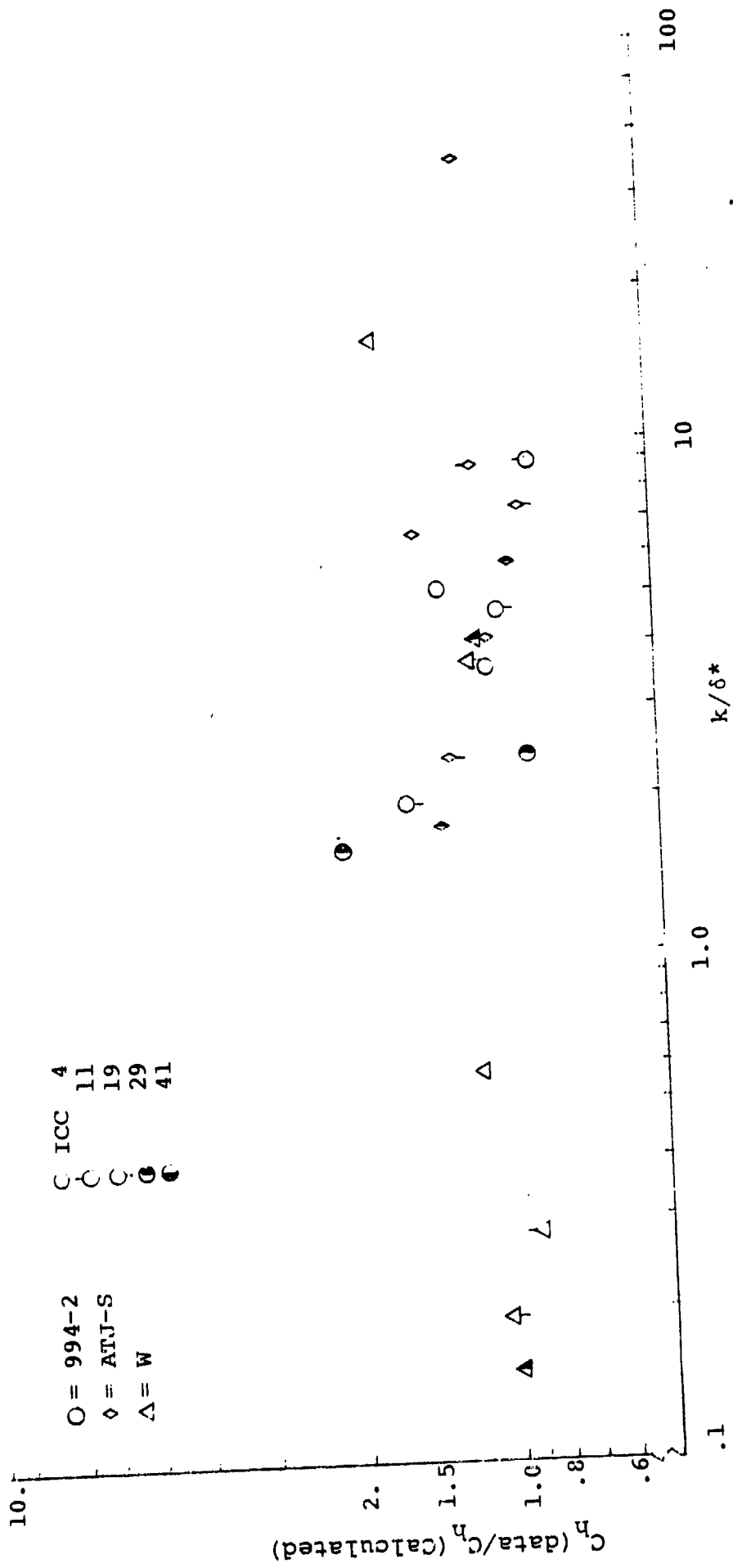


FIGURE 7.10. STAGNATION POINT AUGMENTATION FACTORS FOR 994-2, ATJ-S, W vs.  $k/\delta^*$

most probably a single roughness height cannot adequately represent roughness effects on transition and heating augmentation.

The heat transfer in the transitional region is mainly dependent upon the magnitude of the intermittency factor, width of transitional region, and roughness effects. In the fully turbulent region the heat transfer depends on roughness effects in the transitional ( $K^+ < 70$ ) and fully rough regimes ( $K^+ > 70$ ).

In order to properly derive the magnitudes of the heat transfer augmentation factors around the nosetip the effect of the transition-front location had to be accounted for by fixing the transition location at each ICC location. Therefore, to be consistent with the derived heat transfer data the transition location should be set equal to the experimentally derived location. Predicting the transition location by some methodology, e.g., the PANT correlation, which may not be consistent with the observed transition location, can greatly bias the augmentation factors. This effect will be seen later in this section.

A summary of the steps undertaken to derive the heat transfer augmentation factors around the nosetip is as follows:

- 1) Derive the heat transfer distributions from the mean temperature-history data downrange using CAPER-2D.
- 2) Infer the transition-front location from the heat flux data at each ICC location.
- 3) Predict the smooth wall heat transfer distribution around the nosetip at each ICC location using ASCC-aeroheating option (after setting the transition locations equal to the data derived values).
- 4) Derive the augmentation factors by simply taking the ratio of the data derived heat flux to the computed smooth wall values at each of the body points on the nosetip, and at each ICC locations.

The steps undertaken to verify the ASCC rough wall augmentation predictive methodology were as follows:

- 1) Use the ASCC code in the aeroheating calculation mode at each ICC location using the mean roughness.
- 2) Set the transition location to the data-inferred values.
- 3) Compute the rough wall heat transfer around the nosetip using the ASCC methodology.
- 4) Compare the data derived heat flux to the ASCC computed *rough-wall* heat transfer and/or compare the ASCC computed rough wall augmentation factor to the data derived values.

In the ASCC the turbulent heat transfer enhancement due to roughness is treated via roughness augmentation coefficients given by:

$$I_{h,t,r} = 1 + 0.3 f\left(\frac{k_t}{\theta}\right) g(x)$$

where

$$f\left(\frac{k_t}{\theta}\right) = 1 + 0.09 \left(\frac{k_t}{\theta}\right) + 0.53 (1 - e^{-k_t/\theta})$$

$$g(x) = x + 1.5 (1 - e^{-x}) \text{ for } x > 0$$

$$= 0 \text{ for } x \leq 0$$

$$x = \log_{10} \left( \frac{k^+}{15.5} \right)$$

$$k^+ = \left( \frac{\rho_e U_e k_t}{\mu_e} \right) \left( \frac{\mu_e}{\mu_w} \right) \left( \frac{\rho_w}{\rho_e} \right)^{1/2} \sqrt{C_{f,t,s}/2}$$

$k_t$  is the local turbulent surface roughness and  $C_{f,t,s}$  is the smooth wall turbulent friction coefficient. In the transitional region, the heat transfer is computed via an intermittency factor as given by the ASCC methodology.

### 7.2.1 Data Derived Rough Wall Heat Transfer Augmentation Factors

Figures 7.11 through 7.32 display comparisons between the data derived and smooth wall computed heat transfer distributions as well as, the heat transfer augmentation factors around the nosetip. As an example, Figure 7.11 shows plots of the data-derived and computed smooth wall heat transfer versus the body angle, for ICC 19 and 29 of the tungsten shot 4882. For both ICC locations the transition-front location was set to  $7^\circ$ , as derived from the heat transfer data, and indicated in the figure. Figure 7.12, as an example, shows heat transfer augmentation factors as function of the body angle on the nosetip (ratio of the data-derived to the computed smooth wall heat transfer coefficient).

The super smooth tungsten shot 4963 is of particular interest here. This shot's data essentially calibrates not only the ballistics range data, but also verifies the data reduction scheme utilized in the analysis (i.e., the derivation of the heat transfer distribution from the mean-temperature-time histories at all ICC locations). For this shot and at all ICC's the surface temperature distributions indicated fully laminar flow on the nosetip, as expected since the roughness height,  $K_{rms}$ , was  $\leq .01$  mils. The flow parameters were such that natural transition was not observed. Figure 7.13 and 7.14 indicate very good agreement between the data derived, and computed smooth wall heat transfer coefficients.

Table 7.2 lists the heat transfer augmentation factors (heat transfer data/computed smooth wall heat transfer) at the transition-front location and at  $40^\circ$  off the stagnation point. The details of the heat transfer coefficients ratios are given in Figures 7.11 to 7.32. It can be seen in the table that a maximum of 1.4 was observed for the rough wall augmentation

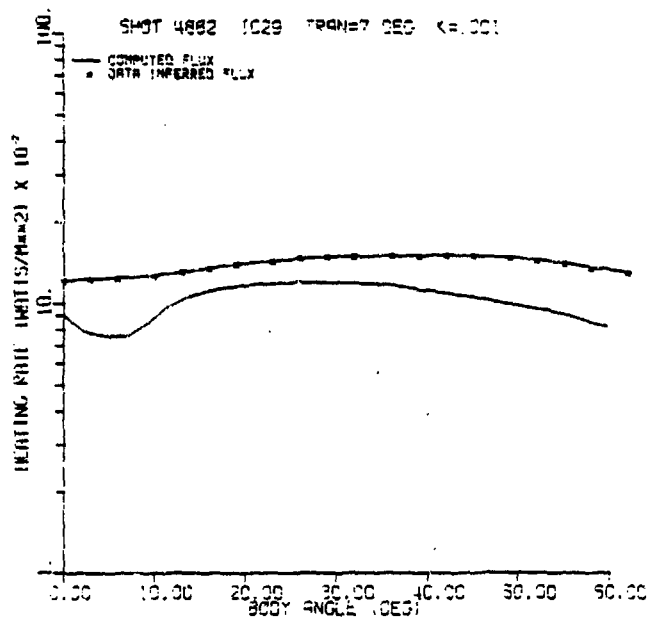
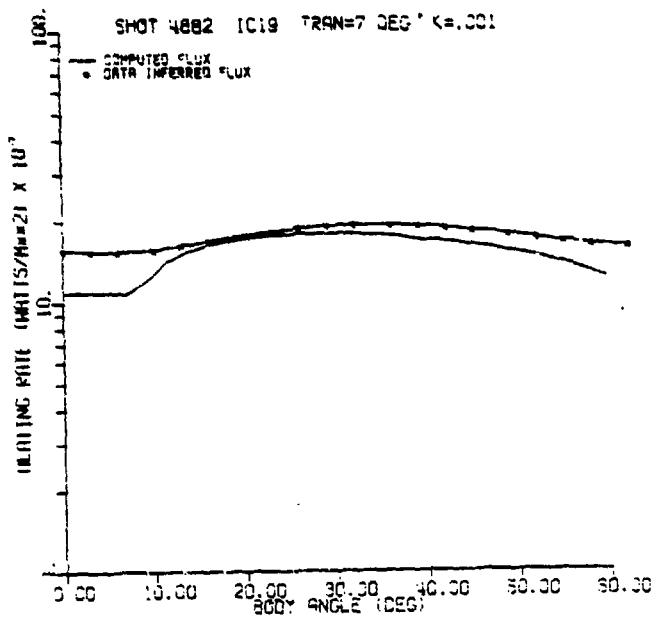


FIGURE 7.11. DATA-INFERRED, AND PREDICTED SMOOTH WALL HEAT TRANSFER DISTRIBUTION AROUND NOSETIP FOR SHOT 4882 (DATA-INFERRED TRANSITION-FRONT LOCATION)

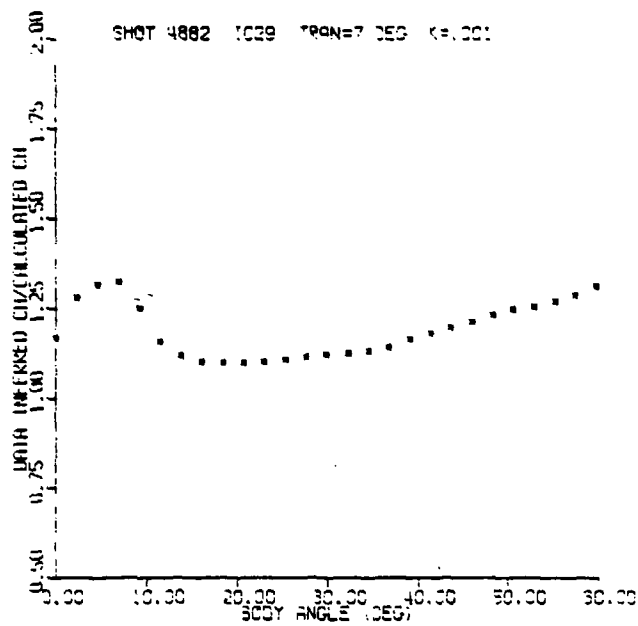
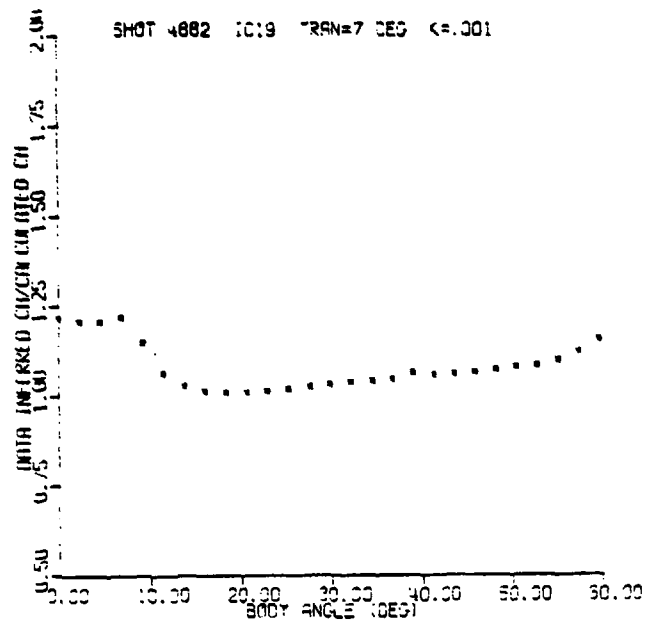


FIGURE 7.12. RATIO OF DATA-INFERRED, TO PREDICTED SMOOTH WALL HEAT TRANSFER COEFFICIENTS AROUND NOSETIP FOR SHOT 4882 (DATA-INFERRED TRANSITION-FRONT LOCATION)

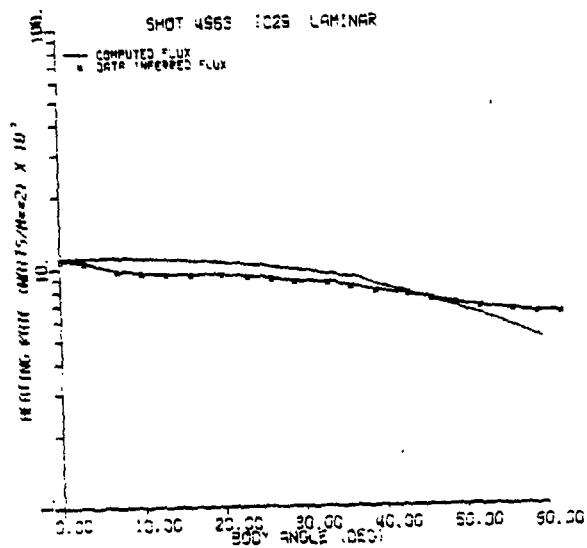
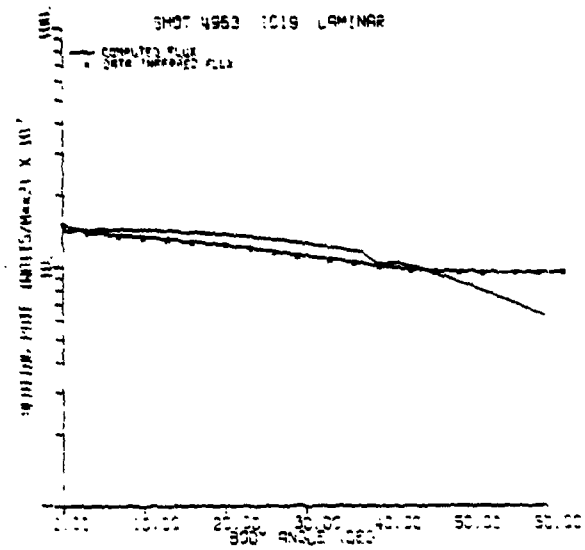
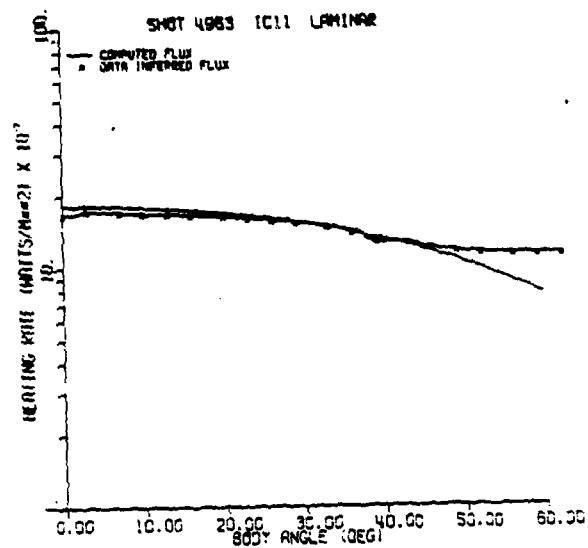


FIGURE 7.13. DATA-INFERRED, AND PREDICTED SMOOTH WALL HEAT TRANSFER DISTRIBUTION AROUND NOSETIP FOR SHOT 4963 (DATA-INFERRED TRANSITION-FRONT LOCATION)

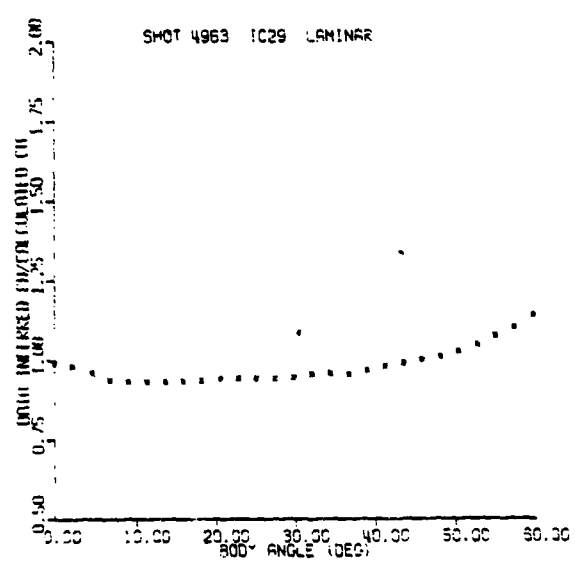
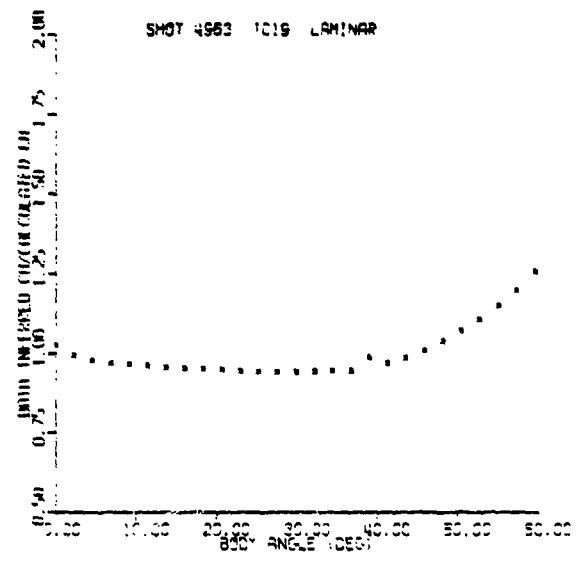
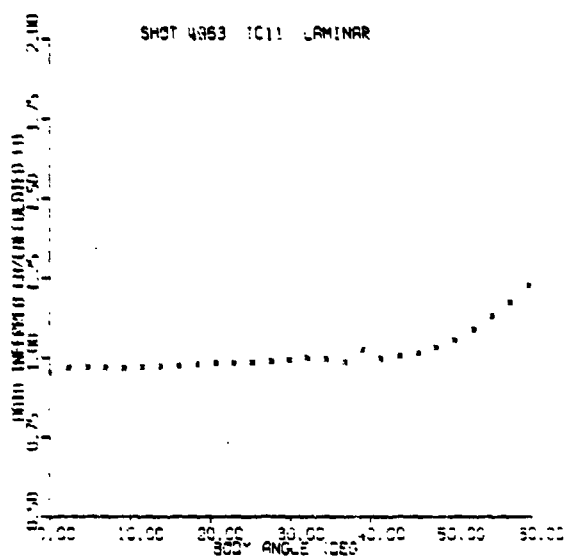


FIGURE 7.14. RATIO OF DATA-INFERRED, TO PREDICTED SMOOTH WALL HEAT TRANSFER COEFFICIENTS AROUND NOSETIP FOR SHOT 4963 (DATA-INFERRED TRANSITION-FRONT LOCATION)

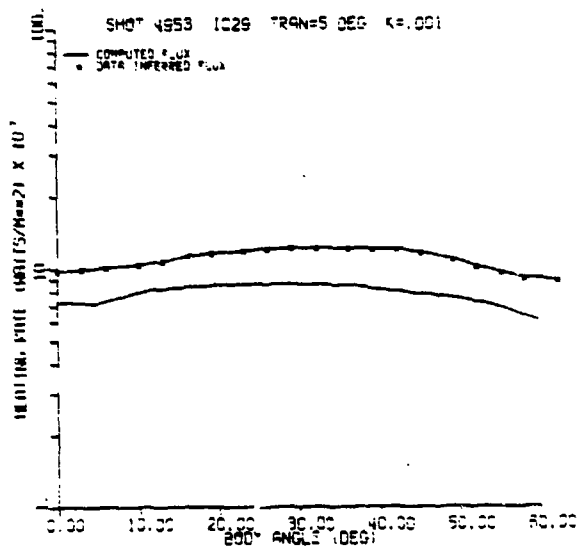
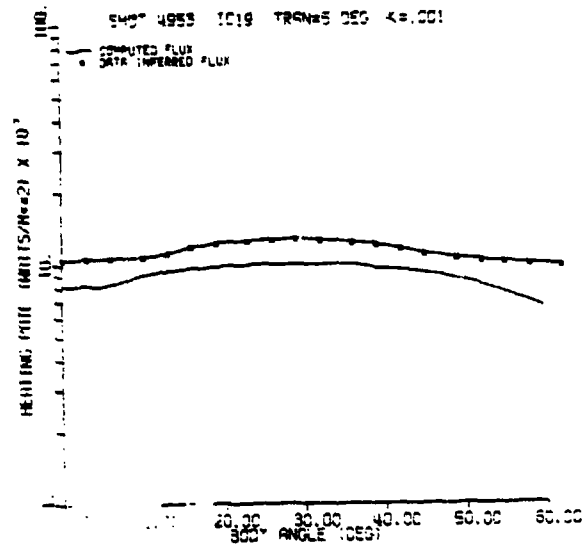
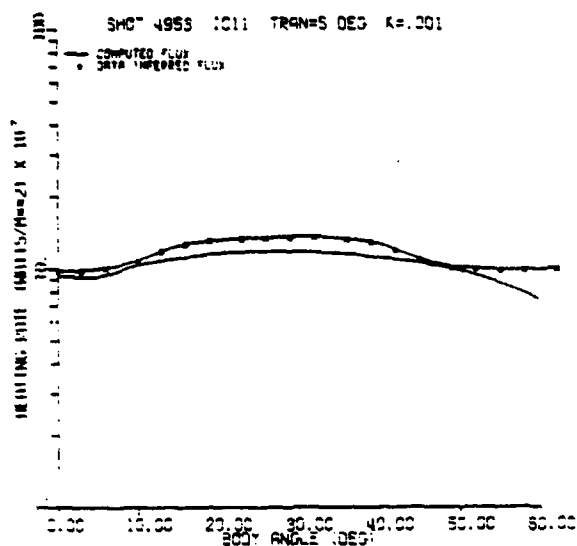


FIGURE 7.15. DATA-INFERRED, AND PREDICTED SMOOTH WALL HEAT TRANSFER DISTRIBUTION AROUND NOSETIP FOR SHOT 4953 (DATA-INFERRED TRANSITION-FRONT LOCATION)

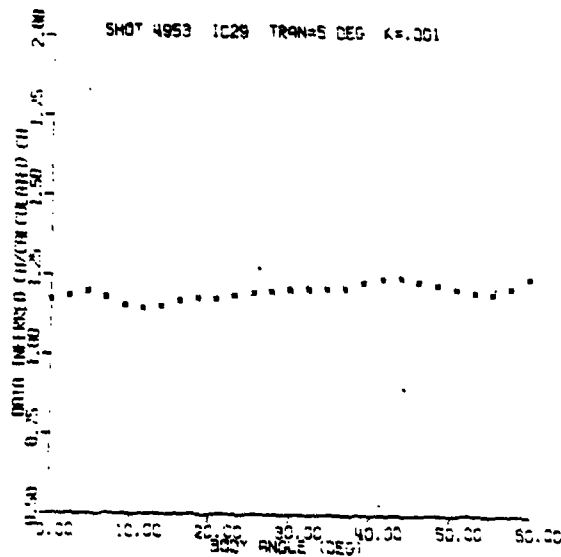
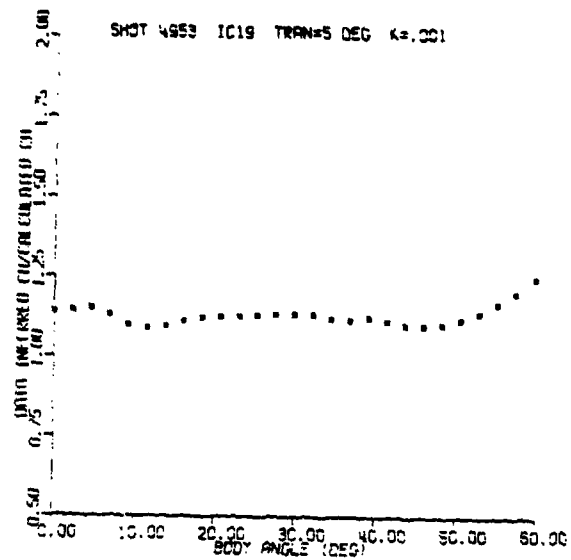
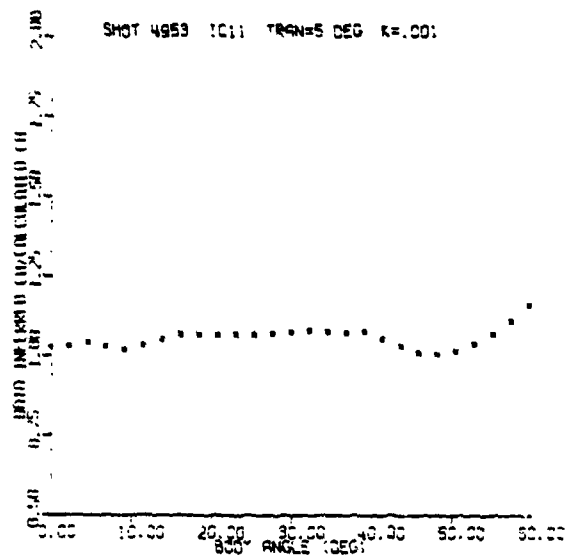


FIGURE 7.16. RATIO OF DATA-INFERRED, TO PREDICTED SMOOTH WALL HEAT TRANSFER COEFFICIENTS AROUND NOSETIP FOR SHOT 4953 (DATA-INFERRED TRANSITION-FRONT LOCATION)

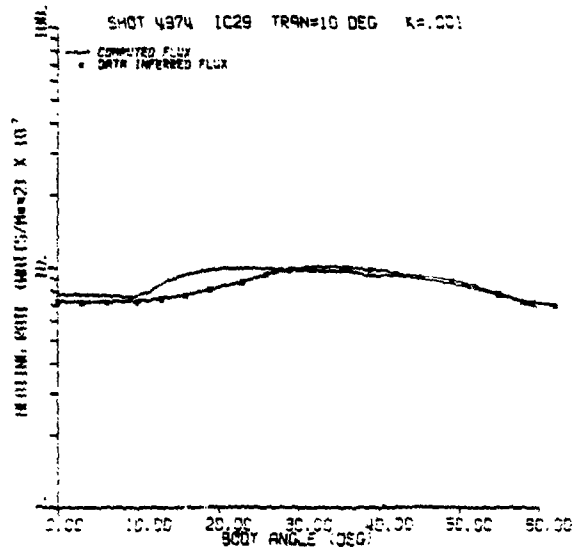
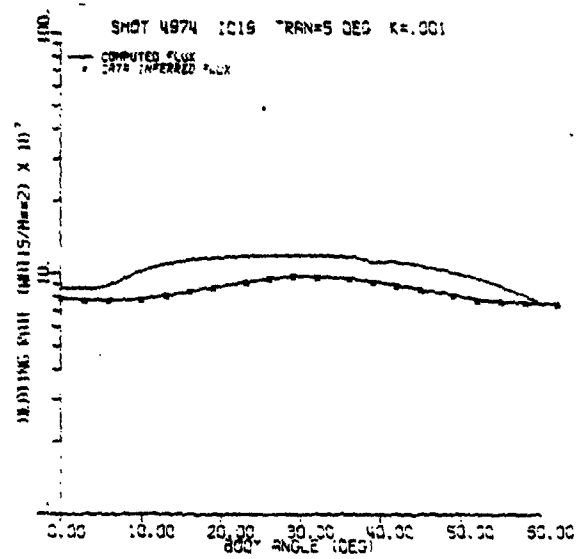
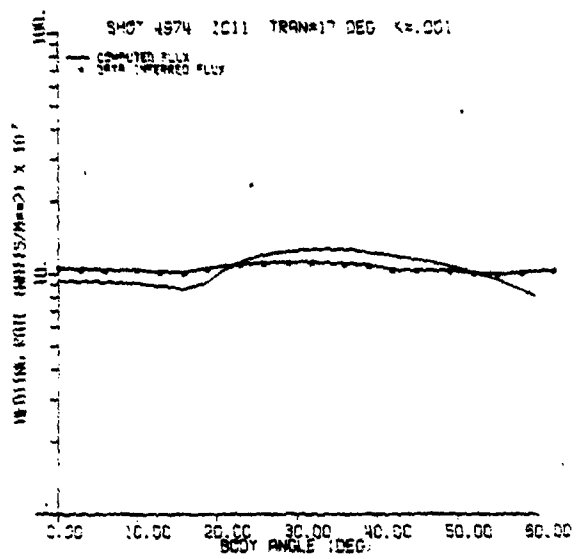


FIGURE 7.17. DATA-INFERRED, AND PREDICTED SMOOTH WALL HEAT TRANSFER DISTRIBUTION AROUND NOSETIP FOR SHOT 4974 (DATA-INFERRED TRANSITION-FRONT LOCATION)

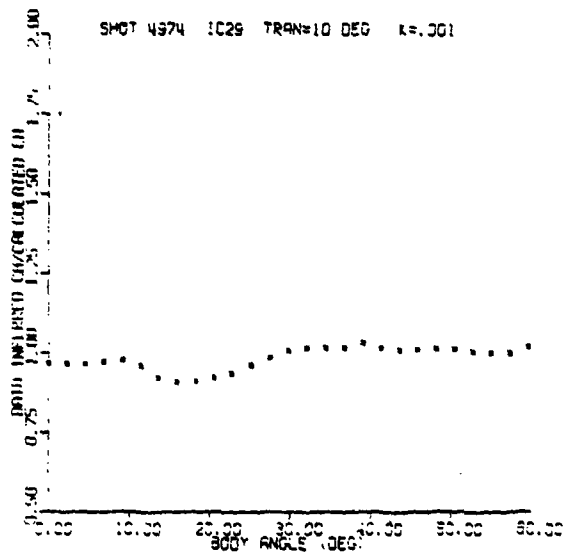
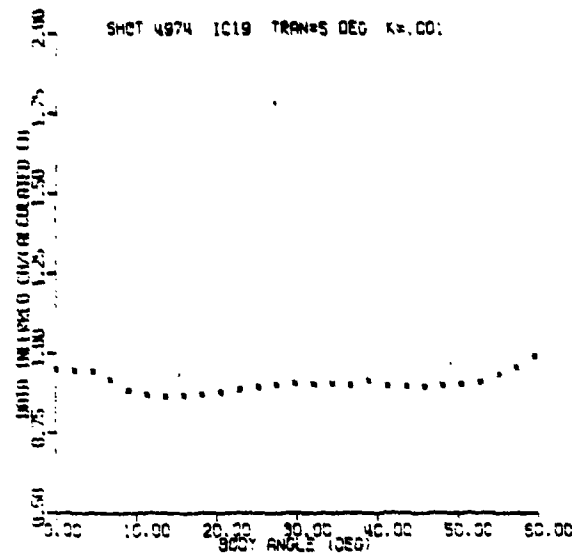
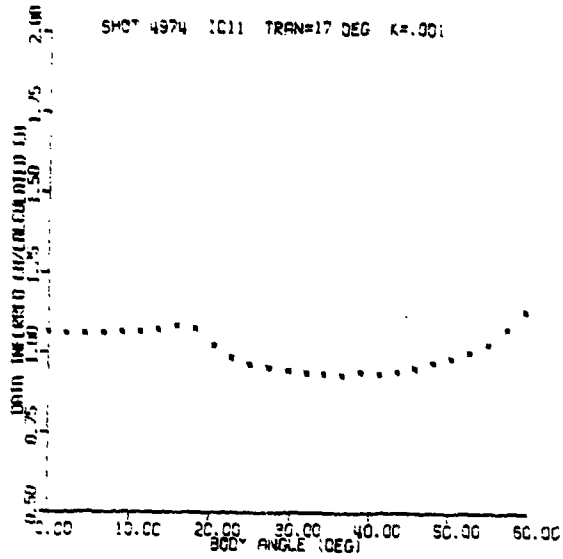


FIGURE 7.18. RATIO OF DATA-INFERRED, TO PREDICTED SMOOTH WALL HEAT TRANSFER COEFFICIENTS AROUND NOSETIP FOR SHOT 4974 (DATA-INFERRED TRANSITION-FRONT LOCATION)

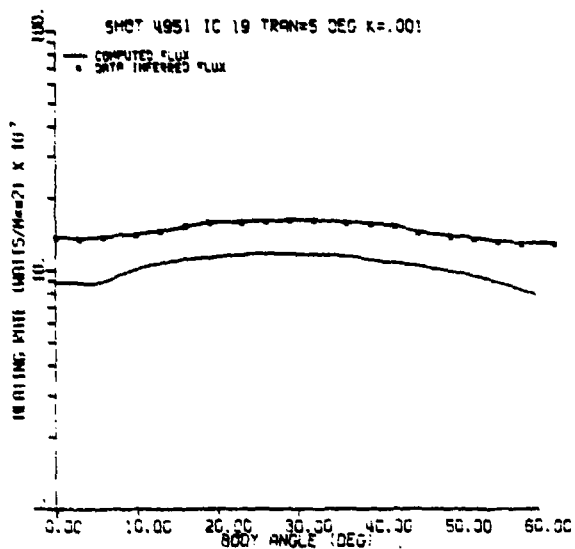
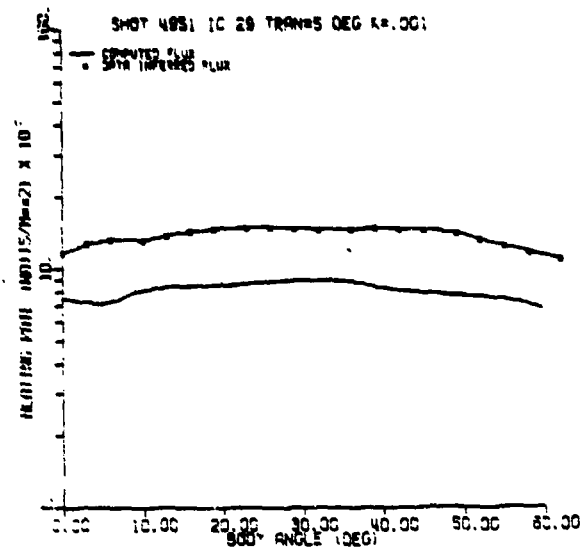
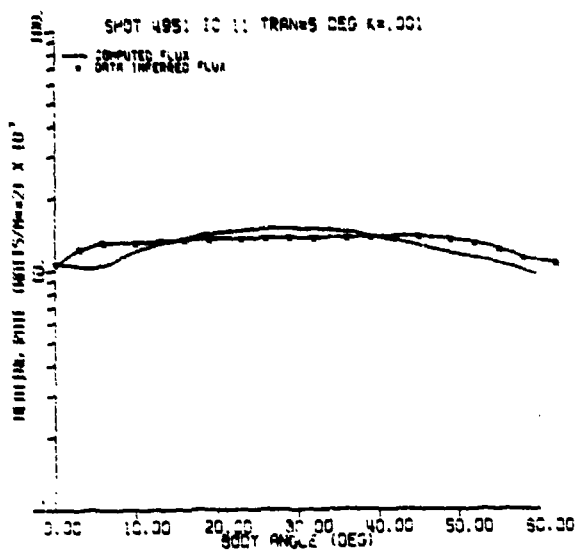


FIGURE 7.19. DATA-INFERRED, AND PREDICTED SMOOTH WALL HEAT TRANSFER DISTRIBUTION AROUND NOSETIP FOR SHOT 4951 (DATA-INFERRED TRANSITION-FRONT LOCATION)

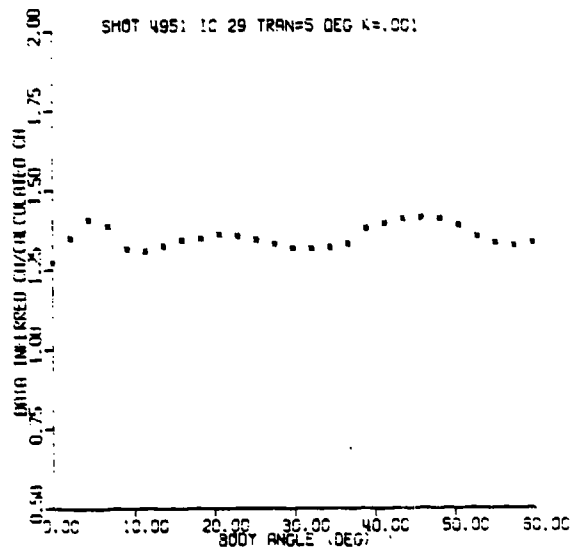
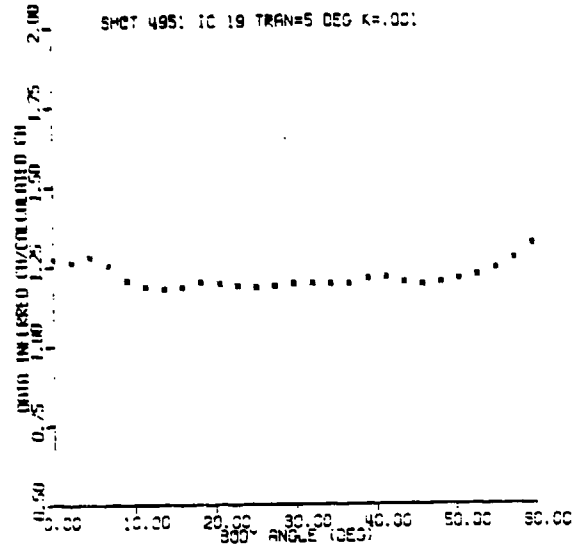
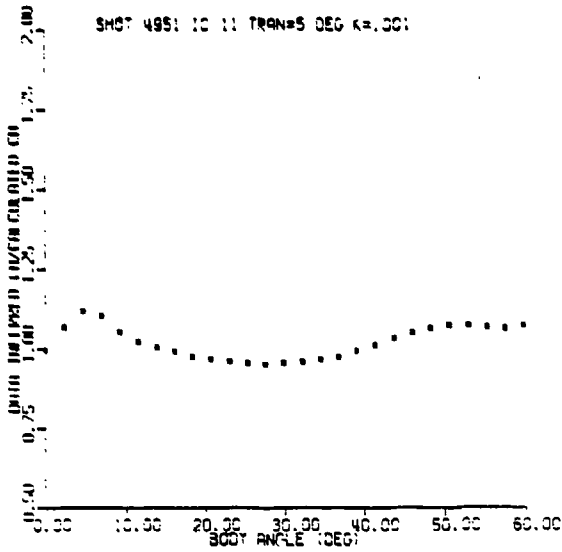


FIGURE 7.20. RATIO OF DATA-INFERRED, TO PREDICTED SMOOTH WALL HEAT TRANSFER COEFFICIENTS AROUND NOSETIP FOR SHOT 4951 (DATA-INFERRED TRANSITION-FRONT LOCATION)

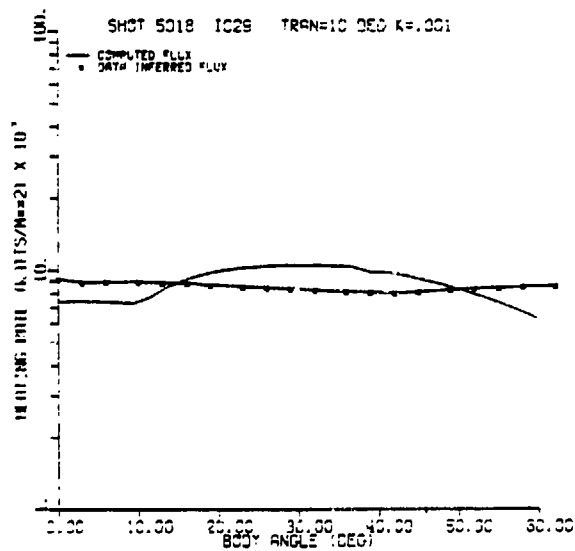
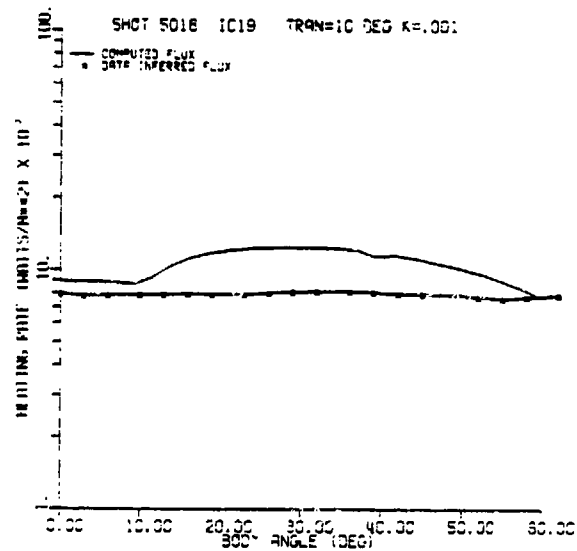
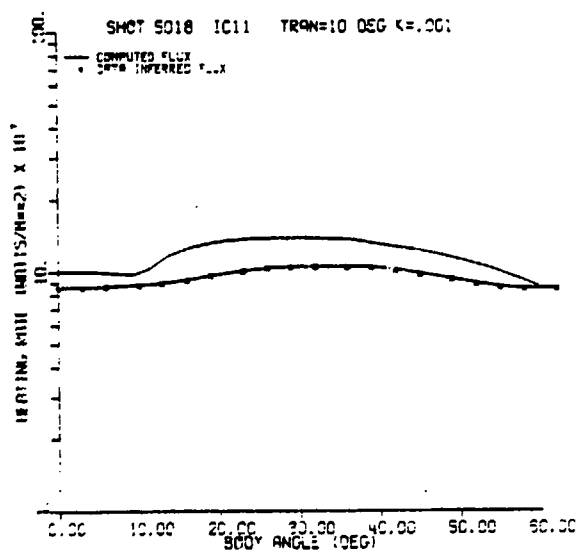


FIGURE 7.21. DATA-INFERRED, AND PREDICTED SMOOTH WALL HEAT TRANSFER DISTRIBUTION AROUND NOSETIP FOR SHOT 5018 (DATA-INFERRED TRANSITION-FRONT LOCATION)

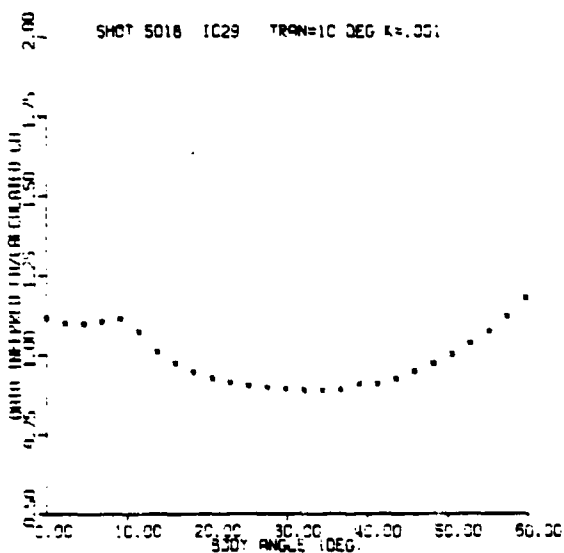
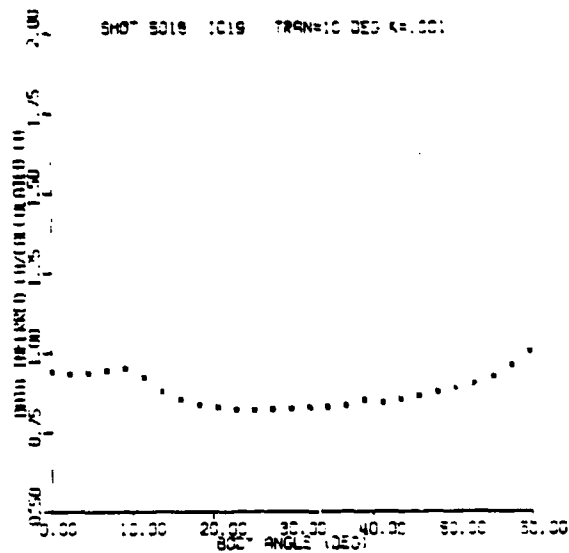
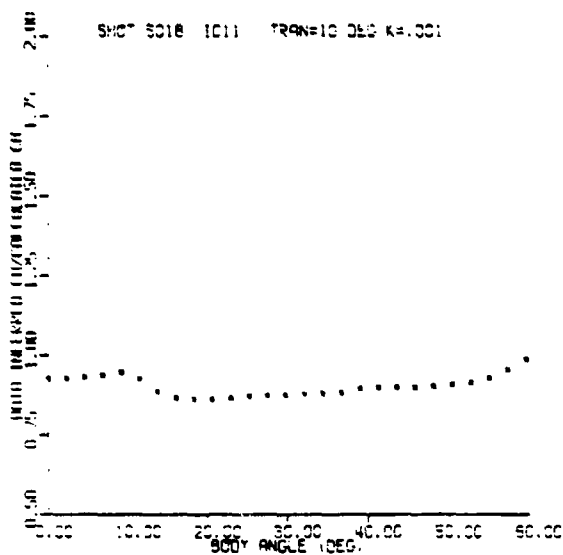


FIGURE 7.22. RATIO OF DATA-INFERRED, TO PREDICTED SMOOTH WALL HEAT TRANSFER COEFFICIENTS AROUND NOSETIP FOR SHOT 5018 (DATA-INFERRED TRANSITION-FRONT LOCATION)

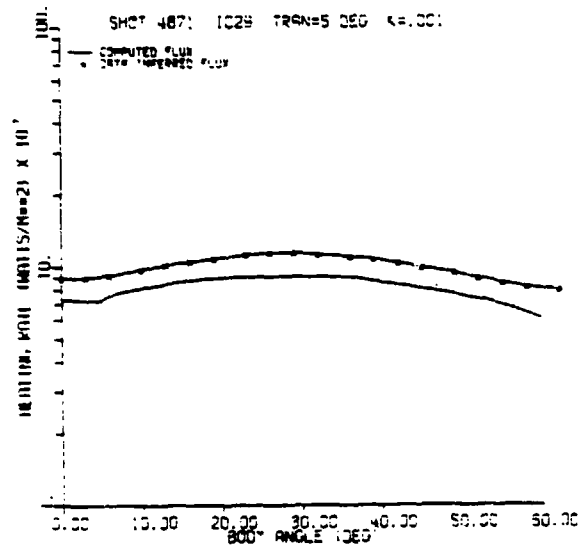
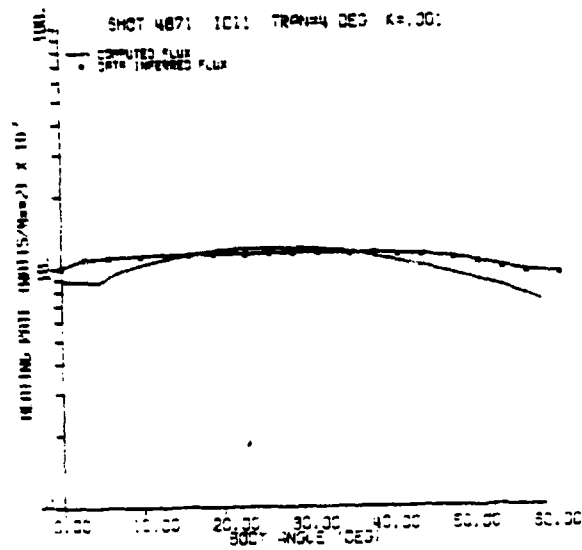


FIGURE 7.23. DATA-INFERRED, AND PREDICTED SMOOTH WALL HEAT TRANSFER DISTRIBUTION AROUND NOSETIP FOR SHOT 4871 (DATA-INFERRED TRANSITION-FRONT LOCATION)

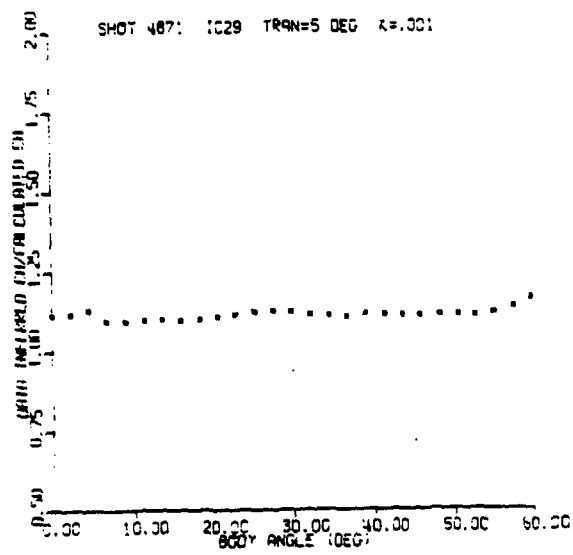
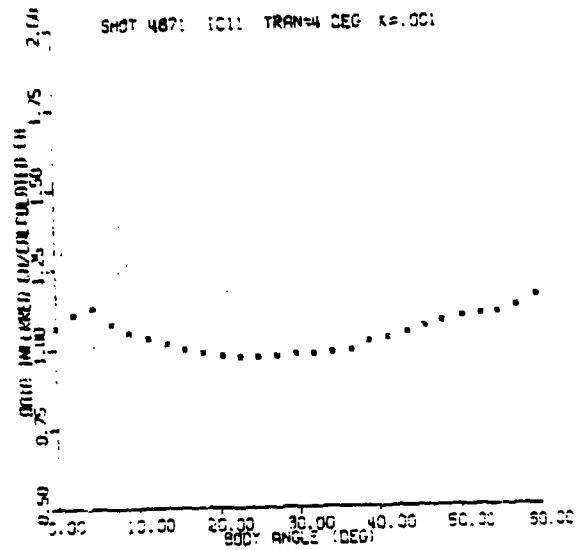


FIGURE 7.24: RATIO OF DATA-INFERRED, TO PREDICTED SMOOTH WALL HEAT TRANSFER COEFFICIENTS AROUND NOSETIP FOR SHOT 487/1 (DATA-INFERRED TRANSITION-FRONT LOCATION)

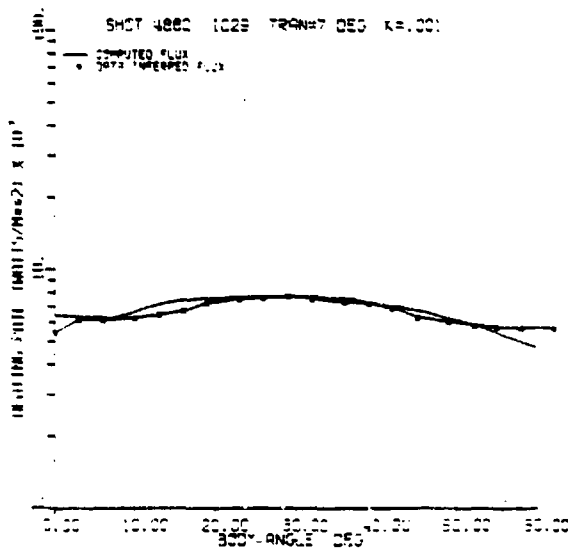
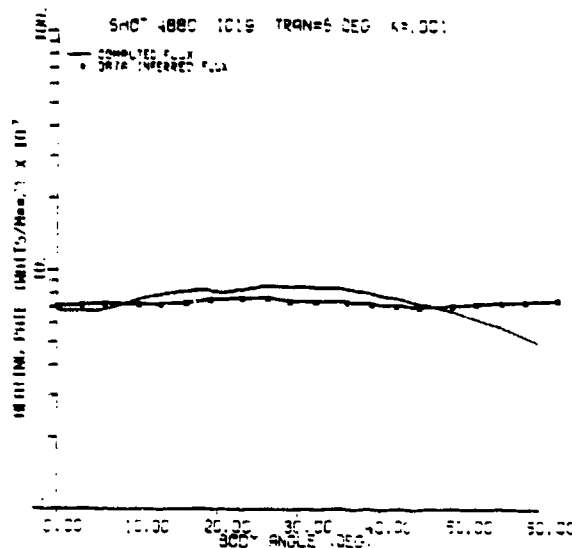
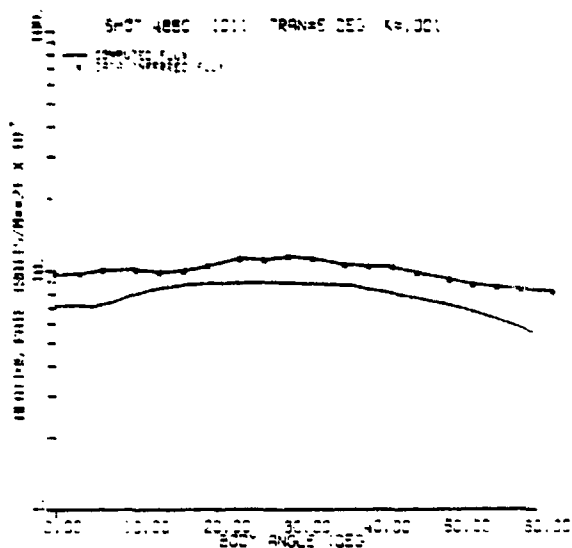


FIGURE 7.25. DATA-INFERRED, AND PREDICTED SMOOTH WALL HEAT TRANSFER DISTRIBUTION AROUND NOSETIP FOR SHOT 4880 (DATA-INFERRED TRANSITION-FRONT LOCATION)

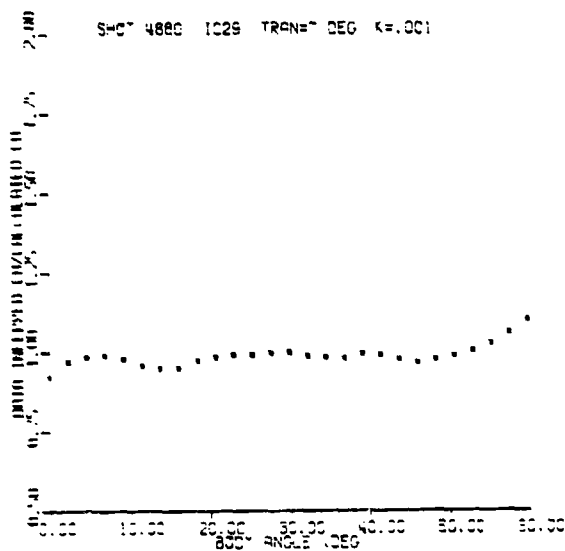
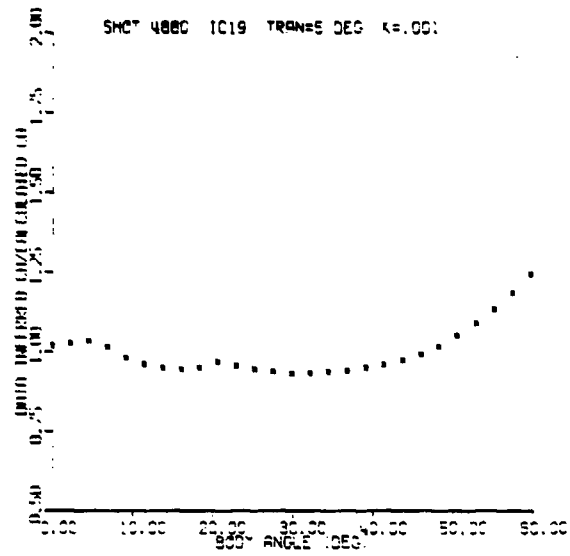
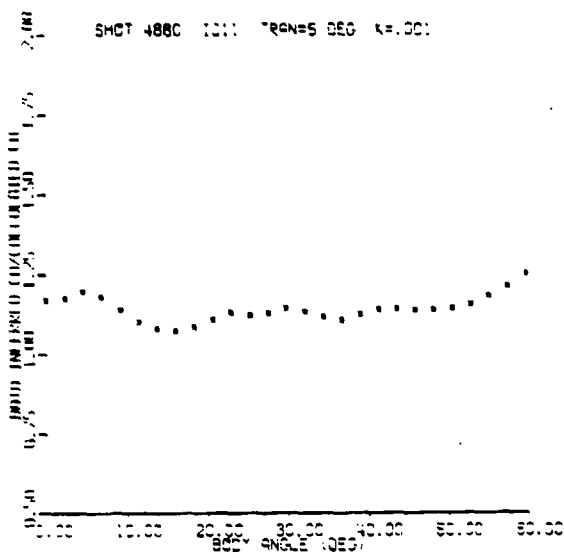


FIGURE 7 26. RATIO OF DATA-INFERRED, TO PREDICTED SMOOTH WALL HEAT TRANSFER COEFFICIENTS AROUND NOSETIP FOR SHOT 4880 (DATA-INFERRED TRANSITION-FRONT LOCATION)

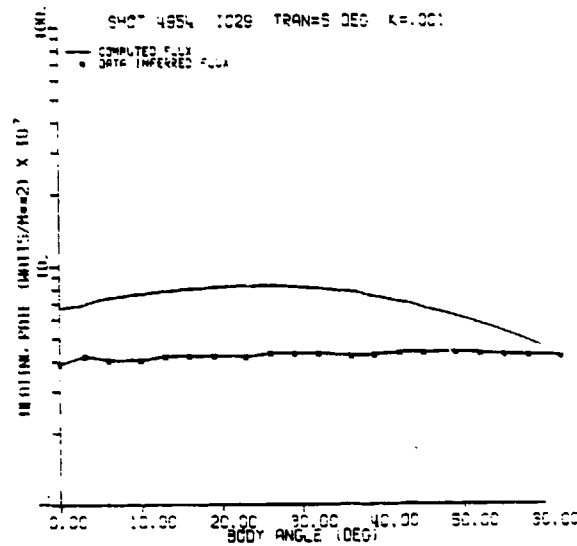
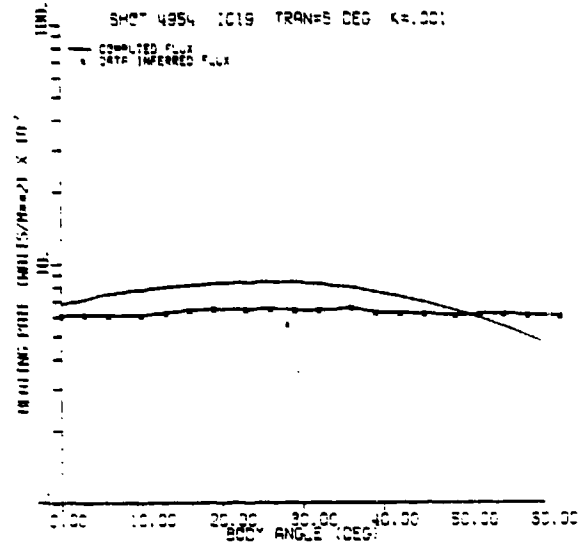
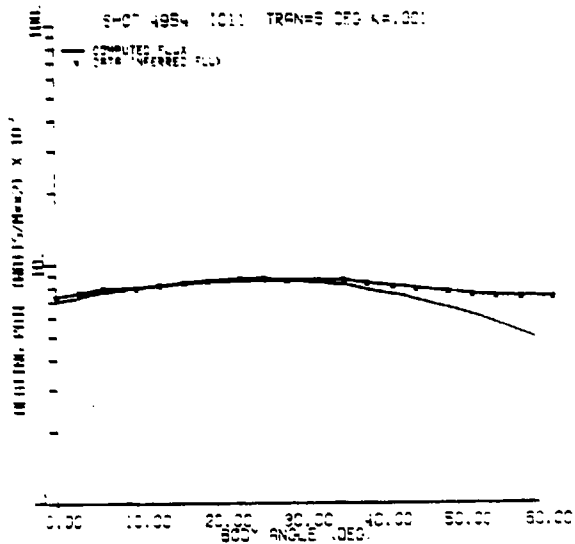


FIGURE 7 27. DATA-INFERRED, AND PREDICTED SMOOTH WALL HEAT TRANSFER DISTRIBUTION AROUND NOSETIP FOR SHOT 4954 (DATA-INFERRED TRANSITION-FRONT LOCATION)

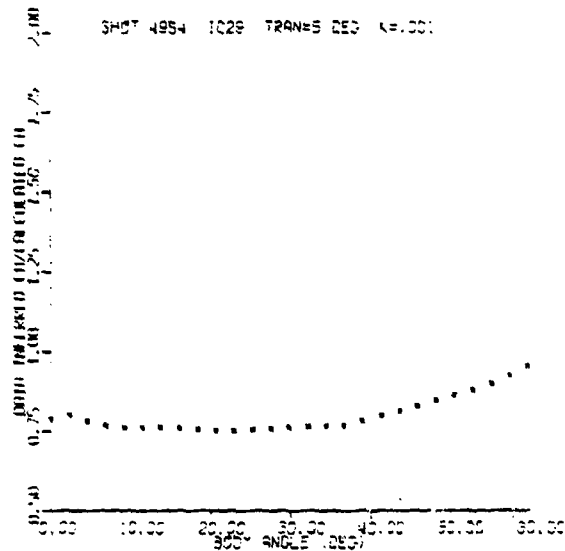
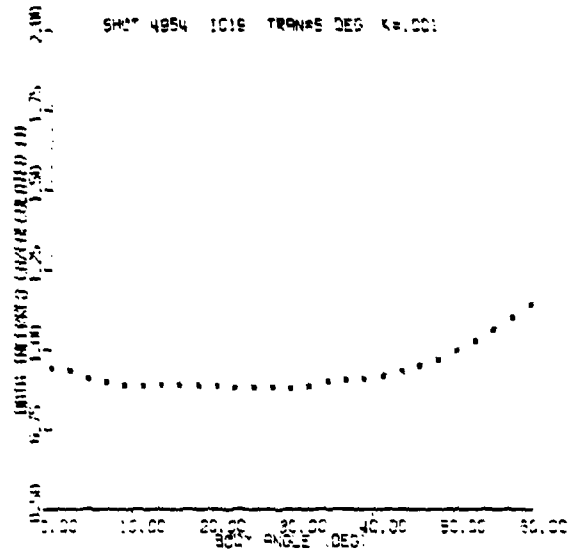
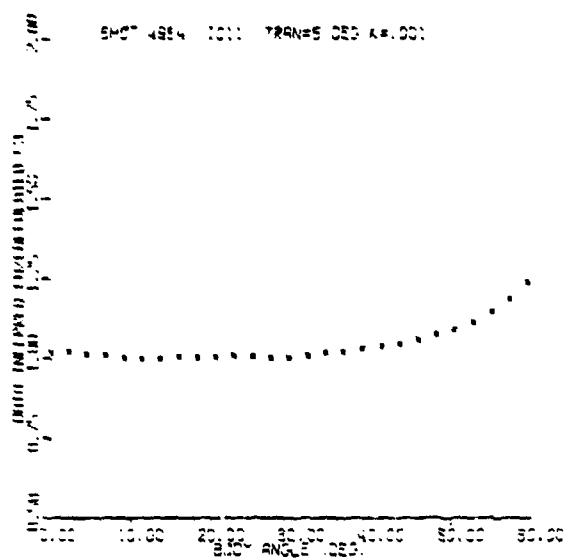


FIGURE 7.28. RATIO OF DATA-INFERRED, TO PREDICTED SMOOTH WALL HEAT TRANSFER COEFFICIENTS AROUND NOSETIP FOR SHOT 4954 (DATA-INFERRED TRANSITION-FRONT LOCATION)

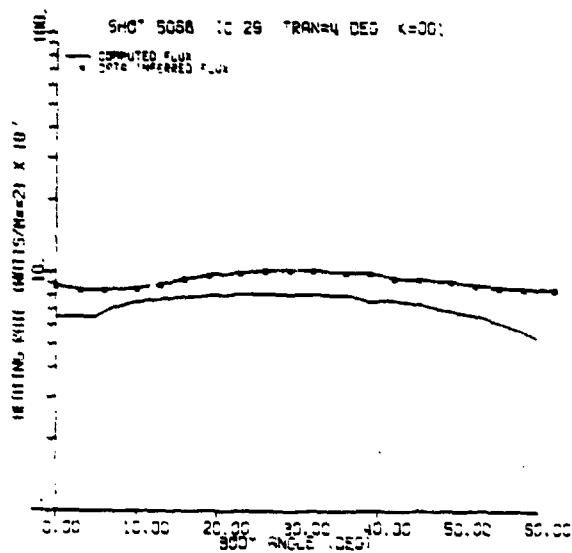
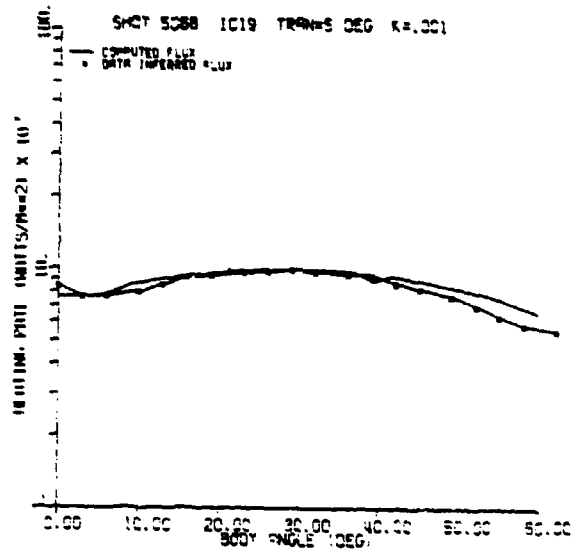
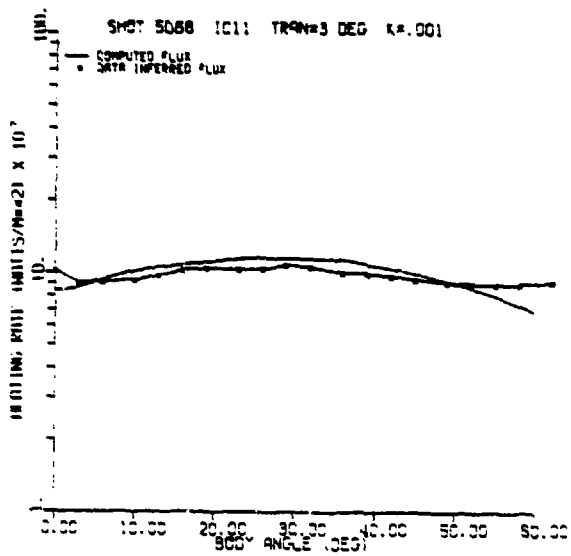


FIGURE 7.29. DATA-INFERRED, AND PREDICTED SMOOTH WALL HEAT TRANSFER DISTRIBUTION AROUND NOSETIP FOR SHOT 5068 (DATA-INFERRED TRANSITION-FRONT LOCATION)

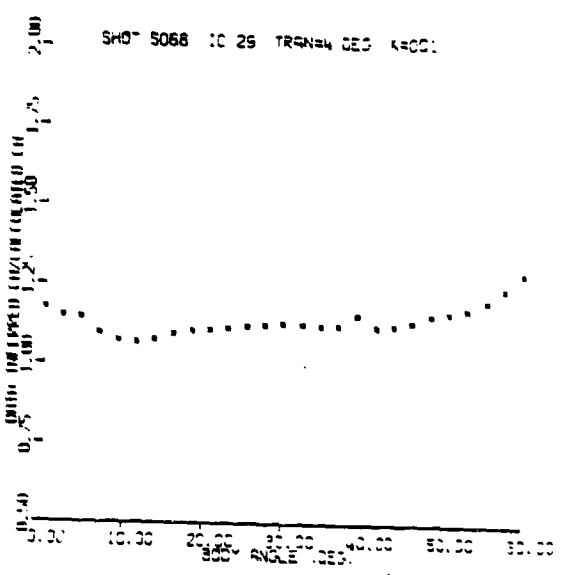
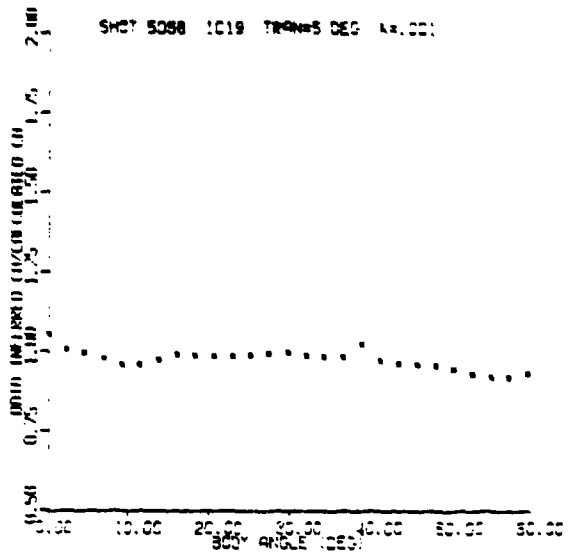
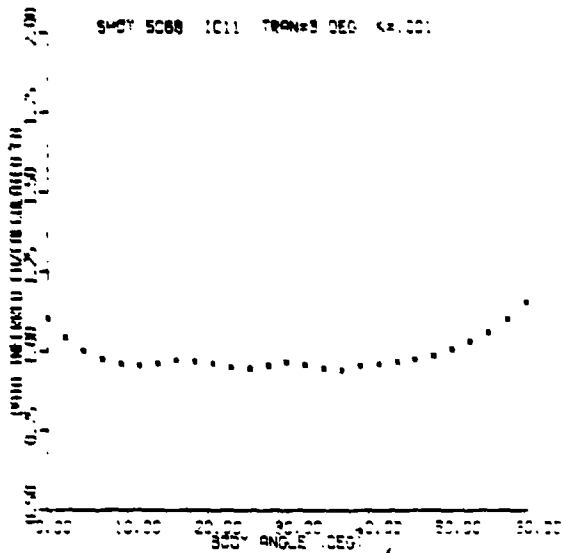


FIGURE 7.30. RATIO OF DATA-INFERRED, TO PREDICTED SMOOTH WALL HEAT TRANSFER COEFFICIENTS AROUND NOSETIP FOR SHOT 5068 (DATA-INFERRED TRANSITION-FRONT LOCATION)

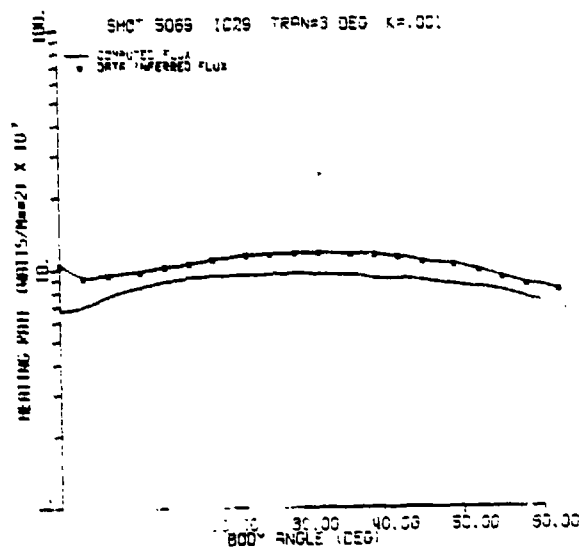
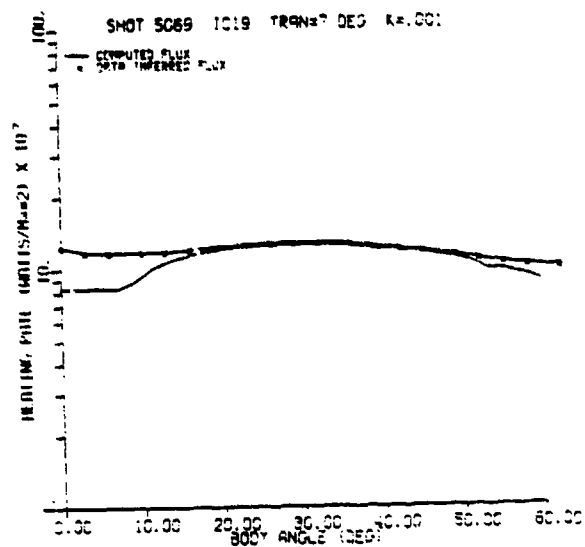
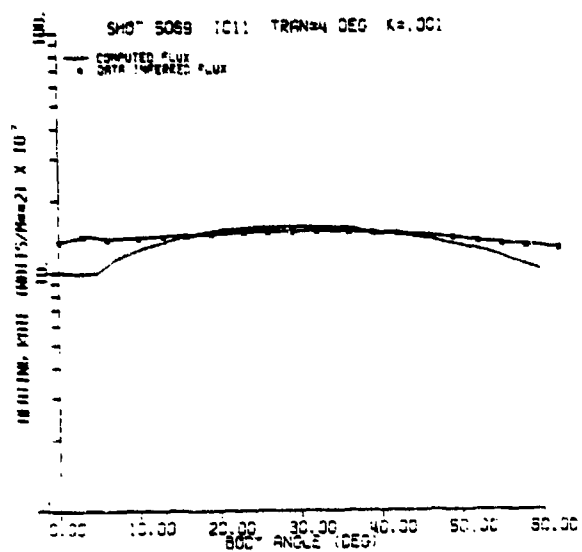


FIGURE 7.31. DATA-INFERRED, AND PREDICTED SMOOTH WALL HEAT TRANSFER DISTRIBUTION AROUND NOSETIP FOR SHOT 5069 (DATA-INFERRED TRANSITION-FRONT LOCATION)

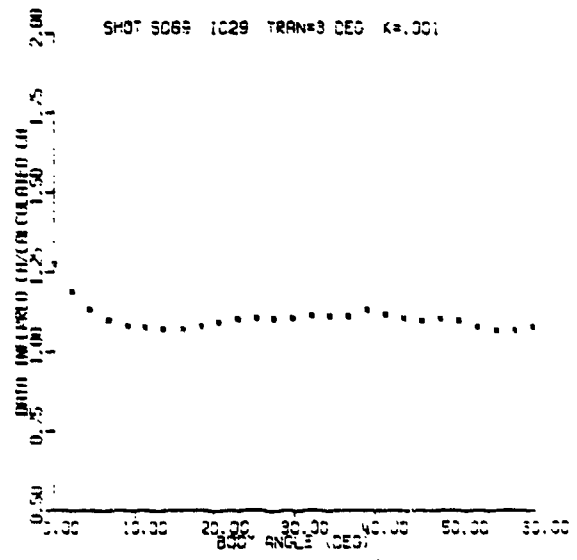
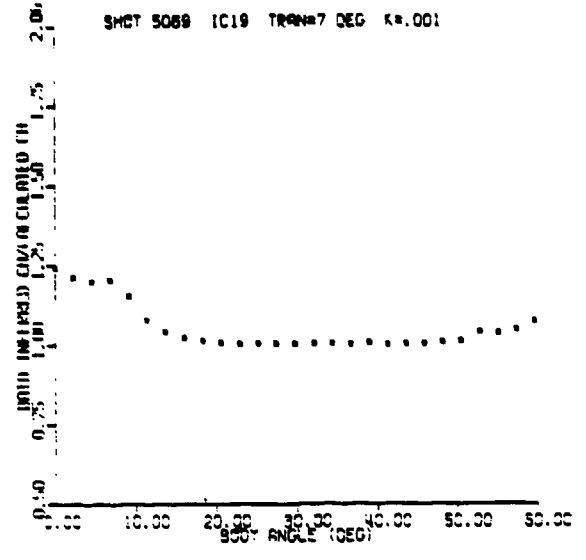
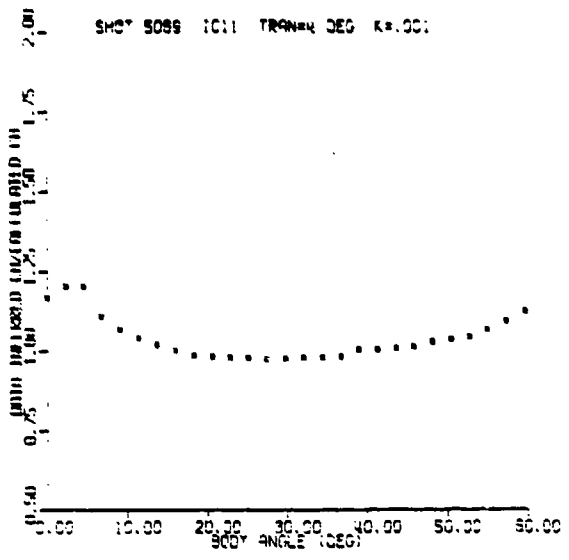


FIGURE 7.32. RATIO OF DATA-INFERRED, TO PREDICTED SMOOTH WALL HEAT TRANSFER COEFFICIENTS AROUND NOSETIP FOR SHOT 5069 (DATA-INFERRED TRANSITION-FRONT LOCATION)

TABLE 7.2. HEAT TRANSFER AUGMENTATION FACTORS

Shot #	Material	ICC	Heat Transfer Augmentation Factor	
			$(Q_{data}/Q_{C-S})^*$ transition	$(Q_{data}/Q_{C-S})_{40}$
4882	W	19	1.23	1.05
		29	1.32	1.16
4963	W	11	Laminar	Laminar
		19	Laminar	Laminar
		29	Laminar	Laminar
4953	ATJ-S	11	1.06	1.07
		19	1.16	1.12
		29	1.20	1.20
4974	ATJ-S	11	1.10	.93
		19	.95	.9
		29	.98	1.0
4951	994-2	11	1.11	1.0
		19	1.28	1.2
		29	1.42	1.4
5018	994-2	11	.96	.9
		19	.96	.85
		29	1.10	.9
4871	CC-223	11	1.13	1.03
		19	1.13	1.11
4880	CC-223	11	1.20	1.14
		19	1.04	.95
		29	.99	.98
4954	CC-223	11	1.03	1.04
		19	.94	.91
		29	.81	.8
5068	CC-223	11	1.10	.95
		19	1.05	.98
		29	1.17	1.1
5069	CC-223	11	1.20	1.0
		19	1.25	1.0
		29	1.28	1.1

\* $Q_{data}$  = data inferred heat transfer

$Q_{C-S}$  = computed smooth wall heat transfer

factors (or ratios), but most of the data indicated small heat transfer augmentation ratios ( $\leq 1.20$ ). This was expected since for the surface roughness and flight conditions tested, the roughness Reynolds number,  $k^+$ , were mainly in the transitionally rough regime ( $k^+ < 70$ ), as indicated by Table 7.3. The calculations indicated that not only were  $k^+$  values small, but that the flow was mainly transitional i.e., the boundary layer was not fully turbulent. (The definition of the roughness regime here is not exact, since it is only applied to fully turbulent flows and the flow here was transitional.)

#### 7.2.2 Comparisons with the ASCC Turbulent Heating Augmentation Methodology

In this section a comparison is made between the data inferred heat distribution around the nosetip, and the rough wall computed values using the rough wall augmentation methodology of the ASC code. The purpose here was to verify extrapolating the ASCC analytical rough wall augmentation model to the ballistics range flight environment.

Figures 7.33 to 7.42 show the distributions of the heat transfer coefficient ratios around the nosetip. These are the ratios of data inferred to the ASCC computed *rough wall* heat transfer. A value of unity to the heat transfer coefficient ratio represent an exact agreement between the data and theory. In computing the heat transfer coefficient around the nosetip at each ICC location the transition-front location was set equal to the data inferred value, and the surface temperature distribution was set equal to the measured data. It was found that, in general, the computed rough wall heat transfer coefficients were higher than the data-inferred values. The calculations were at the most 25% higher than the data.

TABLE 7.3. MAXIMUM ROUGHNESS REYNOLDS NUMBER  
ON THE NOSETIP (COMPUTED BY ASCC)

Shot #	$k_{\text{mean}}$	ICC	$k^+$
4882	.292	19	73
		29	57
4953	.55	11	71
		19	55
		29	44
4974	.55	11	97
		19	84
		29	63
4951	.57	11	90
		19	63
		29	48
5018	.57	11	116
		19	100
		29	80
4871	.25	11	30
		19	20
4880	.25	11	23
		19	22
		29	19
4954	.25	11	20
		19	20
		29	20
5068	.25	11	30
		19	27
		29	20
5069	.25	11	42
		19	34
		29	27

Note:  $k^+$  = Roughness Reynolds Number

Table 7.4 lists a detailed comparison between the data and ASCC predictions at two points on the nosetip. These are the transition and the 40° point. The details at all the points on the nosetip can be found in Figures 7.33 to 7.42. At the 40° point on the nosetip the following is listed.

1.  $Q_{\text{data}}/Q_{\text{ASCC}}$  fixed transition/rough wall: transition-front locations were set equal to the data inferred values, and the rough wall turbulent augmentation was included in the heat transfer calculations. This ratio indicates the degree of agreement between data and rough wall theory. It can be seen in the table that for most of the CC-223 shots the agreements are within 10%. For the graphite shots the agreements are within 20%. That is, for all the flight conditions tested, the roughness effects on enhancing the heat transfer were small, as expected for the calculated values of  $k_t$ .

2.  $Q_{\text{data}}/Q_{\text{ASCC}}$  fixed transition/smooth wall: again the locations of transition in the calculations were set equal to the data inferred values but  $Q_{\text{ASCC}}$  were smooth wall values. This ratio represents one of the following: (a) heat transfer augmentation values due to roughness, (b) degree of agreement between data and laminar theory if roughness effects are small. The heat transfer ratios indicated that roughness effects were small, and fairly good agreement between data and laminar theory was found.

3.  $Q_{\text{data}}/Q_{\text{ASCC}}$  PANT transition/rough wall:  $Q_{\text{ASCC}}$  was based on a transition location predicted by the PANT transition criteria. The heat transfer coefficient ratios become large as indicated in Table 7.4 when the theory predicts laminar flow or transition offset, while the data infer a transitional/turbulent flow. This was the case for the CC-223 Shots 4871, 4880, 4954 and 5068 (ICC's 29, 41). Figure 7.43 shows ratios of data derived to ASCC calculated rough wall heat transfer coefficients. The transition front location was predicted

TABLE 7.4. RATIO OF DATA DERIVED TO COMPUTED HEAT TRANSFER RATES

Shot #	Material	ICC	Heat Transfer Coefficients Ratio					Comments
			$(Q_{data}/Q_{ASCC})$ Transition		$(Q_{data}/Q_{ASCC})$ 40 Degrees			
			PANT* Transition	Fixed Transition	PANT Transition Rough Wall	Fixed Transition†		
			Smooth Wall	Rough Wall				
4882	W	19	1.15	1.23	1.0	1.05	.9	<ul style="list-style-type: none"> <li>ASCC (PANT) predicts transition between 8-10°.</li> <li>Data derived transition is 7°.</li> </ul>
		29	1.66	1.32	1.85	1.16	1.0	
4963	W	11	Laminar	Laminar	Laminar	Laminar	Laminar	<ul style="list-style-type: none"> <li>Laminar-good agreement between data and theory.</li> </ul>
		19	Laminar	Laminar	Laminar	Laminar	Laminar	
		29	Laminar	Laminar	Laminar	Laminar	Laminar	
4953	ATJ-S	11	1.17	1.06	.9	1.07	.92	<ul style="list-style-type: none"> <li>ASCC (PANT) predicts transition at approximately 10-19°.</li> <li>Data indicate transition at approximately 3-5°.</li> <li>Turbulent agreement between data and theory for ASCC with fixed transition fairly good.</li> </ul>
		19	1.35	1.16	.97	1.12	.97	
		29	1.45	1.20	.88	1.2	1.07	
4974	ATJ-S	11	1.1	1.10	1.0	.93	.8	<ul style="list-style-type: none"> <li>ASCC (PANT) predicts transition at approximately 12-19°.</li> <li>Data indicate transition 3-17°.</li> <li>Data and theory are in good agreement for smooth wall case (fixed transition). Rough wall calculations overpredicts data.</li> </ul>
		19	.9	.95	.9	.9	.8	
		29	1.0	.98	.8	1.0	.9	
4951	994-2	11	1.15	1.11	.9	1.0	.93	<ul style="list-style-type: none"> <li>ASCC (PANT) predicts transition between 10-15°.</li> <li>Data derived transition is 5°.</li> <li>Good data theory agreement at IC 11 (fixed transition) for smooth wall.</li> <li>Both smooth and rough wall under-predicted at IC 19 and IC 29.</li> </ul>
		19	1.36	1.28	1.05	1.2	1.2	
		29	1.5	1.42	1.2	1.4	1.4	
5018	994-2	11	.95	.96	.75	.9	.82	<ul style="list-style-type: none"> <li>ASCC (PANT) predicts transition between 10-13° as also the data.</li> <li>Both smooth and rough wall calculations (fixed transition) overpredicts data.</li> </ul>
		19	.96	.96	.75	.85	.8	
		29	1.1	1.10	.80	.9	.85	
4871	CC-223	11	Large*	1.13	Large	1.03	.95	<ul style="list-style-type: none"> <li>ASCC (PANT) predicts laminar flow through entire flight.</li> <li>Data indicates transition at approximately 4°.</li> <li>Good agreement between data and theory for ASCC with fixed transition (both smooth and rough wall).</li> </ul>
		29	Large	1.13	Large	1.11	1.08	
4880	CC-223	11	Large	1.20	Large	1.14	1.1	<ul style="list-style-type: none"> <li>ASCC (PANT) indicates laminar flow through entire flight.</li> <li>Data indicates turbulent flow.</li> <li>Good agreement between data and theory for fixed transition.</li> </ul>
		19	Large	1.04	Large	.95	.9	
		29	Large	.99	Large	.98	.97	
4954	CC-223	11	Large	1.03	Large	1.04	1.0	<ul style="list-style-type: none"> <li>ASCC (PANT) indicates laminar flow through the entire flight.</li> <li>Good agreement between data and fixed transition ASCC for IC 11. Theory over-predicts (smooth and rough) at IC 19-29.</li> </ul>
		19	Large	.94	Large	.91	.9	
		29	Large	.81	Large	.8	.77	
5068	CC-223	11	1.45	1.10	1.05	.95	.9	<ul style="list-style-type: none"> <li>ASCC (PANT) indicates transition at approximately 23-30°.</li> <li>Data indicate transition at approximately 3-5°.</li> <li>PANT transition criteria predicts transition offset at ICC 29.</li> <li>Good agreement between data and theory for ASCC with fixed transition and smooth wall.</li> </ul>
		19	1.47	1.05	1.1	.98	.9	
		29	Large	1.17	Large	1.1	1.07	
5069	CC-223	11	1.55	1.20	1.0	1.0	.9	<ul style="list-style-type: none"> <li>ASCC (PANT) predicts transition at approximately 17-23°.</li> <li>Data indicate transition at approximately 4°.</li> <li>Good turbulent agreement between data and theory for ASCC with fixed transition and smooth wall.</li> </ul>
		19	1.56	1.25	1.05	1.0	.91	
		29	1.9	1.28	1.5	1.1	1.05	

\*Transition- front location was predicted by PANT correlation

†Transition- front location was equal to the data-derived value

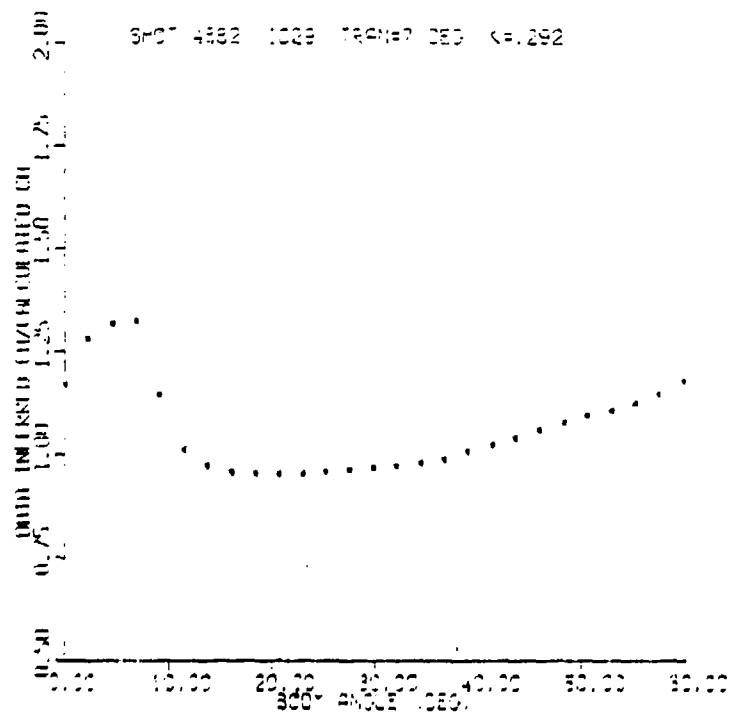
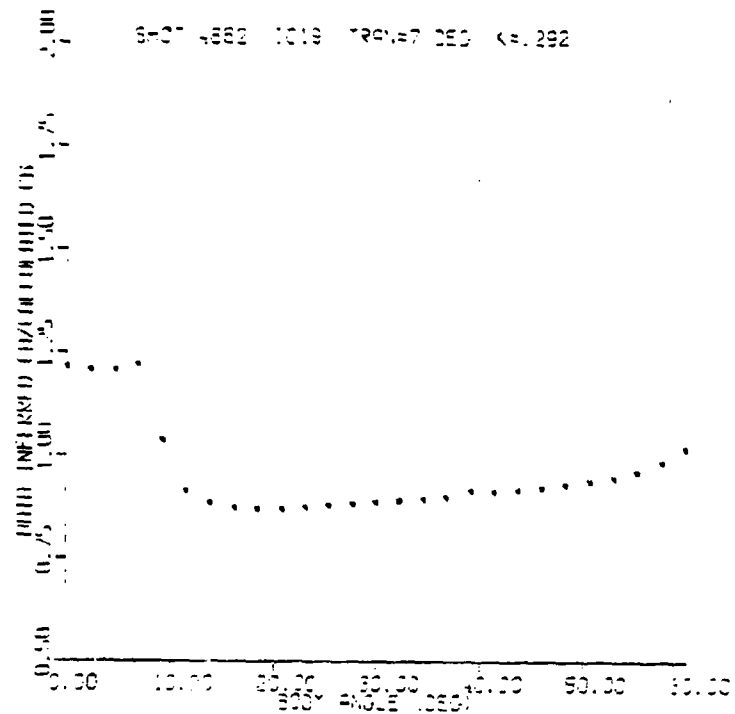


FIGURE 7.33. RATIO OF DATA-INFERRED, TO ASCC PREDICTED ROUGH WALL HEAT TRANSFER COEFFICIENTS AROUND NOSETIP FOR SHOT 4882 (FLUX-INFERRED TRANSITION-FRONT

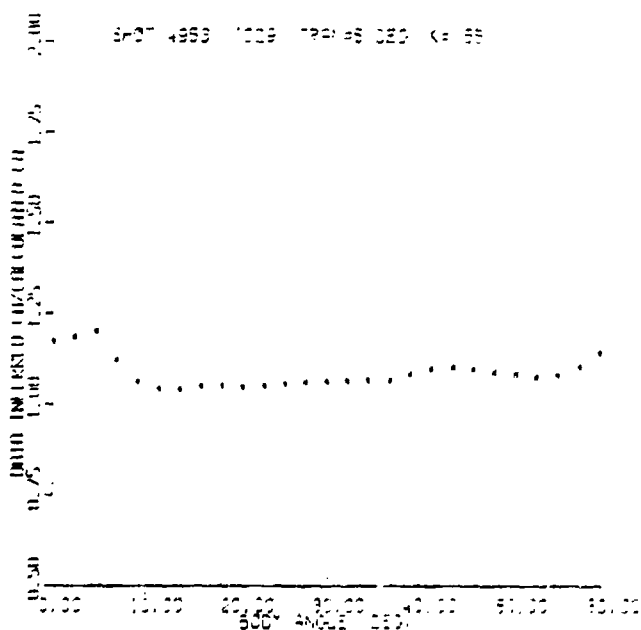
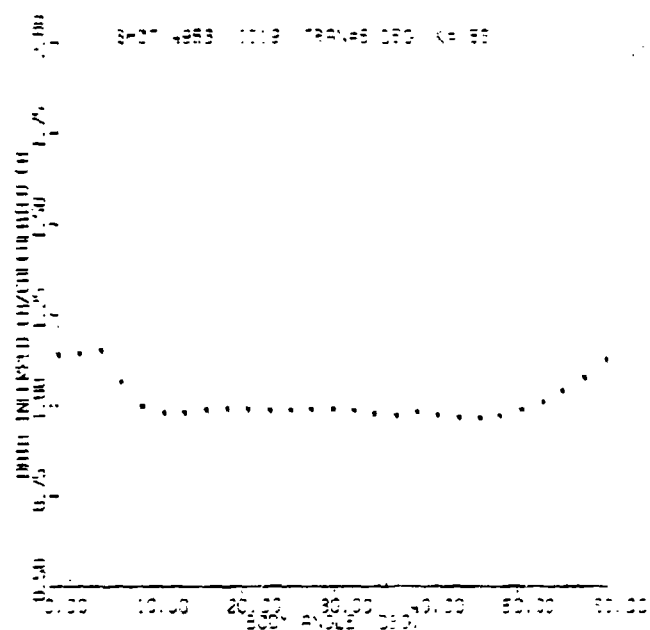
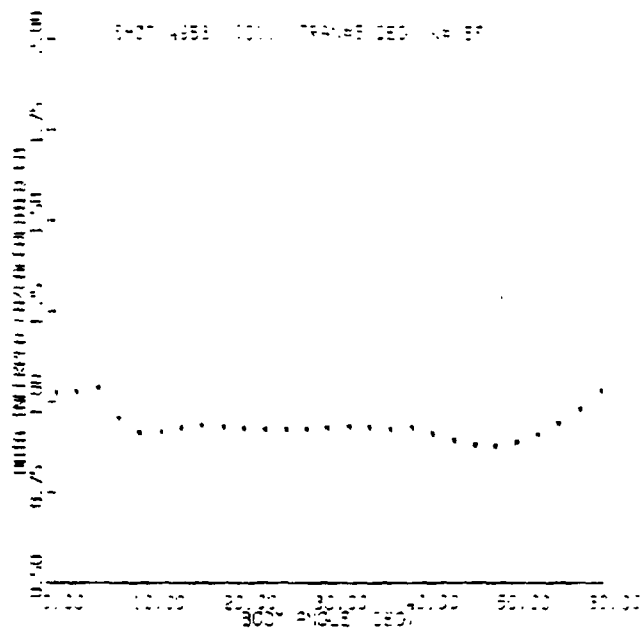


FIGURE 7.34. RATIO OF DATA-INFERRED, TO ASCC PREDICTED ROUGH WALL HEAT TRANSFER COEFFICIENTS AROUND NOSETIP FOR SHOT 4953 (FLUX-INFERRED TRANSITION-FRONT LOCATION)

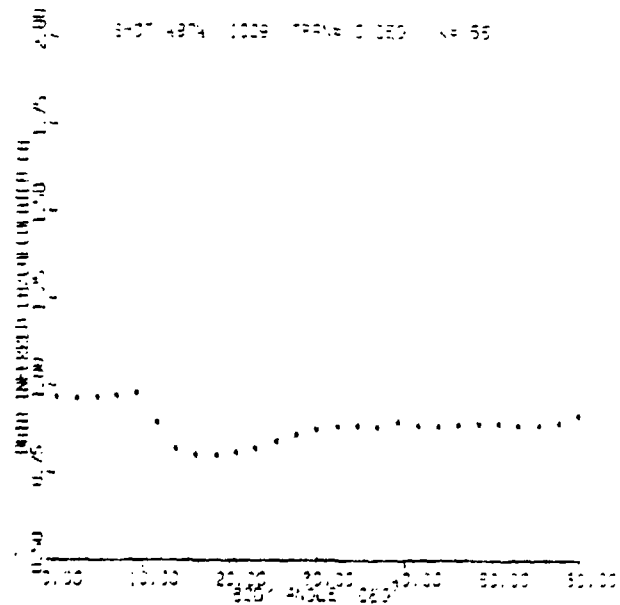
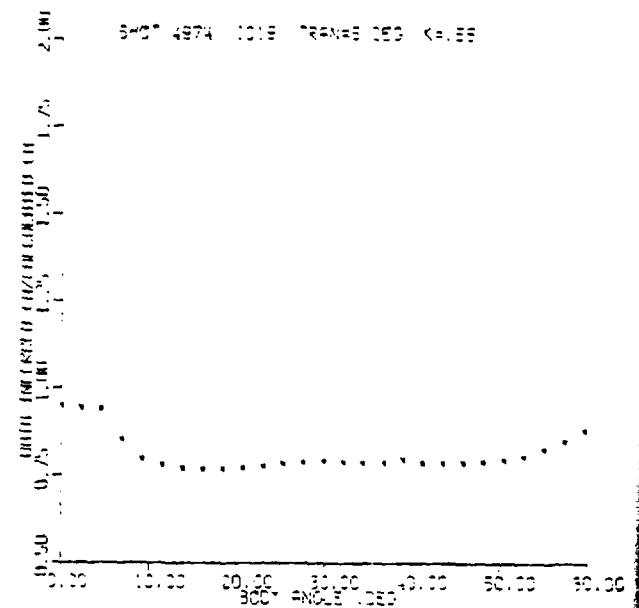
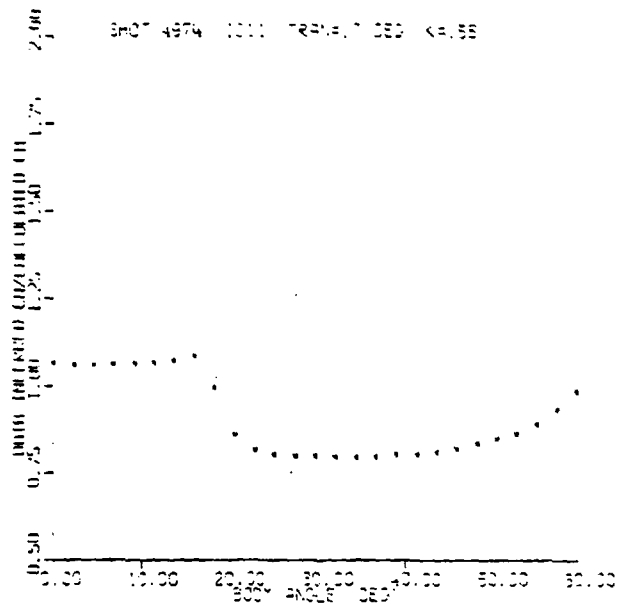


FIGURE 7.35. RATIO OF DATA-INFERRED, TO ASCC PREDICTED ROUGH WALL HEAT TRANSFER COEFFICIENTS AROUND NOSETIP FOR SHOT 4974 (FLUX-INFERRED TRANSITION-FRONT LOCATION)

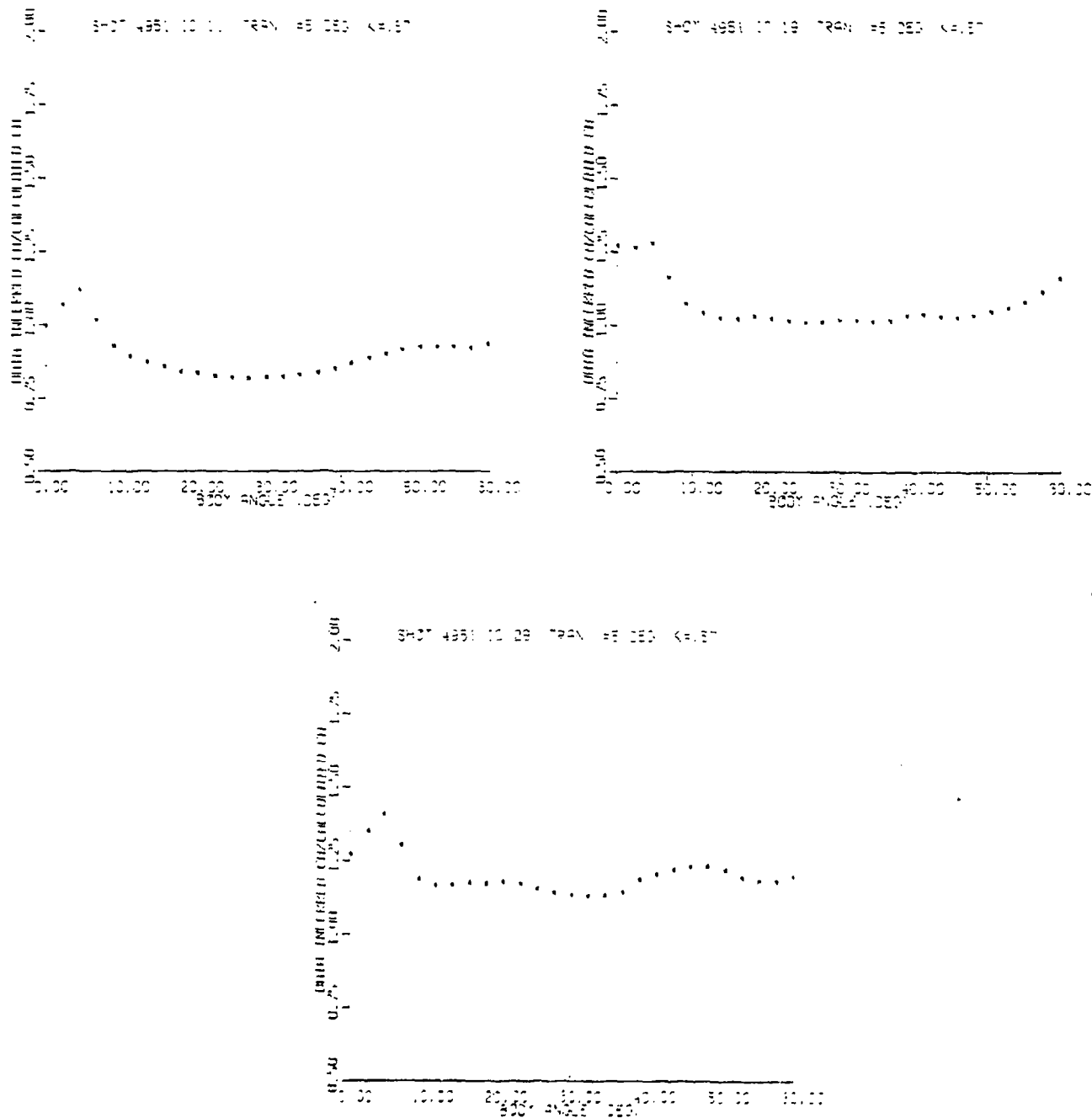


FIGURE 7.36. RATIO OF DATA-INFERRED, TO ASCC PREDICTED ROUGH WALL HEAT TRANSFER COEFFICIENTS AROUND NOSETIP FOR SHOT 4951 (FLUX-INFERRED TRANSITION-FRONT LOCATION)

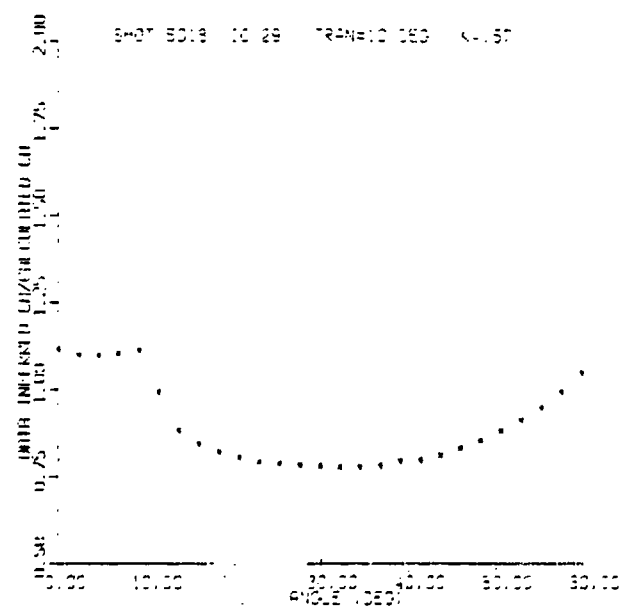
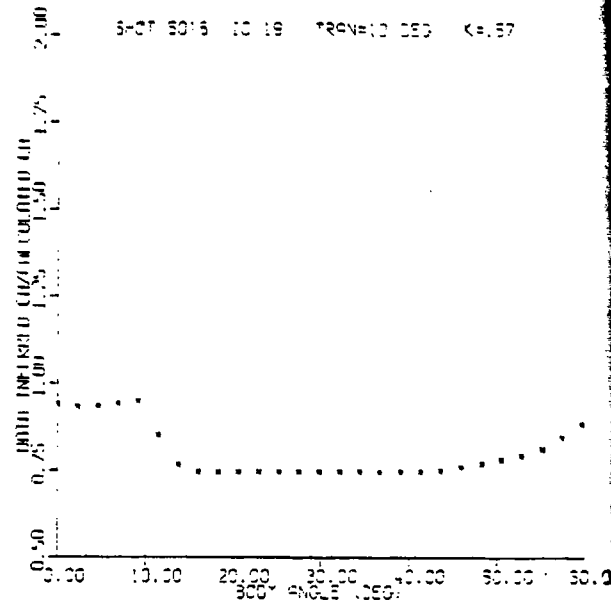
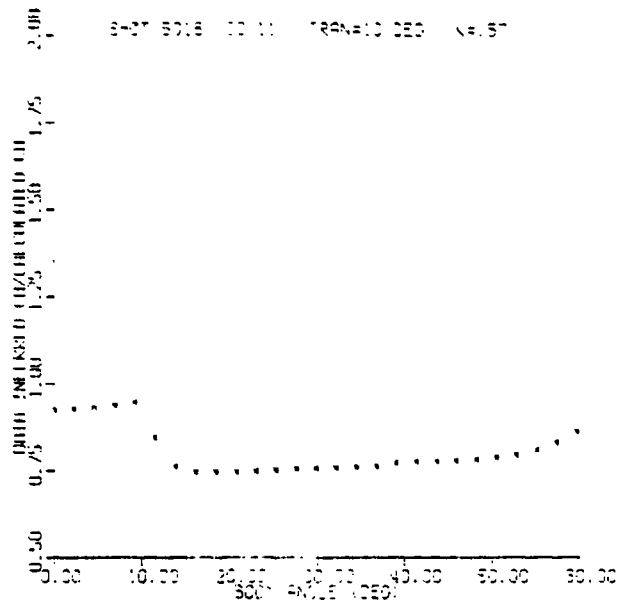


FIGURE 7.37. RATIO OF DATA-INFERRED, TO ASCC PREDICTED ROUGH WALL HEAT TRANSFER COEFFICIENTS AROUND NOSETIP FOR SHOT 5018 (FLUX-INFERRED TRANSITION-FRONT LOCATION)

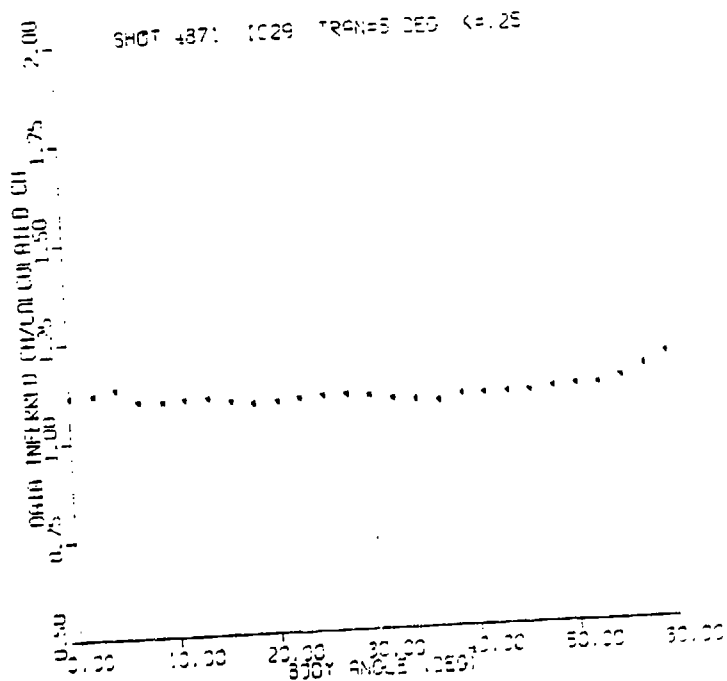
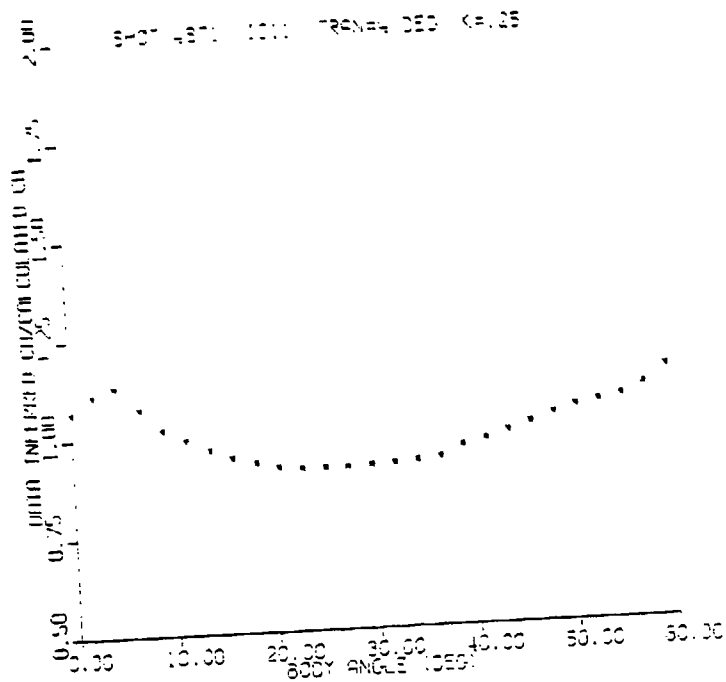


FIGURE 7.38. RATIO OF DATA-INFERRED, TO ASCC PREDICTED ROUGH WALL HEAT TRANSFER COEFFICIENTS AROUND NOSETIP FOR SHOT 4871 (FLUX-INFERRED TRANSITION-FRONT LOCATION)

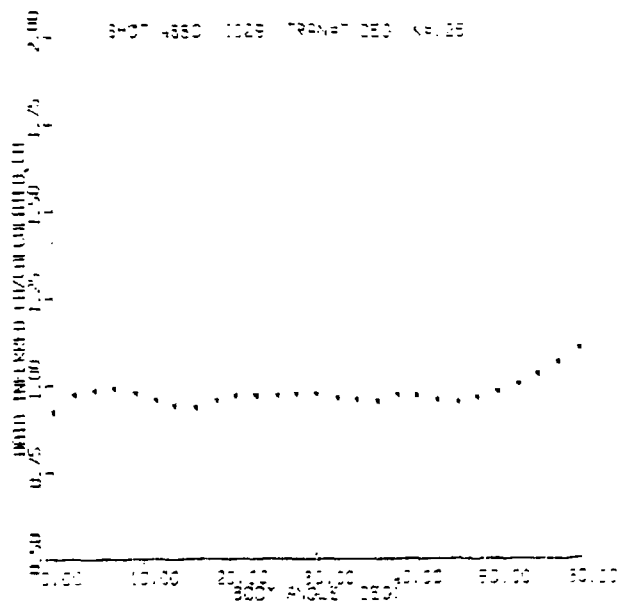
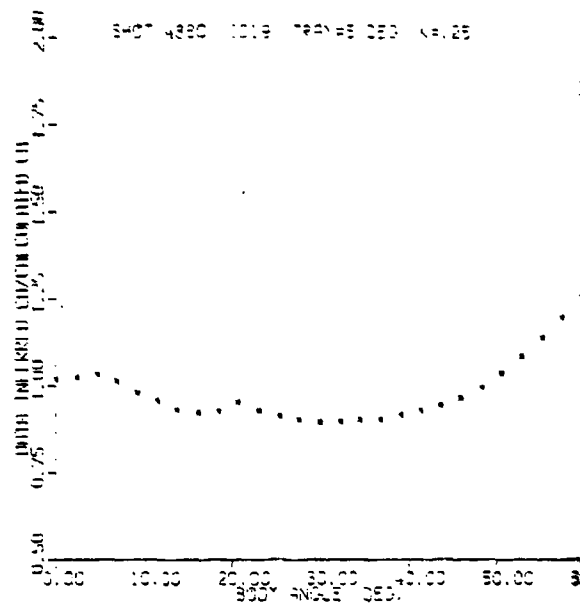
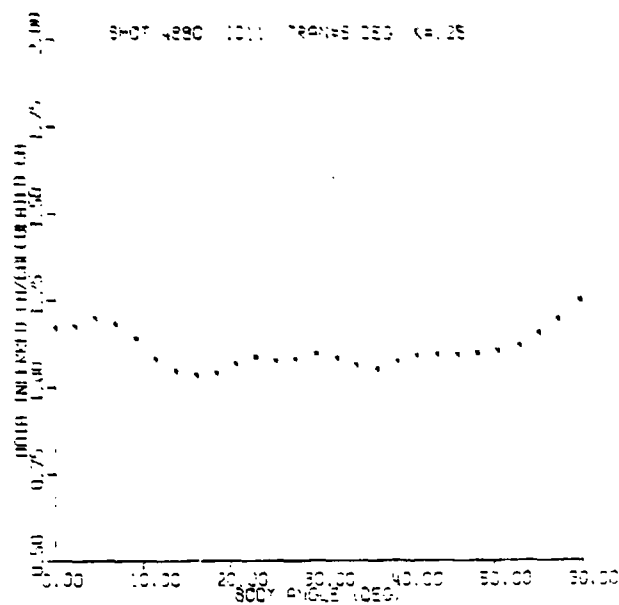


FIGURE 7.39. RATIO OF DATA-INFERRED, TO ASCC PREDICTED ROUGH WALL HEAT TRANSFER COEFFICIENTS AROUND NOSETIP FOR SHOT 4880 (FLUX-INFERRED TRANSITION-FRONT LOCATION)

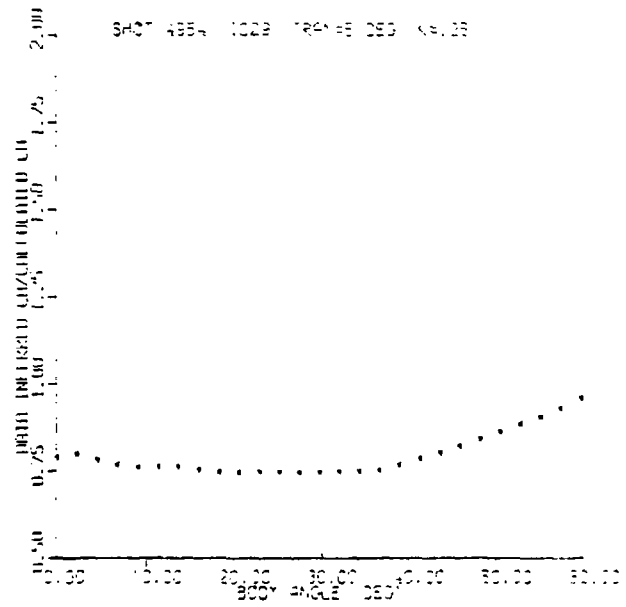
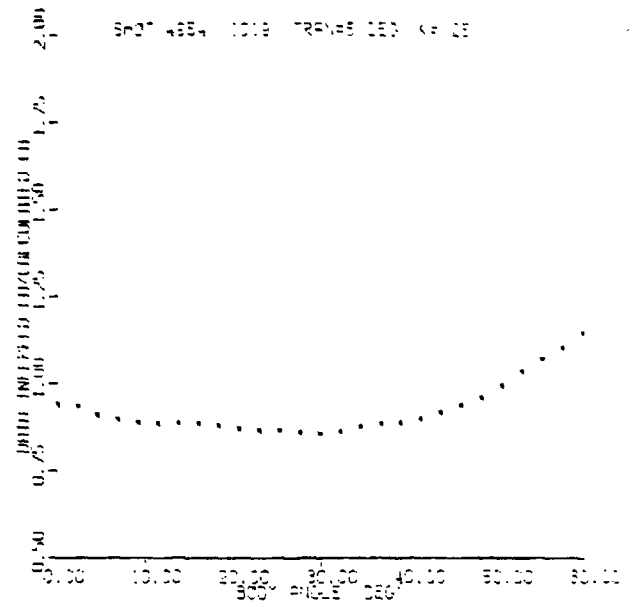
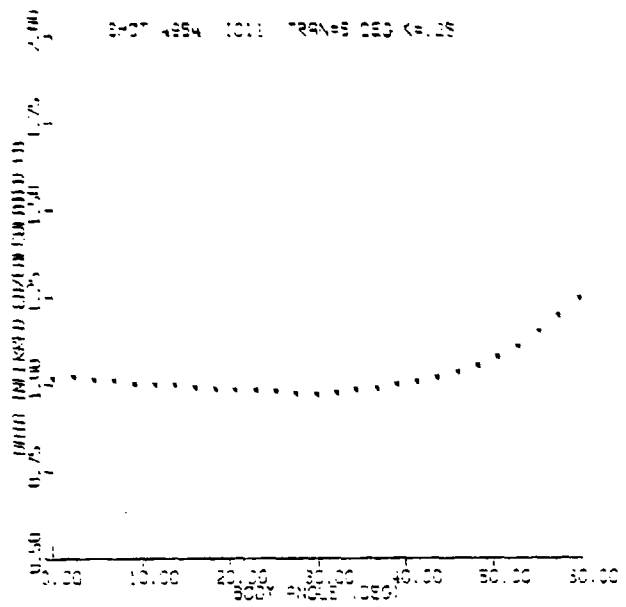


FIGURE 7.40. RATIO OF DATA-INFERRED, TO ASCC PREDICTED ROUGH WALL HEAT TRANSFER COEFFICIENTS AROUND NOSETIP FOR SHOT 4954 (FLUX-INFERRED TRANSITION-FRONT LOCATION)

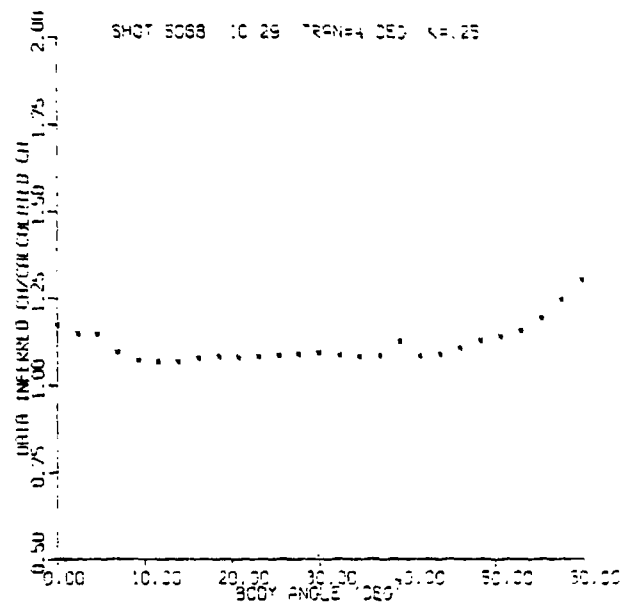
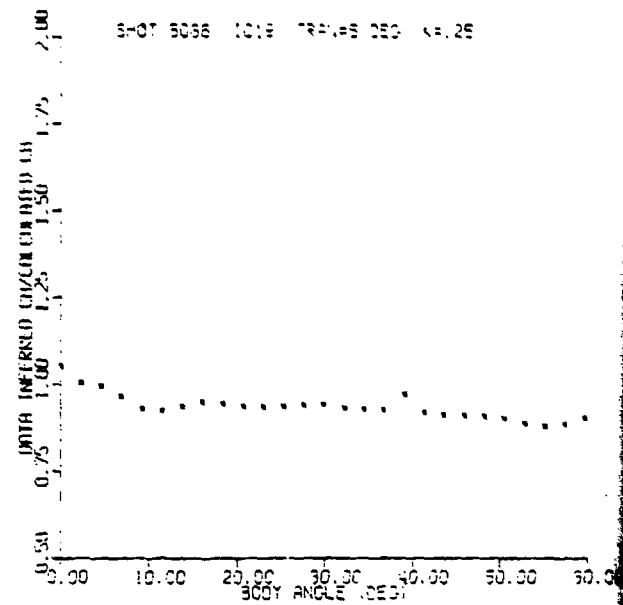
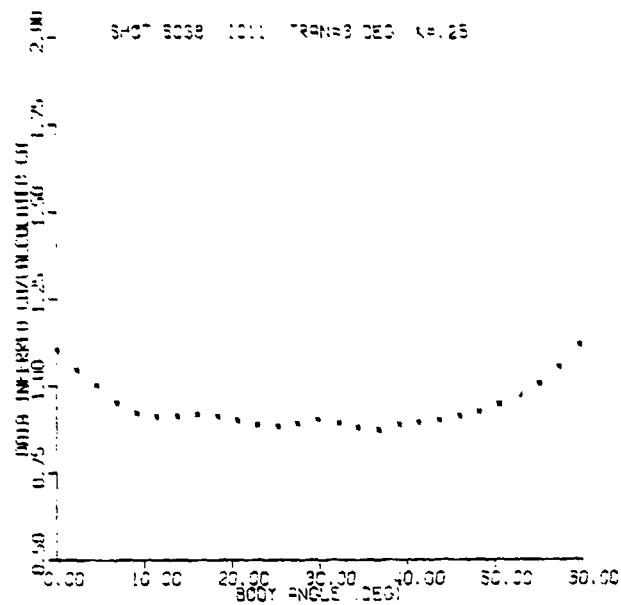


FIGURE 7.41. RATIO OF DATA-INFERRED, TO ASCC PREDICTED ROUGH WALL HEAT TRANSFER COEFFICIENTS AROUND NOSETIP FOR SHOT 5068 (FLUX-INFERRED TRANSITION-FRONT LOCATION)

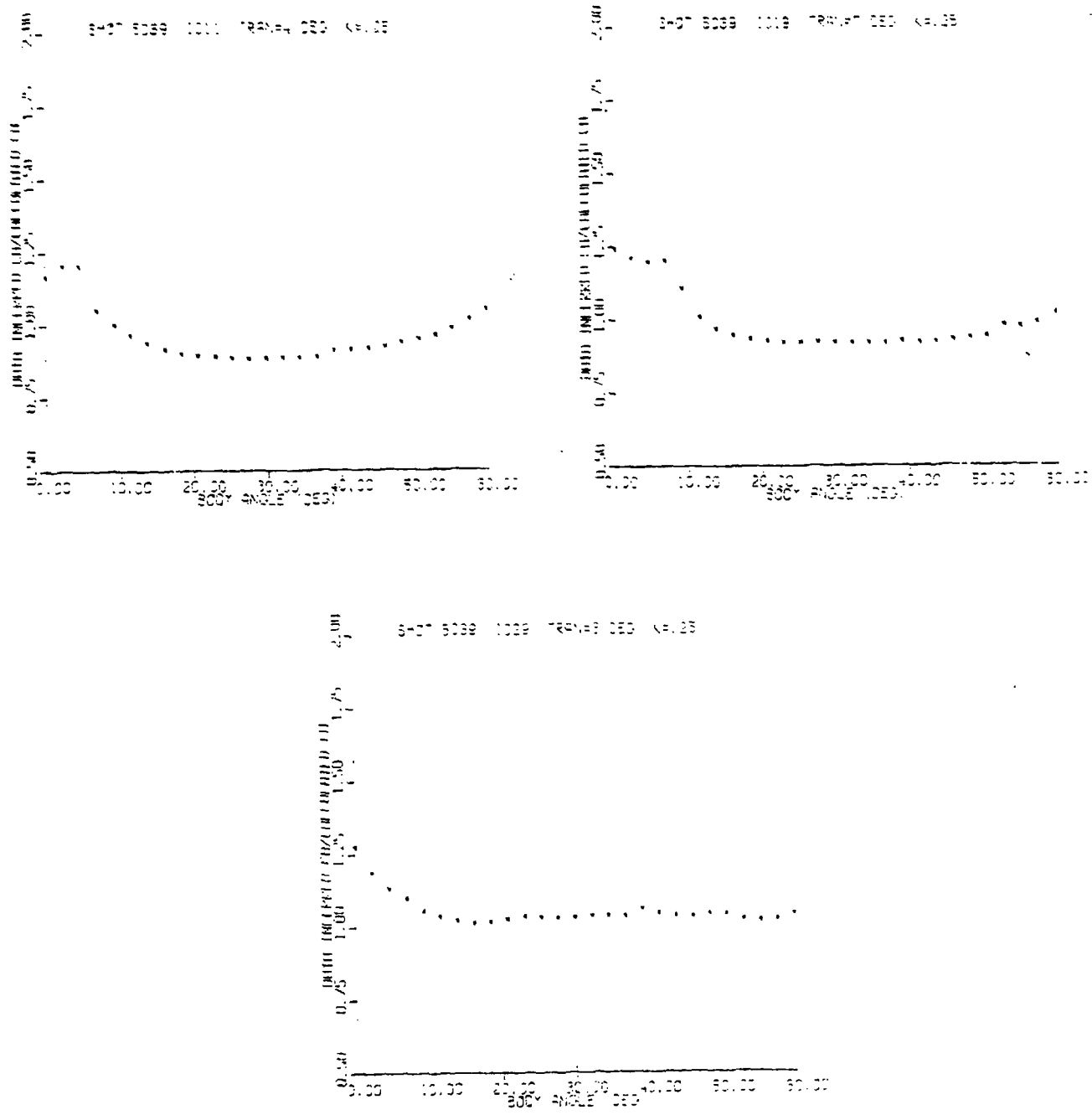


FIGURE 7.42. RATIO OF DATA-INFERRED, TO ASCC PREDICTED ROUGH WALL HEAT TRANSFER COEFFICIENTS AROUND NOSETIP FOR SHOT 5069 (FLUX-INFERRED TRANSITION-FRONT LOCATION)

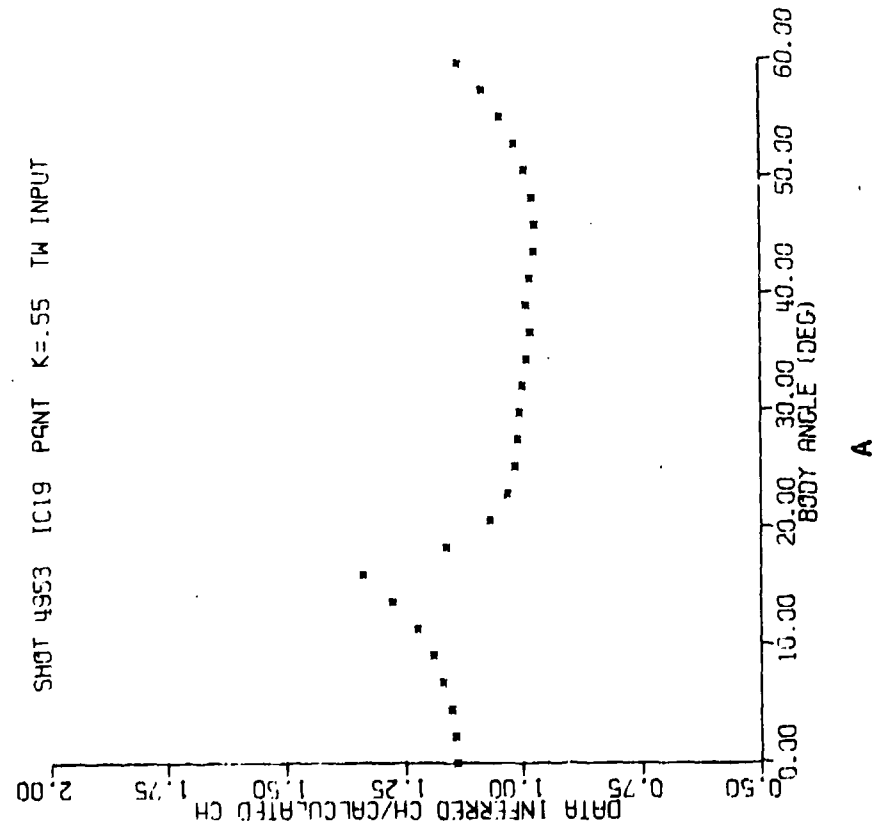
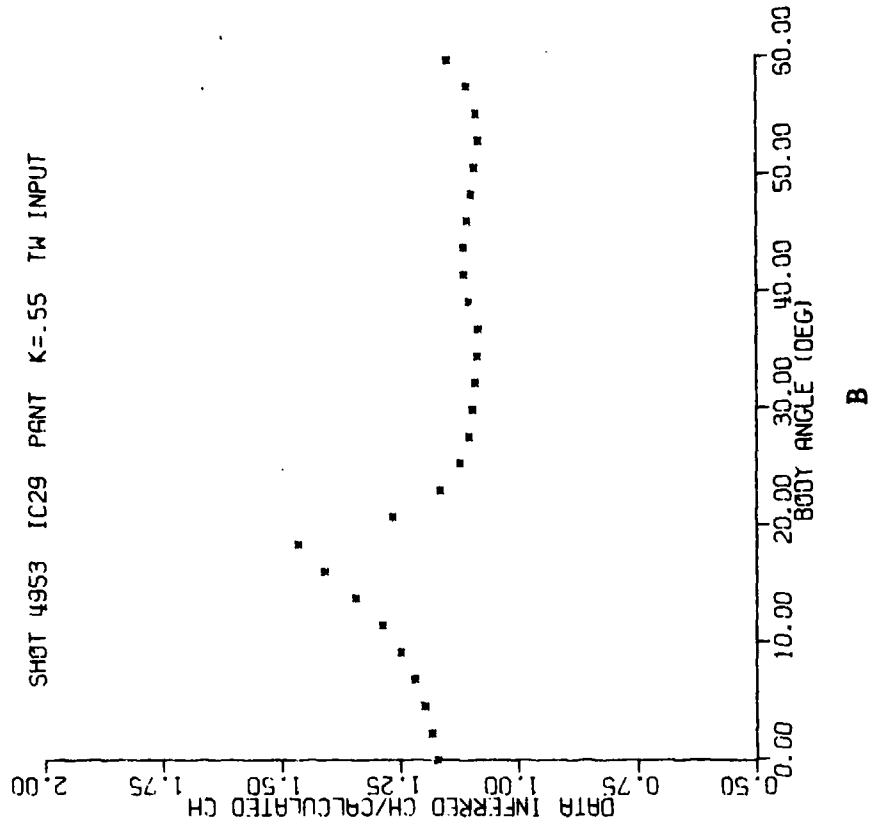


FIGURE 7.43. RATIOS OF DATA DERIVED TO ASCC PREDICTED ROUGH WALL HEAT TRANSFER COEFFICIENTS (TRANSITION PREDICTED BY PANT CORRELATION)

by the PANT correlation. The plots show high heat transfer ratios in the transitional region due to inconsistency in transition location between data and theory.

Similarly, the heat transfer ratios are listed in the table for the case when transition is given by the PANT correlation and transition point set equal to the data inferred values. Detailed comments are also listed in the table.

## 8.0 SUMMARY AND CONCLUSIONS

Transition and heat transfer tests were performed in the AEDC hyperballistics Track-G test facility. The objectives of the tests were:

- 1) Investigate the effects of surface roughness on nosetip transition.
- 2) Investigate the effects of surface roughness on heating augmentation.
- 3) Verify existing simulation methodologies as to their applicability to flight environments.

Tungsten, graphitic and carbon-carbon models were tested. From a flight simulation point of view, the test conditions were selected to simulate altitudes where transition and heating augmentation influence the shape development of nose-tips. From a testing point of view, the test environments were selected to insure nosetip transition and to obtain surface temperatures that are within the dynamic response range of the image converter cameras used to record the nosetip image. This was mainly to ensure more reliable data. The test freestream conditions covered a range of stagnation pressure from approximately 20 to 195 atmospheres and freestream unit Reynolds number from 17 to 70 million/ft.

The surface of the tested models were first preconditioned and then characterized. The tungsten models were either super-polished to obtain a super-smooth surface finish ( $K_{rms} \leq 10 \mu\text{inches} = 0.01 \text{mils}$ ), or preroughened to obtain a uniform surface roughness. The graphite and carbon-carbon models were preablated in the Aerotherm low pressure-high enthalpy arc jet facility, in order to create surface roughnesses similar to those that may develop in a laminar ablation environment prior to nosetip transition. Representative models of each material were then characterized to obtain the surface roughness height statistical distributions. Mean and median roughness heights were then obtained from the roughness distributions.

The temperature data reduction and handling were automated. Temperature data on the entire nosetip were obtained at 3 degree increments along and around the nosetip. The brightness temperature data were recorded on a magnetic tape, which was then processed by computer. For each shot and at each image converter camera location, 120 temperature profiles along the body were obtained. The mean, maximum, and minimum temperatures, as well as standard deviations were then obtained utilizing these 120 profiles.

Sensitivity studies were performed according to Ref. 3 to estimate the level of uncertainties in the measured surface temperature due to surface spectral emissivity, shock layer radiation, surface reactions, motion blur, and gun barrel heating. It is believed that the measured brightness and surface temperatures are accurate to  $\pm 100$  to  $\pm 200$  degrees Kelvin.

The nosetip transition locations were inferred in three ways.

1. At each ICC location the 120 temperature profiles were numerically processed and the transition was taken to be the point of minimum temperature, i.e., the point of zero temperature slope.

2. The 120 temperature profiles were also manually processed, since some engineering judgement was required to determine the transition location, defined as the intersection of the tangents to the laminar and transitional region of the profile.

3. Using the mean temperature profiles at all the ICC locations, the mean heat flux distributions were inferred using a heat conduction code. The transition location was then inferred as the point of intercept of the tangents to the laminar and transitional leg of this mean heat flux curve.

The first approach, though rendering a statistical distribution of the transition front location quite conveniently by the computer, produces results that are biased by the numerical smoothing of the data. The second approach, though tedious, permits a more realistic determination of the transition location. However, inferring transition location from the temperature profiles may

lead to errors due to the smoothing out of the nosetip temperature profiles because of lateral heat conduction, and, more important, due to the transient nature of the tests in the ballistics range, the measured temperature profile shape may be completely different from the corresponding heat transfer distribution. Human judgement must be applied here. However, analyzing 600 temperature profiles per shot is a very tedious task, and an automated system using interactive graphics would be helpful.

Inferring the transition locations from the heat flux distributions allows better definition of the transition-fronts. However, utilizing the mean-temperature histories in deriving the heat flux distribution elements obscures any statistical information on the transition front, due to the averaging process of the surface temperatures around the nosetip at each ICC location.

The results of the transition analyses showed that:

1. For all the tested materials transition was observed on the nosetip and no transition offset occurred. A fully laminar distribution was achieved only on the super smooth tungsten model; otherwise, transition occurred in the stagnation region even for nominally smooth tungsten models.
2. The data indicated transition locations considerably upstream of the PANT transition correlation using the mean roughness height,  $k_{\text{mean}}$ .
3. For certain flight-surface conditions the data indicated transitional flow yet the PANT transition correlation predicted either laminar flow or transition offset.
4. For the test conditions analyzed the PANT transition correlation predictions were upstream of those given by Dirling's and Bishop's transition models.
5. The inferred transition-front locations were quite scattered when compared with the Reda-Raper transition location-range pressure correlation.
6. The inferred roughness heights, that is, roughness heights to produce agreement with the PANT predictions, were of the order of the roughness associated with the matrix or weave structure for CC-223 and considerably higher than the  $k_{\text{mean}}$  for the other tested materials.

Stagnation point heat transfer augmentation factors were derived at each ICC location. The data inferred heat transfer rates were then compared with laminar theory predictions. To eliminate any wall temperature effects, the comparisons were performed for the same wall temperatures as the data. The derived augmentation factors were then compared with the predictions of the PANT and Phinneys laminar augmentation correlations. The stagnation point results can be summarized as follows:

1. Stagnation point augmentation factors were observed in the ballistic range environments.
2. The data were scattered but a 20% excess in heat transfer over and above the laminar theory exists.
3. The PANT laminar augmentation correlation did not predict augmentations for the flight regime considered.
4. The Phinneys augmentation correlation over-predicted the observed factors.

The data-derived heat transfer distributions around the nosetip were then compared with smooth wall predictions, (in order to infer rough wall transitional/turbulent heating augmentation levels) and rough wall predictions (to verify the ASCC rough wall methodology). The comparisons were performed for two situations, where the transition-front locations were either set equal to the data inferred values, or predicted by the PANT transition criteria.

The heat transfer results off the stagnation point showed that:

1. Comparisons between the data derived heat fluxes and the predicted *smooth wall* values, indicated that roughness effects are small ( $\approx 20\%$ ). Although, the transition-front locations in the calculations were set equal to the data inferred values, it is not certain whether the predicted transition region width is equal to that on the model in flight.

2. Comparisons between the data derived heat fluxes and the ASCC predicted *rough wall* values, also indicated that roughness effects are small. The predictions showed relatively small values of the roughness Reynolds numbers,  $k^+$ , and that the boundary layer is mainly transitional. For certain flow situations the ASCC-rough wall overpredicted the data by 25%.

3. In verifying the heat transfer prediction models off the stagnation point, it is essential that the transition front location be consistent between data and theory. For certain test conditions the experimentally observed heat flux showed that the flow was turbulent, while the predictions indicated a laminar or relaminarized flow. In this case one is taking the ratio of a turbulent flux to a laminar one, and the ratio becomes larger, as expected and shown in Section 7.

4. Obtaining the heat transfer augmentation factors by simply taking the ratio of the rough-wall data-inferred heat flux to the smooth wall predicted value at the same streamwise location on the nosetip, is misleading. This ratio can assume any value since the rough wall boundary layer is quite different from that of a smooth wall, hence the boundary layer parameters are different in the two cases. One has to correlate the rough wall heat transfer (and not the augmentation factors) with the rough wall boundary layer parameters e.g.,  $k/\theta$ ,  $k^+$ ,  $h_w/h_e$ .

Based on the above discussion one can conclude the following:

1. The use of in-flight surface temperature to verify nosetip aerothermal predictive methodologies requires complex data reduction, due to the high coupling between transition, heating augmentation and roughness effects.

2. A detailed look at the individual temperature profiles along the nosetip at each ICC location is useful for defining transition front locations. An interactive

graphics system is essential here for the data reduction process. The results however can be very misleading (4 below).

3. Inferring the transition location from the data-derived heat flux eliminates any statistical behavior of the transition front due to the smoothing of the temperature variations affected by the averaging process of the data.

4. It is essential to infer the transition-front locations from the derived heat transfer data. Inferring transition only from the temperature data can be seriously in error in situations where transition offset takes place. Due to the transient nature of the model response the temperature data may indicate a transitional/turbulent distribution but in reality the heat flux indicates a laminar distribution. The temperature data can therefore indicate, erroneously, a forward movement of the transition-front. However, the temperature data can predict transition locations correctly at the early ICC locations (ICC 4 and 11) and give information on statistical distribution of the front.

The approach then should be that transition be inferred from heat flux data and further refined and checked by information obtained from the temperature data. One can not rely only on the temperature data. Heat flux calculations should then be performed and compared with heat flux data for both laminar and turbulent situations in order to insure whether or not transition offset took place.

5. Transition-front locations were considerably upstream of the PANT, Dirling's and Bishop's predictions. Also, no relaminarization was observed. The PANT correlation predicted transition upstream of those of Dirling's and Bishop's, respectively.

6. Due to the transient nature of the problem, predictive models verifications by comparison between the measured and predicted surface temperature at *one* ICC location can be very misleading and markedly in error. Comparisons must be performed at *all* ICC locations. This approach however, is tedious due to the strong coupling between transition, heat transfer and surface roughness effects.

7. While higher roughness levels might seem indicated from the transition data, larger roughness heights will lead to higher heat transfer rates. This may result in poorer agreement between data and theory for the heat transfer. It seems likely that roughness heights that correlate with transition data may not be those correlating with heating augmentation data.

8. The hyperballistics range track facility is a unique ground test facility to simulate a wide range of flight environments. Flow uncertainties that exist in wind tunnel and arc jet facilities, e.g., pressure fluctuations, freestream turbulence, are absent. Other track related problems appear to have been resolved.

## 9.0 RECOMMENDATIONS

It seems clear that the ballistics range will become an increasingly important facility in the study of aerothermal processes on hypervelocity vehicles and in the development of new materials and concepts. Recommendations for utilization and near-term improvements of the ballistics range are summarized below.

1. Continue using the guided track mode of testing in investigating transition characteristics and heat transfer on nosetips.

2. Test well and better characterized materials (W, ATJ-S, 994-2) to understand the basic transition phenomena before investigating more complicated materials (FWPF, CC).

3. Reduce ballistic range data to key boundary layer and material response parameters necessary to more carefully assess the events and shortcomings of competing transition and rough wall heating techniques.

4. Use the developed ballistics range test techniques to investigate transition and heat transfer of non-spherical configurations, e.g., ellipsoids, nosetips at angle of attack and aerodynamic control surfaces.

5. Expand the materials performance characterizations begun in this program to encompass all candidate advanced nose-tip material characterization work, transition modeling studies, nosetip shape change modeling work, and other related experimental programs (CALSPAN, Tunnel F).

6. Make ballistics range testing, using the technology developed under these (and other) programs, an integral part of the pre-flight evaluation process for new materials and concepts, to complement the testing standardly carried out in the AFFDL 50 MW facility.

7. Add high sensitivity image converter cameras at uprange stations to improve data reduction accuracies. Reduction of measured temperatures to heating rates is absolutely essential if any reliable conclusions are to be drawn concerning transition and rough wall heating. Addition of at least one camera would greatly enhance data confidence.

8. Develop an interactive-graphics system at AEDC which enables the detailed investigation of the individual temperature profiles on the nosetip at each ICC location (600 total per shot). This system is essential for investigation of nosetip transition asymmetry and possibly gouge formation.

## 10.0 REFERENCES

1. Holden, M. S., "Studies of Transitional Flow, Unsteady Separation Phenomena and Particle Induced Augmentation Heating on Ablated Nosedtips," AFOSR-TR-76-1066, Oct. 1975.
2. Roda, D. C., Leverance, R. A., "Boundary-Layer Transition Experiments on Pre-Ablated Graphite Nosedtips in a Hyperballistics Range," AIAA Paper 76-356, Presented at the AIAA 9th Fluid and Plasma Dynamics Conference, San Diego, California, July 14-16, 1976.
3. Shih, W. C. L., Wassel, A. T., Kessler, A. J., Courtney, J. F., "Evaluation of Reentry Vehicle Nosedtip Transition and Heat Transfer in the Hyperballistics Range," SAI-79-541-LA, July, 1978.
4. Norfleet, G. D., Hendrix, R. E., "Development of a Hypervelocity Track Facility at AEDC," AIAA paper 77-151, Presented at AIAA 15th Aerospace Sciences Meeting, Los Angeles, Calif., January 24-16, 1977.
5. Dynner, H. B., "Test Facilities Used for Advanced Ballistic Reentry Systems R and D," Aerospace Report No. TOR-0077(2550-71)-2, 20 June 1977.
6. Wool, M. R., et al., "Interim Report - Passive Nosedtip Technology (PANT) Program - Computer User's Manual SAANT Program (U)," SAMSO-TR-74-86, Vol. 7, 1974.
7. Fogaroli, R. P., Brant, D. N., "Re-Evaluation of Graphite Thermo-Chemical Ablation," GE Thermodynamics Laboratory, Fundamentals Memo TRM-9151-060, October 1968.
8. Kratch, K. M., et al., "Graphite Ablation in High-Pressure Environments," AIAA Paper No. 68-1153, December 1968.
9. Dirling, R. B., Jr., "A Method for Computing Rough Wall Heat Transfer Rates on Reentry Nosedtips," AIAA Paper No. 73-763, AIAA 8th Thermophysics Conference, Palm Springs, California, July 1973.
10. R. B. Dirling, Jr., D. A. Eitman and J. D. Binder, "Evaluation of Post-Test Ablation Models," AFML TR-77-225, Dec. 1977.
11. Dugger, P. H., Bock, O. H., Enis, C. P., Gilley, B. W., "Photographic Pyrometry in an Aeroballistics Range," Proceedings of the SPIE 16th Annual Technical Meeting, San Francisco, California, October 1972.

12. Norfleet, G. D., Hendrix, R. E., Raper, R. M., Callens, E. E., Jr., "Development of an Aeroballistics Range Capability for Testing Reentry Materials," JSR 12, 5, pp. 302-307, 1975.
13. Reda, D. C., Leverance, R. A., Dorsey, W. G., Jr., "Application of Electro-Optical Pyrometry to Reentry Vehicle Nosedip Testing in a Hyperballistics Range," 6th International Congress on Instrumentation in Aerospace Simulation Facilities, 22-24 September 1975.
14. Anderson, A. D., "Evaluation of Theoretical Methods for the Predication of Nosedip Boundary Layer Transition," Aerotherm/Accurex TM-75-77.
15. Bishop, "Transition Induced by Distributed Roughness on Blunt Bodies in Supersonic Flows," SAMSO-TR-76-146, 29 Oct. 1976.
16. Dirling, R.B. "The Effect of Transition and Boundary Layer Development on Hypersonic Reentry Shape Change," MDAC Paper WD 2507, May 1975.
17. Dahm, T. J., et al., "Passive Nosedip Technology Program, Vol. I: Inviscid Flow and Heat Transfer Modeling for Reentry Vehicle Nosedips," Aerotherm Report -76-224, Oct. 1976.
18. Clever, R. M. and Denny, V. E., "Two-Dimensional Transient Conduction and Shape Change Analysis," SAI-78-538-LA, March 1977.
19. Hildebrand, F. B., "Introduction to Numerical Analysis," McGraw Hill, N. Y., 1956.
20. Reda, D. C. and Raper, R. M., "Measurements of Transition-Front Asymmetries on Large-Scale, Ablating Graphite Nosedips in Hypersonic Flight," AIAA 79-0268, 17th Aerospace Sciences Meeting, New Orleans, LA., Jan. 15-17, 1979.

## DISTRIBUTION LIST

Ballistic Missile Office  
BMO/SYDT  
Attn: Maj. K. Yelmgren (2)  
Norton AFB, CA 92409

Defense Technical Information Center (2)  
Cameron Station  
Alexandria, VA 22314

Air University Library  
Maxwell AFB, AL 36112

TRW DSSG  
Attn: W. Grabowsky (2)  
P. O. Box 1310  
San Bernardino, CA 92402

TRW Systems Group (2)  
Attn: J. Ohrenberger  
M. Gyetvay  
1 Space Park  
Redondo Beach, CA 92078

Headquarters, Arnold Engineering  
Development Center  
Arnold Air Force Station  
Attn: Library/Documents  
Tullahoma, TN 37389

Armament Development and Test Center  
Attn: Technical Library, DLOSL  
Eglin AFB, FL 32542

Air Force Wright Aeronautical Laboratories (3)  
Air Force Systems Command  
Attn: M. Buck (AFWAL/FIM)  
R. Neumann (AFWAL/FIMG)  
V. Dahlem (AFWAL/FIMG)  
Wright-Patterson AFB, OH 45433

U. S. Army Ballistic Missile  
Defense Agency/ATC-M  
Attn: J. Papadopoulos  
P. O. Box 1500  
Huntsville, AL 35807

Director, Defense Nuclear Agency  
Attn: J. Somers (SPAS)  
Washington, DC 20305

Naval Surface Weapons Center  
Attn: Carson Lyons/K06  
White Oak Laboratories  
Silver Spring, MD 20910

Acurex Aerotherm  
Aerospace Systems Division  
Attn: C. Nardo  
485 Clyde Avenue  
Mountain View, CA 94042

Avco Systems Division  
Attn: N. Thyson  
201 Lowell Street  
Wilmington, Mass 01887

General Electric Company  
Attn: R. Neff  
3198 Chestnut Street  
Philadelphia, PA 19101

Lockheed Missiles and Space Co.  
P. O. Box 504  
Attn: G. T. Chrusciel  
Sunnyvale, CA 94086

McDonnell Douglas Astronautics Co.  
Attn: J. Copper  
5301 Bolsa Avenue  
Huntington Beach, CA 92647

PDA Engineering  
Attn: M. Sherman  
1560 Brookhollow Drive  
Santa Ana, CA 92705

Sandia Laboratories  
P. O. Box 5800  
Attn: Library  
Albuquerque, NM 87115

Science Applications, Inc.  
Attn: A. Martellucci  
994 Old Eagle School Road  
Suite 1018  
Wayne, PA 19087